



HAL
open science

Generation and manipulation of photonic states for quantum communication

Mohamed Faouzi Melalkia

► **To cite this version:**

Mohamed Faouzi Melalkia. Generation and manipulation of photonic states for quantum communication. Quantum Physics [quant-ph]. Université Côte d'Azur, 2022. English. NNT : 2022COAZ4066 . tel-04025939

HAL Id: tel-04025939

<https://theses.hal.science/tel-04025939>

Submitted on 13 Mar 2023

HAL is a multi-disciplinary open access archive for the deposit and dissemination of scientific research documents, whether they are published or not. The documents may come from teaching and research institutions in France or abroad, or from public or private research centers.

L'archive ouverte pluridisciplinaire **HAL**, est destinée au dépôt et à la diffusion de documents scientifiques de niveau recherche, publiés ou non, émanant des établissements d'enseignement et de recherche français ou étrangers, des laboratoires publics ou privés.



$$\rho \left(\frac{\partial v}{\partial t} + v \cdot \nabla v \right) = -\nabla p + \nabla \cdot T + f$$

$$e^{i\pi} + 1 = 0$$

THÈSE DE DOCTORAT

Génération et manipulation d'états photoniques pour la communication quantique

Mohamed Faouzi Melalkia

Institut de Physique de Nice (INPHYNI), CNRS, UMR 7010

**Présentée en vue de l'obtention
du grade de :** docteur en physique
de l'Université Côte d'Azur

Dirigée par : Virginia D'Auria,
Sébastien Tanzilli

Soutenu le : 24 octobre 2022

Devant le jury, composé de :

Juan Ariel Levenson, Directeur de recherche, CNRS, C2N,
Université Paris-Saclay

Florent Baboux, Maître de conférences, MPQ, Université Paris
Cité

Marco Liscidini, Professeur associé, Université de Pavie

Fabrice Raineri, Professeur, INPHYNI, Université Côte d'Azur

Virginia D'Auria, Maîtresse de conférences, INPHYNI,
Université Côte d'Azur

Sébastien Tanzilli, Directeur de recherche, CNRS, INPHYNI,
Université Côte d'Azur

Generation and manipulation of photonic states for Quantum communication

Composition du jury :

<i>Juan Ariel Levenson</i>	Directeur de recherche, CNRS, C2N, Université Paris-Saclay	Rapporteur
<i>Florent Baboux</i>	Maître de conférences, MPQ, Université Paris Cité	Rapporteur
<i>Marco Liscidini</i>	Professeur associé, Université de Pavie	Examineur
<i>Fabrice Raineri</i>	Professeur, INPHYNI, Université Côte d'Azur	Examineur
<i>Virginia D'Auria</i>	Maîtresse de conférences, INPHYNI, Université Côte d'Azur	Directrice de thèse
<i>Sébastien Tanzilli</i>	Directeur de recherche, CNRS, INPHYNI, Université Côte d'Azur	Codirecteur de thèse

To my dear parents, my brother Zakaria, and my sisters Fatma and Sara.

To my wife Ikram. To the best gifts that I have ever had, my son Youcef and my daughter Leile (who was born three weeks after my thesis defense).

To the QPI team, to everyone who had supported me.

— Mohamed Faouzi MELALKIA.

RÉSUMÉ COURT

Dans cette thèse, nous poussons les investigations théoriques, la génération et manipulation expérimentales des états quantiques photoniques un pas vers des applications de communication quantique autonomes hors laboratoire. En particulier, nous montrons la faisabilité des réalisations expérimentales basées sur des approches d'optique guidée et intégrée dans les régimes continus et pulsés à une longueur d'onde télécom. Cela marque un progrès important vers des technologies optiques quantiques pratiques dans des implémentations sur le terrain. De plus, des investigations théoriques montrent la possibilité de produire des états de lumière non gaussiens de haute qualité et de haute amplitude avec des ressources raisonnables, ce qui rend possible la conception des systèmes pour la génération et la manipulation d'états quantiques avec des caractéristiques prometteuses.

SHORT ABSTRACT

In this thesis, we push the theoretical investigations, the experimental generation and the manipulation of photonic quantum states a step towards out-of-the-laboratory stand-alone quantum communication applications. In particular, we show the feasibility of experimental realizations based on guided-wave and integrated approaches in both the CW and the pulsed regimes at a telecom wavelength. This marks an important progress towards practical quantum optical technologies in real field implementations. In addition, theoretical investigations show the possibility of producing high quality and high amplitude non-Gaussian states of light with reasonable resources, making it possible to design systems for quantum state generation and manipulation operations with promising features.

RÉSUMÉ

Le travail présenté dans cette thèse est principalement divisé en deux parties. Une première partie expérimentale dans laquelle des réalisations basées sur des solutions d'optique guidée et d'optique intégrée à une longueur d'onde télécom sont mises en œuvre dans les régimes continu et pulsé. La motivation derrière cette partie est de développer des solutions et techniques expérimentales permettant des implémentations de protocoles de communication quantique sur le terrain. La deuxième partie consiste en l'étude théorique de la génération d'états quantiques non gaussiens de haute qualité et de haute amplitude avec des ressources relativement raisonnables.

Dans la partie expérimentale, trois réalisations sont présentées. La première consiste à générer des états de type chat de Schrödinger en régime continu à une longueur d'onde télécom utilisant une approche d'optique guidée basée sur des composants fibrés disponibles sur le marché. Une deuxième réalisation consiste en la conception et la caractérisation expérimentale d'une source SPDC guidée pour la génération d'états quantiques discrets et continus de haute qualité ainsi que l'intrication hybride. Enfin, le troisième travail expérimental concerne les premières caractérisations des résonateurs de type micro-anneaux en nitrure de silicium à faible perte et à haut facteur de qualité pour la génération d'intrication multimode dans un peigne de fréquence. Ces implémentations expérimentales sont menées dans le but d'évoluer vers des applications de protocoles de communication quantique hors laboratoire.

D'autre part, deux études théorique sont menées dans la deuxième partie. Dans un premier temps, nous développons un cadre théorique pour décrire l'opération de soustraction de photons à partir d'un état quantique multimode. En appliquant ce cadre au cas de la production d'états de type chat de Schrödinger, nous montrons que des états non gaussiens de haute qualité peuvent être obtenus avec des solutions simples et non sélectives de mode dans le régime multimode. Ensuite, nous proposons un nouveau protocole pour la génération d'état non gaussien de haute amplitude basé sur les capacités de multiplexage offertes par les sources photoniques, réduisant considérablement la complexité et augmentant les performances par rapport aux protocoles itératifs déjà existants.

Mots clefs optique quantique à variables continues, communication quantique, optique intégrée, états quantiques non gaussiens, détection homodyne, tomographie des états quantiques

ABSTRACT

The work presented in this thesis is mainly divided into two part. In a first experimental part, experimental realisations based on guided-wave and integrated optical solutions are implemented in the continuous-wave as well as the picosecond pulsed regimes at a telecom wavelength. The motivation behind this part is to develop experimental solutions and techniques enabling real field implementations of quantum communication protocols. The second part consists in theoretically investigating already existing as well as novel approach for high quality and high amplitude non-Gaussian quantum state generation with relatively reasonable resources.

In the experimental part, three realizations are presented. The first one consists in the generation of Schrödinger cat-like state in continuous-wave regime at a telecom wavelength in a guided-wave approach based on off-the-shelf fiber components. A second realization consists in the design and the experimental characterization of an guided-wave SPDC-based source for the generation of high quality discrete- and continuous-variable quantum states as well as hybrid entanglement. Finally, in the third experimental work we perform the first characterizations of low-losses and high quality factor silicon nitride micro-ring resonators for multimode entanglement generation in Kerr frequency comb. These experimental implementations are conducted with the goal of moving towards out-of-the-laboratory applications of quantum communication protocols.

On the other hand, two main studies are conducted within the theoretical part. At first, we develop a theoretical framework to describe photon subtraction operation from a multimode quantum resource. Applying this framework to the case of Schrödinger cat-like state production, we show that high quality non-Gaussian states can be obtained with reasonable non-mode-selective solutions in the multimode regime. Then, we propose a novel protocol for the generation of high amplitude non-Gaussian state based on the multiplexing capabilities offered by the state-of-the-art photonic sources, drastically reducing the complexity and increasing the performances compared to previously proposed iterative protocols.

Keywords continuous variable quantum optics, quantum communication, integrated optics, non-Gaussian quantum states, homodyne detection, quantum state tomography

ACKNOWLEDGMENT

Inn October 2018, I remember when I got the doctoral scholarship from the Algerian government and I started looking for thesis proposals in quantum optics, then I found one proposed by Virginia D'Auria and Sébastien Tanzilli in the Quantum Photonics & Information (QPI) team at the Institute of Physics in Nice (INPHYNI). At that time, I started writing an application email to Sébastien hoping to get a response in the following few months, but the reply was too fast, in fact Sébastien took exactly 33 minutes to email me back. The following days, and after few emails and a phone call with Sébastien, I had the chance to be accepted by the QPI leader to be part of the PhD students within his team, this was the starting point for a three-years scientific journey at the INPHYNI lab.

First, I would like to thank my supervisors. Thanks to Sébastien Tanzilli, who gave me the chance to be a member of one of the best research teams, not only for providing the necessary resources to the students and researchers, but also for offering them the best working conditions. Before starting my PhD, I was a big fan of Sébastien, and here I am, writing his name as a supervisor in my manuscript. Despite his often very busy schedule, he was always there when I needed him, thank you Sébastien. I would also like to thank Virginia D'Auria, for her trust, open-mindedness and her support during my thesis. As I have always said, it is really rare to find such a supervisor who, in addition to her scientific and technical support that allowed me to conduct my thesis, was always there listening to me and providing me social and emotional support when I needed it. I really don't have enough words to thank you. Also, although my first contact with theoretical and experimental quantum optics was during my thesis, it was possible for me to obtain such good results. If so, it is thanks to Jean Etesse, who gave me a scientific boost in such a short time to achieve what I am presenting in this manuscript. I only hope that one day, I will be a Jean-like excellent researcher. Thank you Jean.

I would also like to thank all the permanent members of the QPI team: Laurent Labonté, Olivier Alibart, Anthony Martin, Florent Doutre, Eric Picholle and Grégory Sauder. Also, thanks to all the PhD and post-doctoral students, with whom I was able to interact during my PhD: Elie Gouzien, Léandre Brunel, Xin Hua, François Mondain, Adrien Bensamhoun, Mathis Cohen, Romain Dalidet, Gaspare Esposito, Angela Haykal, Marouane Khelifa, Alek Lagarrigue, Yoann Pelet, Antoine Petitjean, Charlotte Pignol, Tess Troisi.

I would also like to acknowledge our collaborators from the following laboratories: INO-CNR, LENS, CEA-Leti, C2N, and the FEMTO-ST institute. A special thank to Tecla Gabbrielli and her supervisor Alessandro Zavatta, with whom we worked on the experiment presented in [chapter 3](#).

Then, I would like to thank all the administrative and technical staff of the INPHYNI lab with whom I was able to interact during these three years.

I must also thank all my thesis reviewers: Juan Ariel Levenson, Florent Baboux, Marco Liscidini, and Fabrice Raineri for giving me some of their time to evaluate my

work. I would also like to thank the director of the doctoral school EDSFA, Elisabeth Taffin de Givenchy, for her precious help that allowed me to organize a face-to-face thesis defense despite the time restrictions.

My gratitude should go as well to my wife Ikram, who gave me two precious gifts, my son Youcef who was born during the second year of my thesis, and my daughter Leila, born three weeks after my thesis defense. Thank you for your unconditional support during these years, and especially, for taking care of Youcef almost alone when I was writing this manuscript, it was not so easy, especially for a 9 months pregnant lady. Thank you.

Last but not least, I would like to thank my parents for their constant support and encouragement, even being far away all these three years. If I am here now, it is thanks to them, who raised and educated me despite the very limited means. Thank you, Love you.

LIST OF PUBLICATIONS

PEER-REVIEWED ARTICLES

1. MF Melalkia, L Brunel, S Tanzilli, J Etesse, and V D'Auria. « Theoretical framework for photon subtraction with non-mode-selective resources ». In: *Physical Review A* 105.1 (2022), p. 013720. url: <https://journals.aps.org/prabstract/10.1103/PhysRevA.105.013720>.
2. Mohamed F. Melalkia, Tecla Gabbrielli, Antoine Petitjean, Léandre Brunel, Alessandro Zavatta, Sébastien Tanzilli, Jean Etesse, and Virginia D'Auria. « Plug-and-play generation of non-Gaussian states of light at a telecom wavelength ». In: *Optics Express* 30.25 (2022), pp. 45195-45201. url: <https://opg.optica.org/oe/abstract.cfm?URI=oe-30-25-45195>.
3. MF Melalkia, J Huynh, S Tanzilli, V d'Auria, and J Etesse. « A multiplexed synthesizer for non-Gaussian photonic quantum state generation ». In: arXiv preprint arXiv:2206.14915 (2022). url: <https://arxiv.org/abs/2206.14915>.

CONFERENCES

1. M. F. Melalkia, J. Etesse, S. Tanzilli, and V. D'Auria. « Effect of filtering on the generation of Schrödinger cat-like states from a pulsed multimode squeezing ». 11th Colloquium of the CNRS GDR N° 3322 on Quantum Engineering, Foundations & Applications – IQFA, Université Grenoble Alpes (UGA) - France, Dec. 2-4, 2020. url: <https://hal.science/hal-03942672>.
2. M. F. Melalkia, S. Tanzilli, J. Etesse, and V. D'Auria. « Spectral filtering in photon-subtraction experiments: Application to the generation of cat-like states ». 2021 Nongauss Quantum Workshop, Czech Republic, May. 18-20, 2021. url: <https://hal.science/hal-03942724>.
3. M. F. Melalkia, L. Brunel, S. Tanzilli, J. Etesse, and V. D'Auria. « A multimode framework to describe photon subtraction operation ». 13th Italian Quantum Information Science Conference, Naples - Italy, Oct. 11-15, 2021. url: <https://hal.science/hal-03942762>.
4. M. F. Melalkia, L. Brunel, F. Mondain, T. Lunghi, F. Doutre, A. Zavatta, S. Tanzilli, J. Etesse, and V. D'Auria. « Guided-wave solutions for generating and manipulating squeezed light ». *Optique Dijon 2021*, Dijon - France, Jul. 5-9, 2021. url: <https://hal.science/hal-03943121>.
5. M. F. Melalkia, L. Brunel, F. Mondain, T. Lunghi, F. Doutre, A. Zavatta, S. Tanzilli, J. Etesse, and V. D'Auria. « Guided-wave solutions for squeezing generation and manipulation ». *The International Conference on Quantum Communication ICQOM 2021*, Paris - France, Oct. 18-22, 2021. url: <https://hal.science/hal-03943150>.

6. M. F. Melalkia, J. Huynh, S. Tanzilli, V. D'Auria, and J. Etesse. « Generation of non-Gaussian quantum photonic states with multimode input resources ». 12th Colloquium on Quantum Engineering, Fundamental Aspects to Applications – IQFA'XII, ENS de Lyon - France, Nov. 3-5, 2021. url: <https://hal.science/hal-03943197>.
7. M. F. Melalkia, L. Brunel, F. Mondain, T. Lunghi, F. Doutre, A. Zavatta, S. Tanzilli, J. Etesse, and V. D'Auria. « LNbO₃ integrated optics for squeezing generation and manipulation ». In: Integrated Photonics Research, Silicon and Nanophotonics. Optical Society of America. 2021, IW1A-2. url: <https://opg.optica.org/abstract.cfm?uri=IPRSN-2021-IW1A.2>.
8. M. F. Melalkia, L. Brunel, S. Tanzilli, J. Etesse, and V. D'Auria. « Guided-wave solutions for continuous variable quantum optics ». Bristol Quantum Information Technologies - BQIT:22, Bristol - UK, Apr. 25-28, 2022. url: <https://hal.science/hal-03943219>.
9. M. F. Melalkia, T. Gabrielli, A. Petitjean, A. Zavatta, L. Brunel, S. Tanzilli, J. Etesse, and V. D'Auria. « Guided-wave solutions for non-classical state production ». In: Quantum Technologies 2022. Vol. 12133. SPIE. 2022, pp. 7-10. url: <https://www.spiedigitallibrary.org/conference-proceedings-of-spie/12133/1213303/Guided-wave-solutions-for-non-classical-state-production/10.1117/12.2631333.short>.
10. M. F. Melalkia, J. Huynh, L. Brunel, S. Tanzilli, V. D'Auria, and J. Etesse. « Optical quantum state engineering with multimode resources: between a drawback to be circumvented and an advantage to be exploited ». In: Quantum Technologies 2022. Vol. 12133. SPIE. 2022, pp. 47-54. url: <https://www.spiedigitallibrary.org/conference-proceedings-of-spie/12133/1213309/Optical-quantum-state-engineering-with-multimode-resources--between-a/10.1117/12.2621373.short>.
11. M. F. Melalkia, L. Brunel, J. Huynh, S. Tanzilli, V. D'Auria, and J. Etesse. « Multi-mode photonics for high-quality non-gaussian state generation ». In: Quantum 2.0. Optica Publishing Group. 2022, QTh4B-4. url: <https://opg.optica.org/abstract.cfm?uri=QUANTUM-2022-QTh4B.4>.
12. A. Bensemoun, M. F. Melalkia, G. Esposito, Y. Désières, S. Guerber, Q. Wilmart, K. Roux, S. Olivier, S. Tanzilli, J. Etesse, V. D'Auria, and L. Labonté. « Corrélations en intensité générées par mélange à quatre ondes dans un micro-anneau en nitrure de silicium ». Optique Nice 2022, Nice - France, Jul. 4-8, 2022. url: <https://hal.science/hal-03943309>.
13. M. F. Melalkia, J. Huynh, S. Tanzilli, V. D'Auria, and J. Etesse. « Génération d'états quantiques non Gaussiens par multiplexage spectral ». Optique Nice 2022, Nice - France, Jul. 4-8, 2022. url: <https://hal.science/hal-03943319>.
14. M. F. Melalkia, T. Gabbrielli, A. Petitjean, L. Brunel, A. Zavatta, S. Tanzilli, J. Etesse, and V. D'Auria. « Solutions d'optique guidée pour la génération d'états non classiques ». Optique Nice 2022, Nice - France, Jul. 4-8, 2022. url: <https://hal.science/hal-03943355>.

CONTENTS

Introduction

I THEORETICAL AND EXPERIMENTAL TOOLS

1	THEORETICAL TOOLS	9
1.1	Canonical quantization of free radiation	9
1.1.1	Free radiation Hamiltonian	10
1.1.2	Quantization of free radiation	12
1.1.3	Eigenvectors, quantum states and the notion of photon	13
1.2	Mixed states: the density matrix formalism	14
1.2.1	Definition	14
1.2.2	Properties	15
1.2.3	Partial trace	16
1.3	Phase space representation	17
1.3.1	Quantum fluctuations	17
1.3.2	Phasor diagram	17
1.3.3	Wigner function	19
1.4	Particular states in quantum optics	20
1.4.1	Gaussian quantum states	20
1.4.2	Non-Gaussian quantum states	25
1.5	Conclusion	29
2	EXPERIMENTAL TOOLS	31
2.1	Linear and nonlinear interactions	32
2.1.1	Linear interactions	32
2.1.2	Nonlinear interactions	34
2.2	Quantum measurement	36
2.2.1	Photon detection	37
2.2.2	Homodyne detection	39
2.3	Quantum state generation	41
2.3.1	Squeezed state generation	42
2.3.2	Schrödinger kitten state	44
2.4	Quantum state reconstruction	53
2.4.1	Quantum state reconstruction algorithms	53
2.5	Conclusion	56

II NON-GAUSSIAN QUANTUM STATE GENERATION: GUIDED-WAVE APPROACH IN CW AND PULSED REGIMES

3	A FULLY GUIDED-WAVE CW NON-GAUSSIAN QUANTUM STATE GENERATION	59
3.1	Model for the experiment	60
3.1.1	Squeezed vacuum state with losses	61
3.1.2	Photon subtraction with imperfect On/Off photon detector	62
3.1.3	Realistic homodyne detection	65

3.2	Experimental setup	66
3.2.1	Master laser source	67
3.2.2	Squeezed vacuum source	67
3.2.3	Homodyne detection	68
3.2.4	Photon subtraction: filtering the heralding photons	69
3.3	Data post-processing	74
3.3.1	LO phase extraction	75
3.3.2	Quadrature extraction	75
3.4	Experimental results and discussion	76
3.4.1	Squeezed vacuum state generation and losses characterization	77
3.4.2	Wave-packet extraction of the heralded non-Gaussian state	77
3.4.3	Heralded non-Gaussian state	79
3.5	Conclusion	81
4	GUIDED-WAVE, PULSED NON-GAUSSIAN STATE ENGINEERING FOR HYBRID ENTANGLEMENT GENERATION	83
4.1	Encoding information in quantum states	84
4.1.1	Discrete-variable (DV) encoding	84
4.1.2	Continuous variable (CV) encoding	86
4.2	Hybrid entanglement: towards heterogeneous quantum networks	86
4.2.1	Hybrid entanglement with time-bin DV encoding	88
4.2.2	The DV and CV resources for time-bin based hybrid entanglement creation	89
4.3	SPDC based source for DV and CV entangled states	90
4.3.1	JSA shaping for quasi-single-mode DV and CV state production	92
4.3.2	SHG and SPDC source design	94
4.4	SPDC source characterization	102
4.4.1	Fundamental pulsed laser source	103
4.4.2	SHG stage	104
4.4.3	SPDC stage	105
4.5	Conclusion	107
III QUANTUM STATE ENGINEERING WITH MULTIMODE RESOURCES		
5	NON-MODE-SELECTIVE PHOTON SUBTRACTION: A THEORETICAL STUDY IN THE MULTIMODE CASE	111
5.1	Photon subtraction operation applied to multimode quantum states	112
5.1.1	Perfect mode-selective single-photon subtraction	112
5.1.2	Non-mode-selective single-photon subtraction	113
5.1.3	Supermode decomposition	115
5.1.4	Heralded single-photon subtracted state	117
5.2	Case study: heralded Schrödinger kitten state production	118
5.2.1	Wigner function of the heralded state in the multimode case	120
5.3	Multimode-induced heralded state impurity	121
5.3.1	Quantification of the heralded state non-classicality	122
5.4	Heralded state with spectrally filtered heralding photons	123
5.4.1	Application to a practical experimental situation	126
5.5	Conclusion	127

6	A MULTIPLEXED SYNTHESIZER FOR NON-GAUSSIAN QUANTUM STATE GENERATION	129
6.1	Multimode, single-stage quantum state synthesizer	130
6.1.1	Framework: iterative protocols	130
6.1.2	Proposed single-stage generation protocol	131
6.2	Proposed protocol with non-Gaussian input resources	132
6.2.1	The input state state	133
6.2.2	The produced output state	135
6.2.3	Protocol performances	139
6.3	Case study 1: Parallel Schrödinger cat breeding	140
6.3.1	Beam splitter reflectivity	140
6.3.2	Amplitude of the input states	142
6.3.3	Comparison with the iterative cat breeding protocol	142
6.4	Case study 2: GKP state preparation	143
6.4.1	Definition	143
6.4.2	GKP states production with the proposed protocol	146
6.5	Conclusion	146

IV TOWARDS HIGH DIMENSION INTEGRATED QUANTUM OPTICS

7	SILICON NITRIDE CHIP CHARACTERIZATION FOR MULTIMODE QUANTUM STATE GENERATION	151
7.1	Silicon nitride photonic chip	152
7.1.1	Micro-ring resonator	152
7.1.2	Chip structure	152
7.2	Micro-ring resonators characterization	153
7.2.1	Propagation losses	154
7.2.2	Quality factor	155
7.3	Kerr frequency comb generation	157
7.4	Conclusion and perspectives	159

Conclusion

Appendix

A	NUMBER STATE BASIS	169
A.1	Eigenstates and eigenvalues of the number operator	169
A.2	Annihilation and creation operators	169
B	USEFUL FORMULA	171
B.1	Gaussian integral	171
B.2	Integration formulas involving coherent state wave-functions	171
C	GAUSSIAN BEAM PROPAGATION	173
C.1	Gaussian beam	173
C.2	Gaussian beam transformation using two lenses	173
D	CAVITY LOCKING USING PDH TECHNIQUE	177
E	PULSED SHG IN TIME DOMAIN	179
F	SINGLE-PHOTON SUBTRACTION FROM MULTIMODE QUANTUM STATES	181
F.1	Properties of functions $\{\psi_n^{\prime\prime}(\omega), \psi_n^{\prime}(\omega)\}$	181

F.2	Fidelity of the measured state with a target non-Gaussian state	182
F.3	Gaussian and rectangular filters on the heralding path	183
G	MULTIPLEXED NON-GAUSSIAN STATE SYNTHESIZER WITH SINGLE-PHOTON RESOURCES	185
	BIBLIOGRAPHY	187

INTRODUCTION

INTRODUCTION

"Information is quantum" ¹

QUANTUM INFORMATION

Classical information theory consists of developing tools to optimise information manipulation (computing) and transmission (communication) [1]. A classical information is encoded in binary units called *bits*, that can take either a logical 0 or 1. It is with this binary representation that information is processed at the heart of the actual classical computing systems and transmitted via communication networks.

Meanwhile, quantum mechanics - developed in the 1920s - had an unprecedented success. It allowed to understand the fundamental aspects of how nature works and to produce new innovative technologies in the framework of the so-called first quantum revolution, ranging from the invention of transistors [2] to the creation of the first laser [3]. It was until the 1970s that some pioneer physicists started to ask more fundamental questions concerning the ability to manipulate individual quantum objects [4]. Among them, *Richard Feynman* suggested to simulate quantum systems with "quantum" simulators as it is extremely hard to do it with classical computers. Hence, the new field of *quantum information theory*, combining quantum mechanics and information theory, emerged [5]. This new theory is growing up rapidly during the last decades, leading to some promising protocols and applications mainly in three different fields, namely *quantum computation*, *quantum communication* and *quantum metrology*.

Quantum computation, or information processing, has lead to the development of new computation algorithms offering high computational power (for some computational tasks) and overcoming the most powerful classical computers [6-8]. This is possible as quantum information can be in a *superposition* of logical zero ($|0\rangle$) and one ($|1\rangle$), forming what is called *qubit* that enables processing parallelism. On the other hand, the development of such powerful systems threatens the privacy and the confidentiality of information, as most of encryption systems rely on computational complexity to secure data transmission. In this regard, quantum communication allows to secure data transmission against these powerful quantum computers, as it relies on unconditional security taking advantages offered by the laws of quantum mechanics. In this context, several theoretical studies and experimental realizations have been performed to implement the so called Quantum key distribution (QKD) [9, 10], a way of remotely exchanging classical bits (key) for cryptography tasks. Quantum information also can be sent through communication channels via teleportation protocols thanks to *entanglement* [11, 12]. Finally, quantum metrology allows to perform high-resolution measurements with high-sensitivity and precision overcoming the classical limit [13, 14].

1. A talk of Charles H. Bennett: <https://www.youtube.com/watch?v=EqXv40kCahM>

There is a variety of physical systems used as quantum information carriers, such as photons [15], atoms [16], mechanical systems [17] and electric circuits [18, 19]. Light is of particular interest, especially for quantum communication tasks, as it has a high transmission speed and a low interaction with environment. In addition, the ability to exploit the existing optical-fiber based network for quantum communication protocols makes it suitable for this purpose. The wave-particle duality of light has led to the emergence of two parallel growing research axes, namely discrete-variable (DV) and continuous-variable (CV) encodings, depending on what kinds of quantum observables are used to encode information. In a DV regime, information is encoded on a quantum observable with discrete spectrum. In this case, typical systems containing one or few photons are used [20]. On the other hand, in the continuous-variable regime, information is encoded on observables with continuous spectrum such as amplitude, phase and quadratures of light [21]. More recently, combining these two types of information encodings via the so called *hybrid entanglement* has attracted the attention of researchers in this field [22]. This kind of entanglement between DV and CV systems allows to connect networks using different encodings as well as the transfer of information from one encoding to the other [23], making it possible to overcome their individual limitations via hybridization.

CONTEXT AND OUTLINE

This PhD work is devoted to study the generation and manipulation of quantum states of light at the fundamental as well as the applied levels. It aims at theoretically investigating protocols for high quality quantum state generation as well as implementing experimental realizations for real field practical applications of quantum information tasks. In particular, non-Gaussian photonic quantum states - showing a non-Gaussian Wigner function - are of particular interest, as they are essential for advanced quantum computation and communication applications [24–26]. Although these states have already been produced in multiple experimental realizations [27–30], we push in this work the theoretical and experimental engineering techniques to more advanced level in order to reach robust, out-of-the-laboratory applications of quantum communication protocols, compatible with the existing optical fiber-based communication networks. In addition, we focus on the ability of developing integrated sources for the generation and manipulation of highly multimode quantum states of light, enabling the implementation of more complex quantum communication networks.

At first, [Part I](#) introduces the different theoretical and experimental tools that we will use in the rest of the manuscript. We start in [chapter 1](#) by introducing the formalism used to quantize a free electromagnetic radiation. Then, we give the different ways of quantum states representation, namely density matrix and Wigner function, related to particle-like and wave-like aspects of quantized light. Depending on the shape of the associated Wigner function, quantum states can be classified into Gaussian (with Gaussian Wigner function) and non-Gaussian (with non-Gaussian Wigner function) ones. Some examples from these two classes are given at the end of [chapter 1](#). After that, the linear and nonlinear optical interactions as well as the quantum measurement formalism used in this work are given in [chapter 2](#). The association of these experimental

tools allows to generate, manipulate and detect photonic quantum states. More precisely, measurement induced non-linearity is at the heart of non-Gaussian quantum state generation in this work. The particular cases of squeezed state and Schrödinger cat-like state generation are described in this chapter. Finally, we finish [chapter 2](#) by giving the experimental technique used to characterize a given quantum state in the CV regime, allowing to reconstruct its associated Wigner function. This technique is called quantum homodyne tomography.

In [Part II](#), we present the experimental implementations of guided-wave quantum state engineering in both the continuous-wave (CW) as well as the picosecond pulsed regimes at a telecom wavelength. In [chapter 3](#), we show the feasibility of experiments where non-Gaussian state generation entirely relies on plug-&-play components from guided-wave optics technologies. This strategy is demonstrated experimentally with the heralded preparation of Schrödinger cat-like states via single-photon subtraction from a squeezed vacuum in the CW regime. All stages of the experiment are based on off-the-shelf fiber components. This leads to a stable, compact, and easily reconfigurable realization, fully compatible with existing fiber networks and, more in general, with future out-of-the-laboratory quantum communication protocols. In [chapter 4](#), we present the design and experimental characterization of a guided-wave, spontaneous parametric down-conversion (SPDC)-based source for the generation of high-fidelity DV and CV quantum states in the picosecond pulsed regime. The DV source will produce time-bin entangled photon pairs whereas the CV one will be used for Schrödinger cat-like state generation in the picosecond pulsed regime. These two states will then serve as input resources for time-bin based hybrid entanglement generation protocol introduced in [31]. As shown in the same Ref., this kind of encoding is more adapted for fiber-based quantum communication applications.

The study conducted in [chapter 4](#) reveals the fact that SPDC sources, at the heart of most experimental realizations, are naturally spectrally multimode. In the context of quantum state engineering, this aspect can be either advantageous or disadvantageous [32]. In [Part III](#), we study the effect of such multimode aspects on the generation of non-Gaussian quantum states. [chapter 5](#) establishes a versatile theoretical framework that explicitly describes single-photon subtraction from multimode quantum light in the context of non-Gaussian state generation and manipulation. The treatment focuses on easy-to-implement configurations in which no mode-selective operation is available and evaluates features and advantages of schemes where only simple filtering stages are employed in the experiments. Such configuration, by considerably reducing the experimental overheads, makes experiments involving single-photon subtraction easier to be implemented. The obtained theoretical framework allows retrieving, given a multimode input state, optimal conditions required to herald and then to detect non-Gaussian states with high fidelity, providing a practical and powerful toolbox for the design of experiments. The application of the proposed approach to the case study of Schrödinger cat state preparation starting from a frequency multimode squeezed state illustrates the impact of the derived theoretical tools. In [chapter 6](#), we propose an innovative approach that drastically simplifies the preparation of non-Gaussian states as compared to previous proposals, by taking advantage from the multiplexing capabilities offered by modern quantum photonics tools. Our proposal is inspired by iterative protocols, where multiple resources are combined one after the other for obtaining

high-amplitude complex output states [33, 34]. Here, conversely, a large part of the protocol is performed in parallel, by using a single projective measurement along a mode which partially overlaps with all the input modes. We show that our protocol can be used to generate high-quality and high-amplitude Schrödinger cat states as well as more complex states such as error-correcting codes.

Finally, we present in [chapter 7](#) of [Part IV](#) the first characterization results of micro-ring resonators within a Si_3N_4 photonic chip. These resonators will be used for experimental investigation of multimode quantum correlation in Kerr frequency comb. The obtained results show high quality factors and low propagation losses, which make this kind of compact systems suitable for the generation and manipulation of quantum system with relatively low power consumption for high dimensional quantum networks.

Part I

THEORETICAL AND EXPERIMENTAL TOOLS

THEORETICAL TOOLS

1.1	Canonical quantization of free radiation	9
1.1.1	Free radiation Hamiltonian	10
1.1.2	Quantization of free radiation	12
1.1.3	Eigenvectors, quantum states and the notion of photon	13
1.2	Mixed states: the density matrix formalism	14
1.2.1	Definition	14
1.2.2	Properties	15
1.2.3	Partial trace	16
1.3	Phase space representation	17
1.3.1	Quantum fluctuations	17
1.3.2	Phasor diagram	17
1.3.3	Wigner function	19
1.4	Particular states in quantum optics	20
1.4.1	Gaussian quantum states	20
1.4.2	Non-Gaussian quantum states	25
1.5	Conclusion	29

In this chapter, the main theoretical tools and notations needed for the rest of the manuscript are introduced. In [section 1.1](#), we give a brief description of the procedure used to quantize a free electromagnetic radiation, starting from the Maxwell's equations, to the introduction of quantum states in quantum optics, and the notion of "photons". For more details, the reader can refer to the textbook [35]. In [section 1.2](#), the density matrix formalism is introduced, a powerful tool used to describe real situations where the state vector formalism is not well adapted. We give in [section 1.3](#) a brief introduction to the phase space representation of quantum states, focusing on the Wigner function representation, which is widely used to represent quantum states and to visualize their quantum behaviour. We give then, in [section 1.4](#), some examples of usual quantum states that can be found in most quantum optics experiments. Finally, we conclude this chapter in [section 1.5](#). We note that the reader is assumed to be familiar with the postulates of quantum mechanics. More detailed textbooks on quantum mechanics can be found in literature, see for example [4, 36, 37].

1.1 CANONICAL QUANTIZATION OF FREE RADIATION

The classical Hamiltonian formalism consists of describing the energy H of a given system in terms of pairs of conjugate canonical variables $(x_1, x_2, \dots, x_i, \dots; p_1, p_2, \dots, p_i, \dots)$,

such as position x and momentum p of a given particle. In this case, the system dynamics is fully described by first order differential equations of the form:

$$\frac{dx_i}{dt} = \frac{\partial H}{\partial p_i}, \quad (1.1)$$

$$\frac{dp_i}{dt} = -\frac{\partial H}{\partial x_i}, \quad (1.2)$$

known as Hamilton equations. Canonical quantization of the system consists in associating pairs of observables (operators in the quantum mechanics formalism) $(\hat{x}_1, \hat{x}_2, \dots, \hat{x}_i, \dots; \hat{p}_1, \hat{p}_2, \dots, \hat{p}_i, \dots)$ to the conjugate canonical variables $(x_1, x_2, \dots, x_i, \dots; p_1, p_2, \dots, p_i, \dots)$ and imposing the commutation relation $[\hat{x}_i, \hat{p}_j] = i\hbar\delta_{ij}$. By doing so, the quantum Hamiltonian of the system is expressed in terms of these observables. The canonical quantization of free radiation follows this same procedure. Starting from partial differential equations, known as the Maxwell's equations, the electromagnetic radiation, in a given volume V in which the quantization will be performed, can be expanded into a set of *normal modes* with independent dynamics, and then, pairs of conjugate canonical variables can be identified for each *normal mode*, allowing the complete description of its dynamics by the Hamilton equations (Equation 1.1 and Equation 1.2). Once this is done, associating quantum observables to the conjugate canonical variables allows a full quantum description of the free radiation.

1.1.1 Free radiation Hamiltonian

A free electromagnetic radiation obeys the well known Maxwell's equations, which can be written in vacuum in the absence of charges and current as:

$$\nabla \cdot \mathbf{E}(\mathbf{r}, t) = 0, \quad (1.3)$$

$$\nabla \cdot \mathbf{B}(\mathbf{r}, t) = 0, \quad (1.4)$$

$$\nabla \times \mathbf{E}(\mathbf{r}, t) = -\frac{\partial}{\partial t} \mathbf{B}(\mathbf{r}, t), \quad (1.5)$$

$$\nabla \times \mathbf{B}(\mathbf{r}, t) = \frac{1}{c^2} \frac{\partial}{\partial t} \mathbf{E}(\mathbf{r}, t). \quad (1.6)$$

Let us considering a given volume V much larger than the one occupied by the radiation. An electromagnetic field, solution of Maxwell's equations, in this volume can be expanded into a set of modes with independent dynamics, known as *normal modes*. In the travelling plane wave basis, this expansion can be written as:

$$\mathbf{E}(\mathbf{r}, t) = \mathbf{E}^{(+)}(\mathbf{r}, t) + \mathbf{E}^{(-)}(\mathbf{r}, t), \quad (1.7)$$

$$\mathbf{B}(\mathbf{r}, t) = \mathbf{B}^{(+)}(\mathbf{r}, t) + \mathbf{B}^{(-)}(\mathbf{r}, t), \quad (1.8)$$

with:

$$\mathbf{E}^{(+)}(\mathbf{r}, t) = [\mathbf{E}^{(-)}(\mathbf{r}, t)]^* = i \sum_l \boldsymbol{\varepsilon}_l \mathcal{E}_l^{(1)} \alpha_l(t) e^{i\mathbf{k}_l \mathbf{r}}, \quad (1.9)$$

$$\mathbf{B}^{(+)}(\mathbf{r}, t) = [\mathbf{B}^{(-)}(\mathbf{r}, t)]^* = i \sum_l \frac{\mathbf{k}_l \times \boldsymbol{\varepsilon}_l}{\omega_l} \mathcal{E}_l^{(1)} \alpha_l(t) e^{i\mathbf{k}_l \mathbf{r}}. \quad (1.10)$$

Here, $\omega_l = ck_l$, $\boldsymbol{\varepsilon}_l$ is the polarization vector, $\mathcal{E}_l^{(1)}$ is a constant given by:

$$\mathcal{E}_l^{(1)} = \sqrt{\frac{\hbar \omega_l}{2\epsilon_0 V}}, \quad (1.11)$$

and $l = (k_{x,l}, k_{y,l}, k_{z,l}; s)$ with $(k_{x,l}, k_{y,l}, k_{z,l})$ the three spatial components of the wave vector \mathbf{k}_l satisfying the boundary conditions in the volume V , and $\{s = 0, s = 1\}$ represents the polarization mode basis. Note that the polarization basis can be either linear ($\{\rightarrow, \uparrow\}$ or $\{\nearrow, \nwarrow\}$) or circular ($\{\odot, \circlearrowleft\}$). Note also that the *normal mode* basis is not unique, and one can choose another set of *normal modes* depending on the studied situation. By inserting Equation 1.7 and Equation 1.8 in Equation 1.5 and Equation 1.6, we can show that $\alpha(t)$ obeys the equation:

$$\frac{d}{dt} \alpha_l(t) + i\omega_l \alpha_l(t) = 0, \quad (1.12)$$

which has a trivial solution given by:

$$\alpha_l(t) = \alpha_l e^{-i\omega_l t}, \quad (1.13)$$

with $\alpha_l = \alpha_l(0)$ to simplify the notation. The free radiation energy $H(t)$ is given by the integration over the considered volume V of the energy density:

$$H(t) = \frac{\epsilon_0}{2} \int_V [\mathbf{E}^2(\mathbf{r}, t) + c^2 \mathbf{B}^2(\mathbf{r}, t)] d^3r. \quad (1.14)$$

By inserting Equation 1.7 and Equation 1.8 and considering the boundary conditions fulfilled by the electromagnetic radiation in the considered volume, we can show that the radiation energy in the volume V can be simplified as:

$$H(t) = \sum_l H_l(t) = \sum_l \hbar \omega_l |\alpha_l(t)|^2, \quad (1.15)$$

which means that, in the volume V , the total radiation energy is the sum of the energies associated with the independent *normal modes*. Introducing now two variables $X_l(t)$ and $P_l(t)$ as:

$$X_l(t) = \sqrt{2\hbar} \operatorname{Re}\{\alpha_l(t)\}, \quad (1.16)$$

$$P_l(t) = \sqrt{2\hbar} \operatorname{Im}\{\alpha_l(t)\}, \quad (1.17)$$

and taking the real and imaginary parts of Equation 1.12, we can show that:

$$\frac{dX_l(t)}{dt} = \frac{\partial H_l(t)}{\partial P_l(t)}, \quad (1.18)$$

$$\frac{dP_l(t)}{dt} = -\frac{\partial H_l(t)}{\partial X_l(t)}. \quad (1.19)$$

Equation 1.18 and Equation 1.19 are then Hamilton equations for the Hamiltonian $H_l(t)$ (see Equation 1.1 and Equation 1.2), and thus, the variables $X_l(t)$ and $P_l(t)$ given by Equation 1.16 and Equation 1.17 are conjugate canonical variables for each radiation mode l .

1.1.2 Quantization of free radiation

In the Heisenberg picture, the quantization of the free electromagnetic radiation can be performed by associating the operator $\hat{a}_l(t)$ to the *normal mode* complex amplitude $\alpha_l(t)$, or equivalently, the Hermitian operators (observables) $\hat{X}_l(t)$ and $\hat{P}_l(t)$ to the conjugate canonical variables $X_l(t)$ and $P_l(t)$, and imposing the following commutation relations:

$$[\hat{a}_l(t), \hat{a}_{l'}^\dagger(t)] = \delta_{ll'}, \quad [\hat{a}_l(t), \hat{a}_{l'}(t)] = [\hat{a}_l^\dagger(t), \hat{a}_{l'}^\dagger(t)] = 0, \quad (1.20)$$

$$[\hat{X}_l(t), \hat{P}_{l'}(t)] = i\hbar\delta_{ll'}, \quad [\hat{X}_l(t), \hat{X}_{l'}(t)] = [\hat{P}_l(t), \hat{P}_{l'}(t)] = 0. \quad (1.21)$$

The operators $\hat{X}_l(t)$, $\hat{P}_l(t)$ and $\hat{a}_l(t)$ are related by the following expression:

$$\hat{a}_l(t) = \frac{\hat{X}_l(t) + i\hat{P}_l(t)}{\sqrt{2\hbar}}. \quad (1.22)$$

The quantum operator associated with the classical Hamiltonian is then given by:

$$\hat{H}(t) = \sum_l \hat{H}_l(t) = \sum_l \frac{\omega_l}{2} (\hat{X}_l^2(t) + \hat{P}_l^2(t)) = \sum_l \hbar\omega_l \left(\hat{a}_l^\dagger(t)\hat{a}_l(t) + \frac{1}{2} \right), \quad (1.23)$$

which is the same Hamiltonian of an ensemble of independent quantum harmonic oscillators. The observable associated with the classical electric field of the radiation is given by the following operator:

$$\hat{\mathbf{E}}(\mathbf{r}, t) = \hat{\mathbf{E}}^{(+)}(\mathbf{r}, t) + \hat{\mathbf{E}}^{(-)}(\mathbf{r}, t) = i \sum_l \boldsymbol{\varepsilon}_l \mathcal{E}_l^{(1)} \left[\hat{a}_l e^{i(\mathbf{k}_l \mathbf{r} - \omega_l t)} - \hat{a}_l^\dagger e^{-i(\mathbf{k}_l \mathbf{r} - \omega_l t)} \right], \quad (1.24)$$

where we put $\hat{a}_l(t) = \hat{a}_l e^{-i\omega_l t}$ with $\hat{a}_l = \hat{a}_l(0)$. For the rest of the manuscript, we will use the observables $\hat{x}_l(t)$ and $\hat{p}_l(t)$ defined as:

$$\hat{x}_l(t) = \sqrt{\frac{2\sigma_0^2}{\hbar}} \hat{X}_l(t), \quad \hat{p}_l(t) = \sqrt{\frac{2\sigma_0^2}{\hbar}} \hat{P}_l(t), \quad (1.25)$$

and satisfying the commutation relation:

$$[\hat{x}_l, \hat{p}_{l'}] = i2\sigma_0^2 \delta_{ll'}. \quad (1.26)$$

Note that if we replace Equation 1.22 in Equation 1.24, and taking into account definition given by Equation 1.25, we find that the observable associated to the electric field can be written, in terms of the observables \hat{x}_l and \hat{p}_l , as:

$$\hat{\mathbf{E}}(\mathbf{r}, t) = - \sum_l \varepsilon_l \frac{\mathcal{E}_l^{(1)}}{\sigma_0} [\hat{x}_l \sin(\mathbf{k}_l \mathbf{r} - \omega_l t) + \hat{p}_l \cos(\mathbf{k}_l \mathbf{r} - \omega_l t)], \quad (1.27)$$

with:

$$\hat{x}_l = \sigma_0 (\hat{a}_l + \hat{a}_l^\dagger), \quad (1.28)$$

$$\hat{p}_l = -i\sigma_0 (\hat{a}_l - \hat{a}_l^\dagger). \quad (1.29)$$

The observables \hat{x}_l and \hat{p}_l are then called quadrature observables. More generally, for any quadrature basis rotation of angle θ , the quadrature observables \hat{x}_{θ_l} and \hat{p}_{θ_l} are given by:

$$\hat{x}_{\theta_l} = \sigma_0 (\hat{a}_l e^{-i\theta} + \hat{a}_l^\dagger e^{i\theta}) = \hat{x}_l \cos \theta + \hat{p}_l \sin \theta, \quad (1.30)$$

$$\hat{p}_{\theta_l} = -i\sigma_0 (\hat{a}_l e^{-i\theta} - \hat{a}_l^\dagger e^{i\theta}) = -\hat{x}_l \sin \theta + \hat{p}_l \cos \theta. \quad (1.31)$$

1.1.3 Eigenvectors, quantum states and the notion of photon

According to the postulates of quantum mechanics, a *pure* quantum state of a given system (free radiation in our case) is described by a unit vector called *state vector* $|\psi\rangle$ defined in a vector space called *Hilbert space* \mathcal{H} , a basis of which can be constructed by the set of eigenvectors (or eigenstates) of the Hamiltonian given by Equation 1.23. In order to find these eigenvectors, one can start by finding the eigenvectors of the operator $\hat{N}_l = \hat{a}_l^\dagger \hat{a}_l$. The radiation Hamiltonian for each normal mode l can be written in terms of this operator as:

$$\hat{H}_l = \hbar\omega_l \left(\hat{N}_l + \frac{1}{2} \right). \quad (1.32)$$

Using the Dirac method [37], we can show that the eigenvalues of the operator \hat{N}_l are given by the set of non-negative integers $n_l \geq 0$ (see section A.1 in Appendix A). Doing so, the eigenvectors $|n_l\rangle_l$ satisfy the relation:

$$\hat{N}_l |n_l\rangle_l = n_l |n_l\rangle_l. \quad (1.33)$$

These eigenvectors form a basis for the Hilbert space \mathcal{H}_l of the radiation states of the normal mode l , and they satisfy the following relations (see section A.2 in Appendix A):

$$\hat{a}_l |n_l\rangle_l = \sqrt{n_l} |n_l - 1\rangle_l \quad |_{n_l > 0}, \quad (1.34)$$

$$\hat{a}_l |0_l\rangle_l = 0, \quad (1.35)$$

$$\hat{a}_l^\dagger |n_l\rangle_l = \sqrt{n_l + 1} |n_l + 1\rangle_l, \quad (1.36)$$

and any eigenstate $|n_l\rangle_l$ can be obtained from the ground state $|0_l\rangle_l$ as following:

$$|n_l\rangle_l = \frac{(\hat{a}_l^\dagger)^{n_l}}{\sqrt{n_l!}} |0_l\rangle_l. \quad (1.37)$$

Since the normal modes l are independent, the eigenstates of the Hamiltonian \hat{H} are given by the tensor product of the states $|n_l\rangle_l$:

$$\otimes_l |n_l\rangle_l = |n_1, n_2, \dots, n_l, \dots\rangle, \quad (1.38)$$

satisfying the relation:

$$\hat{H} |n_1, n_2, \dots, n_l, \dots\rangle = \left[\sum_l \hbar\omega_l \left(n_l + \frac{1}{2} \right) \right] |n_1, n_2, \dots, n_l, \dots\rangle, \quad (1.39)$$

and any radiation state $|\psi\rangle$ can be written as a coherent superposition of the Hamiltonian eigenstates:

$$|\psi\rangle = \sum_{n_1, n_2, \dots, n_l, \dots} C_{n_1, n_2, \dots, n_l, \dots} |n_1, n_2, \dots, n_l, \dots\rangle, \quad (1.40)$$

where $C_{n_1, n_2, \dots, n_l, \dots}$ are complex numbers. Note that the Hamiltonian \hat{H}_l has an eigenvalue $\hbar\omega_l(n_l + 1/2)$ associated with the eigenstate $|n_l\rangle_l$. Compared with the ground state $|0_l\rangle_l$ with an eigenvalue $\hbar\omega_l/2$, the eigenstate $|n_l\rangle_l$ has an extra energy of $n_l\hbar\omega_l$. This state can then be seen as a collection of exactly n_l particles each with an energy $\hbar\omega_l$, hence, the notion of photon - elementary excitation of the quantized electromagnetic field - emerges. The ground state $|0_l\rangle_l$ is then called vacuum state, and the state $|n_l\rangle_l$ is called number state, or Fock state, a radiation states in which the number of photons is well defined. According to [Equation 1.34](#), [Equation 1.35](#), and [Equation 1.36](#), applying the operator \hat{a}_l (\hat{a}_l^\dagger) to the Fock state $|n_l\rangle_l$ reduces (increases) the photon number by one, hence, the operators \hat{a}_l and \hat{a}_l^\dagger are called annihilation and creation operators, respectively, and the operator \hat{N}_l is the quantum observable characterizing the number of photons in the normal mode l in the quantization volume V .

1.2 MIXED STATES: THE DENSITY MATRIX FORMALISM

1.2.1 Definition

As mentioned in [subsection 1.1.3](#), a *pure* quantum state of a given system is defined by a the state vector $|\psi\rangle$. However, in several situations, the quantum state is not completely known, typically when the preparation of the system is not completely controlled leading to a statistical mixture of possible preparation outcomes. In this case, the system can be described as a probabilistic *mixture* of several quantum states, which is known as *mixed state*. This situation can be well described using the *density operator* or *density matrix* formalism. The density matrix $\hat{\rho}$ of a *pure* quantum state $|\psi\rangle$ is given by:

$$\hat{\rho} = |\psi\rangle\langle\psi|. \quad (1.41)$$

For a quantum state being in a statistical mixture of several *pure* states $\{|\psi_i\rangle\}$ with associated probabilities $\{p_i\}$, the density matrix is defined as:

$$\hat{\rho} = \sum_i p_i |\psi_i\rangle\langle\psi_i|, \quad (1.42)$$

or more generally, it can be written as:

$$\hat{\rho} = \sum_i p_i \hat{\rho}_i, \quad (1.43)$$

where $\hat{\rho}_i$ is also a density matrix describing a quantum state that can also be in a statistical *mixture* of *pure* quantum states, and p_i is the associated probability. It is always possible to decompose it into a *mixture* of *pure* states of the form of [Equation 1.42](#).

1.2.2 Properties

The density matrix of a quantum system has several properties:

Hermitian

According to the definition given by [Equation 1.42](#), the density matrix is Hermitian:

$$\hat{\rho}^\dagger = \hat{\rho}. \quad (1.44)$$

Unit trace

By calculating the trace of the density matrix given by [Equation 1.42](#) we find:

$$\text{Tr} [\hat{\rho}] = \sum_i p_i \text{Tr} [|\psi_i\rangle\langle\psi_i|] = \sum_i p_i = 1. \quad (1.45)$$

So, the trace of a density matrix is equal to one.

Positivity

Considering an arbitrary vector $|\varphi\rangle$, we have:

$$\langle\varphi|\hat{\rho}|\varphi\rangle = \sum_i p_i \langle\varphi|\psi_i\rangle\langle\psi_i|\varphi\rangle = \sum_i p_i |\langle\varphi|\psi_i\rangle|^2 \geq 0, \quad (1.46)$$

so, the density matrix is a positive operator.

Expectation value

Considering a given quantum state $\hat{\rho}$, the expectation value of a given observable \hat{O} is given by:

$$\langle\hat{O}\rangle_{\hat{\rho}} = \text{Tr} [\hat{O}\hat{\rho}]. \quad (1.47)$$

Purity

The purity \mathcal{P} of a given quantum state $\hat{\rho}$ is defined as:

$$\mathcal{P} = \text{Tr} [\hat{\rho}^2]. \quad (1.48)$$

One can show easily that $\mathcal{P} \leq 1$. If $\mathcal{P} = 1$, the state is said to be *pure*, otherwise ($\mathcal{P} < 1$), the state is said to be *mixed*.

Fidelity

The fidelity \mathcal{F} between two quantum states quantifies the likeness between them. Two states are said to be identical if the fidelity between them is equal to one ($\mathcal{F} = 1$). This fidelity is null ($\mathcal{F} = 0$) if the two quantum states are orthogonal. In the general case, the fidelity takes its value between zero and one ($0 \leq \mathcal{F} \leq 1$). For two mixed states $\hat{\rho}_1$ and $\hat{\rho}_2$, the fidelity between them can be defined as [38]:

$$\mathcal{F} = \left(\text{Tr} \left[\sqrt{\sqrt{\hat{\rho}_2} \hat{\rho}_1 \sqrt{\hat{\rho}_2}} \right] \right)^2, \quad (1.49)$$

however, if one of the two states is pure, Equation 1.49 can be simplified as:

$$\mathcal{F} = \text{Tr} [\hat{\rho}_1 \hat{\rho}_2]. \quad (1.50)$$

1.2.3 Partial trace

One of the most pertinent case study to show the usefulness of the density matrix formalism is the description of a subsystem of a composite quantum system. Let us consider at first the case of two independent quantum systems A and B , according to quantum mechanics, the density matrix of the whole system is given by the tensor product of the density matrices of each system:

$$\hat{\rho}_{AB} = \hat{\rho}_A \otimes \hat{\rho}_B, \quad (1.51)$$

and the density matrix of the system A (or B) can be obtained by tracing out the density matrix $\hat{\rho}_{AB}$ over the subsystem B (or A):

$$\text{Tr}_B [\hat{\rho}_{AB}] = \text{Tr}_B [\hat{\rho}_A \otimes \hat{\rho}_B] = \hat{\rho}_A \text{Tr}_B [\hat{\rho}_B] = \hat{\rho}_A. \quad (1.52)$$

which seems to be trivial. However, there is a class of states for composite systems, known as entangled states, where one cannot describe them as tensor product of independent states. Let us take the example of two quantum systems A and B defined in a Hilbert space $\mathcal{H}_{AB} = \mathcal{H}_A \otimes \mathcal{H}_B$ where \mathcal{H}_A and \mathcal{H}_B are two dimensional Hilbert spaces, and $\{|0\rangle_A, |1\rangle_A\}$ and $\{|0\rangle_B, |1\rangle_B\}$ the associated bases, respectively. The state given by:

$$|\psi\rangle_{AB} = \frac{1}{\sqrt{2}} (|0\rangle_A |0\rangle_B + |1\rangle_A |1\rangle_B), \quad (1.53)$$

on of the well known Bell states, is a maximally entangled state. The associated density matrix is given by:

$$\hat{\rho}_{AB} = \frac{1}{2} (|0\rangle_A \langle 0| \otimes |0\rangle_B \langle 0| + |1\rangle_A \langle 0| \otimes |1\rangle_B \langle 0| + |0\rangle_A \langle 1| \otimes |0\rangle_B \langle 1| + |1\rangle_A \langle 1| \otimes |1\rangle_B \langle 1|). \quad (1.54)$$

This state is a *pure* state. However, the density matrix of the subsystem A , obtained by performing a partial trace over B , is given by:

$$\hat{\rho}_A = Tr_B [\hat{\rho}_{AB}] = \frac{1}{2} (|0\rangle_A \langle 0| + |1\rangle_A \langle 1|), \quad (1.55)$$

which is a mixed state with a purity $\mathcal{P} = 0.5$. With the state vector formalism, it is not possible to describe the subsystem A in this case, hence the usefulness of the density matrix formalism.

1.3 PHASE SPACE REPRESENTATION

1.3.1 Quantum fluctuations

In this section, and for the rest of the manuscript, we omit the subscript l in all expressions when we consider single-mode quantum states of radiation. Taking into account the properties of the annihilation and creation operators given by [Equation 1.20](#), [Equation 1.34](#), [Equation 1.35](#), and [Equation 1.36](#), the expectation values and the variances of the quadrature observables of vacuum state in mode l can be written as:

$$\langle 0 | \hat{x} | 0 \rangle = \langle 0 | \hat{p} | 0 \rangle = 0, \quad (1.56)$$

$$\langle 0 | \hat{x}^2 | 0 \rangle = \langle 0 | \hat{p}^2 | 0 \rangle = \sigma_0^2. \quad (1.57)$$

As we can see, the expectation values of quadrature observables of vacuum state are null, whereas the variances are not null, this is what we call quantum fluctuations. In fact, for any quantum state $\hat{\rho}$ and any basis rotation of angle θ , the measurement outcomes x_θ and p_θ of the quadrature observables \hat{x}_θ and \hat{p}_θ , respectively, are random and they follow given probability distributions $P(x_\theta)$ and $P(p_\theta)$. The corresponding standard deviations, σ_{x_θ} and σ_{p_θ} , satisfy always the following inequality:

$$\sigma_{x_\theta} \sigma_{p_\theta} \geq \sigma_0^2, \quad (1.58)$$

which is a direct consequence of the Heisenberg uncertainty principle [4], describing the fact that one cannot measure simultaneously the quadrature observables \hat{x}_θ and \hat{p}_θ with infinite precision. The equality is satisfied for many quantum states called *minimum uncertainty* states, as we will see in the next section.

1.3.2 Phasor diagram

Let us consider a single-mode radiation, by omitting the subscript l and the polarization vector ε_l , the scalar operator $\hat{E}^{(+)}(\mathbf{r}, t)$ can be written as:

$$\hat{E}^{(+)}(\mathbf{r}, t) = \frac{\mathcal{E}^{(1)}}{2\sigma_0} (\hat{x} + i\hat{p}) e^{i(\mathbf{k}\mathbf{r} - \omega t + \pi/2)}, \quad (1.59)$$

or, by a proper choice of time (or space) origin, it can be written as:

$$\hat{E}^{(+)}(\mathbf{r}, t) = \frac{\mathcal{E}^{(1)}}{2\sigma_0} (\hat{x} + i\hat{p}) e^{i(\mathbf{k}\mathbf{r} - \omega t)}, \quad (1.60)$$

In this case, the operator associated to the scalar electric field can be written as:

$$\hat{E}(\mathbf{r}, t) = \hat{E}^{(+)}(\mathbf{r}, t) + [\hat{E}^{(+)}(\mathbf{r}, t)]^\dagger = \frac{\mathcal{E}^{(1)}}{\sigma_0} [\hat{x} \cos(\mathbf{k}\mathbf{r} - \omega t) - \hat{p} \sin(\mathbf{k}\mathbf{r} - \omega t)]. \quad (1.61)$$

It can be seen that the quadrature components \hat{x} and \hat{p} , up to a factor, are given by the real and imaginary parts of the operator $\hat{E}^{(+)}(\mathbf{r}, t)$, respectively. Then, the quantum field can be represented by a phasor diagram as shown in [Figure 1.1](#).

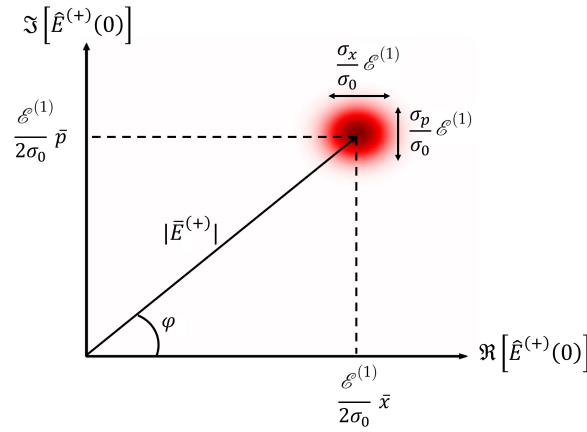


Figure 1.1 – Phasor diagram of a quantum field with Gaussian distribution of quadratures \hat{x} and \hat{p} .

where $\hat{E}^{(+)}(0) = \hat{E}^{(+)}(\mathbf{r} = 0, t = 0)$, and \bar{x} , \bar{p} and $\bar{E}^{(+)} = |\bar{E}^{(+)}| e^{i\varphi}$ are the expectation values of the operators \hat{x} , \hat{p} and $\hat{E}^{(+)}(0)$, respectively. As mentioned before, the observables \hat{x} and \hat{p} cannot be measured with infinite precision, which is a direct result of the commutation relation in [Equation 1.26](#). This is represented in the phasor diagram by a dispersion region describing the fact that measurement outcomes of an electric field (or equivalently the quadrature operators) are random (with random amplitudes and phases). These random measurement outputs follow given probability distributions which vary from a quantum state of radiation to another one.

In many cases, the quadrature fluctuations are Gaussian, and therefore, the dispersion region in phasor diagram representation can be a suitable tool to describe the quantum state of a radiation for its simplicity. However, for some quantum states, the quadrature fluctuations are not Gaussian, and a more suitable tool to represent these states is a quasi-probability distribution called *the Wigner function*.

1.3.3 Wigner function

In 1932, a two dimensional function was introduced by *E. Wigner* [39], which now bears his name, that describes the joint quasi-probability distribution of the observables \hat{x} and \hat{p} in a similar way to the joint probability distribution of two classical random variables. This function, contrary to its classical counterpart, can take negative values for some quantum states. It completely describes the quantum state of a given system and it is useful to visualize it. The Wigner function of a single-mode quantum state $\hat{\rho}$ is defined as:

$$W_{\hat{\rho}}(x, p) = \frac{1}{2\pi\sigma_0^2} \int e^{iyp/\sigma_0^2} \langle x - y | \hat{\rho} | x + y \rangle dy, \quad (1.62)$$

which can be generalized in the multimode case with N modes as:

$$W_{\hat{\rho}}(\mathbf{x}, \mathbf{p}) = (2\pi\sigma_0^2)^{-N} \int_{\mathbb{R}^N} e^{i\mathbf{y}^T \mathbf{p} / \sigma_0^2} \langle \mathbf{x} - \mathbf{y} | \hat{\rho} | \mathbf{x} + \mathbf{y} \rangle d\mathbf{y}, \quad (1.63)$$

with $\mathbf{x} = (x_0, x_1, x_2, \dots, x_{N-1})^T$, $\mathbf{y} = (y_0, y_1, y_2, \dots, y_{N-1})^T$, $\mathbf{p} = (p_0, p_1, p_2, \dots, p_{N-1})^T$ and $|\mathbf{x} \pm \mathbf{y}\rangle = |x_0 \pm y_0, x_1 \pm y_1, x_2 \pm y_2, \dots, x_{N-1} \pm y_{N-1}\rangle$.

1.3.3.1 Properties

Like the density matrix, the Wigner function of a quantum state satisfy some properties, and here some of them.

Real function

The Wigner function is a useful tool to visualize quantum states since it has always real values ($W_{\hat{\rho}}(x, p) \in \mathbb{R} \forall (x, p) \in \mathbb{R}^2$). This is related to the fact that the operator $\hat{\rho}$ is Hermitian (see [Equation 1.44](#)).

Integral

The integral of the Wigner function in \mathbb{R}^2 is equal to one:

$$\int \int W_{\hat{\rho}}(x, p) dx dp = 1. \quad (1.64)$$

Purity

The purity of a given quantum state is given by:

$$\mathcal{P} = 4\pi\sigma_0^2 \int \int W_{\hat{\rho}}^2(x, p) dx dp. \quad (1.65)$$

Fidelity

In the case where at least one of two quantum states $\hat{\rho}_1$ and $\hat{\rho}_2$ is pure, the fidelity between them is given by:

$$\mathcal{F} = 4\pi\sigma_0^2 \int \int W_{\hat{\rho}_1}(x, p) W_{\hat{\rho}_2}(x, p) dx dp. \quad (1.66)$$

Marginal distribution

When measuring the quadrature \hat{x}_θ of a given quantum state $\hat{\rho}$, the probability $P(x_\theta)$ of obtaining a given value x_θ is given by:

$$P(x_\theta) = \langle x_\theta | \hat{\rho} | x_\theta \rangle = |\psi(x_\theta)|^2, \quad (1.67)$$

where $|x_\theta\rangle$ is the eigenstate of the observable \hat{x}_θ ($\hat{x}_\theta |x_\theta\rangle = x_\theta |x_\theta\rangle$) and $\psi(x_\theta)$ is the wave-function of the state $\hat{\rho}$. Using the Wigner function representation, this probability distribution can be written as:

$$P(x_\theta) = \int W_{\hat{\rho}}(x_\theta \cos \theta - p_\theta \sin \theta, x_\theta \sin \theta + p_\theta \cos \theta) dp_\theta. \quad (1.68)$$

1.4 PARTICULAR STATES IN QUANTUM OPTICS

In quantum optics experiments, a large set of quantum states can be encountered. These states can be classified into two main classes: the Gaussian and non-Gaussian quantum states. In this section, some examples of quantum states for each class are given.

1.4.1 Gaussian quantum states

Gaussian states are the easiest, on demand produced quantum states in laboratory. Like the vacuum state, no matter the measured observable \hat{x}_θ , the measurement outcomes x_θ are random and follow a Gaussian probability distribution $P(x_\theta)$. A complete description of a Gaussian state can be given by the covariance matrix, which is written in the monomode case as:

$$V = \begin{pmatrix} \langle \hat{x}^2 \rangle - \langle \hat{x} \rangle^2 & \langle \frac{1}{2} (\hat{x}\hat{p} + \hat{p}\hat{x}) \rangle - \langle \hat{x} \rangle \langle \hat{p} \rangle \\ \langle \frac{1}{2} (\hat{x}\hat{p} + \hat{p}\hat{x}) \rangle - \langle \hat{x} \rangle \langle \hat{p} \rangle & \langle \hat{p}^2 \rangle - \langle \hat{p} \rangle^2 \end{pmatrix}, \quad (1.69)$$

or equivalently, the monomode Wigner function of a Gaussian state is given by:

$$W_g(x, p) = \frac{1}{2\pi\sigma_x\sigma_p} e^{-\frac{(x-\bar{x})^2}{2\sigma_x^2} - \frac{(p-\bar{p})^2}{2\sigma_p^2}}, \quad (1.70)$$

where $\bar{x} = \langle \hat{x} \rangle$ and $\bar{p} = \langle \hat{p} \rangle$. In this case, the probability distribution $P(x_\theta)$ is given by:

$$P(x_\theta) = \int W_g(x_\theta \cos \theta - p_\theta \sin \theta, x_\theta \sin \theta + p_\theta \cos \theta) dp_\theta = \frac{1}{\sqrt{2\pi\sigma_\theta^2}} e^{-\frac{(x_\theta - \bar{x}_\theta)^2}{2\sigma_\theta^2}}, \quad (1.71)$$

with $\sigma_\theta^2 = \sigma_x^2 \cos^2 \theta + \sigma_p^2 \sin^2 \theta$ and $\bar{x}_\theta = \bar{x} \cos \theta + \bar{p} \sin \theta$.

1.4.1.1 Vacuum state

The vacuum state, or ground state, is the most elementary state in quantum physics. It represents, in quantum optics, the state in the absence of radiation (zero photon state). As seen in [subsection 1.3.1](#), the vacuum state has null mean quadratures \hat{x} and \hat{p} and non-null quadrature variances $\sigma_x^2 = \sigma_p^2 = \sigma_0^2$. This means that if one try to measure the electromagnetic field, or equivalently the quadrature \hat{x} or \hat{p} , where there is no radiation, fluctuations will be observed (called shot noise). This can be seen in the Wigner function representation of the vacuum state, depicted in [Figure 1.2](#).

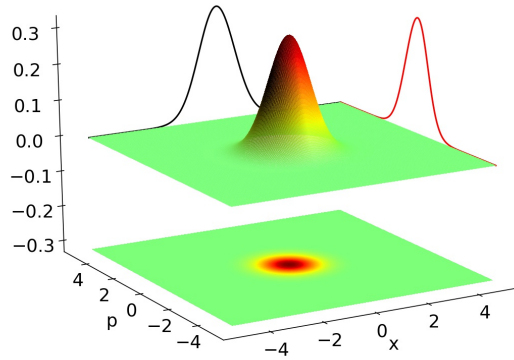


Figure 1.2 – Wigner function of the vacuum state, and the quadrature distributions $P(x)$ (black) and $P(p)$ (red). The marginal distributions are rescaled for visualization purpose.

1.4.1.2 Coherent state

The coherent state (or quasi-classical state) was introduced in [40]. Its properties are similar to the classical field. By definition, a coherent state $|\alpha\rangle$ of amplitude α is the eigenstate of the annihilation operator \hat{a} with eigenvalue α :

$$\hat{a} |\alpha\rangle = \alpha |\alpha\rangle. \quad (1.72)$$

Considering the expansion in the Fock states basis, the coherent state can be written as:

$$|\alpha\rangle = \sum_n c_n |n\rangle. \quad (1.73)$$

[Equation 1.72](#) applied to [Equation 1.73](#) gives the following recurrence relation:

$$c_{n+1} = \frac{\alpha}{\sqrt{n+1}} c_n, \quad (1.74)$$

which leads to the following expression of the coherent state $|\alpha\rangle$:

$$|\alpha\rangle = e^{-|\alpha|^2/2} \sum_n \frac{\alpha^n}{\sqrt{n!}} |n\rangle. \quad (1.75)$$

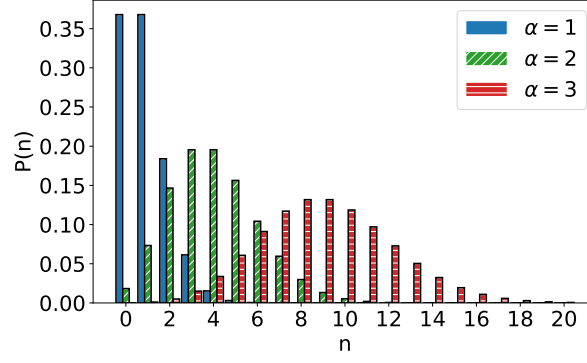


Figure 1.3 – Photon number distribution in a coherent state $|\alpha\rangle$ for different amplitudes: $\alpha = 1$, $\alpha = 2$ and $\alpha = 3$.

It is a superposition of Fock states $|n\rangle$ with a photon number probability distribution given by:

$$P_\alpha(n) = |c_n|^2 = e^{-|\alpha|^2} \frac{(|\alpha|^2)^n}{n!}, \quad (1.76)$$

which is a Poissonian distribution with a mean value $\bar{n}(\alpha) = \langle \alpha | \hat{N} | \alpha \rangle = |\alpha|^2$ and a variance $\sigma_n^2(\alpha) = \langle \alpha | \hat{N}^2 | \alpha \rangle - \bar{n}^2 = |\alpha|^2$. [Figure 1.3](#) illustrates the photon number distribution in coherent states with different amplitudes α .

The quadrature variance of a coherent state is equal to those of vacuum state ($\sigma_x^2(\alpha) = \sigma_p^2(\alpha) = \sigma_0^2$), thus, the coherent state is a minimum uncertainty state ($\sigma_x(\alpha)\sigma_p(\alpha) = \sigma_0^2$). Its wave-function, $\psi_\alpha(x_\theta)$ is given by:

$$\psi_\alpha(x_\theta) = \langle x_\theta | \alpha \rangle = e^{-\frac{|\alpha|^2}{2}} \frac{e^{-\frac{x_\theta^2}{4\sigma_0^2}}}{\sqrt{\sigma_0\sqrt{2\pi}}} e^{-(e^{-i2\theta}\alpha^2/2) + 2(e^{-i\theta}\alpha)\frac{x_\theta}{2\sigma_0}}, \quad (1.77)$$

and the corresponding quadrature probability distribution is:

$$P_\alpha(x_\theta) = |\psi_\alpha(x_\theta)|^2 = \frac{e^{-(|\alpha|^2 - \alpha^2)}}{\sigma_0\sqrt{2\pi}} e^{-\left(\frac{x_\theta}{\sigma_0\sqrt{2}} - \alpha\sqrt{2}\cos\theta\right)^2}. \quad (1.78)$$

This state can be easily produced, it is in fact, in good approximation, the quantum state of a single-mode laser radiation operating far above threshold. The Wigner function of a coherent state of amplitude α , depicted in [Figure 1.4](#) for $\alpha = 2e^{i\frac{\pi}{4}}$, is given by [Equation 1.70](#) with $\sigma_x = \sigma_p = \sigma_0$, $\bar{x} = 2\sigma_0 \text{Re}(\alpha)$ and $\bar{p} = 2\sigma_0 \text{Im}(\alpha)$. It is the same as the Wigner function of vacuum state (see [Figure 1.2](#)) displaced in phase space. We can thus obtain a coherent state of amplitude α by applying a displacement operator $\hat{D}(\alpha)$ to the vacuum state:

$$|\alpha\rangle = \hat{D}(\alpha) |0\rangle = e^{\alpha\hat{a}^\dagger - \alpha^*\hat{a}} |0\rangle. \quad (1.79)$$

The overlap between two coherent states with different amplitudes α and β is [\[41\]](#):

$$\langle \alpha | \beta \rangle = e^{-\frac{1}{2}(|\alpha|^2 + |\beta|^2 - 2\alpha^*\beta)}. \quad (1.80)$$

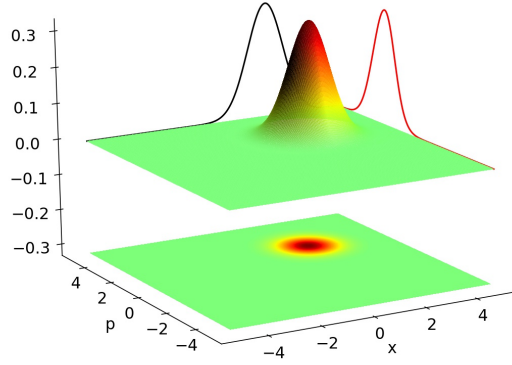


Figure 1.4 – Wigner function of a coherent state $|\alpha\rangle$ of amplitude $\alpha = 2e^{i\frac{\pi}{4}}$, and the quadrature distributions $P(x)$ (black) and $P(p)$ (red). The vacuum state is a coherent state with amplitude $\alpha = 0$. The marginal distributions are rescaled for visualization purpose.

1.4.1.3 Squeezed vacuum state

A squeezed vacuum state, noted $|\zeta\rangle$, is obtained by applying the squeezing operator $\hat{S}(\zeta)$ to the vacuum state:

$$|\zeta\rangle = \hat{S}(\zeta) |0\rangle = e^{-\frac{1}{2}(\zeta\hat{a}^{\dagger 2} - \zeta^*\hat{a}^2)} |0\rangle. \quad (1.81)$$

with $\zeta = re^{i\phi}$ being the squeezing parameter. It can be expressed in the Fock basis as:

$$|\zeta\rangle = (1 - \mu^2)^{1/4} \sum_n \frac{\sqrt{(2n)!}}{n!} e^{in(\phi+\pi)} \left(\frac{\mu}{2}\right)^n |2n\rangle, \quad (1.82)$$

where $\mu = \tanh(r)$.

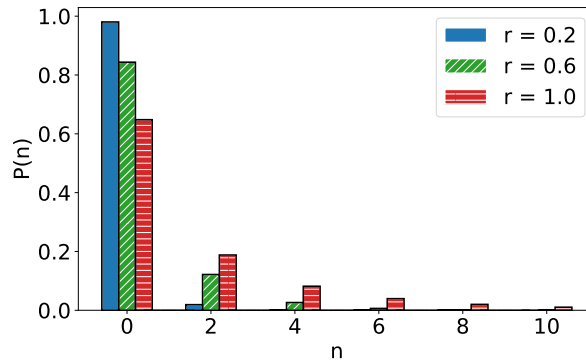


Figure 1.5 – Photon number distribution in a squeezed vacuum state $|\zeta\rangle$ for different squeezing parameter r .

The photon number probability distribution for a squeezed vacuum state is given by:

$$\begin{cases} P_\zeta(2n) = \sqrt{1 - \mu^2} \frac{(2n)!}{(n!)^2} \left(\frac{\mu}{2}\right)^{2n}, \\ P_\zeta(2n+1) = 0. \end{cases} \quad (1.83)$$

which gives a mean photon number $\bar{n}(\zeta) = \langle \zeta | \hat{N} | \zeta \rangle = \sinh^2 r$, and a photon number variance of $\sigma_n^2(\zeta) = \langle \zeta | \hat{N}^2 | \zeta \rangle - \bar{n}^2 = 2\bar{n}(\bar{n} + 1)$. **Figure 1.5** shows the photon number distribution in squeezed vacuum states with different squeezing parameter r ($\phi = 0$).

Like for the vacuum state, the expectation value of the quadrature operator \hat{x}_θ is null for all values of θ , this is the "vacuum" part of the squeezed vacuum. However, contrary to the vacuum state, the variance of \hat{x}_θ depends on θ and it is given by:

$$\sigma_{x_\theta}^2(\zeta) = \langle \zeta | \hat{x}_\theta^2 | \zeta \rangle - (\langle \zeta | \hat{x}_\theta | \zeta \rangle)^2 = \sigma_0^2 [e^{2r} \sin^2(\theta - \phi/2) + e^{-2r} \cos^2(\theta - \phi/2)]. \quad (1.84)$$

This variance varies between a minimum value $\sigma_{min}^2(\zeta) = e^{-2r} \sigma_0^2$, which is less than the one of vacuum state ($\sigma_{min}^2(\zeta) < \sigma_0^2$), and a maximum value $\sigma_{max}^2(\zeta) = e^{2r} \sigma_0^2$ greater than the one of vacuum state ($\sigma_{max}^2(\zeta) > \sigma_0^2$). We can then define a squeezing factor, s , as the ratio between the minimum variance of the quadrature \hat{x}_θ and the variance of the vacuum state quadrature σ_0^2 :

$$s = e^{-2r}. \quad (1.85)$$

In all cases, the squeezed state is a minimum uncertainty state saturating the inequality given by **Equation 1.58** ($\sigma_{x_\theta}(\zeta) \sigma_{p_\theta}(\zeta) = \sigma_0^2$). In the case where the squeezed quadrature is the quadrature \hat{p} ($\phi = \pi$), the Wigner function of the squeezed vacuum state is obtained by replacing $\sigma_x^2 = \sigma_0^2/s$, $\sigma_p^2 = \sigma_0^2 s$, and $\bar{x} = \bar{p} = 0$ in **Equation 1.70**. This Wigner function is shown in **Figure 1.6** for two different squeezing parameters.

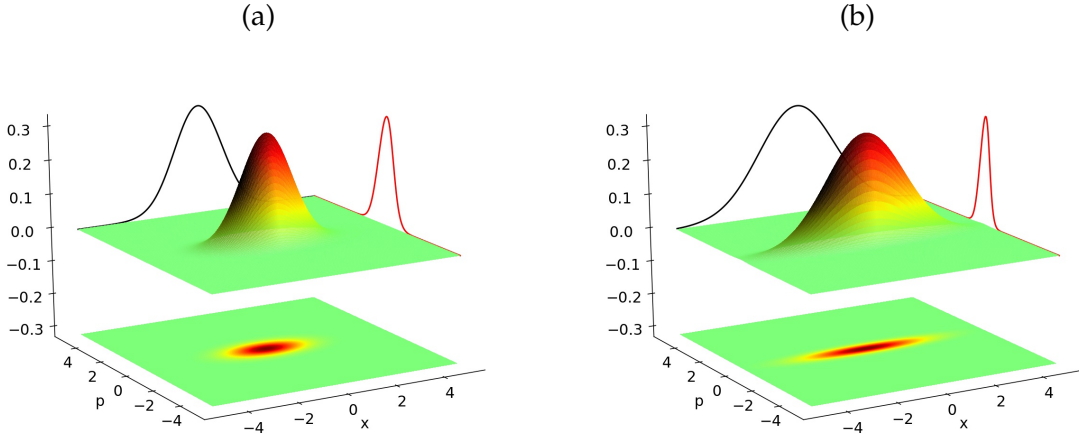


Figure 1.6 – Wigner function of squeezed vacuum state with a squeezing parameter (a): $r = 0.35$ ($s = -3$ dB) and (b): $r = 0.81$ ($s = -7$ dB) and the corresponding quadrature distributions $P(x)$ (black) and $P(p)$ (red). The marginal distributions are rescaled for visualization purpose.

1.4.2 Non-Gaussian quantum states

Compared to Gaussian quantum states introduced previously, non-Gaussian states have a non-Gaussian Wigner function, or equivalently, a non-Gaussian probability distribution of measurement outcomes of the quadrature x_θ for at least some phases θ . These states are extremely relevant in fundamental quantum physics as well as quantum information processing [24] and quantum communication [25, 26]. It has been shown that, for a pure non-Gaussian quantum state, the associated Wigner function have negative values [42]. In this subsection, we introduce some examples of non-Gaussian states.

1.4.2.1 Fock states

As mentioned in subsection 1.1.3, n photon Fock states are the eigenstates of the radiation Hamiltonian. These states contain an exact number of photons, and they form a complete basis for the Hilbert space. The wave-function of the n photon Fock state, $|n\rangle$, is given by:

$$\psi_n(x_\theta) = \langle x_\theta | n \rangle = \frac{e^{-in\theta}}{\sqrt{2^n n! \sigma_0 \sqrt{2\pi}}} H_n \left(\frac{x_\theta}{\sigma_0 \sqrt{2}} \right) e^{-\frac{x_\theta^2}{4\sigma_0^2}}, \quad (1.86)$$

with $H_n(x)$ is the n -th Hermite polynomial. This leads to an associated quadrature probability distribution $P_n(x_\theta)$ independent of θ , given by:

$$P_n(x_\theta) = |\psi_n(x_\theta)|^2 = \frac{1}{2^n n! \sigma_0 \sqrt{2\pi}} H_n^2 \left(\frac{x_\theta}{\sigma_0 \sqrt{2}} \right) e^{-\frac{x_\theta^2}{2\sigma_0^2}}, \quad (1.87)$$

where $L_n(x)$ is the n -th Laguerre polynomial. The Wigner function of the Fock state $|n\rangle$ is given by:

$$W_n(x, p) = \frac{(-1)^n}{2\pi\sigma_0^2} L_n \left(\frac{x^2 + p^2}{\sigma_0^2} \right) e^{-\frac{x^2 + p^2}{2\sigma_0^2}}. \quad (1.88)$$

Except the vacuum state $|n=0\rangle$, the Wigner function is non-Gaussian and it has negative values. We note that the Fock states are phase invariant (rotation symmetry in the Wigner function, or equivalently, marginal distribution $P_n(x_\theta)$ does not depend on the phase θ). This can be seen clearly in Figure 1.7, where the Wigner function of states $|n=1\rangle$, $|n=2\rangle$, $|n=3\rangle$, and $|n=4\rangle$ are displayed. The number of sign change in the Wigner function (and the number of zeros in the marginal distribution $P_n(x_\theta)$) is equal to the number of photons in the Fock state.

1.4.2.2 Schrödinger cat states

In 1935, *Erwin Schrödinger* proposed a thought experiment, in which he illustrates the weirdness of quantum superposition in the macroscopic world [43]. This experiment was introduced by considering a cat as a macroscopic system, being in a coherent superposition between "alive" and "dead" states, which are macroscopically distinguishable. In optics, the "alive" and "dead" cat states are replaced by a coherent state (introduced

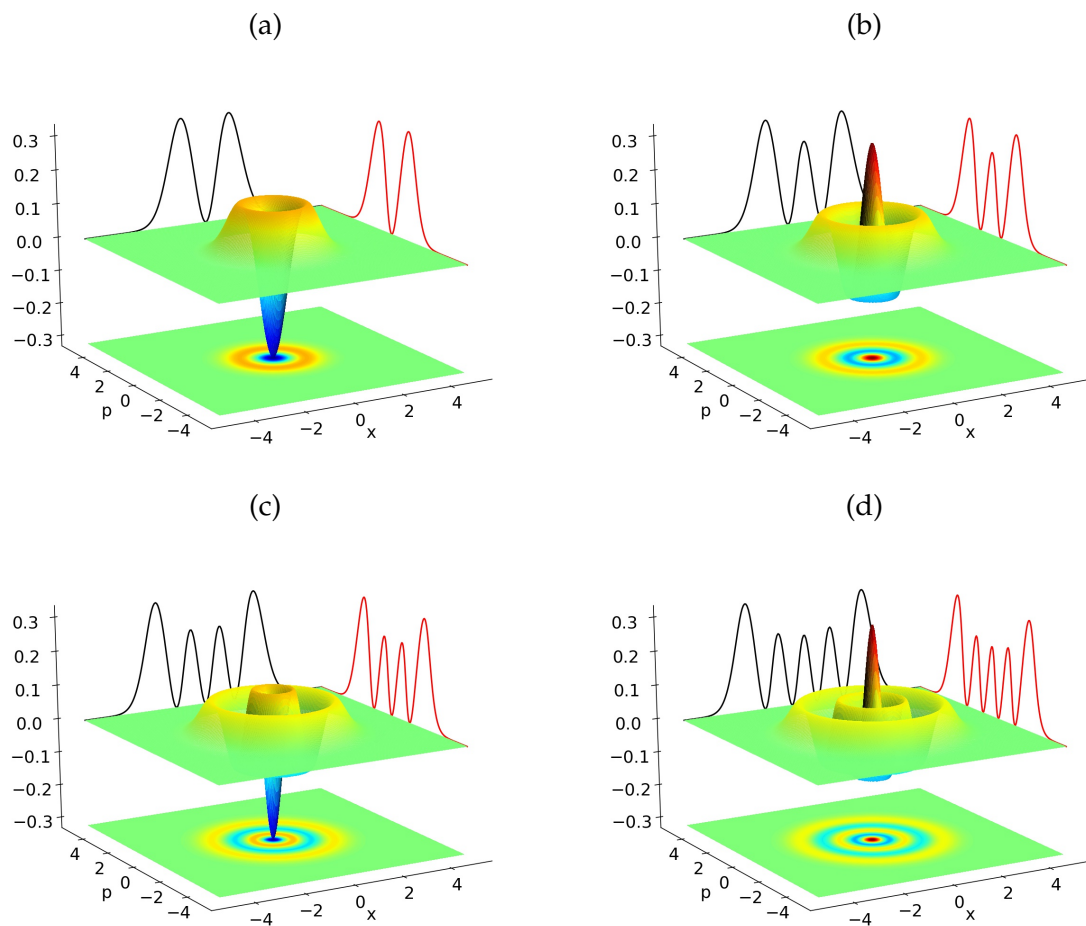


Figure 1.7 – Wigner function of Fock states $|n\rangle$ with (a): $n = 1$, (b): $n = 2$, (c): $n = 3$ and (d): $n = 4$ and the corresponding quadrature distributions $P_n(x)$ (black) and $P_n(p)$ (red). The marginal distributions are rescaled for visualization purpose.

in [subsection 1.4.1.2](#)) with opposite phases $|\alpha\rangle$ and $|\alpha\rangle$. The optical Schrödinger cat state with amplitude α is then given by:

$$|cat_\phi\rangle = \frac{1}{\sqrt{2(1 + e^{-2|\alpha|^2} \cos(\phi))}} \left(|\alpha\rangle + e^{i\phi} |\alpha\rangle \right), \quad (1.89)$$

where ϕ is the superposition phase. In the Fock basis, this state can be written as:

$$|cat_\phi\rangle = \frac{e^{-|\alpha|^2/2}}{\sqrt{2(1 + e^{-2|\alpha|^2} \cos(\phi))}} \sum_n \frac{[1 + (-1)^n e^{i\phi}] \alpha^n}{\sqrt{n!}} |n\rangle. \quad (1.90)$$

Two particular cases can be emphasised here, if the superposition phase is null ($\phi = 0$), the state in [Equation 1.90](#), noted $|cat_+\rangle$, is a superposition of Fock states with only even photon number, and then called even Schrödinger cat state. The photon number probability distribution is given by:

$$\begin{cases} P_+(2n) = \frac{2e^{-|\alpha|^2}}{1+e^{-2|\alpha|^2}} \frac{|\alpha|^{4n}}{(2n)!}, \\ P_+(2n+1) = 0. \end{cases} \quad (1.91)$$

In the other case, where the superposition phase is equal to pi ($\phi = \pi$), the state in [Equation 1.90](#), noted $|cat_-\rangle$, is a superposition of Fock states with only odd photon number, it is then called odd Schrödinger cat state. The photon number probability distribution is given by:

$$\begin{cases} P_-(2n) = 0, \\ P_-(2n+1) = \frac{2e^{-|\alpha|^2}}{1-e^{-2|\alpha|^2}} \frac{|\alpha|^{4n+2}}{(2n+1)!}. \end{cases} \quad (1.92)$$

[Figure 1.8](#) shows the photon number distribution in even and odd Schrödinger cat states with amplitude $\alpha = 2$.

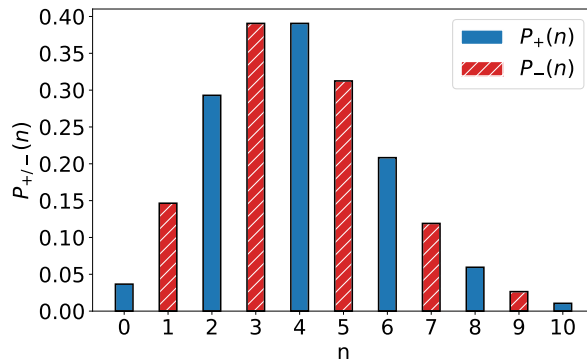


Figure 1.8 – Photon number distribution in an even (red) and odd (blue) Schrödinger cat state.

In the case where the amplitude α is real (which can be fulfilled by a proper choice of the quadrature basis), the Wigner function of a Schrödinger cat state is given by:

$$W_\phi(x, p) = \frac{e^{-\frac{x^2+p^2}{2\sigma_0^2}}}{2\pi\sigma_0^2(1 + e^{-2\alpha^2} \cos \phi)} \left[e^{-2\alpha^2} \cosh\left(\frac{2\alpha x}{\sigma_0}\right) + \cos\left(\frac{2\alpha p}{\sigma_0} - \phi\right) \right], \quad (1.93)$$

and the associated quadrature probability distribution $P_\phi(x_\theta)$ is given by:

$$P_\phi(x_\theta) = \frac{e^{-\left(\frac{x^2}{2\sigma_0^2} + 2\alpha^2 \cos^2 \theta\right)}}{\sigma_0 \sqrt{2\pi} (1 + e^{-2\alpha^2 \cos \phi})} \left[\cosh\left(\frac{2x\alpha}{\sigma_0} \cos \theta\right) + \cos\left(\phi - \frac{2x\alpha}{\sigma_0} \sin \theta\right) \right]. \quad (1.94)$$

Figure 1.9 shows the Wigner function of even ((a)-(b)) and odd ((c)-(d)) Schrödinger cat states with amplitudes $\alpha = 1$ ((a)-(c)) and $\alpha = 2$ ((b)-(d)).

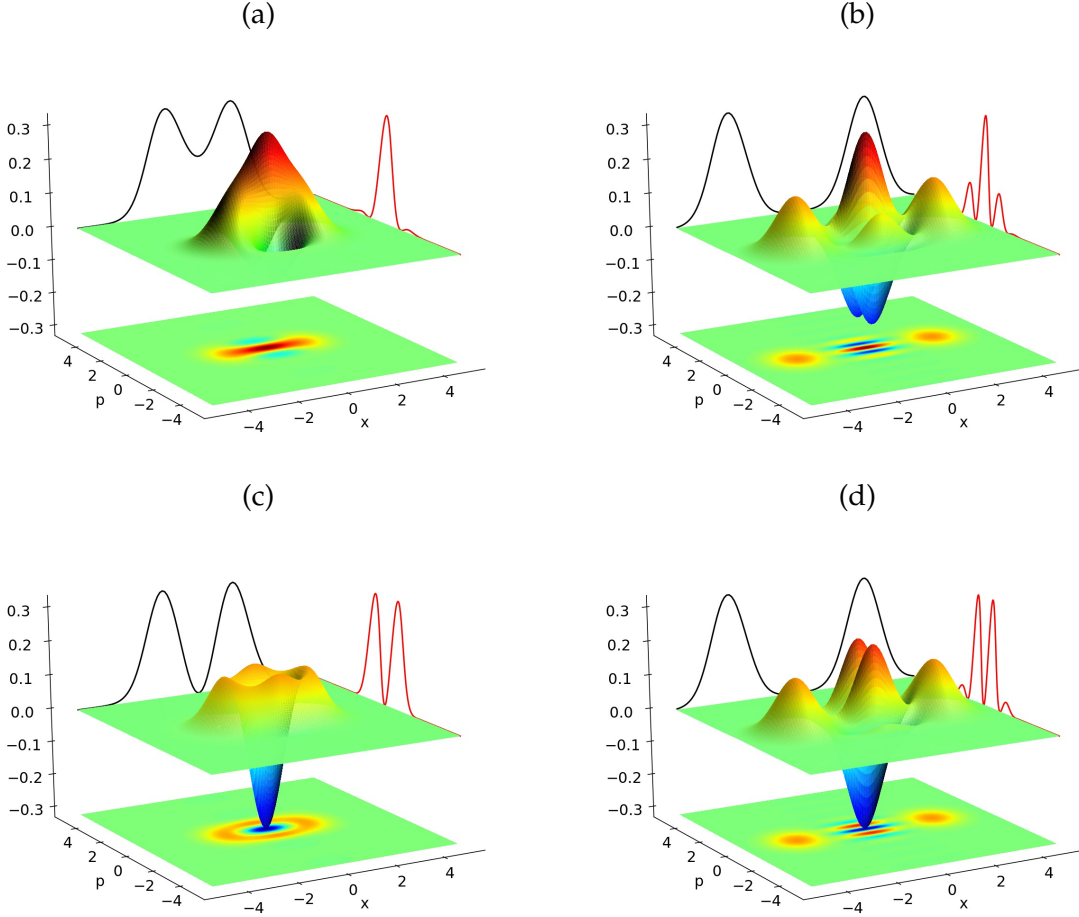


Figure 1.9 – Wigner functions of different Schrödinger cat states with: (a): $\phi = 0$ and $\alpha = 1$, (b): $\phi = 0$ and $\alpha = 2$, (c): $\phi = \pi$ and $\alpha = 1$ and (d): $\phi = \pi$ and $\alpha = 2$ and the corresponding quadrature distributions $P_\phi(x)$ (black) and $P_\phi(p)$ (red). The marginal distributions are rescaled for visualization purpose.

For an increasing amplitude α , we can distinguish the two lobes in the Wigner function, corresponding to the components $|\alpha\rangle$ and $|\!-\alpha\rangle$. In addition, interference fringes appear around the phase space origin, which is a sign of quantum interferences between $|\alpha\rangle$ and $|\!-\alpha\rangle$. This also can be seen in the quadrature distributions, where the distribution $P_\phi(x)$ contains two lobes corresponding to the two coherent state components in the Schrödinger cat state and the distribution $P_\phi(p)$ is oscillating, giving a sign

of quantum interference due to the coherent superposition of the two coherent states $|\alpha\rangle$ and $|-\alpha\rangle$. More and more oscillations in the Wigner function (and equivalently the quadrature distribution $P_\phi(p)$) appear when the amplitude α of the Schrödinger cat state increases.

1.5 CONCLUSION

We have introduced in this chapter the procedure often used to quantize the free electromagnetic field. This leads to a full quantum description of radiation that is needed to describe some phenomenon encountered in experiments and cannot be fully explained by the classical treatment. Then, the density matrix formalism was introduced. This formalism, is extremely useful to describe some situation where the state vector formalism cannot be used, such as dealing with mixed states. After that, the Wigner function representation was introduced, a very powerful tool to visualize quantum states and to show their quantum behaviour (Wigner function negativity for example). Finally, we gave some examples of quantum states that are frequently encountered in quantum optics experiment. These states can be classified into two main classes: the Gaussian states, displaying Gaussian Wigner function, and the non-Gaussian states, displaying non-Gaussian Wigner functions with negative values. In the next chapter, we will present some experimental tools, showing how to create, transform and measure quantum states of light.

EXPERIMENTAL TOOLS

2.1	Linear and nonlinear interactions	32
2.1.1	Linear interactions	32
2.1.2	Nonlinear interactions	34
2.2	Quantum measurement	36
2.2.1	Photon detection	37
2.2.2	Homodyne detection	39
2.3	Quantum state generation	41
2.3.1	Squeezed state generation	42
2.3.2	Schrödinger kitten state	44
2.4	Quantum state reconstruction	53
2.4.1	Quantum state reconstruction algorithms	53
2.5	Conclusion	56

As mentioned in the previous chapter, non-Gaussian states are of particular interest for implementing quantum information processing and communication tasks. Among the various possible ways to produce these kind of states, the association of unitary transformations and quantum measurements is widely used as these operations are relatively easy-to-implement. Some unitary transformations can be implemented using linear and nonlinear optical components. In nonlinear optics, interaction between different optical modes, mediated by a nonlinear optical response of a given material, allows to create states with quantum properties starting from a quasi-classical one. This is the case for example of squeezed vacuum state production using the second order nonlinear optical interaction called spontaneous parametric down conversion. These quantum states can then be manipulated and transformed using linear passive optical component such as beam splitters and phase shifters. In [section 2.1](#), we introduce some of these unitary transformation that will be used in the rest of the manuscript. In addition to this, quantum measurement plays an important role in quantum information protocols. It allows not only to characterize quantum states of light, but also to transform them in order to produce other states. In [section 2.2](#), we introduce the quantum measurement formalism and focus on two main examples: photon detection and homodyne measurement. In [section 2.3](#), we exploit the notions introduced in [section 2.1](#) and [section 2.2](#) to show how we can experimentally produce squeezed vacuum and Schrödinger cat-like states. Then, in [section 2.4](#), we show how we can characterise these photonic states using quantum state reconstruction algorithms. Finally, we conclude the chapter in [section 2.5](#).

2.1 LINEAR AND NONLINEAR INTERACTIONS

A wide range of optical quantum states can be produced by applying unitary transformations on quantum radiation. This is possible thanks to linear and nonlinear optical interactions, which are very useful and easy-to-implement experimental tools for quantum state creation and manipulation. In this section, we introduce the linear and nonlinear interactions that we will use in this work.

2.1.1 Linear interactions

The most elementary building blocks of linear optical circuits are phase shifters and beam splitters. Despite their simplicity, these ingredients are powerful and used almost in all quantum optics experiments. In fact, any $N \times N$ linear unitary transformation of the form:

$$\hat{a}'_k = \sum_m U_{km} \hat{a}_m, \quad (2.1)$$

can be implemented with a sequence of phase shifters and beam splitters [44]. The unitary operator \hat{U} acting on N modes can be written in terms of a quadratic Hamiltonian as [21]:

$$\hat{U} = e^{-i\hat{a}^\dagger \mathbf{H} \hat{a}}, \quad (2.2)$$

where $\hat{a}^\dagger = (\hat{a}_1^\dagger, \hat{a}_2^\dagger, \dots, \hat{a}_N^\dagger)$, $\hat{a} = (\hat{a}_1, \hat{a}_2, \dots, \hat{a}_N)^T$, and \mathbf{H} is an $N \times N$ Hermitian matrix.

2.1.1.1 Phase shift

The simplest form of phase shift is the free propagation of radiation. It can for example be implemented in a controlled manner by means of electro optic modulators. In the Heisenberg picture, the action of a phase shift operator $\hat{U}(\theta)$ on the annihilation and creation operators is given by:

$$\hat{a}_\theta = \hat{U}^\dagger(\theta) \hat{a} \hat{U}(\theta) = e^{-i\theta} \hat{a}, \quad \hat{a}_\theta^\dagger = \hat{U}^\dagger(\theta) \hat{a}^\dagger \hat{U}(\theta) = e^{i\theta} \hat{a}^\dagger, \quad (2.3)$$

here, the matrix \mathbf{H} in Equation 2.2 is replaced by the scalar θ ($\hat{U}(\theta) = e^{-i\theta \hat{a}^\dagger \hat{a}}$). In terms of quadrature operators \hat{x} and \hat{p} , the action of a phase shift is given by:

$$\begin{pmatrix} \hat{x}_\theta \\ \hat{p}_\theta \end{pmatrix} = \begin{pmatrix} \cos \theta & \sin \theta \\ -\sin \theta & \cos \theta \end{pmatrix} \begin{pmatrix} \hat{x} \\ \hat{p} \end{pmatrix}, \quad (2.4)$$

which correspond to a rotation in the phase space (see Equation 1.30, Equation 1.31 and section 1.3).

2.1.1.2 Beam splitter

A beam splitter (BS) is an optical device that mixes two input beams (1) and (2) to give two output beams (3) and (4) (see Figure 2.1). In quantum optics, the action of

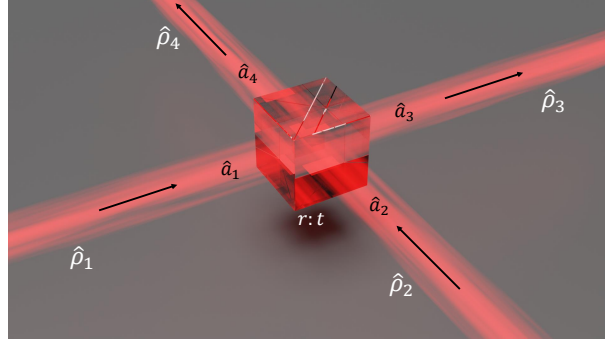


Figure 2.1 – Optical beam splitter of reflection coefficient r and transmission coefficient t .

a lossless beam splitter with a reflection coefficient r and transmission coefficient t in amplitude is described by the unitary transformation:

$$\hat{U}_{BS} = e^{\theta(\hat{a}_1^\dagger \hat{a}_2 - \hat{a}_1 \hat{a}_2^\dagger)}, \quad (2.5)$$

where $r = \sin \theta$ and $t = \cos \theta$. This operator is obtained by replacing the matrix \mathbf{H} in Equation 2.2 by:

$$\mathbf{H} = \begin{pmatrix} 0 & \theta \\ -\theta & 0 \end{pmatrix}. \quad (2.6)$$

Its action on the annihilation operators is given by:

$$\begin{pmatrix} \hat{a}_3 \\ \hat{a}_4 \end{pmatrix} = \hat{U}_{BS}^\dagger \begin{pmatrix} \hat{a}_1 \\ \hat{a}_2 \end{pmatrix} \hat{U}_{BS} = \begin{pmatrix} t & -r \\ r & t \end{pmatrix} \begin{pmatrix} \hat{a}_1 \\ \hat{a}_2 \end{pmatrix}, \quad (2.7)$$

which is also true for the quadrature operators:

$$\begin{pmatrix} \hat{x}_3 \\ \hat{x}_4 \end{pmatrix} = \begin{pmatrix} t & -r \\ r & t \end{pmatrix} \begin{pmatrix} \hat{x}_1 \\ \hat{x}_2 \end{pmatrix}, \quad \begin{pmatrix} \hat{p}_3 \\ \hat{p}_4 \end{pmatrix} = \begin{pmatrix} t & -r \\ r & t \end{pmatrix} \begin{pmatrix} \hat{p}_1 \\ \hat{p}_2 \end{pmatrix}. \quad (2.8)$$

In other words, a beam splitter acts on the quadrature eigenstates $|x_1, x_2\rangle = |x_1\rangle_1 \otimes |x_2\rangle_2$ as:

$$\hat{U}_{BS} |x_1, x_2\rangle = |x_3, x_4\rangle = |tx_1 - rx_2, rx_1 + tx_2\rangle. \quad (2.9)$$

Despite the state $|x_1, x_2\rangle$ is not physical, the relation given by Equation 2.9 is mathematically useful. It allows to deduce the action of a beam splitter on the input states wave-function as:

$$\psi(x_1, x_2) \longrightarrow \psi(tx_3 + rx_4, -rx_3 + tx_4), \quad (2.10)$$

or equivalently, the Wigner function of the input state is transformed as:

$$W(x_1, p_1; x_2, p_2) \longrightarrow W(tx_3 + rx_4, tp_3 + rp_4; -rx_3 + tx_4, -rp_3 + tp_4). \quad (2.11)$$

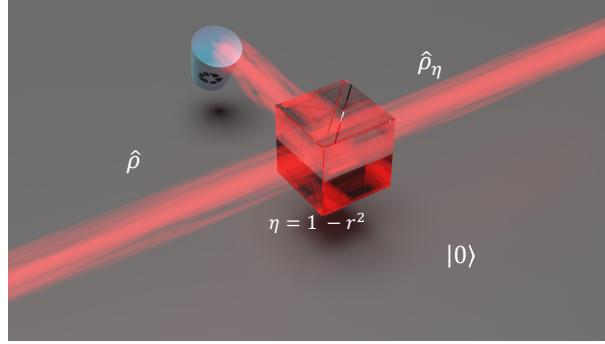


Figure 2.2 – Beam splitter based model for optical losses.

A model for optical losses

The BS unitary transformation just introduced is useful not only to model experiments involving beam splitters, but also to model the effect of losses. In fact, replacing the state $\hat{\rho}_2$ in Figure 2.1 by the vacuum state, the output state in mode (3) after tracing out the mode (4), noted $\hat{\rho}_\eta$, is equivalent to the state in mode (1) subject to losses given by the square of the reflection coefficient r^2 and a transmission efficiency $\eta = 1 - r^2$ (see Figure 2.2). The Wigner function of the output state is given by:

$$\begin{aligned} W_\eta(x, p) &= \int \int W(tx + rx_0, tp + rp_0) W_{|0\rangle}(-rx + tx_0, -rp + tp_0) dx_0 dp_0 \\ &= \frac{1}{r^2 t^2} \int \int W\left(\frac{x'}{t}, \frac{p'}{t}\right) W_{|0\rangle}\left(\frac{x - x'}{r}, \frac{p - p'}{r}\right) dx' dp'. \end{aligned} \quad (2.12)$$

The Wigner function of the state after losses $W_\eta(x, p)$ is then given by the convolution of the Wigner function of the state before losses $W(x, p)$ and a Gaussian function given by the Wigner function of the vacuum state $W_{|0\rangle}(x_0, p_0)$. It is important to note that the information is not completely lost, since measuring the state $\hat{\rho}_\eta$ allows to deduce the state before losses $\hat{\rho}$ as we will see in section 2.4.

2.1.2 Nonlinear interactions

Squeezed and entangled states are important resources in many quantum information protocols. Squeezing has been demonstrated in many experimental realizations thanks to the nonlinear interactions of light with matter [45, 46]. This nonlinear interaction is induced by the propagation of electromagnetic field in a nonlinear medium. The polarisation (dipole moment) of the medium in this case is given by [47].

$$\mathbf{P}(t) = \epsilon_0 \left[\chi^{(1)} \mathbf{E}(t) + \chi^{(2)} \mathbf{E}^2(t) + \chi^{(3)} \mathbf{E}^3(t) + \dots \right], \quad (2.13)$$

where $\chi^{(1)}$ is the linear susceptibility, and $\chi^{(2)}$ and $\chi^{(3)}$ are the second and third order nonlinear susceptibilities, respectively. One particular widely exploited nonlinear interaction for quantum state generation is the *spontaneous parametric down conversion* process. It is a second order nonlinear process that consists of converting photons from

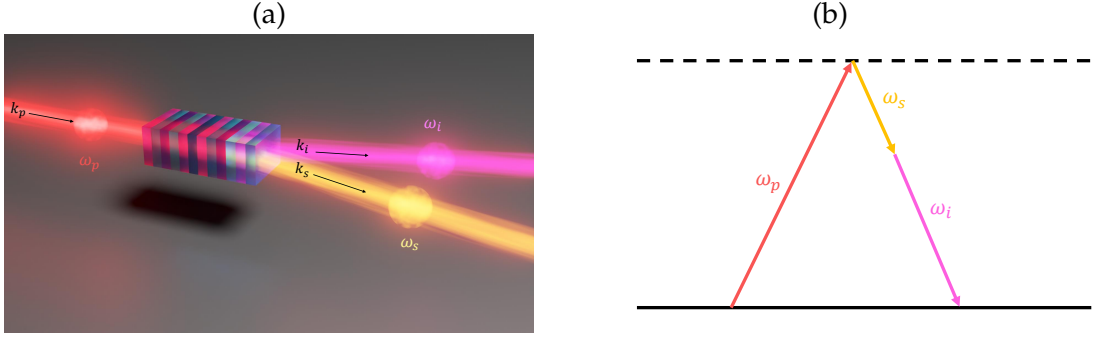


Figure 2.3 – Schematic representation (a) and the energy diagram (b) of parametric down conversion process. A pump photon at frequency ω_p is destroyed and two photons at frequencies ω_s and ω_i are created. This interaction is mediated by a nonlinear medium.

a strong pump field at frequency ω_p into pairs of photons, generally called signal and idler, at frequencies ω_s and ω_i (see Figure 2.3).

In this nonlinear process, the energy and momentum conservation conditions must be fulfilled, which leads to the following relations:

$$\omega_p = \omega_s + \omega_i, \quad (2.14)$$

$$\mathbf{k}_p = \mathbf{k}_s + \mathbf{k}_i. \quad (2.15)$$

In quantum optics, this process can be described by the interaction Hamiltonian given by:

$$\hat{H}_{int} = i\hbar\chi^{(2)}|\alpha_p| \left(e^{i\phi}\hat{a}_s^\dagger\hat{a}_i^\dagger - e^{-i\phi}\hat{a}_s\hat{a}_i \right). \quad (2.16)$$

The first term in the interaction Hamiltonian describes the process of destruction of a pump photon and creation of signal and idler photons, and the second term describes the inverse process. Note that, in the approximation of strong coherent pump field, the pump annihilation operator \hat{a}_p in the interaction Hamiltonian (Equation 2.16) is replaced by the complex scalar $\alpha_p = |\alpha_p|e^{i\phi}$ [48]. We can now define a two mode unitary evolution operator as:

$$\hat{U} = e^{-\frac{i}{\hbar}\hat{H}_{int}t} = e^{-(\zeta\hat{a}_s^\dagger\hat{a}_i^\dagger - \zeta^*\hat{a}_s\hat{a}_i)} = \hat{S}_{s,i}(\zeta), \quad (2.17)$$

with $\zeta = re^{i\phi}$ and $r = -\chi^{(2)}|\alpha_p|t = -\chi^{(2)}|\alpha_p|nL/c$, where $t = nL/c$ is the interaction time, and n and L are the refractive index and the length of the nonlinear medium, respectively. This unitary evolution is equivalent to the squeezing operator (Equation 1.81) acting on a two mode state, thus, it is called two mode squeezing operator. Its action on the annihilation operators \hat{a}_s and \hat{a}_i is given by¹:

$$\hat{a}'_s = \hat{S}_{s,i}^\dagger(\zeta)\hat{a}_s\hat{S}_{s,i}(\zeta) = \hat{a}_s \cosh r - \hat{a}_i^\dagger e^{i\phi} \sinh r, \quad (2.18)$$

1. These transformations can be retrieved in the Heisenberg picture by solving the evolution equation $i\hbar\frac{d}{dt}\hat{a}_{s,i} = [\hat{H}_{int}, \hat{a}_{s,i}]$.

$$\hat{a}'_i = \hat{S}_{s,i}^\dagger(\zeta) \hat{a}_i \hat{S}_{s,i}(\zeta) = \hat{a}_i \cosh r - \hat{a}_s^\dagger e^{i\phi} \sinh r. \quad (2.19)$$

In the case where $\phi = 0$, which is always possible with a proper choice of the phase origin, the quadrature operators are transformed as:

$$\hat{x}'_s \pm \hat{x}'_i = (\hat{x}_s \pm \hat{x}_i) e^{\mp r}, \quad (2.20)$$

$$\hat{p}'_s \pm \hat{p}'_i = (\hat{p}_s \pm \hat{p}_i) e^{\pm r}, \quad (2.21)$$

and the corresponding variances are given by:

$$\sigma_{x'_s \pm x'_i}^2 = e^{\mp 2r} \sigma_{x_s \pm x_i}^2, \quad (2.22)$$

$$\sigma_{p'_s \pm p'_i}^2 = e^{\pm 2r} \sigma_{p_s \pm p_i}^2. \quad (2.23)$$

2.2 QUANTUM MEASUREMENT

A measurement operation on a given quantum state $\hat{\rho}$ is described by a set of measurement operators $\{\hat{M}_m\}$ acting on the Hilbert space where the state $\hat{\rho}$ evolves. These operators satisfy the completeness relation:

$$\sum_m \hat{M}_m^\dagger \hat{M}_m = \hat{\mathbb{1}}. \quad (2.24)$$

Each operator \hat{M}_m is related to a possible measurement outcome, noted m , which occurs with a probability:

$$p(m) = \text{Tr} \left[\hat{M}_m \hat{\rho} \hat{M}_m^\dagger \right], \quad (2.25)$$

and the state just after the measurement operation is given by:

$$\hat{\rho}_m = \frac{1}{p(m)} \hat{M}_m \hat{\rho} \hat{M}_m^\dagger. \quad (2.26)$$

This is the most general quantum measurement formalism, giving the statistics of the measurement outcomes (Equation 2.25) and the post-measurement state (Equation 2.26). However, in some situations, we focus on the statistics of measurement outcomes without considering the state after measurement (traced out), especially when the measurement is destructive. In this case, a well adapted formalism, called POVM (Positive Operator-Valued Measure) is used. Taking again the probability of obtaining a measurement outcome m (Equation 2.25), it can be written as:

$$p(m) = \text{Tr} \left[\hat{M}_m \hat{\rho} \hat{M}_m^\dagger \right] = \text{Tr} \left[\hat{M}_m^\dagger \hat{M}_m \hat{\rho} \right] = \text{Tr} \left[\hat{\Pi}_m \hat{\rho} \right], \quad (2.27)$$

where $\hat{\Pi}_m = \hat{M}_m^\dagger \hat{M}_m$ is called the POVM element associated with the measurement outcome m and the set $\{\hat{\Pi}_m\}$ is called the POVM. These POVM elements satisfy the following completeness relation:

$$\sum_m \hat{\Pi}_m = \hat{\mathbb{1}}. \quad (2.28)$$

In the next subsections, we give two measurement operations widely used in quantum optics, namely photon detection and homodyne detection.

2.2.1 Photon detection

There is mainly two classes of photon detectors, photon counting detectors that are able to discriminate the number of incoming photons, and the On/Off detectors that can only give information about the presence or absence of photons without photon number discrimination. In both cases, available detectors are characterized by several parameters:

- The quantum efficiency η_{det} : describing the fact that an incoming photon can be lost leading to an absence of detection.
- Dark counts: related to false detection events in the absence of light.
- Dead time: which is the time window in which the detector is blind after a detection event.
- Timing jitter: describing the temporal resolution of the detector.
- Afterpulsing: describing the fact that the detector delivers several electrical pulses per single detection event.

In this thesis, photon detectors are mainly used to herald the creation of non-Gaussian states of light. In this case, the detector dead time doesn't really affect the quality of the produced state, it just limits the heralding rate. Moreover, afterpulsing can completely be eliminated in state-of-the-art photon detectors, such as superconducting nanowire single-photon detectors. On the other hand, detectors with low timing jitter (few tens of picoseconds) are available [49]. This range of timing jitter is negligible in our case, since the produced non-Gaussian state has a temporal width of around 100 ns (see ??). Theoretical models describing situations where the jitter is non-negligible are available in literature [50, 51]. In this paragraph, we give the model of photon detection operation focusing on the quantum efficiency η_{det} and the dark counts. The POVM elements for a perfect photon counter (with unit quantum efficiency and without dark counts) are given by:

$$\hat{\Pi}_n = |n\rangle\langle n|, \quad (2.29)$$

where n is the number of photons. However, in this thesis, we use mainly On/Off detectors that have two possible outcomes, a "click" when photons are detected (any number of photons) and a "non-click" when there is no detected photon. The two POVM elements associated with these two events are:

$$\hat{\Pi}_{Off} = |0\rangle\langle 0|, \quad (2.30)$$

$$\hat{\Pi}_{On} = \hat{\mathbb{1}} - |0\rangle\langle 0|. \quad (2.31)$$

These POVM elements are given for a perfect On/Off detector with unit quantum efficiency and without dark counts. Nevertheless, real On/Off detectors have most of the time a limited quantum efficiency $\eta_{det} < 1$ and a non-null dark count rate, and these two parameters depend on the detector technology. At telecommunication wavelength for example, avalanche photodiodes (APD) have a quantum efficiency around 25% and a dark count rate up to 1 kHz, whereas superconducting nanowire single-photon detectors (SNSPD) have a quantum efficiency $> 70\%$ and dark count rate < 100 Hz.

To take the limited quantum efficiency into account, a realistic On/Off detector can be modelled as a perfect On/Off detector with optical losses upstream it, as illustrated in [Figure 2.4](#)-(a), where the BS model presented previously (see [subsection 2.1.1.2](#)) is used to model losses.

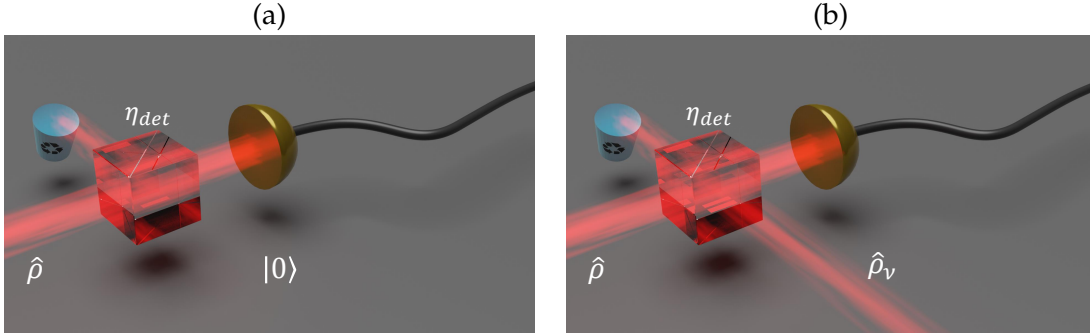


Figure 2.4 – Model of an On/Off detector with limited efficiency η_{det} (a and b) without dark counts (a) and with non-null dark counts (b).

In this case, the POVM elements associated with the two responses of the detector are given by:

$$\hat{\Pi}_{Off}(\eta_{det}) = \sum_{k=0}^{\infty} (1 - \eta_{det})^k |k\rangle\langle k|, \quad (2.32)$$

$$\hat{\Pi}_{On}(\eta_{det}) = \hat{\mathbb{1}} - \hat{\Pi}_{Off}(\eta_{det}), \quad (2.33)$$

which means that, despite the presence of photons impinging the detector, some of them can be lost, giving in some cases a "non-click" event on the detector. In addition, the background noise, responsible for the dark counts, can be modelled by sending a quantum state $\hat{\rho}_\nu$ instead of vacuum state to the second input port of the losses-equivalent BS, as it is illustrated in [Figure 2.4](#)-(b). The choice of the state $\hat{\rho}_\nu$ depends on what kind of noise we want to model. For calculation simplicity, a thermal noise is adopted in this manuscript, and thus, the state $\hat{\rho}_\nu$ is chosen to be a thermal state with mean photon number $\bar{n}_t = \nu / (1 - \eta_{det})$, which gives a background noise with mean photon number impinging the perfect On/Off detector $\bar{n}_b = \nu$. In this case, the POVM elements associated with the two responses of the detector are given by [\[52\]](#):

$$\hat{\Pi}_{Off}(\eta_{det}, \nu) = \frac{1}{1 + \nu} \sum_{k=0}^{\infty} \left(1 - \frac{\eta_{det}}{1 + \nu}\right)^k |k\rangle\langle k|, \quad (2.34)$$

$$\hat{\Pi}_{On}(\eta_{det}, \nu) = \hat{\mathbb{1}} - \hat{\Pi}_{Off}(\eta_{det}, \nu). \quad (2.35)$$

Since $\hat{\Pi}_{On}(\eta_{det}, \nu)$ is Hermitian, we can calculate its associated Wigner function using the definition given by Equation 1.62. By doing so, we find that:

$$W_{\hat{\Pi}_{On}}(x, p, \eta_{det}, \nu) = \frac{1}{4\pi\sigma_0^2} \left[1 - \frac{2}{2(1+\nu) - \eta_{det}} e^{-\frac{\eta_{det}}{2(1+\nu) - \eta_{det}} \frac{x^2 + p^2}{2\sigma_0^2}} \right]. \quad (2.36)$$

It is clear that the Wigner function associated to the POVM element $\hat{\Pi}_{On}(\eta_{det}, \nu)$ is non-Gaussian, and thus, a photon detection measurement with "click" events is a non-Gaussian measurement. Applied to an initially Gaussian quantum state, it can transform it into a non-Gaussian one, as we will see in section 2.3.

2.2.2 Homodyne detection

Homodyne detection is a widely used detection strategy in classical and quantum optics. As proposed in [53], it can be used to detect the quantum fluctuations of an arbitrary quantum state, opening the way to a wide panel of applications, ranging from quantum state tomography [54] and quantum correlation measurement [55] to quantum random number generation [56] and quantum communication [57, 58].

2.2.2.1 Principle of homodyne detection

The principle of homodyne detection is illustrated in Figure 2.5.

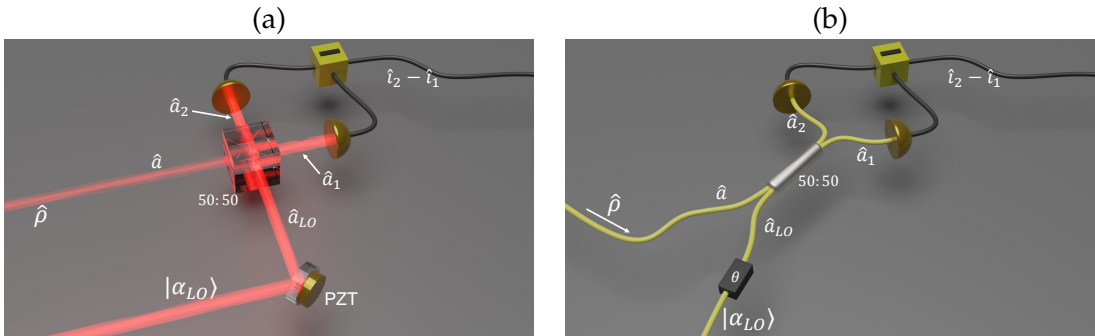


Figure 2.5 – Homodyne detection principle in bulk optics configuration (a) and guided optics configuration (b). A state $\hat{\rho}$ is mixed with a local oscillator $|\alpha_{LO}\rangle$ through a balanced BS. The two BS outputs are then measured with two photodiodes and the corresponding photocurrents are subtracted.

It consists of mixing a state $\hat{\rho}$ with a bright coherent state of amplitude α_{LO} , called local oscillator (LO), through a balanced BS ($r = t = 1/\sqrt{2}$). The two output modes of the beam splitter are then measured with two photodiodes, and the subtraction of the resulting photocurrents gives a signal proportional to a given quadrature \hat{x}_θ of the state $\hat{\rho}$. The phase θ of the measured quadrature can simply be scanned by controlling the phase of the LO (generally using PZT in bulk optics configuration and fibred phase shifter in guided optics configuration).

Let us consider the annihilation operators \hat{a} and \hat{a}_{LO} associated to the state $\hat{\rho}$ and the LO $|\alpha_{LO}\rangle$, respectively. By applying the beam splitter transformation given by

Equation 2.7, the annihilation operators at the output of the beam splitter are written as:

$$\hat{a}_1 = \frac{\hat{a} - \hat{a}_{LO}}{\sqrt{2}}, \quad (2.37)$$

$$\hat{a}_2 = \frac{\hat{a} + \hat{a}_{LO}}{\sqrt{2}}. \quad (2.38)$$

According to the semi-classical theory of light-matter interaction, the photocurrent at the output of a photodiode is proportional to the intensity of the light being detected, or in a simple picture, this photocurrent is proportional to the number of detected photons. The difference between the responses of the two photodiodes in this case can be approximated by:

$$\hat{i} = \hat{i}_2 - \hat{i}_1 \propto \hat{n}_2 - \hat{n}_1 = \hat{a}_2^\dagger \hat{a}_2 - \hat{a}_1^\dagger \hat{a}_1 = \hat{a}_{LO} \hat{a}^\dagger + \hat{a}_{LO}^\dagger \hat{a}. \quad (2.39)$$

As mentioned in subsection 2.1.2, the bright coherent beam can be considered as classical field, and so, by replacing the annihilation operator \hat{a}_{LO} by the scalar $\alpha_{LO} = |\alpha_{LO}|e^{i\theta}$, the homodyne detection response can be written as:

$$\hat{i} \propto |\alpha_{LO}| \left(e^{i\theta} \hat{a}^\dagger + e^{-i\theta} \hat{a} \right) \propto |\alpha_{LO}| \hat{x}_\theta = |\alpha_{LO}| (\hat{x} \cos \theta + \hat{p} \sin \theta). \quad (2.40)$$

So, the response of the homodyne detection is proportional to the quadrature \hat{x}_θ of the state $\hat{\rho}$, with an amplification factor given by the amplitude of the LO α_{LO} . The quadrature phase θ is directly given by the LO phase, and so, by controlling the LO phase, one can measure any quadrature \hat{x}_θ of any arbitrary state $\hat{\rho}$.

By comparing Equation 2.40 and Equation 1.61 with $\mathbf{r} = \mathbf{0}$, we can see that measuring the quadrature \hat{x}_θ is equivalent to measuring the electric field $\hat{E}(t)$, sampled at time t given by:

$$t = \frac{\theta \pm 2k\pi}{\omega}, \quad (2.41)$$

and so, scanning the LO phase θ allows the reconstruction of time evolution of the measured field $\hat{E}(t)$.

2.2.2.2 POVM of homodyne detection

For a fixed phase θ of the LO, the POVM elements of the homodyne detection, associated with the measurement outcomes x_θ of the operator \hat{x}_θ are given by:

$$\hat{\Pi}(x_\theta) = |x_\theta\rangle\langle x_\theta|, \quad (2.42)$$

and satisfy the completeness relation:

$$\int \hat{\Pi}(x_\theta) dx_\theta = \hat{\mathbb{1}}, \quad (2.43)$$

where $|x_\theta\rangle$ is the eigenstate of the observable \hat{x}_θ . The associated Wigner function is:

$$W_{\hat{\Pi}(x_\theta)}(x, p) = \frac{1}{4\pi\sigma_0^2} \delta(x \cos \theta + p \sin \theta - x_\theta), \quad (2.44)$$

and the marginal distribution of the measurement outcomes x_θ for a given quantum state $\hat{\rho}$ is:

$$P(x_\theta) = \text{Tr} [\hat{\Pi}(x_\theta)\hat{\rho}]. \quad (2.45)$$

Figure 2.6 shows simulated measurement outcomes of a perfect homodyne detection for some quantum states introduced in section 1.4.

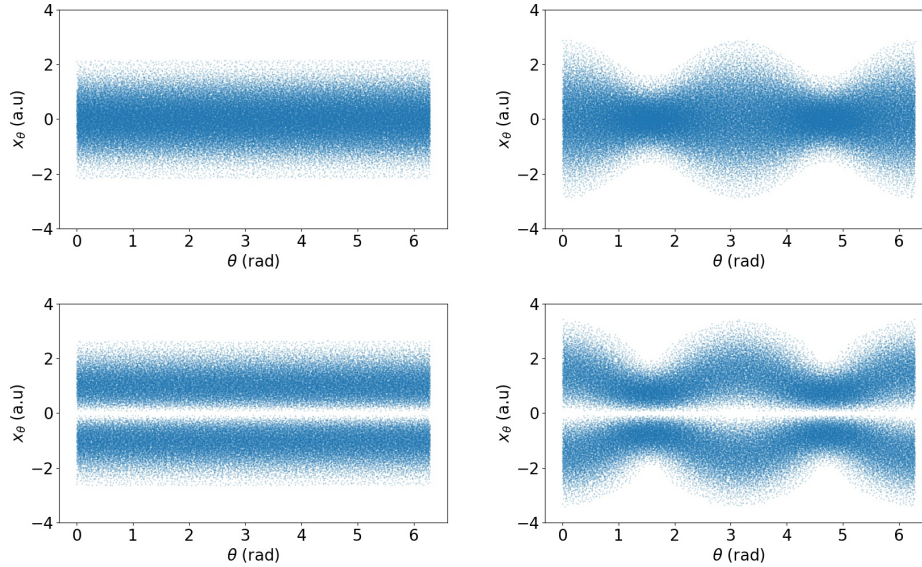


Figure 2.6 – Simulated homodyne detection outcomes x_θ for some quantum states introduced in section 1.4. Top left: vacuum state, top right: squeezed vacuum state with squeezing factor $s = -3$ dB, bottom left: single-photon Fock state $|1\rangle$ and bottom right: odd Schrödinger cat state with amplitude $\alpha = 1$.

As mentioned before, we can see that quantum fluctuations of the squeezed vacuum state are smaller than vacuum fluctuations for some phases θ and greater for other phases. Also, we can see clearly that for some quantum states, the homodyne detection outcomes - which are a direct picture of the evolution in time of the electric field - are counter intuitive, it is the case here of single-photon (bottom left) and Schrödinger cat (bottom right) states, showing strange and highly non-classical patterns. For the Schrödinger cat state, we can distinguish two oscillations with opposite phases in the homodyne trace x_θ . These oscillations are related to the electric field oscillations in time of the components $|\alpha\rangle$ and $|\alpha\rangle$, at the same time, with quantum interferences in the intersection regions.

2.3 QUANTUM STATE GENERATION

We introduced in section 1.4 some Gaussian and non-Gaussian quantum states that we find in most quantum optics experiments. As mentioned before, vacuum and coherent states are the easiest produced Gaussian states. In this section, we will focus on the generation of two very important resources in quantum information protocols, namely squeezed states (Gaussian) and Schrödinger cat states (non-Gaussian).

2.3.1 Squeezed state generation

Many techniques can be used to generate squeezed states of light. At first, squeezing was observed experimentally using Four-Wave Mixing in an atomic vapour [45]. After that, several experimental realizations have been set up to generate squeezed states using different techniques, such as second order, and third order nonlinearities in nonlinear crystals [59], and optical fibers [60], respectively. In this section, we focus on squeezed state generation using parametric down conversion process, which is the basis for the experimental realizations presented in [chapter 3](#) and [chapter 4](#).

2.3.1.1 Degenerate parametric down conversion process

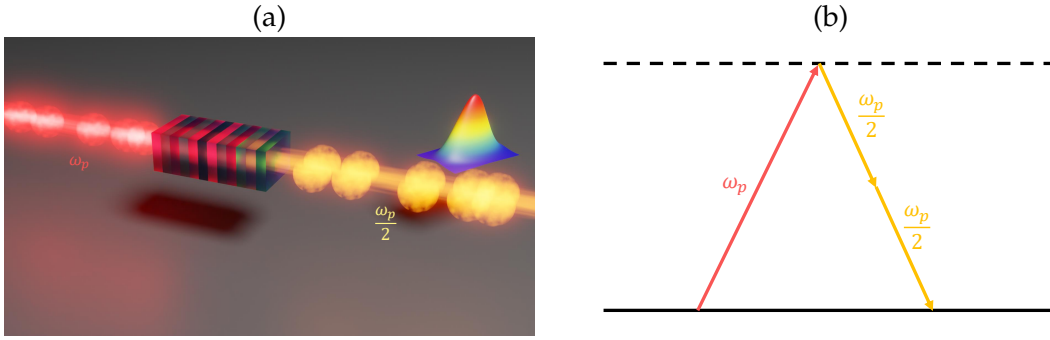


Figure 2.7 – Schematic representation (a) and the energy diagram (b) of squeezed vacuum generation via degenerate parametric down conversion process. The photons are generated at frequency $\omega_p/2$ where ω_p is the frequency of the pump photons.

In [subsection 2.1.2](#), we introduced the second order nonlinear interaction called parametric down conversion process in the general case (signal and idler photons can be distinguishable). In the degenerate case ([Figure 2.7](#)), where the signal and idler photons are managed to be indistinguishable in all degrees of freedom (polarization, spatial mode, spectral mode), we can replace the annihilation operators \hat{a}_s and \hat{a}_i is [Equation 2.16](#) by \hat{a} . The interaction Hamiltonian can then be written as:

$$\hat{H}_{int} = i\hbar\chi^{(2)}|\alpha_p| \left(e^{i\phi}\hat{a}^{\dagger 2} - e^{-i\phi}\hat{a}^2 \right), \quad (2.46)$$

and the unitary evolution operator is given by:

$$\hat{U} = e^{-\frac{i}{\hbar}\hat{H}_{int}t} = e^{-\frac{1}{2}(\zeta\hat{a}^{\dagger 2} - \zeta^*\hat{a}^2)} = \hat{S}(\zeta), \quad (2.47)$$

with $\zeta = re^{i\phi}$ and $r = -2\chi^{(2)}|\alpha_p|nL/c$. It is the single mode squeezing operator given by [Equation 1.81](#). Hence, the generated state by the degenerate parametric down conversion process is a single mode squeezed state introduced in [subsubsection 1.4.1.3](#). The action of the single mode squeezing operator on the annihilation operator \hat{a} is given by:

$$\hat{a}' = \hat{S}^\dagger(\zeta)\hat{a}\hat{S}(\zeta) = \hat{a} \cosh r - \hat{a}^\dagger e^{i\phi} \sinh r. \quad (2.48)$$

In the case where $\phi = 0$, the amplitude quadrature \hat{x} and phase quadrature \hat{p} are transformed as:

$$\hat{x}' = e^{-r} \hat{x}, \quad (2.49)$$

$$\hat{p}' = e^r \hat{p}, \quad (2.50)$$

and the corresponding variances are given by:

$$\sigma_{x'}^2 = e^{-2r} \sigma_x^2, \quad (2.51)$$

$$\sigma_{p'}^2 = e^{2r} \sigma_p^2. \quad (2.52)$$

For an input state being vacuum (with the associated annihilation operator \hat{a}), the variance of the quadrature \hat{x}_θ of the generated squeezed vacuum state is given by:

$$\sigma_{x_\theta}^2 = [e^{-2r} \cos^2 \theta + e^{2r} \sin^2 \theta] \sigma_0^2. \quad (2.53)$$

Figure 2.8 shows the variance of the quadrature \hat{x}'_θ of a 3 dB and a 6 dB squeezed vacuum state as functions of the phase θ .

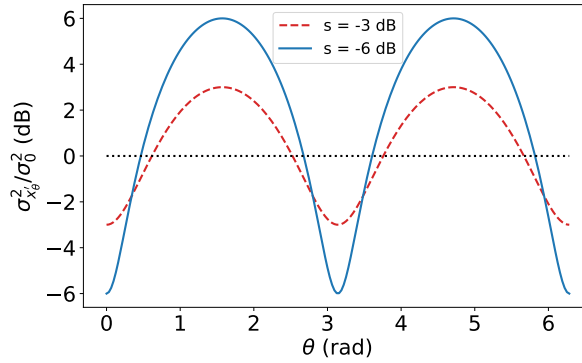


Figure 2.8 – The variance of the quadrature \hat{x}'_θ , normalized to the shot noise level, of a squeezed vacuum state with squeezing factor $s = -3$ dB (dashed red line) and $s = -6$ dB (solid blue line). The dotted black line represents the shot noise level.

As it can be seen, for some phases, the variance the quadrature \hat{x}'_θ of a squeezed vacuum state is below the shot noise level.

2.3.1.2 Effect of losses

Equation 2.53 gives the variance of the quadrature \hat{x}'_θ of squeezed vacuum state. However, in real experimental realizations, optical losses and the limited efficiency of realistic homodyne detections affect the measured squeezing level. In this case, the overall detection efficiency, η , can be included in Equation 2.53, leading to a quadrature variance given by:

$$\sigma_{x'_\theta}^2(\eta) = [\eta (e^{-2r} \cos^2 \theta + e^{2r} \sin^2 \theta) + 1 - \eta] \sigma_0^2. \quad (2.54)$$

Figure 2.9 shows the maximum and minimum quadrature variance as functions of the overall detection efficiency η for different squeezing level.

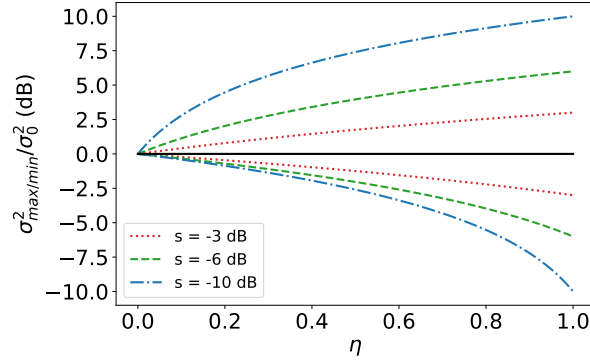


Figure 2.9 – The maximum and minimum variance of the quadrature \hat{x}'_{θ} , normalized to the shot noise level, of a squeezed vacuum state with squeezing factor $s = -3$ dB (dotted red line), $s = -6$ dB (dashed green line) and $s = -10$ dB (dash-dotted blue line) as functions of the overall detection efficiency η . The solid black line represents the shot noise level.

We can see that for a decreasing detection efficiency η (increasing losses), the maximum and minimum variances of the quadrature \hat{x}'_{θ} of a squeezed vacuum state converges to the shot noise level, leading to a detection of less squeezing due to contamination with vacuum. We note that although losses affect the measured squeezing level, the information is not completely lost. In fact, by measuring the minimum variance (squeezing) and maximum variance (antisqueezing), one can deduce the overall detection efficiency η and the squeezing level s before losses. From Equation 2.54, we can write the minimum and maximum variances as:

$$\sigma_{min}^2 = (\eta s + 1 - \eta) \sigma_0^2, \quad (2.55)$$

$$\sigma_{max}^2 = \left(\frac{\eta}{s} + 1 - \eta \right) \sigma_0^2. \quad (2.56)$$

These two equations allow to rewrite the overall detection efficiency η and the squeezing level s as functions of the measured squeezing and antisqueezing:

$$\eta = \frac{(\sigma_{max}^2 / \sigma_0^2 - 1)(1 - \sigma_{min}^2 / \sigma_0^2)}{\sigma_{max}^2 / \sigma_0^2 + \sigma_{min}^2 / \sigma_0^2 - 2}, \quad (2.57)$$

$$s = \frac{1 - \sigma_{min}^2 / \sigma_0^2}{\sigma_{max}^2 / \sigma_0^2 - 1}. \quad (2.58)$$

2.3.2 Schrödinger kitten state

As seen in subsection 1.4.2.2, an optical Schrödinger cat state is a superposition of two coherent states $|\alpha\rangle$ and $|- \alpha\rangle$ with the same amplitude and opposite phases. We have seen also that an odd Schrödinger cat state $|cat_{-}\rangle$ is a particular case, which

contains only odd photon number, whereas a squeezed vacuum state (see [subsubsection 1.4.1.3](#)) contains only even photon number. It is on the base of these photon number statistics that the proposal in [61] was made, where generation of Schrödinger cat-like state based on photon subtraction from squeezed vacuum state was proposed. Starting from squeezed vacuum state, an easily produced state by means of nonlinear interactions ([subsection 2.3.1](#)), a subtraction of single photon leads to the production of a state with only odd photon number, very similar to an odd Schrödinger cat state $|cat_{-}\rangle$ with small amplitude α , called Schrödinger kitten state. In fact, subtraction of any photon number n from squeezed vacuum state leads to the generation of a non-Gaussian state with only even/odd photon number distribution, which can be a very good approximation of a Schrödinger cat state with amplitude α that increases with respect to the number of subtracted photons.

2.3.2.1 Toy model

[Figure 2.10](#) shows the generation scheme based on photon subtraction from squeezed vacuum state using a low reflectivity beam splitter and a photon detector.

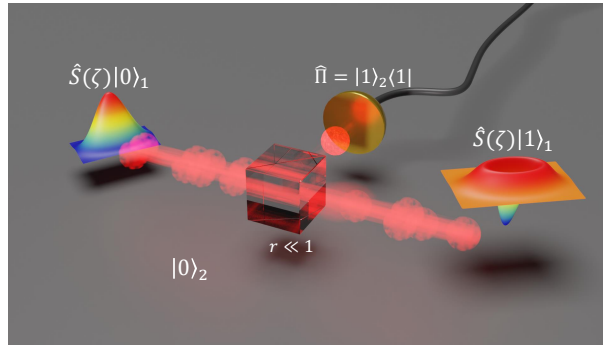


Figure 2.10 – Generation of Schrödinger cat-like states by photon subtraction from a squeezed vacuum state.

The state at the input of the beam splitter is given by:

$$\hat{\rho} = \hat{\rho}_1 \otimes \hat{\rho}_2 = \hat{S}(\zeta) |0\rangle_1 \langle 0| \hat{S}^\dagger(\zeta) \otimes |0\rangle_2 \langle 0|. \quad (2.59)$$

In the approximation of low reflectivity r , the beam splitter unitary transformation given by [Equation 2.5](#) can be approximated by:

$$\hat{U}_{BS} \approx \hat{\mathbb{1}} + \theta \left(\hat{a}_1^\dagger \hat{a}_2 - \hat{a}_1 \hat{a}_2^\dagger \right). \quad (2.60)$$

Applied to the state $\hat{\rho}$, the output state $\hat{\rho}'$ can be written as:

$$\begin{aligned} \hat{\rho}' = \hat{U}_{BS} \hat{\rho} \hat{U}_{BS}^\dagger \approx & \hat{S}(\zeta) |0\rangle_1 \langle 0| \hat{S}^\dagger(\zeta) \otimes |0\rangle_2 \langle 0| - \theta \hat{a}_1 \hat{S}(\zeta) |0\rangle_1 \langle 0| \hat{S}^\dagger(\zeta) \otimes |1\rangle_2 \langle 0| \\ & - \theta \hat{S}(\zeta) |0\rangle_1 \langle 0| \hat{S}^\dagger(\zeta) \hat{a}_1^\dagger \otimes |0\rangle_2 \langle 1| + \theta^2 \hat{a}_1 \hat{S}(\zeta) |0\rangle_1 \langle 0| \hat{S}^\dagger(\zeta) \hat{a}_1^\dagger \otimes |1\rangle_2 \langle 1|. \end{aligned} \quad (2.61)$$

The Detection of a single-photon in the mode 2, described by the POVM element $\hat{\Pi}_1 = |1\rangle_2 \langle 1|$, transforms the state in mode 1 as:

$$\hat{\rho}'_1 \propto \text{Tr}_2 [\hat{\Pi}_1 \hat{\rho}'] \propto \hat{a}_1 \hat{S}(\zeta) |0\rangle_1 \langle 0| \hat{S}^\dagger(\zeta) \hat{a}_1^\dagger. \quad (2.62)$$

By considering the transformation given by Equation 2.48, the annihilation operator \hat{a}_1 , applied to the squeezed vacuum state $\hat{S}(\zeta) |0\rangle_1$, is equivalent to squeezing a single-photon:

$$\hat{a}_1 \hat{S}(\zeta) |0\rangle_1 = \hat{S}(\zeta) \hat{S}^\dagger(\zeta) \hat{a}_1 \hat{S}(\zeta) |0\rangle_1 = \hat{S}(\zeta) \left(\hat{a}_1 \cosh r - \hat{a}_1^\dagger \sinh r \right) |0\rangle_1 \propto \hat{S}(\zeta) |1\rangle_1, \quad (2.63)$$

and the corresponding Wigner function is:

$$W_{\hat{\rho}'_1}(x, p) = \frac{1}{2\pi\sigma_0^2} \left[s \frac{x^2}{\sigma_0^2} + \frac{1}{s} \frac{p^2}{\sigma_0^2} - 1 \right] e^{-\frac{x^2}{2\sigma_0^2/s} - \frac{p^2}{2s\sigma_0^2}}. \quad (2.64)$$

As it can be seen in Figure 2.6, if we take the quadrature measurement outcomes x_θ of a single-photon state (bottom left) and squeeze them, we get a pattern similar to the one of an odd Schrödinger cat state with small amplitude (bottom right). The generated squeezed single-photon state $\hat{\rho}'_1$ is then an approximation of an odd Schrödinger cat state with small amplitude α . The fidelity between a perfect odd Schrödinger cat state $|cat_-\rangle$ and the squeezed single photon state $\hat{S}(r) |1\rangle$ is given by:

$$\mathcal{F} = |\langle cat_- | \hat{S}(r) |1\rangle|^2 = \frac{16\alpha^2 e^{-\frac{2\alpha^2 s}{1+s}}}{1 - e^{-2\alpha^2}} \left(\frac{\sqrt{s}}{1+s} \right)^3. \quad (2.65)$$

Figure 2.11-(top) shows this fidelity as a function of the amplitude α and the squeezing factor s . In Figure 2.11-(bottom), the Wigner functions of a squeezed single-photon state with squeezing factor $s = -2.7$ dB (right) and a perfect odd Schrödinger cat state of amplitude $\alpha = 1$ (left) are displayed. We can see in Figure 2.11-(top) that the fidelity between a squeezed single-photon state and an odd Schrödinger cat state is high for small amplitudes α , and it starts to decrease with respect to an increased amplitude. For each amplitude α , the optimal squeezing that maximises the fidelity between the two states is given by the dashed black curve. In Figure 2.11-(bottom), the similarity between the Wigner functions (and the marginal distributions) of an odd Schrödinger cat state of amplitude $\alpha = 1$ (left) and a squeezed single-photon state with a squeezing factor $s = -2.7$ dB (right) is clear, confirming that photon subtraction from squeezed vacuum state is a way to produce states that are considered as good approximations of small amplitude Schrödinger cat states.

2.3.2.2 What about "bigger" cats?

We have just seen that approximation of small amplitude Schrödinger cat states can be obtained by single-photon subtraction from squeezed vacuum state. However, to obtain larger amplitude states, the number of subtracted photons need to be increased, which is more challenging and requires photon number resolving detection schemes. Another way to obtain large amplitude Schrödinger cat states is to use fock states $|n\rangle$ instead of squeezed vacuum state [62], associated with Gaussian operations, which is also challenging. In [63], a relatively simple scheme was proposed, which consists of

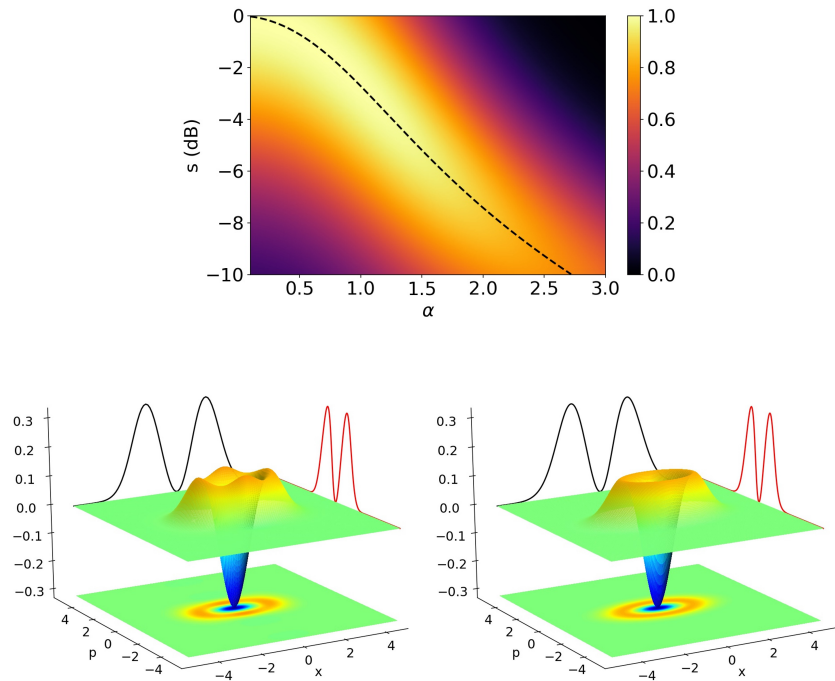


Figure 2.11 – (top): Fidelity between a squeezed single-photon state with a squeezing factor s and a perfect odd Schrödinger cat state of amplitude α . The black dashed curve represents the optimal fidelity. (Bottom): Wigner functions of an odd Schrödinger cat state of amplitude $\alpha = 1$ (left) and of a squeezed single-photon state with squeezing parameter $s = -2.7$ dB (right).

interfering two small amplitude Schrödinger cat states to generate "bigger" one. The principle of this proposal is depicted in [Figure 2.12](#).

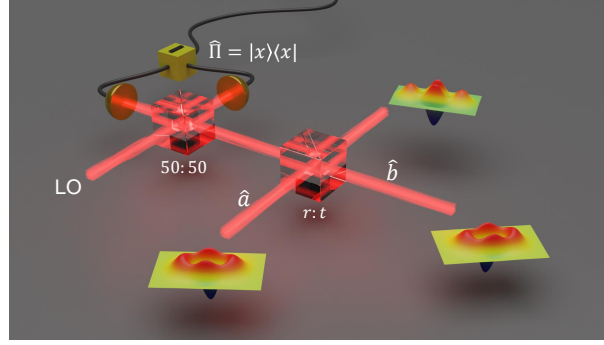


Figure 2.12 – Schrödinger cat state amplification (breeding) principle. Two Schrödinger cat states are sent to a BS of reflection coefficient r . On one of the output of the BS, a homodyne measurement is performed, and depending on its outcome, a Schrödinger cat state of larger amplitude is heralded in the other output of the BS.

It consists of interfering two Schrödinger cat states of amplitudes α and β with a BS of reflection coefficient r . The state impinging the BS is given by:

$$|\psi\rangle_{in} = |Cat_{\pm}(\alpha)\rangle_a |Cat_{\pm}(\beta)\rangle_b = \frac{|\alpha\rangle_a |\beta\rangle_b + |-\alpha\rangle_a |-\beta\rangle_b \pm |\alpha\rangle_a |-\beta\rangle_b \pm |-\alpha\rangle_a |\beta\rangle_b}{\mathcal{N}_{\pm}(\alpha)\mathcal{N}_{\pm}(\beta)}, \quad (2.66)$$

where we considered here two input states with the same parity (even or odd). The normalization constant $\mathcal{N}_{\pm}(\alpha)$ is given by:

$$\mathcal{N}_{\pm}(\alpha) = \sqrt{2(1 \pm e^{-2|\alpha|^2})}. \quad (2.67)$$

By applying the BS transformation ([Equation 2.7](#)), the state at the output of the BS can be written as:

$$|\psi\rangle_{out} = \frac{1}{\mathcal{N}_{\pm}(\alpha)\mathcal{N}_{\pm}(\beta)} (|t\alpha + r\beta\rangle_a |-\alpha + t\beta\rangle_b + |-\alpha - r\beta\rangle_a |r\alpha - t\beta\rangle_b \pm |t\alpha - r\beta\rangle_a |-\alpha - t\beta\rangle_b \pm |-\alpha + r\beta\rangle_a |r\alpha + t\beta\rangle_b). \quad (2.68)$$

This expression can be simplified by considering the particular case of a balance BS ($r = t = 1/\sqrt{2}$) and two input states with the same amplitude ($\alpha = \beta$). In this case, the state at the output of the BS is:

$$|\psi\rangle_{out} = \frac{[|\sqrt{2}\alpha\rangle_a + |-\sqrt{2}\alpha\rangle_a] |0\rangle_b \pm |0\rangle_a [|\sqrt{2}\alpha\rangle_b + |-\sqrt{2}\alpha\rangle_b]}{\mathcal{N}_{\pm}^2(\alpha)}, \quad (2.69)$$

which is an entangled state with vacuum contribution that results from the destructive interferences, and a larger amplitude Schrödinger cat state contribution resulting from the constructive interferences of the input "smaller" states. In order to produce a Schrödinger cat state amplified by a factor $\sqrt{2}$ in one output mode of the BS, we need

to distinguish between the *cat* and the *vacuum* components in the other output mode. As it can be seen in Figure 2.13, this can be done by performing a quadrature measurement in one of the output modes of the BS. The probability of having a measurement outcome $x = 0$ is high for the vacuum state compared to a Schrödinger cat state with amplitude $\sqrt{2}$, thus, it provides a good way to distinguish the two components and then heralds the success of Schrödinger cat state amplification (breeding).

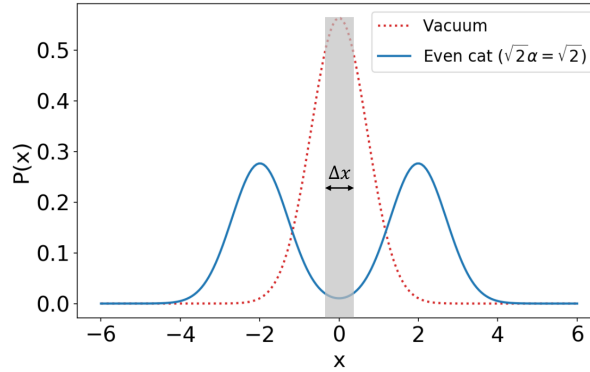


Figure 2.13 – Quadrature distribution $P(x)$ of vacuum state (dotted red line) and an even Schrödinger cat state of amplitude $\sqrt{2}\alpha$ with $\alpha = 1$ (solid blue line).

Let us consider the ideal case, where the amplified Schrödinger cat state is heralded by measuring exactly $x = 0$ in the output mode b of the BS. The heralded state, noted $|\psi\rangle_H$, is given by:

$$|\psi\rangle_H \propto {}_b\langle x = 0 | \psi \rangle_{out}. \quad (2.70)$$

In the case where α is real (with a proper choice of phase origin), and taking into account the wave-functions of the vacuum state (Equation 1.86 with $n = 0$) and the coherent state (Equation 1.77), the heralded state $|\psi\rangle_H$, after normalization, is given by:

$$|\psi\rangle_H = \frac{|\sqrt{2}\alpha\rangle_a + |-\sqrt{2}\alpha\rangle_a \pm 2e^{-2\alpha^2}|0\rangle_a}{2e^{-\alpha^2} [\cosh(2\alpha^2) + e^{-2\alpha^2} \pm 2e^{-\alpha^2}]^{1/2}}. \quad (2.71)$$

As it can be seen, the heralded state is a superposition of a perfect even Schrödinger cat state of amplitude $\sqrt{2}\alpha$ (amplified by a factor of $\sqrt{2}$) and a vacuum state with corresponding weight exponentially decreasing with respect of the amplitude of input states. This vacuum contribution is related to the fact that we cannot discriminate perfectly the vacuum state from Schrödinger cat state in the heralding path, since these two states are not orthogonal. To amplify more and more Schrödinger cat states, iterative schemes can be implemented by cascading elementary amplification stages [64, 65].

Schrödinger cat breeding in the real world

The heralded state, given by Equation 2.71, was obtained by considering heralding with the measurement outcome $x = 0$ in the heralding path. However, in realistic scenarios, restricting the heralding with the exact null quadrature leads to a very low success probability of the amplification operation. A more convenient way to perform Schrödinger cat state breeding is to accept measurement outcomes close to $x = 0$ within

a given width Δx (see [Figure 2.13](#)). This width needs to be small enough to maintain a good fidelity of the heralded state, and large enough to guaranty a high success probability. The heralded state, $\hat{\rho}_H$, is given by:

$$\hat{\rho}_H = \frac{\text{Tr}_b [\hat{\Pi} \hat{\rho}_{out}]}{P}, \quad (2.72)$$

where $\hat{\rho}_{out}$ is the state at the output of the BS, $\hat{\Pi}$ is the POVM element corresponding to the accepted events in the heralding path, and P is the success probability given by:

$$P = \text{Tr}_{ab} [\hat{\Pi} \hat{\rho}_{out}]. \quad (2.73)$$

For the rest of this section, we will consider two cases. The case where all homodyne measurement outcomes $\Delta x/2 \leq x = x_i \leq \Delta x/2$ in the heralding path are accepted with the same weight, the POVM element $\hat{\Pi}$ is expressed as:

$$\hat{\Pi} = \int_{-\frac{\Delta x}{2}}^{\frac{\Delta x}{2}} |x\rangle_b \langle x| dx, \quad (2.74)$$

we will call this case *rectangular window heralding*. The second case is where the homodyne measurement outcomes $x = x_i$ are accepted with a Gaussian distributed weight with standard deviation Δx and centred on $x = 0$, the POVM element $\hat{\Pi}$ in this case is given by:

$$\hat{\Pi} = \int_{-\infty}^{\infty} e^{-\frac{x^2}{2\Delta x^2}} |x\rangle_b \langle x| dx, \quad (2.75)$$

we will call this case *Gaussian window heralding*. We can show in both cases, using the wave-functions given by [Equation 1.77](#) and [Equation 1.86](#) and the integration formula given in [Appendix B](#), that the heralded state $\hat{\rho}_H$ is given by:

$$\hat{\rho}_H = p_1 |\psi\rangle_a \langle \psi| + p_2 |0\rangle_a \langle 0|, \quad (2.76)$$

with:

$$|\psi\rangle_a = \frac{1}{\mathcal{N}_{|\psi\rangle_a}} \left(|\sqrt{2}\alpha\rangle_a + |-\sqrt{2}\alpha\rangle_a \pm \frac{C}{A} |0\rangle_a \right), \quad (2.77)$$

$$p_1 = \frac{A \mathcal{N}_{|\psi\rangle_a}^2}{A (2 + 2e^{-4\alpha^2}) + B \pm 4Ce^{-\alpha^2}}, \quad (2.78)$$

$$p_2 = \frac{B - C^2/A}{A (2 + 2e^{-4\alpha^2}) + B \pm 4Ce^{-\alpha^2}}, \quad (2.79)$$

$$\mathcal{N}_{|\psi\rangle_a} = \sqrt{2 + \frac{C^2}{A^2} + 2e^{-4\alpha^2} \pm 4\frac{C}{A}e^{-\alpha^2}}, \quad (2.80)$$

and the success probability is:

$$P = \frac{1}{\mathcal{N}_{\pm}^4(\alpha)} \left[A (2 + 2e^{-4\alpha^2}) + B \pm 4Ce^{-\alpha^2} \right]. \quad (2.81)$$

Parameters	$\hat{\Pi} = x=0\rangle\langle x=0 $	$\hat{\Pi} = \int_{-\frac{\Delta x}{2}}^{\frac{\Delta x}{2}} x\rangle\langle x dx$	$\hat{\Pi} = \int_{-\infty}^{\infty} e^{-\frac{x^2}{2\Delta x^2}} x\rangle\langle x dx$
A	1	$\text{erf}\left(\frac{1}{2\sqrt{2}} \frac{\Delta x}{\sigma_0}\right)$	$\frac{1}{\sqrt{1 + \frac{\sigma_0^2}{\Delta x^2}}}$
B	$4e^{-4\alpha^2}$	$\text{erf}\left(2\alpha + \frac{1}{2\sqrt{2}} \frac{\Delta x}{\sigma_0}\right) - \text{erf}\left(2\alpha - \frac{1}{2\sqrt{2}} \frac{\Delta x}{\sigma_0}\right) + 2e^{-4\alpha^2} A$	$\frac{e^{-4\alpha^2}}{\sqrt{1 + \frac{\sigma_0^2}{\Delta x^2}}} \left(2 + 2e^{-\frac{8\alpha^2}{2\left(1 + \frac{\sigma_0^2}{\Delta x^2}\right)}}\right)$
C	$2e^{-2\alpha^2}$	$e^{-\alpha^2} \left[\text{erf}\left(\alpha + \frac{1}{2\sqrt{2}} \frac{\Delta x}{\sigma_0}\right) - \text{erf}\left(\alpha - \frac{1}{2\sqrt{2}} \frac{\Delta x}{\sigma_0}\right) \right]$	$2e^{-\frac{-2\alpha^2}{2\left(1 + \frac{\sigma_0^2}{\Delta x^2}\right)}} \frac{1}{\sqrt{1 + \frac{\sigma_0^2}{\Delta x^2}}}$

Table 2.1 – The different parameters appearing the expression of the heralded state for different heralding scenarios.

The parameters A , B and C are summarized in [Table 2.1](#) for the different heralding scenarios.

The heralded state is then a statistical mixture of a state $|\psi\rangle$, similar to the one obtained in the ideal case (see [Equation 2.71](#)), and a vacuum state, with probabilities p_1 and p_2 , respectively. The state $\hat{\rho}_H$ ([Equation 2.76](#)) converges to the state $|\psi\rangle_H$ ([Equation 2.71](#)) when the width Δx converges to zero ($p_2 \rightarrow 0$ when $\Delta x \rightarrow 0$). The fidelity between this state and a perfect even Schrödinger cat state with amplitude γ is given by:

$$\begin{aligned} \mathcal{F} &= \text{Tr}_b \left[\hat{\rho}_H \hat{\rho}_{\text{Cat}_+(\gamma)} \right] = p_1 \text{Tr}_b \left[\hat{\rho}_{|\psi\rangle} \hat{\rho}_{\text{Cat}_+(\gamma)} \right] + p_2 \text{Tr}_b \left[\hat{\rho}_{|0\rangle} \hat{\rho}_{\text{Cat}_+(\gamma)} \right] \\ &= p_1 |\langle \psi | \text{Cat}_+(\gamma) \rangle|^2 + p_2 |\langle 0 | \text{Cat}_+(\gamma) \rangle|^2. \end{aligned} \quad (2.82)$$

Taking into account the overlap formula given by [Equation 2.86](#), this fidelity can be simplified as:

$$\mathcal{F} = \frac{4}{\mathcal{N}_+^2(\gamma)} \left[\frac{p_1}{\mathcal{N}_+^2(\psi)} \left(e^{-\frac{1}{2}(\sqrt{2}\alpha - \gamma)^2} + e^{-\frac{1}{2}(\sqrt{2}\alpha + \gamma)^2} \pm \frac{C}{A} e^{-\frac{1}{2}\gamma^2} \right)^2 + p_2 e^{-\gamma^2} \right]. \quad (2.83)$$

[Figure 2.14](#)-(a) shows, in the case of rectangular window heralding, the fidelity between the heralded state and a perfect even Schrödinger cat state as a function of the amplitude of the input states and for different width Δx . In [Figure 2.14](#)-(b), by changing the width Δx , we plot the success probability of the amplification protocol as a function of the fidelity between the heralded state and a perfect Schrödinger cat state in the case of rectangular window heralding (solid blue line) and Gaussian window heralding (dashed red line) for input states of amplitude $\alpha = 1$.

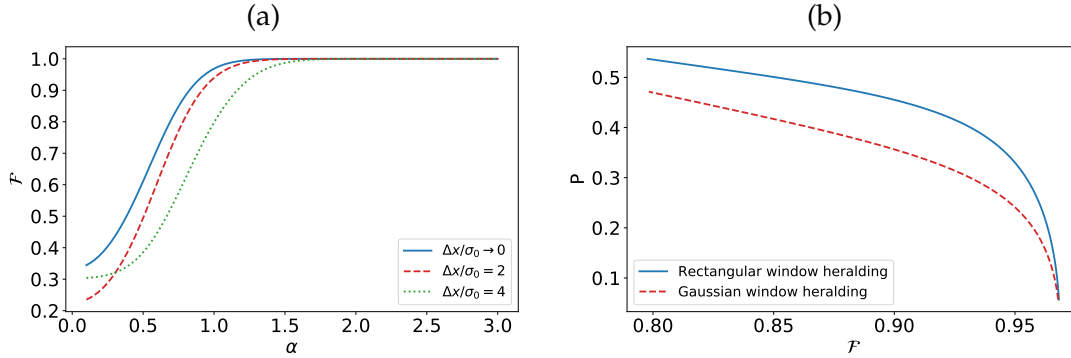


Figure 2.14 – (a): The fidelity between the heralded state and a perfect even Schrödinger cat state, in the case of rectangular window heralding, as a function of the amplitude of the input states and for different width Δx . (b): The success probability P of the amplification protocol as a function of the fidelity between the heralded state and a perfect Schrödinger cat state in the case of rectangular window heralding (solid blue line) and Gaussian window heralding (dashed red line) for input states of amplitude $\alpha = 1$.

We can see in [Figure 2.14](#)-(a) that decreasing the width Δx (for a fixed amplitude of the input states) or increasing the amplitude of the input states lead to a better

discrimination between vacuum and cat components in the heralding path, which gives a better fidelity of the output state. By increasing the width Δx , the success probability of the amplification protocol can be increased. However, the cost to pay is a decreased fidelity, as it is shown in Figure 2.14-(b). We see also that, for a given fidelity, the rectangular window heralding strategy is slightly better than the Gaussian window heralding one in terms of success probability.

2.4 QUANTUM STATE RECONSTRUCTION

We introduced in subsection 2.2.2 the homodyne detection, and we said that it is a powerful tool in quantum optics experiments, it allows to measure the quadrature \hat{x}_θ of an arbitrary quantum state $\hat{\rho}$ by simply making it beat with a LO. However, to fully characterize a given quantum state, we need to know its Wigner function. In fact, by constructing the histograms of the measured quadratures x_θ for different phases θ at the output of the homodyne detection, we obtain directly a good estimation of marginal distributions $P(x_\theta)$, which are the projections of the Wigner function of the measured state onto a vertical plane rotated by an angle θ in the phase space (see Equation 1.68 and Figure 2.15).

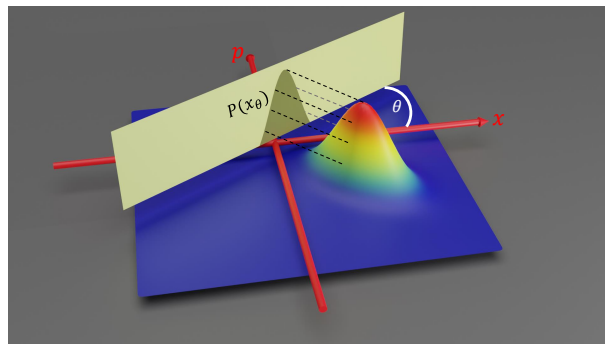


Figure 2.15 – The projection of the Wigner function onto a vertical plane rotated by an angle θ in the phase space gives the marginal distribution $P(x_\theta)$.

In analogy with the tomography technique used in medical imaging, which consists of reconstructing 3D images of a given object using several 2D projections of it, the Wigner function of the state $\hat{\rho}$ can be reconstructed, using different algorithms, starting from the marginal distributions $P(x_\theta)$. It's what we call quantum state tomography.

2.4.1 Quantum state reconstruction algorithms

Quantum state reconstruction algorithms can be classified into two main classes, the *inverse linear transform* and the *statistical inference* techniques [66]. *Inverse linear transform* techniques use the fact that the marginal distributions $P(x_\theta)$ are direct projections of the Wigner function, and thus, by inverting Equation 1.68, the Wigner function can be reconstructed. We will give two examples of *inverse linear transform* techniques, namely the inverse Radon transformation and the Pattern functions (see references [67–69] for more examples). The problem with these techniques is that they suffer from statistical

and systematic noise, and to guaranty a good quantum state reconstruction, a large number of highly precise measurements is needed. To overcome this limitation, *statistical inference* techniques are a good alternative. Among the different existing algorithms, the MaxLik one, that we will introduce briefly, is largely used. It consists of searching the state $\hat{\rho}$ that maximises the probability of obtaining the observed measurement results.

2.4.1.1 Inverse Radon transformation

The Wigner function $W(x, p)$ can be found by inverting [Equation 1.68](#):

$$W(x, p) = \frac{1}{2\pi^2} \int_0^\pi \int_{-\infty}^\infty P(x_\theta) K(x \cos \theta + p \sin \theta - x_\theta) dx_\theta d\theta, \quad (2.84)$$

where $K(x)$ is the integration kernel given by:

$$K(x) = \frac{1}{2} \int_{-\infty}^\infty |\zeta| e^{i\zeta x} d\zeta \propto -\frac{1}{x^2}. \quad (2.85)$$

At $x = 0$, the kernel is infinite. In order to numerically implement this method, a filtered version is used by replacing the infinite integration limits in [Equation 2.85](#) with finite ones, which leads to an inevitable extra noise in the reconstructed state. In addition, it directly provides the Wigner function of the reconstructed state, and thus, obtaining its density matrix is a little bit difficult.

2.4.1.2 Pattern functions

Let us consider two operators \hat{A} and \hat{B} , satisfying the following overlap formula:

$$\text{Tr} [\hat{A}\hat{B}] = 4\pi\sigma_0^2 \int \int W_{\hat{A}}(x, p) W_{\hat{B}}(x, p) dx dp, \quad (2.86)$$

where $W_{\hat{A}}(x, p)$ and $W_{\hat{B}}(x, p)$ are the associated Wigner functions. In the case where $\hat{B} = \hat{\rho}$, and taking into account the expression given by [Equation 2.84](#), this formula can be written as the statistical average of a given function $F_{\hat{A}}(x_\theta, \theta)$:

$$\text{Tr} [\hat{A}\hat{\rho}] = \langle F_{\hat{A}}(x_\theta, \theta) \rangle_{x_\theta, \theta} = \int_0^\pi \int_{-\infty}^\infty P(x_\theta) F_{\hat{A}}(x_\theta, \theta) dx_\theta d\theta. \quad (2.87)$$

The function $F_{\hat{A}}(x_\theta, \theta)$ is called the sampling function, and it is given by:

$$F_{\hat{A}}(x_\theta, \theta) = \frac{2\sigma_0^2}{\pi} \int \int K(x \cos \theta + p \sin \theta - x_\theta) W_{\hat{A}}(x, p) dx dp. \quad (2.88)$$

In the Fock state basis, the elements ρ_{nm} of the density matrix $\hat{\rho}$ can then be found as:

$$\rho_{nm} = \text{Tr} [|m\rangle\langle n| \hat{\rho}] = \langle n | \hat{\rho} | m \rangle = \langle F_{|m\rangle\langle n|}(x_\theta, \theta) \rangle_{x_\theta, \theta}, \quad (2.89)$$

where:

$$F_{|m\rangle\langle n|}(x_\theta, \theta) = \frac{2\sigma_0^2}{\pi} e^{i(m-n)\theta} M_{nm}(x_\theta), \quad (2.90)$$

and $M_{nm}(x_\theta)$ are called pattern functions [70]. These functions can be numerically calculated efficiently using different algorithms [71], and then, by statistically averaging Equation 2.90 with the obtained measurement results (x_i, θ_i) , one can reconstruct the elements of the density matrix of the state being measured (Equation 2.89) and its Wigner function.

2.4.1.3 MaxLik algorithm

Quantum state reconstruction using MaxLik (Maximum Likelihood) algorithm, introduced in [72], is a state reconstruction method based on *statistical inference* technique. It consists of statistically estimating the density matrix elements ρ_{nm} of a state $\hat{\rho}$ by maximising a likelihood function. This technique allows to find the state $\hat{\rho}$ that maximises the probability of obtaining the observed quadrature measurement results $\{(x_i, \theta_i)\}$. The likelihood function of the observed data $\{(x_i, \theta_i)\}$ is given by:

$$\mathcal{L} = \prod_i P_{\hat{\rho}}(x_i, \theta_i), \quad (2.91)$$

where $P_{\hat{\rho}}(x_i, \theta_i)$ is the probability of obtaining the outcome (x_i, θ_i) , given by:

$$P_{\hat{\rho}}(x_i, \theta_i) = \text{Tr} [\hat{\Pi}(x_i, \theta_i) \hat{\rho}]. \quad (2.92)$$

The elements of the projector $\hat{\Pi}(x_i, \theta_i)$ in the Fock state basis are given by:

$$\langle n | \hat{\Pi}(x_i, \theta_i) | m \rangle = \frac{e^{-i(m-n)\theta_i}}{2^n n! \sigma_0 \sqrt{2\pi}} H_n^2 \left(\frac{x_i}{\sigma_0 \sqrt{2}} \right) e^{-\frac{x_i^2}{2\sigma_0^2}}. \quad (2.93)$$

Here, we used the wave-function given by Equation 1.86. It is shown in [73] that the state $\hat{\rho}_0$ maximizing the likelihood \mathcal{L} satisfies the relation:

$$\hat{R}(\hat{\rho}_0) \hat{\rho}_0 \hat{R}(\hat{\rho}_0) = \hat{\rho}_0, \quad (2.94)$$

with:

$$\hat{R}(\hat{\rho}) = \sum_i \frac{\hat{\Pi}(x_i, \theta_i)}{P_{\hat{\rho}}(x_i, \theta_i)}. \quad (2.95)$$

Based on Equation 2.94, the optimal state that maximises the likelihood \mathcal{L} can be obtained by an iterative scheme:

$$\hat{\rho}^{(k+1)} = \frac{\hat{R}(\hat{\rho}^{(k)}) \hat{\rho}^{(k)} \hat{R}(\hat{\rho}^{(k)})}{\mathcal{N}}, \quad (2.96)$$

with an initial state density matrix:

$$\hat{\rho}^{(0)} = \frac{\hat{\mathbb{1}}}{\mathcal{N}}. \quad (2.97)$$

Here, \mathcal{N} is a normalization constant to keep a unit trace of the density matrix ($\text{Tr}[\hat{\rho}^{(k)}] = 1$). Two parameters in this algorithm need to be fixed, the first is the dimension of the Hilbert space, which means that measured state is assumed to have a limited amplitude, and the second is the number of iterations.

Losses correction

One of the advantages of MaxLik algorithm is that it allows to include losses in the reconstruction procedure. Suppose that the state $\hat{\rho}$ is measured with a given efficiency η (that includes the optical losses and the homodyne detection efficiency). In this case, the measured state, noted $\hat{\rho}_\eta$, is expressed in the Fock state basis as:

$$\langle k | \hat{\rho}_\eta | m \rangle = \sum_n \sqrt{B_k^{k+n}(\eta) B_m^{m+n}(\eta)} \langle k+n | \hat{\rho} | m+n \rangle, \quad (2.98)$$

with $B_k^m(\eta)$ is the Bernoulli distribution given by:

$$B_k^m(\eta) = \binom{m}{k} \eta^k (1-\eta)^{m-k}. \quad (2.99)$$

This gives a probability distribution:

$$P_\eta(x, \theta) = \sum_k \sum_m \sum_n \sqrt{B_k^{k+n}(\eta) B_m^{m+n}(\eta)} \langle x_\theta | k \rangle \langle m | x_\theta \rangle \langle k+n | \hat{\rho} | m+n \rangle, \quad (2.100)$$

and projectors:

$$\hat{\Pi}_\eta(x, \theta) = \sum_k \sum_m \sum_n \sqrt{B_k^{k+n}(\eta) B_m^{m+n}(\eta)} \langle x_\theta | k \rangle \langle m | x_\theta \rangle |m+n\rangle \langle k+n|. \quad (2.101)$$

By replacing [Equation 2.100](#) and [Equation 2.101](#) in [Equation 2.95](#), we can directly reconstruct the state before losses, as if it had been measured with a perfect homodyne detection (of course, the efficiency η must be known).

2.5 CONCLUSION

The association of linear and nonlinear optical interaction, in addition to quantum measurements, is essential in quantum optics experiments in order to produce, manipulate, and characterize quantum states of light. These experimental tools were introduced in this chapter. In the next chapter, we will present the implementation of an experimental setup used to generate Schrödinger kitten states at a telecommunication wavelength, an important ingredient for several quantum information protocols.

Part II

NON-GAUSSIAN QUANTUM STATE GENERATION: GUIDED-WAVE APPROACH IN CW AND PULSED REGIMES

A FULLY GUIDED-WAVE CW NON-GAUSSIAN QUANTUM STATE GENERATION

3.1	Model for the experiment	60
3.1.1	Squeezed vacuum state with losses	61
3.1.2	Photon subtraction with imperfect On/Off photon detector	62
3.1.3	Realistic homodyne detection	65
3.2	Experimental setup	66
3.2.1	Master laser source	67
3.2.2	Squeezed vacuum source	67
3.2.3	Homodyne detection	68
3.2.4	Photon subtraction: filtering the heralding photons	69
3.3	Data post-processing	74
3.3.1	LO phase extraction	75
3.3.2	Quadrature extraction	75
3.4	Experimental results and discussion	76
3.4.1	Squeezed vacuum state generation and losses characterization	77
3.4.2	Wave-packet extraction of the heralded non-Gaussian state	77
3.4.3	Heralded non-Gaussian state	79
3.5	Conclusion	81

Non-Gaussian quantum states of light, such as Fock [74] and Schrödinger cat-like states [62], are essential ingredients for fault-tolerant optical quantum information processing [24] and long distance quantum communication [25, 26]. A common strategy to benefit from these resources is to implement conditional state preparation, often starting from a (Gaussian) squeezed state [75]. This idea has been demonstrated in multiple experiments [62, 74, 76], including the recent trend of employing a nonlinear waveguide as squeezing source [77]. Reported realizations, however, rely entirely or largely on bulk-optics setups that are generally hardly scalable and require careful spatial alignments [75].

The work presented in this chapter addresses the need for compact and stable realizations that can be easily assembled out-of-the-laboratory, as demanded to push current quantum optical experiments towards practical demonstrations. More specifically, it shows the feasibility of non-Gaussian state generation setups fully employing plug-&-play components from guided-wave technologies. Strategically, we applied this concept to single-photon subtraction from a squeezed vacuum state [78], a commonly used strategy for Schrödinger kitten state preparation (see [subsection 2.3.2](#)) and can be considered as an archetypal configuration, gathering Gaussian and non-Gaussian resources and lying at the heart of multiple complex architectures[75].

This chapter is organized as following, in [section 3.1](#), we introduce a theoretical model for the experiment taking into account the different experimental imperfections (losses at the different preparation stages) and realistic aspects of the On/Off and homodyne detectors. The experimental setup is then detailed in [section 3.2](#) and data post-processing techniques for the extraction of the heralded state quadratures and LO phase, needed for quantum tomography of the heralded non-Gaussian state, are presented in [section 3.3](#). Finally, the obtained results are given in [section 3.4](#) with discussions and we finish by concluding the chapter in [section 3.5](#).

3.1 MODEL FOR THE EXPERIMENT

In general, experimental preparation of quantum states of light suffers from implementation imperfections. In our experimental setup, in particular, the use of fiber optics components adds extra losses to the experiment compared to implementations based on bulk optics components. In addition, imperfections such as additional noise and limited quantum efficiency of realistic On/Off and homodyne detectors used to herald and characterize the produced state are unavoidable. Following an approach similar to the one in [79, 80], we give in this section a model using the Wigner function formalism to describe the experimental setup taking into account the experimental imperfections of different preparation stages. These imperfections are summarized in [Figure 3.1](#) where the squeezed vacuum state is subject to optical losses $1 - \eta_l$, the photon subtraction operation is applied using BS2 (of transmission η_s) and a realistic On/Off detector with efficiency η_{det} and dark count parameter ν , and the heralded state is characterized using a realistic homodyne detector with limited quantum efficiency η_{hd} .

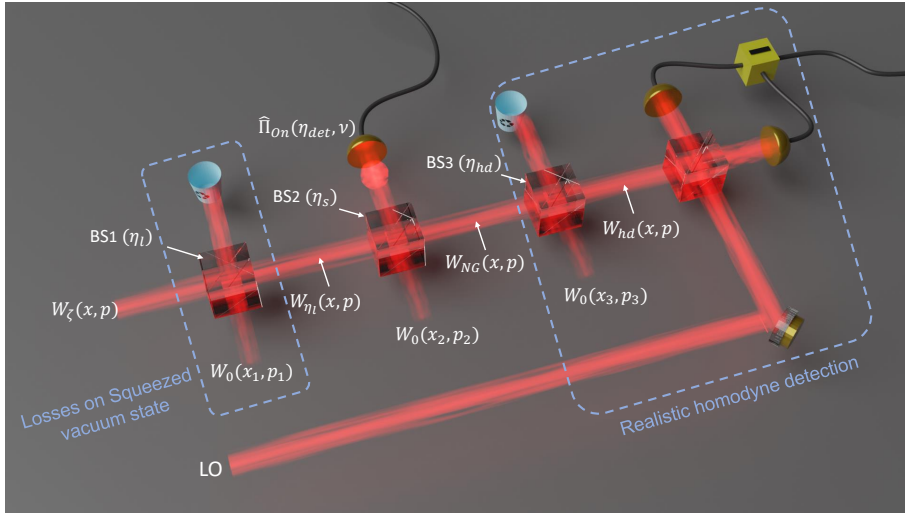


Figure 3.1 – Experimental imperfections in heralded non-Gaussian state generation.

The constants used in the different subsections of this section are summarized in [Table 3.1](#).

subsection 3.1.1	subsection 3.1.2	subsection 3.1.3
$\alpha_1^2 = \frac{\eta_l}{s} + 1 - \eta_l$	$\alpha_2^2 = \eta_s \alpha_1^2 + 1 - \eta_s$	$\alpha_3^2 = \eta_{hd} \alpha_2^2 + 1 - \eta_{hd}$
$\beta_1^2 = \eta_l s + 1 - \eta_l$	$\beta_2^2 = \eta_s \beta_1^2 + 1 - \eta_s$	$\beta_3^2 = \eta_{hd} \beta_2^2 + 1 - \eta_{hd}$
	$c^2 = \frac{2(1+\nu) - \eta_{det}}{\eta_{det}}$	
	$\frac{1}{\alpha_2'^2} = \frac{\eta_s}{\alpha_1^2} + 1 - \eta_s - \frac{\eta_{det}(1-\eta_s)(1/\alpha_1^2-1)^2}{\alpha_2^2 + \frac{1}{c^2}}$	$\alpha_3'^2 = \eta_{hd} \alpha_2'^2 + 1 - \eta_{hd}$
	$\frac{1}{\beta_2'^2} = \frac{\eta_s}{\beta_1^2} + 1 - \eta_s - \frac{\eta_s(1-\eta_s)(1/\beta_1^2-1)^2}{\beta_2^2 + \frac{1}{c^2}}$	$\beta_3'^2 = \eta_{hd} \beta_2'^2 + 1 - \eta_{hd}$

Table 3.1 – The constants used in the different formulas of this section.

3.1.1 Squeezed vacuum state with losses

In [Figure 3.1](#), BS₁, with a transmission η_l , models optical losses that the squeezed vacuum state undergoes before applying the photon subtraction operation. The Wigner function of the state at the input of BS₁ is give by:

$$W_{in_1}(x, p; x_1, p_1) = W_\zeta(x, p) \cdot W_0(x_1, p_1) = \frac{1}{4\pi^2\sigma_0^4} e^{-\frac{1}{2\sigma_0^2}(sx^2 + p^2/s + x_1^2 + p_1^2)}, \quad (3.1)$$

where $W_\zeta(x, p)$ and $W_0(x_1, p_1)$ are the Wigner functions of the squeezed vacuum state before losses (with squeezing factor $s = e^{-2|\zeta|}$) and the vacuum state, respectively. Taking into account the BS transformation given by [Equation 2.7](#), the quadrature variables $x(p)$ and $x_1(p_1)$ are transformed as:

$$\begin{aligned} x(p) &\longrightarrow \sqrt{\eta_l}x(p) + \sqrt{1-\eta_l}x_1(p_1), \\ x_1(p_1) &\longrightarrow -\sqrt{1-\eta_l}x(p) + \sqrt{\eta_l}x_1(p_1), \end{aligned} \quad (3.2)$$

and the Wigner function of the state at the output of BS₁ can be written as:

$$W_{out_1}(x, p, x_1, p_1) = \frac{1}{4\pi^2\sigma_0^4} e^{-\frac{1}{2\sigma_0^2} \left[\frac{x^2}{\alpha_1^2} + s\alpha_1^2 \left(x_1 + \frac{\sqrt{\eta_l(1-\eta_l)(1-1/s)}x}{\alpha_1^2} \right)^2 + \frac{p^2}{\beta_1^2} + \frac{1}{s}\beta_1^2 \left(p_1 + \frac{\sqrt{\eta_l(1-\eta_l)(1-s)}p}{\beta_1^2} \right)^2 \right]}. \quad (3.3)$$

Using the integration formula given by [Equation B.1](#), the Wigner function of the squeezed vacuum state after losses, obtained by tracing out the mode (1), is given by:

$$W_{\eta_l}(x, p) = \iint W_{out_1}(x, p, x_1, p_1) dx_1 dp_1 = \frac{1}{2\pi\alpha_1\beta_1\sigma_0^2} e^{-\frac{1}{2\sigma_0^2} \left(\frac{x^2}{\alpha_1^2} + \frac{p^2}{\beta_1^2} \right)}. \quad (3.4)$$

The variances of the squeezed and antisqueezed quadratures are then given by $\sigma_{min}^2 = \beta_1^2\sigma_0^2$ and $\sigma_{max}^2 = \alpha_1^2\sigma_0^2$, respectively, which are already mentioned in [subsection 2.3.1.2](#) (see [Equation 2.54](#)).

3.1.2 Photon subtraction with imperfect On/Off photon detector

The Wigner function of the heralded non-Gaussian state, obtained by photon subtraction from squeezed vacuum state enduring optical losses and using realistic On/Off detector, can now be computed. In [Figure 3.1](#), BS₂, with a transmission η_s close to 1, sends a small part of the squeezed vacuum state to an On/Off detector, characterized by a quantum efficiency η_{det} and a background noise (responsible for the dark counts) with mean photon number ν (see [subsection 2.2.1](#)). The state at the input of BS₂ is given by:

$$W_{in_2}(x, p; x_2, p_2) = W_{\eta_l}(x, p) \cdot W_0(x_2, p_2) = \frac{1}{4\pi^2\alpha_1\beta_1\sigma_0^4} e^{-\frac{1}{2\sigma_0^2} \left(\frac{x^2}{\alpha_1^2} + \frac{p^2}{\beta_1^2} + x_2^2 + p_2^2 \right)}. \quad (3.5)$$

By applying the BS transformation given by [Equation 3.2](#) (with η_s instead of η_l), the Wigner function of the state at the output of BS₂ can be written as:

$$W_{out_2}(x, p, x_2, p_2) = \frac{1}{4\pi^2\alpha_1\beta_1\sigma_0^4} e^{-\frac{1}{2\sigma_0^2} \left[\frac{1}{\alpha_1^2} (\sqrt{\eta_s}x + \sqrt{1-\eta_s}x_2)^2 + (\sqrt{1-\eta_s}x - \sqrt{\eta_s}x_2)^2 + \frac{1}{\beta_1^2} (\sqrt{\eta_s}p + \sqrt{1-\eta_s}p_2)^2 + (\sqrt{1-\eta_s}p - \sqrt{\eta_s}p_2)^2 \right]}. \quad (3.6)$$

According to the quantum measurement formalism introduced in [section 2.2](#), the non-Gaussian state, heralded by a "click" event in the On/Off detector in mode (2), is given by:

$$\hat{\rho}_{NG} = \frac{\text{Tr}_2[\hat{\Pi}_{On}(\eta_{det}, \nu)\hat{\rho}_{out_2}]}{\text{Tr}[\hat{\Pi}_{On}(\eta_{det}, \nu)\hat{\rho}_{out_2}]} \quad (3.7)$$

Using the overlap formula given by [Equation 2.86](#), the Wigner function of the heralded non-Gaussian state is given by:

$$W_{NG}(x, p) = \frac{\iint W_{out_2}(x, p, x_2, p_2) \cdot W_{\hat{\Pi}_{On}}(x_2, p_2) dx_2 dp_2}{\iiint W_{out_2}(x, p, x_2, p_2) \cdot W_{\hat{\Pi}_{On}}(x_2, p_2) dx dp dx_2 dp_2}, \quad (3.8)$$

where $W_{\hat{\Pi}_{On}}(x_2, p_2)$, given by [Equation 2.36](#), is the Wigner function associated to the POVM element $\hat{\Pi}_{On}(\eta_{det}, \nu)$ [[81](#)]. Taking into account [Equation 2.36](#) and [Equation 3.6](#), we can write:

$$\begin{aligned}
W_{out_2}(x, p, x_2, p_2) \times W_{\hat{\Pi}_{On}}(x_2, p_2) &= \frac{1}{16\pi^3\alpha_1\beta_1\sigma_0^6} \\
&\left[e^{-\frac{1}{2\sigma_0^2} \left[\frac{x_2^2}{\alpha_2^2} + \frac{\alpha_2^2}{\alpha_1^2} \left(x_2 + \frac{\sqrt{\eta_s(1-\eta_s)}(1-\alpha_1^2)}{\alpha_2^2} x \right)^2 + \frac{p_2^2}{\beta_2^2} + \frac{\beta_2^2}{\beta_1^2} \left(p_2 + \frac{\sqrt{\eta_l(1-\eta_l)}(1-\beta_1^2)}{\beta_2^2} p \right)^2 \right]} \right. \\
&\left. - \frac{2}{\eta_{det}c^2} e^{-\frac{1}{2\sigma_0^2} \left[\left(\frac{\alpha_2^2}{\alpha_1^2} + \frac{1}{c^2} \right) \left(x_2 + \frac{\sqrt{\eta_s(1-\eta_s)}(1/\alpha_1^2 - 1)}{\frac{\alpha_2^2}{\alpha_1^2} + \frac{1}{c^2}} \right)^2 + \frac{x_2^2}{\alpha_2^2} + \left(\frac{\beta_2^2}{\beta_1^2} + \frac{1}{c^2} \right) \left(p_2 + \frac{\sqrt{\eta_s(1-\eta_s)}(1/\beta_1^2 - 1)}{\frac{\beta_2^2}{\beta_1^2} + \frac{1}{c^2}} \right)^2 + \frac{p_2^2}{\beta_2^2} \right]} \right], \quad (3.9)
\end{aligned}$$

and then, the Wigner function of the heralded non-Gaussian state is given by:

$$W_{NG}(x, p) = \frac{1}{\mathcal{N}_{NG}} \left[\frac{1}{\alpha_2\beta_2} e^{-\frac{1}{2\sigma_0^2} \left(\frac{x^2}{\alpha_2^2} + \frac{p^2}{\beta_2^2} \right)} - \frac{2}{\eta_{det} \sqrt{(\alpha_1^2 + c^2\alpha_2^2) (\beta_1^2 + c^2\beta_2^2)}} e^{-\frac{1}{2\sigma_0^2} \left(\frac{x^2}{\alpha_2^2} + \frac{p^2}{\beta_2^2} \right)} \right], \quad (3.10)$$

with a normalization constant \mathcal{N}_{NG} given by:

$$\mathcal{N}_{NG} = 2\pi\sigma_0^2 \left[1 - \frac{2\alpha_2'\beta_2'}{\eta_{det} \sqrt{(\alpha_1^2 + c^2\alpha_2^2) (\beta_1^2 + c^2\beta_2^2)}} \right]. \quad (3.11)$$

The quality of the heralded non-Gaussian state can be quantified by looking at its Wigner function negativity, defined as the volume of the negative part of the Wigner function, as it is a well established non-classicality criteria in quantum optics [82]. For simplicity, we will consider the minimum of the Wigner function, which is at the phase origin in our case ($W_{min} = W_{NG}(0,0)$), to see the effect of the different experimental parameters on the heralded non-Gaussian state. As seen in [subsection 2.3.2](#), for a squeezing parameter around $s = 0.5$ (−3 dB), the single-photon subtracted squeezed vacuum state approximates the perfect odd Schrödinger cat state with a high fidelity (with amplitude $\alpha \approx 1$), and so, we will consider a squeezing factor $s = -3$ dB in all numerical simulations in this section. [Figure 3.2](#) shows the contour plot of $W_{NG}(0,0)$ as a function of the reflection ratio $1 - \eta_s$ of BS2 (called tapping ratio) and the efficiency η_{det} of the On/Off detector without considering dark counts ($\nu = 0$).

We can see that, for a given efficiency η_{det} of the On/Off detector, the minimum $W_{NG}(0,0)$ of the Wigner function of the heralded state increases for an increasing tapping ratio. This is related to the fact that increasing $1 - \eta_s$ increases the probability that more than one photon are reflected and detected by the On/Off detector, leading to heralding events originating from multi-photon subtraction, which degrades the quality of the heralded non-Gaussian state. Moreover, if the efficiency η_{det} decreases, the probability that heralding events come from single-photon component decreases with respect to those related to higher photon numbers. In this case, the tapping ration must

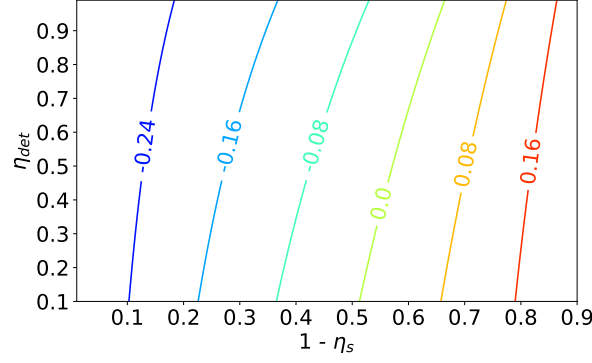


Figure 3.2 – The minimum $W_{NG}(0,0)$ of the Wigner function of the heralded non-Gaussian state as a function of the reflection ratio of BS2 ($1 - \eta_s$) and the efficiency η_{det} of the On/Off detector without considering dark counts ($\nu = 0$). The squeezing factor is $s = 0.5$ (-3 dB).

be decreased to maintain the same Wigner function negativity (decrease higher photon number contributions to the heralding events). In general, a tapping ratio less than 10% is enough to minimise multi-photon subtraction from a 3 dB squeezed vacuum state.

In Figure 3.3, we plot $W_{NG}(0,0)$ as a function of losses $1 - \eta_l$ that the squeezed vacuum state undergoes, for different dark count probabilities P_{dc} (defined as the ratio between the mean photon number originating from background noise and the total mean photon number reaching the On/Off detector), for a squeezing factor $s = 0.5$ (-3 dB), a tapping ratio $1 - \eta_s = 0.05$ and an efficiency $\eta_{det} = 1$.

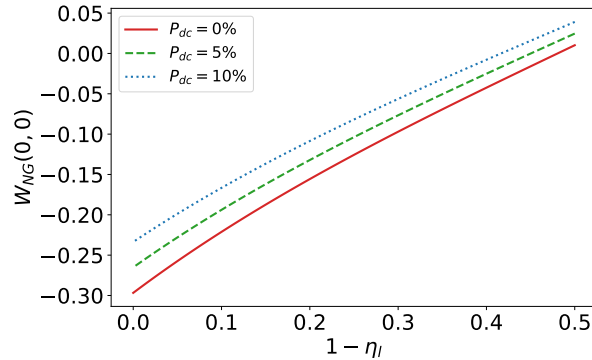


Figure 3.3 – The minimum $W_{NG}(0,0)$ of the Wigner function of the heralded non-Gaussian state as a function of losses $1 - \eta_l$ on the squeezed vacuum state for different dark count probabilities P_{dc} . The squeezing factor is $s = 0.5$ (-3 dB), the tapping ratio is $1 - \eta_s = 0.05$ and the On/Off detector efficiency is $\eta_{det} = 1$.

As it is expected, losses on the squeezed vacuum state affect directly the quality of the heralded non-Gaussian state. This can be interpreted as following: losses applied to a squeezed vacuum state change its photon statistics and odd photon number components appear, and so, the heralded state after photon subtraction contains also even and odd photon number components, which leads to a decreased purity. On the other hand, dark counts on the On/Off detector affect also the heralded state. In this case, if the On/Off detector detects a photon coming from the squeezed vacuum state, the her-

alded state is the one desired, otherwise, detection of photons coming from background noise heralds a squeezed vacuum state instead of photon-subtracted squeezed vacuum state, which means that the heralded state is a statistical mixture of photon-subtracted and non-photon-subtracted squeezed vacuum states.

3.1.3 Realistic homodyne detection

In [Figure 3.1](#), the realistic homodyne detector with limited efficiency η_{hd} is modeled by a perfect homodyne detector and the BS₃ with a transmission η_{hd} . The Wigner function of the state at the input of BS₃ is given by:

$$W_{in_3}(x, p; x_3, p_3) = W_{NG}(x, p) \cdot W_0(x_3, p_3). \quad (3.12)$$

We can notice that the Wigner function $W_{NG}(x, p)$ is a difference of two Gaussian functions, and so, we can use directly the result obtained in [subsection 3.1.1](#), applied to the two Gaussian components of $W_{NG}(x, p)$. The detected Wigner function, using a limited efficiency homodyne detector, is then given by:

$$W_{hd}(x, p) = \frac{1}{\mathcal{N}_{NG}} \left[\frac{1}{\alpha_3 \beta_3} e^{-\frac{1}{2\sigma_0^2} \left(\frac{x^2}{\alpha_3^2} + \frac{p^2}{\beta_3^2} \right)} - \frac{2\alpha'_2 \beta'_2}{\eta_{det} \alpha'_3 \beta'_3 \sqrt{(\alpha_1^2 + c^2 \alpha_2^2) (\beta_1^2 + c^2 \beta_2^2)}} e^{-\frac{1}{2\sigma_0^2} \left(\frac{x^2}{\alpha_3'^2} + \frac{p^2}{\beta_3'^2} \right)} \right]. \quad (3.13)$$

[Figure 3.4](#) displays a section $W_{hd}(x, 0)$ of the Wigner function of the heralded state as seen by the homodyne detection with different efficiencies η_{hd} and without losses on the squeezed state ($\eta_l = 1$). The squeezing factor is $s = 0.5$ (−3 dB), the tapping ratio is $1 - \eta_s = 0.01$, and the On/Off detector is considered to be perfect ($\eta_{det} = 1$ and $\nu = 0$).

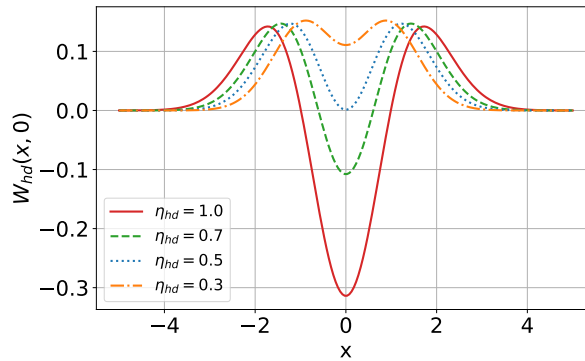


Figure 3.4 – A section $W_{hd}(x, 0)$ of the Wigner function of the heralded state as seen by the homodyne detection with different efficiencies η_{hd} . The squeezing factor is $s = 0.5$ (−3 dB), the tapping ratio is $1 - \eta_s = 0.01$, and the On/Off detector is supposed to be perfect ($\eta_{det} = 1$ and $\nu = 0$).

We can see clearly that the heralded state is highly affected by the efficiency of the homodyne detector. As it can be seen, for an ideal case (squeezed state without losses: $\eta_l = 1$, very low tapping ratio: $1 - \eta_s = 0.01$, and an ideal On/Off detector: $\eta_{det} = 1$ and $\nu = 0$), the Wigner function of the heralded state is no more negative for a homodyne detection efficiency less than 50%.

3.2 EXPERIMENTAL SETUP

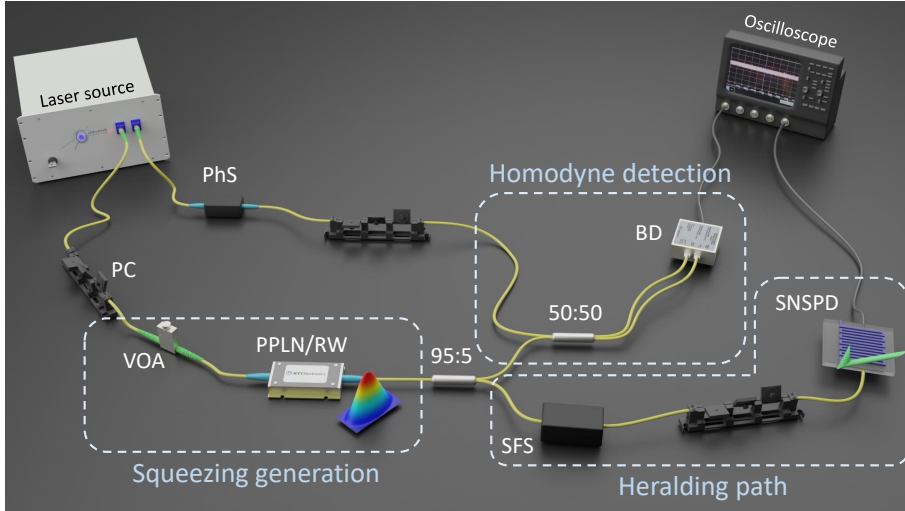


Figure 3.5 – Experimental setup. A fiber-coupled continuous wave (CW) laser delivers outputs at $\lambda = 1560.44$ nm and $\lambda = 780.22$ nm. The $\lambda = 780.22$ nm output passes through a polarization controller (PC) and a variable fiber optical attenuator (VOA) to be used as pump source for periodically poled lithium niobate ridge waveguide (PPLN/RW) generating the single-mode squeezed vacuum. Downstream of the PPLN/RW, squeezed light is sent to a 95:5 fiber beam-splitter. The 5% output undergoes a spectral filtering stage (SFS) and is sent to a superconducting nanowire single-photon detector (SNSPD), whose signal heralds the non-Gaussian state generation. The 95% output is sent to a homodyne detection (HD) made of a 50:50 fiber beam-splitter and a commercial balanced detector (BD). The HD local oscillator (LO) is given by laser output at $\lambda = 1560.44$ nm, passing through a fiber phase shifter (PhS) and a polarization controller (PC).

Figure 3.5 shows the experimental setup for heralded non-Gaussian state generation. The master source is a continuous wave (CW) fiber-coupled laser delivering outputs at $\lambda = 1560.44$ nm and its second harmonic (SH) at half of the wavelength ($\lambda = 780.22$ nm). The SH output is sent to fiber polarization controller (PC) and a variable optical attenuator (VOA) that allow adjusting its polarization and intensity. This set of plug-&-play telecom components is then directly connected to a periodically poled lithium niobate ridge waveguide (PPLN/RW). Single-mode squeezed vacuum state at $\lambda = 1560.44$ nm is generated via type-0 frequency degenerate spontaneous parametric down conversion (SPDC) process and collected by the optical fiber at the PPLN/RW output. As mentioned in subsection 2.3.2, and largely documented in the literature [75], heralded non-Gaussian state generation can be implemented by sending squeezed light to a low reflectivity BS followed by a single-photon detection stage. In our experiment, a 95:5 fiber beam-splitter (f-BS) splits squeezed light into two paths: the 5% output is sent to the heralding path, whereas the 95% output, carrying the heralded non-Gaussian state, goes to the homodyne detection (HD) for non-Gaussian state characterization. A commercial fiber phase shifter (PhS) from General photonics is used to modulate the phase of the laser output at $\lambda = 1560.44$ nm, used as a local oscillator (LO) for the HD. In this experiment, both photon subtraction operation and heralded state characterization

via HD are then implemented using standard fiber components from classical telecom technology.

3.2.1 Master laser source

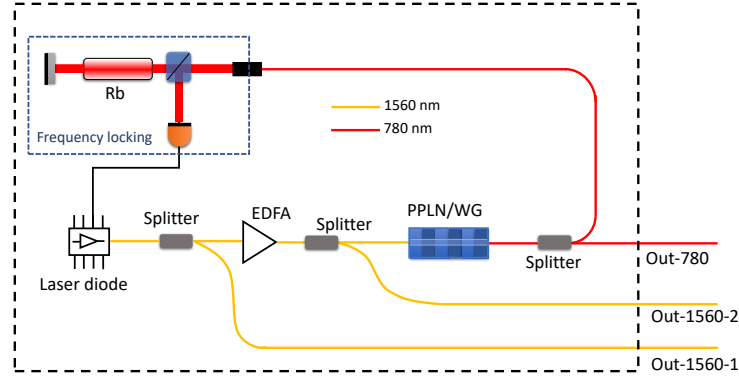


Figure 3.6 – Diagram of the master laser source.

The master laser source is a CW laser from Muquans, whose diagram is depicted in [Figure 3.6](#). A laser diode output at 1560 nm is split into two parts, one is sent directly to the user (Out-1560-1) and used as a LO for the HD in the experiment. The other part is amplified via an Erbium doped fiber amplifier (EDFA) and divided into two parts, one directly provided to the user, noted Out-1560-2 (not shown in [Figure 3.5](#)), and the other one frequency doubled via second harmonic generation (SHG) using a periodically poled lithium niobate waveguide (PPLN/WG). A part of the SH is used to lock the laser diode frequency on a ^{85}Rb absorption line, and the remaining visible light is sent to the output Out-780. All the outputs of the laser source are 2 m polarization maintaining (PM) fibers, and the linewidth of the laser at the output Out-1560-1 is around 8 kHz.

3.2.2 Squeezed vacuum source

The squeezed vacuum source is a commercial wavelength conversion module from NTT Electronics corp. It consists of a packaged PPLN/RW with a thermoelectric cooler and a thermistor. The input and output of the conversion module are fiber-pigtailed and the PPLN/RW temperature is controlled via a TEC Driver from Thorlabs (MTD451T). Squeezed vacuum state is obtained via single-pass frequency degenerate, type-0 SPDC process by pumping the PPLN/RW with the output Out-780 of the master laser source. In [Figure 3.7](#), the SPDC emission spectrum is plotted.

We can see that the SPDC emission spectrum is large, with a full width at half maximum (FWHM) of 87 nm (11 THz) and centred at 1560.44 nm (the stabilized wavelength of the master laser source). We note that the combined effect of guide-to-fiber coupling and propagation losses inside the nonlinear waveguide leads to a reduced transmission efficiency $\eta_t = \eta_{wg} \cdot \eta_c$ of squeezed vacuum state, where η_{wg} is the nonlinear ridge

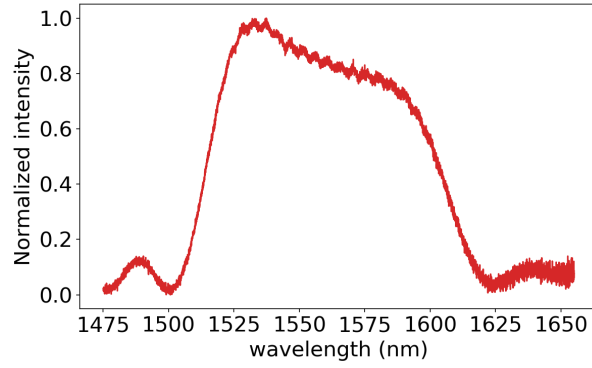


Figure 3.7 – Emission spectrum of the frequency degenerate type-0 SPDC process.

waveguide transmission efficiency (propagation losses of $1 - \eta_{wg}$), and η_c is the guide-to-fiber coupling efficiency at the output of the PPLN/RW.

3.2.3 Homodyne detection

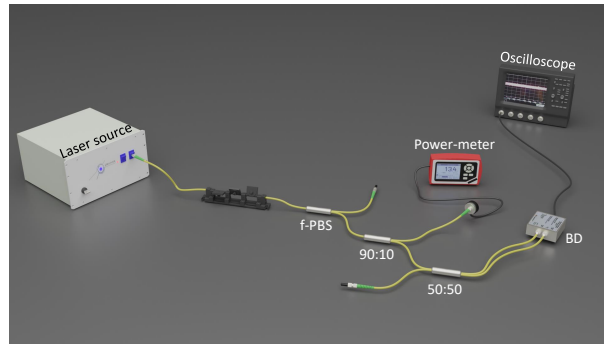


Figure 3.8 – The HD characterization setup. f-PBS: fiber polarization beam splitter, BD: balanced detector.

Following a common approach, the HD is realized by means of a 50:50 f-BS whose outputs are connected to a commercial balanced detector (BD) from Insight Photonic Solutions, Inc. Figure 3.8 shows the HD characterization setup, in which the output Out-1560-1 of the master laser source is sent to a fiber polarization beam splitter (f-PBS) to control the LO power, and then to a 90:10 f-BS, whose 90% output is sent to the HD whereas the 10% output is sent to an optical power-meter. The second input of the HD is not used in this case (vacuum input) and its output is monitored using an oscilloscope (HDO6104A from Teledyne LeCroy).

In Figure 3.9-(a), we plot the variance of the output signal (shot noise) of the HD for different values of the LO power. We can see that the HD response is linear and displays a signal to noise ratio (SNR) of 14 dB at a LO power $P_{LO} = 3.1$ mW. This LO power will be used for the whole experiment. In Figure 3.9-(b), the power spectral density (PSD) of the HD output is plotted for different values of the LO power, displaying a bandwidth of 300 MHz.

We note that the overall detection efficiency is given by:

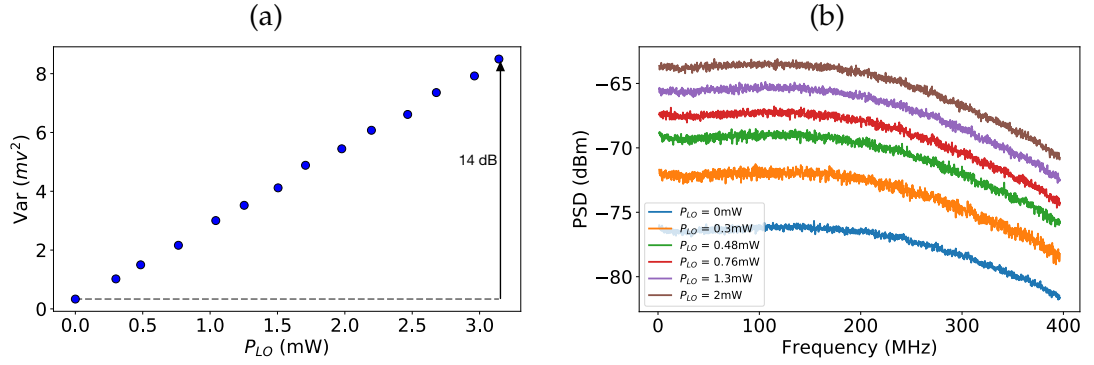


Figure 3.9 – HD response. The shot noise variance (a) and the power spectral density (b) of the HD output for different values of the LO power.

$$\eta_{hd} = \eta_t \cdot \eta_{pd} \cdot \eta_{el}, \quad (3.14)$$

where η_t is the transmission efficiency due to losses before the BD including the 50:50 f-BS, η_{pd} is the efficiency of the photodiodes of the BD and η_{el} accounts for the residual HD electronic noise. We measured experimentally $\eta_t = 0.94$ and $\eta_{el} = (\text{SNR} - 1)/\text{SNR} = 0.96$ [83], whereas $\eta_{pd} = 0.80$ is given by the manufacturer. This leads to an overall HD efficiency of $\eta_{hd} = 0.72$.

3.2.4 Photon subtraction: filtering the heralding photons

Due to a strong mismatch between the HD electronic bandwidth (300 MHz) and the broad SPDC emission bandwidth (11 THz), the 5% tapped light from the squeezed vacuum must be spectrally filtered. Indeed, photon-counting events of wavelengths far away from the CW LO could herald states whose non-Gaussian features are out-of-the-reach of HD electronics. This would weave data corresponding to the desired non-Gaussian states with those relative to squeezed vacuum, eventually resulting in the measurement of a mixed state. Such an effect further combines with the fact that single-pass squeezing can be not pure over its whole bandwidth [84]. As we will see in [chapter 5](#), spectral filtering in the heralding path allows circumventing these imperfections [84, 85]. In this experiment, the 5% tapped light from the squeezed vacuum state is filtered using a cascade of a commercial 500 MHz FWHM tunable fiber Bragg grating filter (FBG from AOS GmbH) and an in-house fiber-coupled Fabry-Pérot cavity with a target bandwidth of 10 MHz. Note that, as an alternative, plug-&-play optical filters with bandwidths of a few tens of MHz are commercially available.

3.2.4.1 FBG filter

The FBG filter is a thermally adjustable ultra narrow transmission filter from Advanced Optics Solutions (AOS) GmbH. Its transmission spectrum in dB as a function of the wavelength is depicted in [Figure 3.10](#)-(a). It has an attenuation of 4 dB at its maximum transmission, and reaches a rejection ratio of 46 dB out of its transmission window. In [Figure 3.10](#)-(b), we plot the fit of the FBG filter transmission spectrum in

linear scale with a Lorentzian function. This fit allows to retrieve its FWHM bandwidth, which is found to be $\Delta\nu_{FBG} = 585$ MHz.

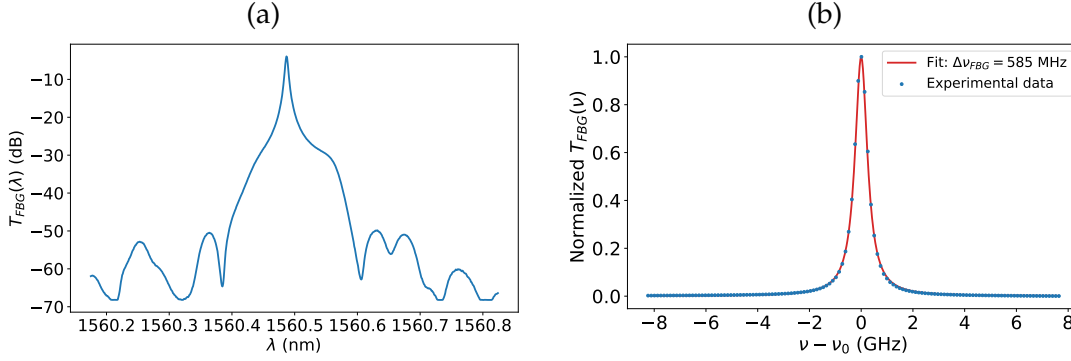


Figure 3.10 – (a) The transmission spectrum in dB of the FBG filter as a function of the wavelength. (b) Fitting the FBG transmission in linear scale with a Lorentzian function gives a FWHM bandwidth of $\Delta\nu_{FBG} = 585$ MHz.

3.2.4.2 Fabry-Pérot cavity design

In order to ensure that the FBG filter keeps only one cavity transmission peak (at 1560.44 nm) and rejects all other transmission peaks, the free spectral range, noted $\Delta\nu_{FP}$, of the Fabry-Pérot cavity should be greater than twice the FWHM FBG bandwidth: $\Delta\nu_{FP} \geq 1.2$ GHz. For a fixed $\Delta\nu_{FP} = 1.2$ GHz, a target cavity bandwidth of $\delta\nu_{FP} = 10$ MHz is equivalent to a cavity finesse of $F = \Delta\nu_{FP}/\delta\nu_{FP} = 120$. To build a cavity satisfying these requirements, a plane mirror M_1 (ref: 109761) and a concave mirror M_2 (ref: 109332) with a curvature radius $R_{M2} = 1$ m from LAYERTEC are chosen. The reflection coefficients are $r_1^2 = 0.98$ and $r_2^2 = 0.99$, respectively. The cavity finesse in this case is:

$$F \approx \pi \frac{\sqrt{r_1 r_2}}{1 - r_1 r_2} = 208, \quad (3.15)$$

which satisfies our need. Due to a limited wavelength resolution of our measurement system, a first experimental characterization of the cavity finesse is performed by aligning it with higher bandwidth. Figure 3.11 illustrates the cavity transmission peaks in the wavelength range from 1500 nm to 1600 nm (a) and a Lorentzian fit of one peak around 1560 nm (b).

We measured an approximated mean free spectral range of $\Delta\nu_{FP} \approx 12$ GHz and a cavity bandwidth of $\delta\nu_{FP} \approx 80$ MHz, which gives a finesse of $F = 150$, different from the calculated one (208) but still satisfying our requirements (> 120). The difference between the measured and calculated value of the finesse can be explained by the fact that the wavelength resolution in the experimental measurement is not high enough, which leads to errors in the estimated cavity bandwidth and free spectral range. Once the mirrors are chosen, we need now to fix the cavity length L_{FP} for a target bandwidth of $\delta\nu_{FP} = 10$ MHz, this length is given by:

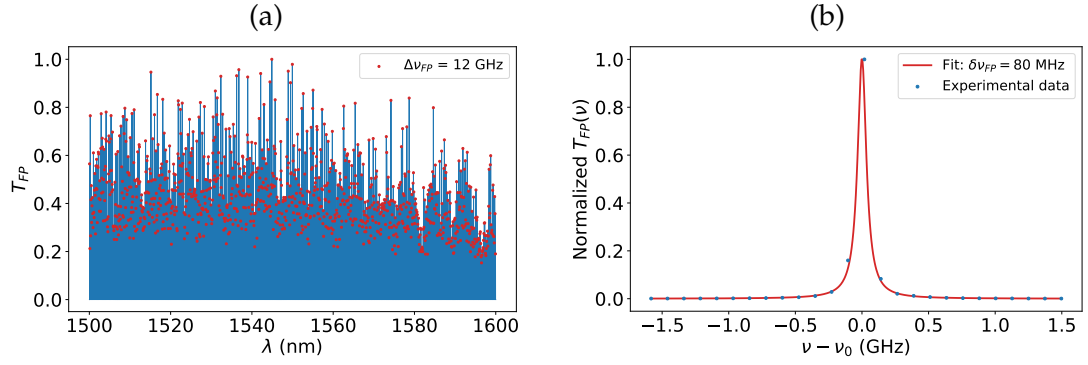


Figure 3.11 – (a) The transmission peaks of the Fabry-Pérot cavity aligned with a high bandwidth. (b) The fit of the a cavity transmission peak around 1560nm with a Lorentzian function.

$$L_{FP} = \frac{c}{2F\delta\nu_{FP}} \approx 70 \text{ mm.} \quad (3.16)$$

To have a single-mode oscillating cavity, the fundamental TEM_{00} Gaussian beam impinging it must be shaped so that its waist w'_0 will be located at the plane mirror M_1 , and the curvature radius of its wave-front matches the one of the concave mirror M_2 after a propagation distance $z_{prob} = 70 \text{ mm}$. This wave-front curvature radius is given by:

$$R(z) = z \left[1 + \left(\frac{\pi w_0'^2}{\lambda z} \right)^2 \right]. \quad (3.17)$$

For a curvature radius $R(z_{prob}) = R_{M2} = 1 \text{ m}$, the waist w'_0 must be:

$$w'_0 = \sqrt{\frac{\lambda z_{prob}}{\pi} \sqrt{\frac{R(z_{prob})}{z_{prob}} - 1}} \approx 356 \mu\text{m.} \quad (3.18)$$

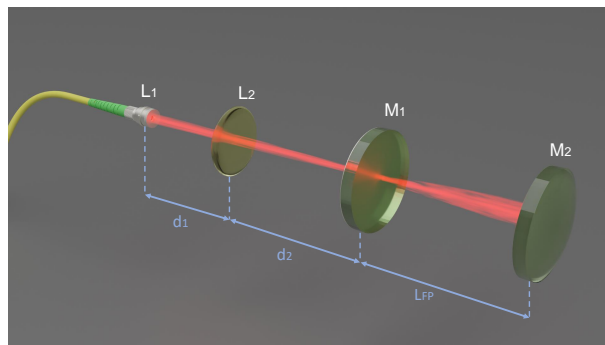


Figure 3.12 – Fiber to cavity beam shaping using a ser of two lenses L1 and L2.

In this experiment, the Fabry-Pérot cavity is fiber-coupled, and so, we need to design an appropriate optical system to transform the beam waist at the output of the optical fiber ($w_0 = 5.25 \mu\text{m}$ for SMF-28 fiber) to obtain the desired waist at the mirror M_1 .

Actually, a combination of two lenses is sufficient for this purpose (see Figure 3.12). A first adjustable fiber collimator L1 (CFC5-C from Thorlabs) with a focal length $f_1 = 4.6$ mm is used to collimate the beam at the output of the optical fiber. Another lens L2 with a focal length f_2 is placed at a distance d_1 from L1 to focus the beam on the plane mirror M1 with a target waist $w'_0 = 356\mu\text{m}$. The distance between the lens L2 and the mirror M1 is noted d_2 . In Figure 3.13, we plot the distances d_1 and d_2 as functions of the lens focal length f_2 for a target waist $w'_0 = 356\mu\text{m}$ (see Appendix C for detailed calculations).

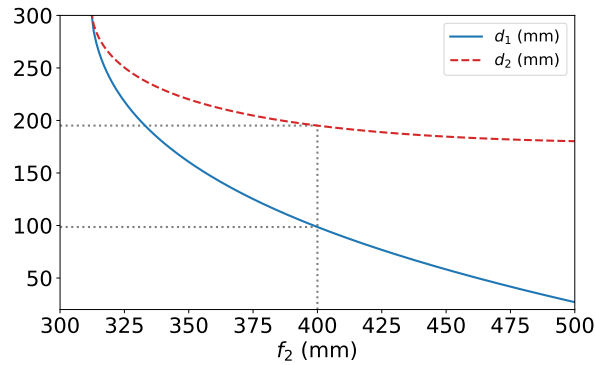


Figure 3.13 – The distances d_1 between the fiber collimator L1 and the lens L2 (solid blue curve) and d_2 between the lens L2 and the plane mirror M1 (dashed red curve) as functions of the focal length f_2 of L2 to obtain a target waist $w'_0 = 356\mu\text{m}$ at the mirror M1.

As we can see, a lens of focal length $f_2 = 400$ mm placed at a distance $d_1 \approx 100$ mm from the fiber collimator L1 allows to obtain a waist $w'_0 = 356\mu\text{m}$ at the plane mirror M1 located at a distance $d_2 \approx 195$ mm, which is reasonable.

3.2.4.3 Cavity locking

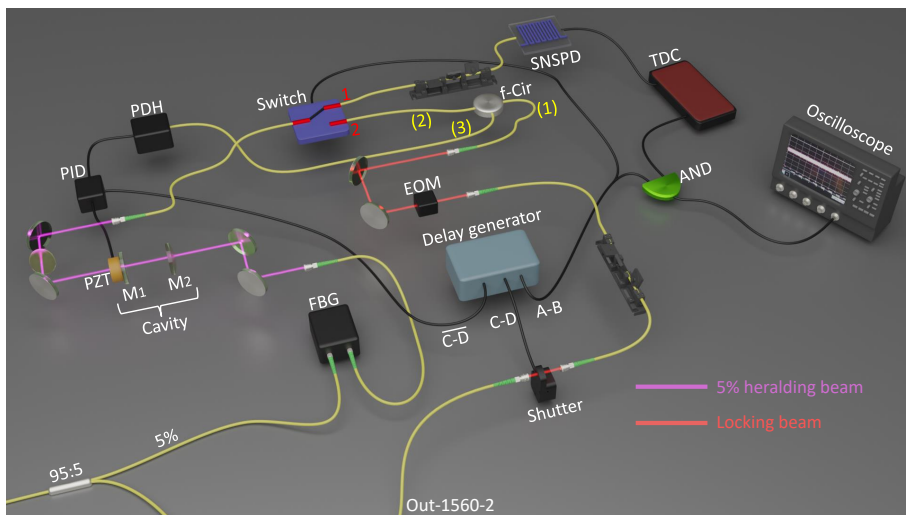


Figure 3.14 – Spectral filtering stage. See text for details.

To maintain a stable response of the filtering stage in the heralding path, the length of the Fabry-Pérot cavity needs to be locked. For this purpose, we use the Pound Drever Hall (PDH) technique [86]. Switching between the measurement and the locking cycles during the experiment is insured by an optical switch (OSW_{12-1310E} MEMS 1x2 Fiber Optic Switch Kit from Thorlabs) controlled by a DG535 4 channel digital delay/pulse generator from Stanford Research Systems (see Figure 3.14). In the measurement cycle, the optical switch is in position 1, which allows the 5% tapped light from the squeezed vacuum and passing through the FBG filter and the Fabry-Pérot cavity to reach the superconducting nanowire single-photon detector (Id281 SNSPD from IDQuantique), whose output response after detecting a photon is transformed to a TTL pulse using a time controller (Id900 TDC from IDQuantique). The homodyne data acquisition on the oscilloscope is then triggered by photon counting events from the heralding path.

During the cavity locking cycle, the optical switch is in position 2. In this case, the phase of the output Out-1560-2 of the master laser source is modulated at 24.2 MHz using an electro-optic modulator (EOM) from QUBIG GmbH (PM7-SWIR) and then passes through a fiber optic circulator f-Cir (path (1) \rightarrow (2)) and the switch to reach the Fabry-Pérot cavity. The reflected light from the cavity is then directed to the output (3) of the fiber optic circulator and used to generate the error signal using the PDH locking technique. A proportional-integral-derivative (PID) controller (Teensy 3.2 USB Development Board) then generates the control signal, which is amplified using an amplifier (TD250 from PiezoDrive) and sent to a piezo ring stack actuator from PiezoDrive to control the length of the Fabry-Pérot cavity. In Figure 3.15, the reflection of the cavity at port (3) of the fiber optic circulator (a) and the corresponding PDH error signal (b) are plotted by scanning the length of the cavity.

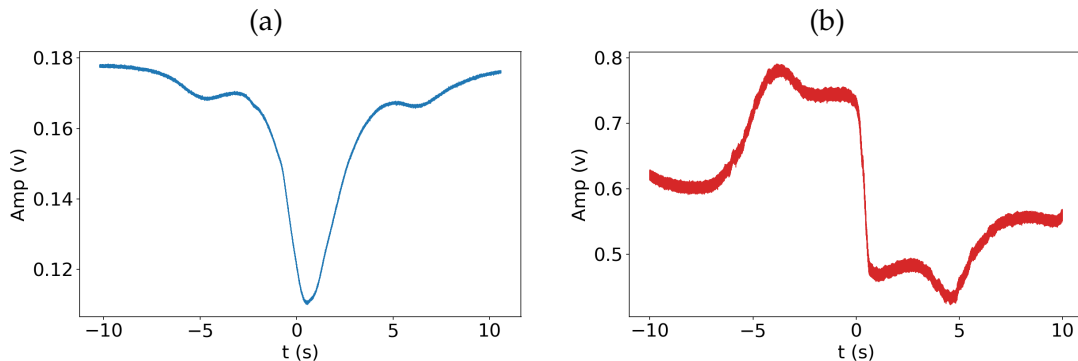


Figure 3.15 – (a) The reflection signal of the Fabry-Pérot cavity and (b) the corresponding PDH error signal obtained by scanning the length of the cavity.

As we can see, unlike the cavity reflection signal, the error signal is an odd function, which allows to correct the drift of the cavity length in both directions (increased or decreased cavity length).

Due to a cross talk between the two paths inside the optical switch, click events originating from the locking beam (Out-1560-2) during the measurement and the locking cycles lead to heralding a squeezed vacuum state instead of photon-subtracted squeezed vacuum state. To avoid this, an optical beam shutter (SH05 from Thorlabs) controlled by the DG535 delay/pulse generator is used to block the locking beam dur-

ing the measurement cycle which allows to keep only click events originating from the 5% tapped light. During the locking phase, the use of an AND logic gate whose inputs are the SNSPD response (after pulse reshaping using Id900) and the switch control signal allows to ignore all click events. Figure 3.16 shows a representation of the synchronization signals used to control the switch, the optical beam shutter and the AND logic gate.

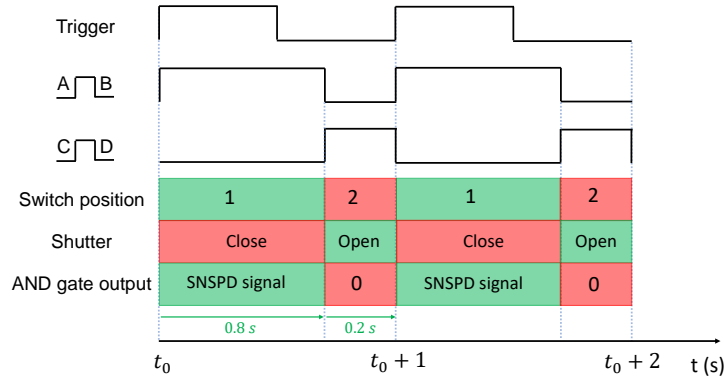


Figure 3.16 – Synchronization signals for the switch, the shutter and the AND gate.

During the measurement cycle (800 ms), the output A-B of the delay/pulse generator is equal to 1. In this case, the optical switch is in position 1 and the output of the logic AND gate is given directly by the response of the SNSPD. At the same time, the output C-D of the delay/pulse generator is equal to 0, which closes the beam shutter and blocks the locking beam, and the PID controller maintains the last control signal until a new locking cycle. During the locking cycle (200 ms), the outputs A-B and C-D pass to 0 and 1, respectively, putting the switch in the position 2 and opening the beam shutter. In this case, the output of the AND gate is equal to 0 since one of its inputs (A-B) is a logic zero. Note that, due to the different lengths of the used electric cables and the slightly slow response of the optical beam shutter, the different time windows in Figure 3.16 are slightly shifted to minimize the dark counts in the SNSPD ($t_A = t_0$, $t_B = t_A + 0.8$ s, $t_C = t_0 + 0.796$ s and $t_D = t_C + 0.184$ s). The detailed PDH locking scheme can be found in Appendix D.

3.3 DATA POST-PROCESSING

For each click event in the heralding path, a homodyne trace $x_i(t)$ is recorded using the oscilloscope. As we have seen in chapter 2, photon-subtracted squeezed vacuum states are phase dependent, and so, in order to be able to reconstruct the Wigner function of the heralded non-Gaussian state, the heralded state quadrature values X_i and the corresponding LO phases θ_i need to be extracted. In this section, data post-processing techniques used for this purpose are presented.

3.3.1 LO phase extraction

As we mentioned before, the Fabry-Pérot cavity was designed so that cascading it with the FBG filter gives a filtering bandwidth of 10 MHz in the heralding path. In this case, the characteristic time of the heralded state wave-packet is around 100 ns. Recorded homodyne traces $x_i(t)$ of a duration much larger than this characteristic time contains mostly data corresponding to squeezed vacuum state, which is also phase dependent. Since squeezed vacuum is a Gaussian state, knowing its quadrature variance σ_{sq}^2 allows to retrieve the LO phase (see Equation 2.54). In Figure 3.17, we plot the variance of 1000 consecutive traces $x_i(t)$ of a duration of $5\mu\text{s}$ with a sampling rate of 5 Gs/s.

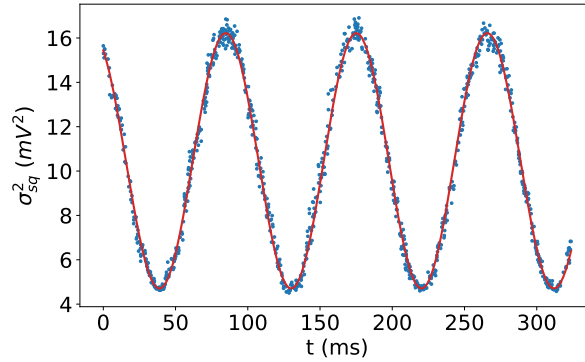


Figure 3.17 – The variance σ_{sq}^2 of the squeezed vacuum state calculated using 1000 consecutive homodyne traces $x_i(t)$ over the whole duration of $5\mu\text{s}$ (blue dots) and its fit with a cosine function (red curve).

The LO phase is spanned with a fiber phase shifter driven by a ramp generated by a DS345 synthesized function generator from Stanford Research Systems and amplified via the TD250 PiezoDrive amplifier, with a speed of approximately $9\pi/s$ and, therefore, it can be considered as constant over the time window of a single homodyne trace (a LO phase shift around 1.4×10^{-4} rad in a single homodyne trace of a duration of $5\mu\text{s}$). Due to the nonlinear response of the phase shifter, the squeezed vacuum variance is fitted with the function:

$$\sigma_{fit}^2(t) = a \cos(\alpha t^2 + \beta t + \gamma) + b. \quad (3.19)$$

This fit allows to retrieve the LO phase θ_i for each trace $x_i(t)$.

3.3.2 Quadrature extraction

In the CW regime, the quadrature X_i of the heralded non-Gaussian state can be obtained from raw homodyne data $x_i(t)$ as [87]:

$$X_i = \int f(t)x_i(t)dt, \quad (3.20)$$

where $f(t)$ is the wave-packet of the heralded non-Gaussian state, as determined by the filtering stage in the heralding path whose transmission function is given by:

$$T(\nu) = \frac{T_0}{1 + \frac{(\nu - \nu_0)^2}{\gamma^2}}. \quad (3.21)$$

When the squeezing bandwidth is much broader than the bandwidth of this filter ($\Delta\nu = 2\gamma$), the theoretical $f(t)$ is expected to be an exponential rising function:

$$f(t) \approx e^{2\pi\gamma t} u(-t), \quad (3.22)$$

where $u(t)$ is the Heaviside step function. As proposed in [88], this wave-packet can be experimentally extracted by performing a singular value decomposition of the autocorrelation function of the heralded homodyne traces, $\langle x(t)x(t') \rangle$. This is based on the fact that the variance of the heralded non-Gaussian state quadratures, X_i , is greater than the one of the squeezed vacuum state quadratures. Using Equation 3.20, this variance can be written as:

$$\sigma^2(X) = \iint f(t)f(t') \langle x(t)x(t') \rangle dt dt'. \quad (3.23)$$

By decomposing the autocorrelation function $\langle x(t)x(t') \rangle$ and the wave-packet $f(t)$ using a set of orthonormal functions $\{f_k(t)\}$ as:

$$\langle x(t)x(t') \rangle = \sum_k \lambda_k f_k(t) f_k(t'), \quad (3.24)$$

$$f(t) = \sum_k \lambda'_k f_k(t), \quad (3.25)$$

with a normalization condition: $\sum_k \lambda_k'^2 = 1$, the variance given by Equation 3.23 can be written as:

$$\sigma^2(X) = \sum_{k,m,p} \lambda'_k \lambda'_m \lambda'_p \int f_k(t) f_p(t) dt \int f_m(t') f_p(t') dt' = \sum_k \lambda_k'^2 \lambda_k \leq \max\{\lambda_k\}. \quad (3.26)$$

The function $f(t)$ that maximises the variance $\sigma^2(X)$ corresponds then to the eigenfunction of the autocorrelation function $\langle x(t)x(t') \rangle$ with the highest eigenvalue.

3.4 EXPERIMENTAL RESULTS AND DISCUSSION

Losses in the heralding path lead to an overall heralding detection efficiency $\eta_{det} \approx 0.06$. during the experiment, the heralding rate is of 3 kHz and the dark count rate is about 80 Hz, giving a signal to noise ratio (SNR) of 15.7 dB. A series of 43000 homodyne traces $x_i(t)$ of a duration of $5\mu s$ each at a sampling rate of 5 Gs/s are recorded using the oscilloscope. For each acquisition $x_i(t)$, the LO phase θ_i is inferred from the phase dependency of the measured squeezed vacuum variance as explained in subsection 3.3.1. We first measure the squeezing to characterize the overall transmission efficiency $\eta_{tot} = \eta_l \cdot \eta_s \cdot \eta_{hd}$ where $\eta_s = 0.96$ is the transmission of the subtracting 95:5 f-BS, this allows to deduce the squeezing transmission efficiency η_l before the subtracting f-BS since η_{hd} is already characterized ($\eta_{hd} = 0.72$). After that, these parameters are

used in the theoretical model introduced in [section 3.1](#) to compare the experimentally obtained heralded non-Gaussian state with the theoretical one.

3.4.1 Squeezed vacuum state generation and losses characterization

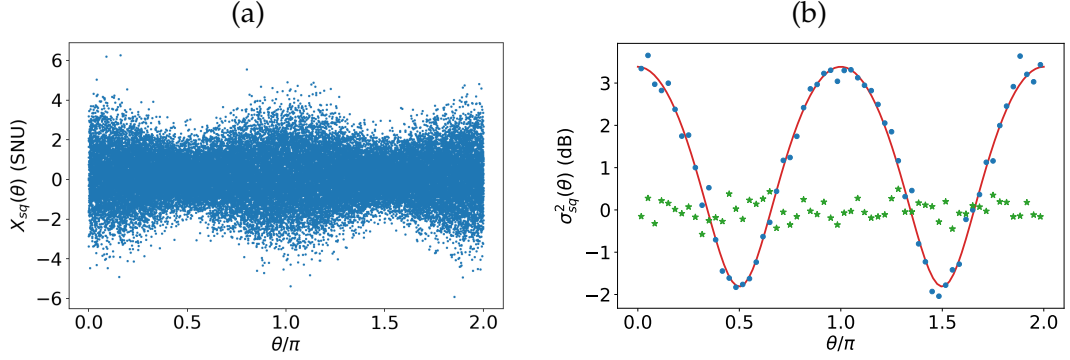


Figure 3.18 – (a) The measured squeezed vacuum quadratures X_{sq} as a function of the LO phase θ . (b) The variance of the squeezed vacuum quadrature σ_{sq}^2 as a function of the LO phase θ (blue dots) and its fit using the theoretical formula given by [Equation 2.54](#) (red curve) with a phase shift of $\pi/2$. The green stars in (b) represent the measured shot noise variance.

In [Figure 3.18\(a\)](#), we show the measured quadrature values X_{sq} of the squeezed vacuum state as a function of the LO phase θ . The variance of this quadrature is plotted in [Figure 3.18\(b\)](#) (blue points), with its fit using the theoretical formula given by [Equation 2.54](#) (red curve). As expected, this variance is smaller than the shot noise level (green stars) for some LO phases (squeezing) and greater than the shot noise level for other phases (antisqueezing). We measured a squeezing of -1.80 ± 0.05 dB and an antisqueezing of 3.36 ± 0.05 dB. This corresponds to an initial squeezing of -5.39 ± 0.05 dB and a total transmission efficiency $\eta_{tot} = 0.48$, which means that the transmission efficiency η_l due to propagation losses in the PPLN/RW ($1 - \eta_{wg}$) and guide-to-fiber coupling efficiency (η_c) is: $\eta_l = 0.69$.

3.4.2 Wave-packet extraction of the heralded non-Gaussian state

The duration of the acquired homodyne traces $x_i(t)$ ($5\mu s$) is much larger than the characteristic time of the heralded non-Gaussian state wave-packet (~ 100 ns). In addition to this, one homodyne trace contains 25000 points, and so, using the whole 43000 homodyne traces to determine the wave-packet of the heralded non-Gaussian state via singular value decomposition of the autocorrelation function (see [subsection 3.3.2](#)) is time consuming. To reduce this processing time, we determine at first the temporal position t_0 of the heralded non-Gaussian state wave-packet in the homodyne trace $x_i(t)$. Knowing that the length of the heralding path is longer than the one of the homodyne detection, we analyse only the negative time part of the traces $x_i(t)$ ($t_0 < 0$). To do so, the homodyne traces $x_i(t)$ corresponding to a LO phase $\theta_i < 0.2$ rad are filtered using the theoretical wave-packet given by [Equation 3.22](#) for a bandwidth $\delta\nu = 2\gamma = 10$ MHz

of the spectral filter in the heralding path and with a time resolution of 1 ns. [Figure 3.19](#) shows the density plot of the filtered homodyne traces.

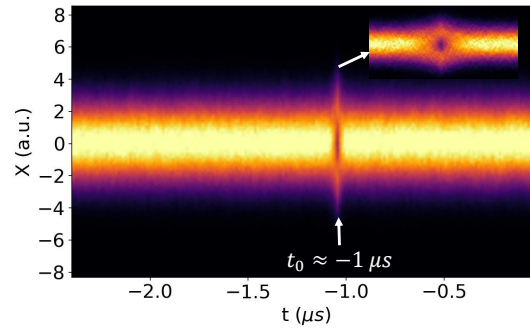


Figure 3.19 – The density plot of the filtered homodyne traces $x_i(t)$ with $\theta_i < 0.2$ rad using the theoretical wave-packet given by [Equation 3.22](#) with a bandwidth $\delta\nu = 2\gamma = 10$ MHz of the spectral filter in the heralding path and a time resolution of 1 ns.

Most of the time, we have a Gaussian distribution of the filtered homodyne traces which corresponds to squeezed vacuum state, and at a time around $-1\mu s$, a non-Gaussian distribution appears (zoomed in the inset). This corresponds to the quadratures of the heralded non-Gaussian state, and thus, its wave-packet is located around $t_0 = -1\mu s$. Autocorrelation function $\langle x(t)x(t') \rangle$ is then computed around t_0 with a time duration of 250 ns and a higher time resolution. The eigenvalues of this autocorrelation function, obtained by singular value decomposition, are shown in [Figure 3.20](#)-(a) for both the squeezed vacuum state (red) and the heralded non-Gaussian state (blue).

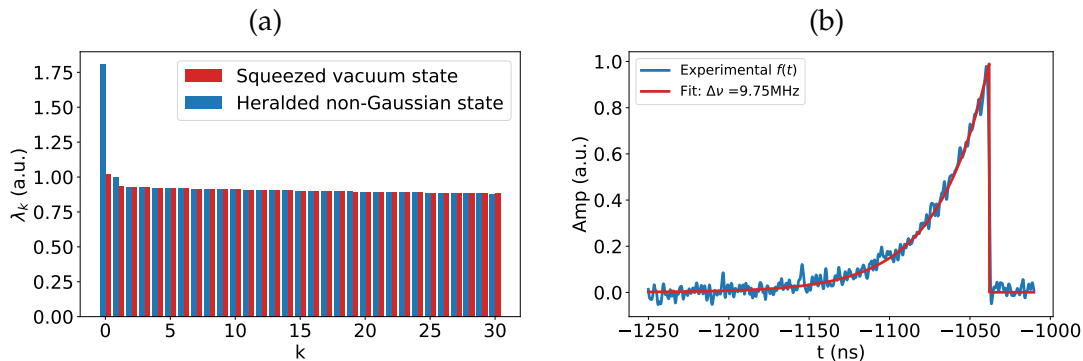


Figure 3.20 – (a) The eigenvalues of the autocorrelation function for the squeezed vacuum state (red) and the heralded non-Gaussian state (blue) obtained by singular value decomposition. (b) The temporal eigenmode $f_k(t)$ corresponding to the highest eigenvalue of the autocorrelation function (blue) and the fit with the theoretical wave-packet (red). The cascade of the Fabry-Pérot cavity and the FBG filter in the heralding path gives a filtering bandwidth of $\delta\nu = 9.75$ MHz.

All the eigenvalues are almost equal for the squeezed vacuum state (red) whereas for the heralded non-Gaussian state (blue), one eigenvalue is higher than the others. It corresponds to the temporal eigenmode $f_k(t)$ that maximizes the variance of the filtered quadratures, shown in [Figure 3.20](#)-(b) (blue curve). Fitting this eigenmode with

the theoretical wave-packet given by Equation 3.22 (red curve) gives a filtering bandwidth of $\delta\nu = 9.75$ MHz at FWHM, in agreement with the filtering stage characteristics. This wave-packet is then used to extract the quadrature values X_i of the heralded non-Gaussian state.

3.4.3 Heralded non-Gaussian state

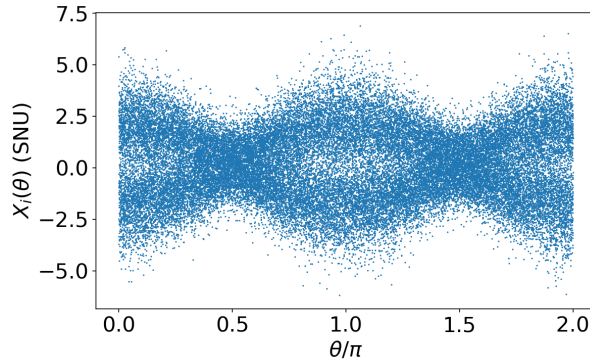


Figure 3.21 – The extracted quadrature values X_i of the heralded non-Gaussian state as a function of the phase θ of the LO.

By exploiting Equation 3.20, the obtained heralded state wave-packet is used to extract the quadrature values X_i the heralded non-Gaussian state. These quadratures are displayed in Figure 3.21. As we can see, the non-Gaussian behaviour of the heralded state appears in the quadrature distribution, showing holes around the zero quadrature. These quadrature values and phases are then used to perform the tomography of the heralded non-Gaussian state with the maximum-likelihood algorithm (see subsection 2.4.1.3) with 200 iterations [66].

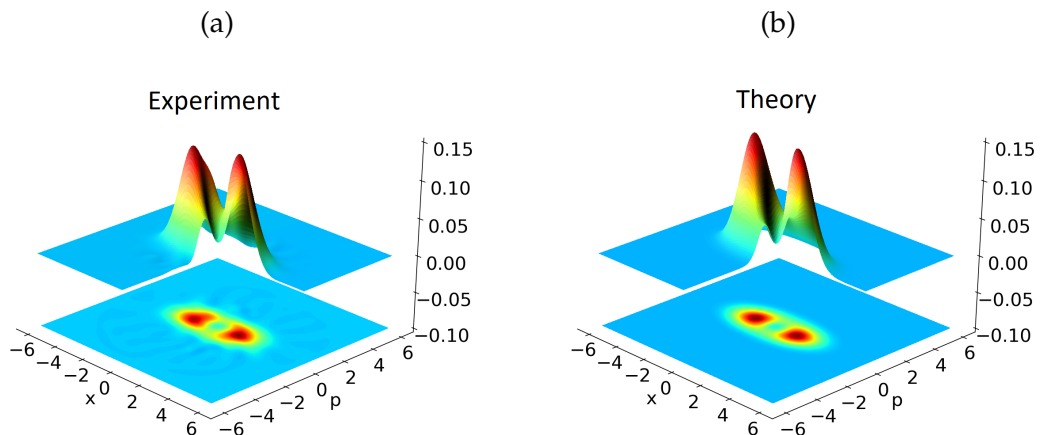


Figure 3.22 – (a) The Wigner function $W_{hd}(x, p)$ of the heralded non-Gaussian state as seen by the HD and (b) the theoretical Wigner function of photon-subtracted squeezed vacuum state $W_{Th}(x, p)$ obtained with the model introduced in section 3.1 using the different experimental parameters and imperfections.

Figure 3.22 shows the Wigner function $W_{hd}(x, p)$ of the generated non-Gaussian state as seen by the HD (a) and the theoretical one $W_{Th}(x, p)$ obtained with the model introduced in section 3.1 using the different experimental parameters and imperfections. As can be seen, the produced state has a highly non-Gaussian Wigner function with a minimum at phase origin $W_{hd}(0, 0) = 0.016 \pm 0.004$. Its profile matches the one predicted by theory ($W_{Th}(0, 0) = 0.015$) taking into account the different experimental imperfections. As mentioned in subsection 2.4.1.3, raw data can be corrected by the homodyne limited efficiency $\eta_{hd} = 0.72$ [67]. As extensively discussed in the literature [75, 89, 90], such a very common procedure allows assessing the impact of novel approaches to quantum state generation or manipulation without being penalized by the limitations of detection technology. In Figure 3.23, the Wigner function of the produced non-Gaussian state just before the homodyne detection stage is displayed.

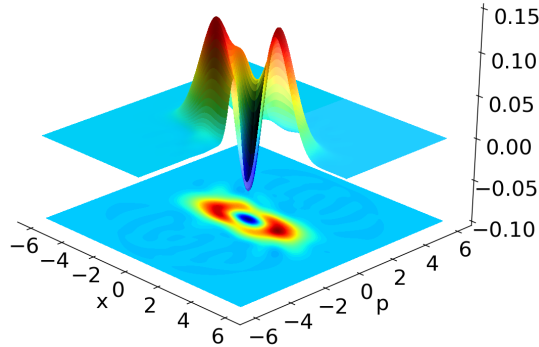


Figure 3.23 – The Wigner function $W_{NG}(x, p)$ of the heralded non-Gaussian state just before the HD stage, obtained by correcting the raw data with the limited efficiency $\eta_{hd} = 0.72$ of the HD.

As expected for Schrödinger kitten states, the produced non-Gaussian state correctly exhibits a negative Wigner function with a minimum value at the origin $W_{NG}(0, 0) = -0.065 \pm 0.004$. This result represents the very first demonstration of non-Gaussian states in a fully guided-wave setup and it attests the impact of our approach towards compact, simple, and plug-&-play experiments involving both Gaussian and non-Gaussian operations. We point out that limitations in the detection system are not intrinsic to the guided-wave approach but only to our specific realization. In particular, the lack of efficient photodiodes, that represent the most critical loss factor in the HD, affects in the same way both guided-wave and bulk realizations.

To conclude, we note that a further improvement of the Wigner negativity could be obtained by pushing η_l towards higher values. The measured value of η_l is in agreement with realistic performances in commercial fiber-coupled ridge waveguides. At the same time, the propagation and coupling losses at the SPDC stage degrade the purity of the squeezed state on which the subtraction protocol is applied. This deleterious effect can be circumvented by adopting a full integrated setup including on-chip squeezing generation, photon subtraction and homodyne detection, in a configuration similar to those shown for Gaussian state generation, manipulation, and detection

on lithium niobate circuits [91–93]. Such a strategy would push propagation losses down to 0.03 dB/cm and coupling losses to 0, thus giving for a typical chip length of 5 cm, a total $\eta_l = 0.97$. In this condition, the Wigner function negativity would go to $W_{NG}(0,0) = -0.22$.

3.5 CONCLUSION

We have demonstrated that a plug-&-play, fully guided-wave approach to quantum optics experiments is definitely reachable with off-the-shelves standard components and devices. This concept has been pushed, for the first time, to the generation of non-Gaussian states of light, including with a negative Wigner function, showing the possibility of implementing complex setups free from any bulk optics stage. The obtained realization enables reconfigurable and easy-to-mount systems compatible with integrated photonics [91–93]. These ingredients are essential to scale-up realizations of increasingly complex optical quantum systems capable of enabling disruptive but realistic quantum information protocols.

GUIDED-WAVE, PULSED NON-GAUSSIAN STATE ENGINEERING FOR HYBRID ENTANGLEMENT GENERATION

4.1	Encoding information in quantum states	84
4.1.1	Discrete-variable (DV) encoding	84
4.1.2	Continuous variable (CV) encoding	86
4.2	Hybrid entanglement: towards heterogeneous quantum networks	86
4.2.1	Hybrid entanglement with time-bin DV encoding	88
4.2.2	The DV and CV resources for time-bin based hybrid entanglement creation	89
4.3	SPDC based source for DV and CV entangled states	90
4.3.1	JSA shaping for quasi-single-mode DV and CV state production	92
4.3.2	SHG and SPDC source design	94
4.4	SPDC source characterization	102
4.4.1	Fundamental pulsed laser source	103
4.4.2	SHG stage	104
4.4.3	SPDC stage	105
4.5	Conclusion	107

Quantum information is at the heart of the development of new computation and communication protocols in which, entanglement and superposition are the two main ingredients allowing ultrafast, highly secure information processing and transmission. This development has been traditionally conducted along two parallel research axes, namely discrete-variable (DV) and continuous-variable (CV) quantum information, depending on what kind of quantum observables are used to encode information. More recently, efforts have been invested to combine these two different axes leading to the development of hybrid approaches opening the frontiers to more interesting protocols and applications. More precisely, entanglement between a DV and a CV encodings represents a key feature to bridge these two axes allowing to bypass their individual limitations, and hence, implement more advanced quantum information tasks [94–97]. Among all the possible encodings [98], hybrid entanglement generation protocol using time-bin DV encoding was proposed in [31], showing the advantage of using this kind of encoding in optical fiber-based telecommunication networks. Indeed, time-bin encoding makes hybrid entanglement particularly well adapted to applications involving long-distance propagation in optical fibers.

In this chapter, we present the design and characterization of a guided-wave source for the generation of high quality DV and CV state, used as resources for time-bin based hybrid entanglement generation, at a telecom wavelength in the picosecond

pulsed regime. We start in [section 4.1](#) by introducing the main ways of coding the information on quantum states of light. Next, we introduce the hybrid entanglement between DV and CV encoding in [section 4.2](#) and we focus on the DV and CV resource state production for time-bin based hybrid entanglement generation. Then, we present in [section 4.3](#) the design of a guided-wave source for the generation of high quality DV and CV states in picosecond pulsed regime at a telecom wavelength. After that, experimental characterizations of this source are presented in [section 4.4](#) and finally, the chapter is concluded in [section 4.5](#).

4.1 ENCODING INFORMATION IN QUANTUM STATES

Depending on the observables used to encode information in quantum state, we can principally identify two ways of coding the quantum information, namely DV [4, 20] and CV [21, 99, 100]. In the DV case, the observable has discrete spectrum (discrete set of eigenvalues) which means that the outcome of the measurement of such observable will be a random output from a discrete set. On the other hand, if the observable used to encode information has a continuous spectrum (continuous set of eigenvalues), we talk about CV encoding. In this case, measuring the observable gives a continuous set of outputs.

4.1.1 Discrete-variable (DV) encoding

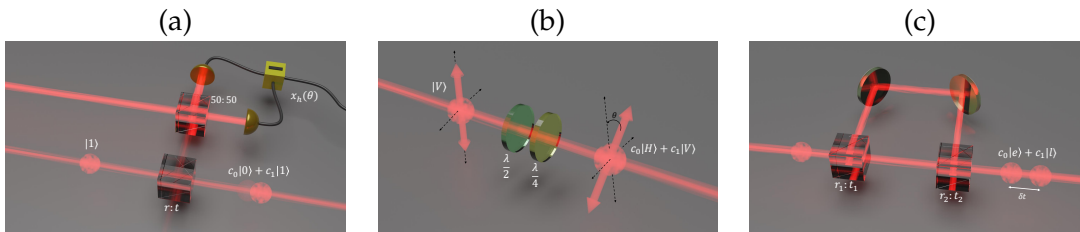


Figure 4.1 – Examples of optical qubit production in (a): single rail encoding, (b): polarization encoding and (c): time-bin encoding.

Let us consider the simple case of two dimensional Hilbert space, where quantum information is encoded using binary digits. Like a classical bit, a quantum bit of information, called *qubit*, can take either a logical value zero or one, noted $|0\rangle$ and $|1\rangle$, respectively, forming a discrete basis $\{|0\rangle, |1\rangle\}$. these two digits are generally given by the orthogonal eigenstates of a given observable of a single quantum system. In addition to this, quantum mechanics allows this state to be in a superposition of these digits:

$$|\psi\rangle = c_0 |0\rangle + c_1 |1\rangle, \quad (4.1)$$

which is, in addition to entanglement, at the heart of quantum information protocols.

Among the various systems used to encode quantum information, photons are a promising candidates due to their ability to be used as information carrier for commu-

nication tasks. In this case, a quantum system containing at most a single-photon is sufficient to implement the qubit given by Equation 4.1. To do so, different observables can be used, such as the presence or absence of a single-photon (single rail qubit), the polarization or the arrival time of a single-photon (dual rail qubits). The nomination "single rail" or "dual rail" is related to the fact that only a single-mode or two modes are considered, respectively, as illustrated in Figure 4.1.

4.1.1.1 Single rail qubit

For a single rail qubit, the observable being the number of photons, the digits $|0\rangle$ and $|1\rangle$ are encoded by Fock states with photon number $n = 0$ (vacuum) and $n = 1$ (single-photon), respectively. This kind of encoding can be achieved by sending a single-photon Fock state to a beam splitter (BS), and performing a homodyne measurement on one of the two outputs of the BS [101]. In this case, the superposition amplitudes c_0 and c_1 are determined by the reflectivity of the BS and the homodyne measurement output $x_h(\theta)$ used to herald the creation of the qubit, as shown in Figure 4.1-(a).

4.1.1.2 Polarization qubit

A widely used observable to encode information in a DV way is the polarization of a single-photon. In this case, the basis $\{|0\rangle, |1\rangle\}$ can be formed by the two eigenstates $|H\rangle$ and $|V\rangle$ of the polarization of the single-photon, where $|0\rangle = |H\rangle = |1\rangle_H |0\rangle_V$ and $|1\rangle = |V\rangle = |0\rangle_H |1\rangle_V$ are the horizontal and vertical polarization eigenstates of a single-photon, respectively. An alternative basis can be formed by the diagonal $|D\rangle \propto |H\rangle + |V\rangle$ and the anti-diagonal $|A\rangle \propto |H\rangle - |V\rangle$ polarization states or even the circular right $|R\rangle \propto |H\rangle + e^{i\frac{\pi}{2}} |V\rangle$ and circular left $|L\rangle \propto |H\rangle + e^{-i\frac{\pi}{2}} |V\rangle$ single-photon polarization eigenstates. A simple way to produce any superposition of the digits $|0\rangle$ and $|1\rangle$ is to transform the polarization of a single-photon using half and quarter waveplates (see Figure 4.1-(b)). A combination of wave-plates, a polarization beam splitter (PBS) and photoncounters allows to fully characterize a given qubit by measuring the superposition amplitudes c_0 and c_1 .

4.1.1.3 Time-bin qubit

In a time-bin qubit, the observable used to encode information is the arrival time of a single-photon. By defining two time slots separated by $\delta t > t_c$ where t_c is the coherence time of the single-photon, the digit $|0\rangle$ can be encoded in the state $|e\rangle = |1\rangle_e |0\rangle_l$ and the digit $|1\rangle$ in the state $|l\rangle = |0\rangle_e |1\rangle_l$. Here, the subscripts e and l denote the "early" and "late" time slots, respectively. A photon delocalized in the two time slots encodes the qubit given by Equation 4.1 where the photon can be found in the "early" time slot with a probability $|c_0|^2$ and in the "late" one with a probability $|c_1|^2$. This type of qubit can be produced by sending a single-photon state to an unbalanced Mach-Zehnder interferometer as shown in Figure 4.1-(c). Contrary to the the single rail qubit introduced previously, this kind of encoding is robust against optical losses, since losing the photon destroys the whole state instead of altering its coherence (the c_0 and c_1 constants). In addition, the single-photon polarization is not important in this

case, which makes the time-bin qubits more suitable for guided-wave implementations of quantum information protocols, where losses and polarization mode dispersion are not negligible [31].

4.1.2 Continuous variable (CV) encoding

In the CV encoding, a *qumode* (the CV equivalent of a DV *qubit*) is encoded using a continuous set of eigenstates of a given observable instead of a discrete basis for the DV encoding. Typically, the continuous spectrum quadrature observable \hat{x} with its set of eigenstates $\{|x\rangle\}$ is suitable for this purpose. In this case, the information can be encoded in the wave-function $\psi(x)$ of a given state $|\psi\rangle$:

$$|\psi\rangle = \int \psi(x) |x\rangle dx, \quad (4.2)$$

which can be represented by its Wigner function. Some quantum information protocols require only Gaussian states, such as coherent and squeezed states, that are deterministically produced, which is an advantage compared to the DV encoding. However, non-Gaussian resources are necessary to achieve fault-tolerant quantum information processing [24] and efficient quantum teleportation-based protocols [102]. In this case, superposition of coherent states with opposite phases are good candidates [103–105]. As seen in section 2.4, a simple homodyne detection stage allows to reconstruct the Wigner function of any quantum state, and thus, to fully characterize a given qumode. The main limitation of CV encoding is that it is very sensitive to losses (see subsection 2.3.1 and section 3.1). In Table 4.1, we summarize the main characteristics of each type of quantum information encoding.

4.2 HYBRID ENTANGLEMENT: TOWARDS HETEROGENEOUS QUANTUM NETWORKS

As highlighted in section 4.1, and based on the *wave-particle* duality of quantum mechanical systems (light among them), quantum information science and technologies have been developed following two directions based either on CV or DV encoding of information. Each of them has its advantages and drawbacks [106], however, they can be complementary, where the disadvantage of one can be seen as advantage for the other (see Table 4.1). Following this, a more recent research axis based on combining these two types of information encoding is growing [98, 107, 108]. In this context, entanglement between *particle-like* (DV) and *wave-like* (CV) encodings of the type:

$$|\psi\rangle = \frac{|0\rangle_A |\psi_0\rangle_B + e^{i\varphi} |1\rangle_A |\psi_1\rangle_B}{\sqrt{2}}, \quad (4.3)$$

has been demonstrated using either single rail [109, 110] or polarization [111] DV encoding (part A). This enables the connection of networks using different kinds of encodings [112]. However, for guided-wave implementations, single rail and polarization DV qubits are sensitive to optical losses and polarization dispersion, respectively, therefore pushing hybrid quantum information protocols towards real world implementations in

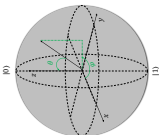
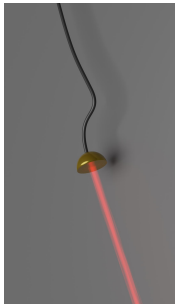
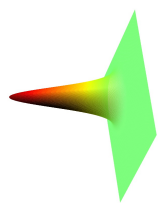
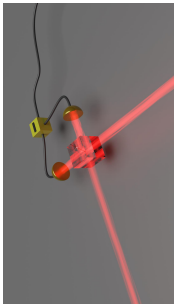
Encoding	Information carrier	Representation	Measurement	Main advantage	Main drawback
DV	qubit: $ \psi\rangle = c_0 0\rangle + c_1 1\rangle$	Bloch sphere 	Photon counting 	robust against losses	Probabilistic production
CV	qumode: $ \psi\rangle = \int \psi(x) x\rangle dx$	Wigner function 	Homodyne measurement 	Deterministic production (in some cases)	sensitive to losses

Table 4.1 – Main characteristics of DV and CV quantum information encoding.

fiber optic-based networks is a more challenging task. Recently, a hybrid entanglement generation scheme with time-bin encoding for the DV part of the two entangled modes was proposed [31] (see Figure 4.2), showing the robustness of this kind of hybrid states against losses on the DV part and hence, making it more suitable for real world implementations of hybrid quantum information protocols in fiber optic communication networks.

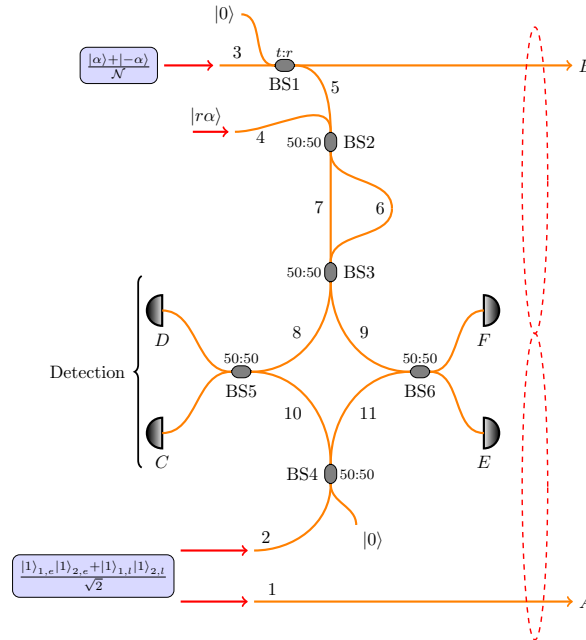


Figure 4.2 – Hybrid entanglement generation with time-bin DV encoding. Figure taken from [31] with permission.

4.2.1 Hybrid entanglement with time-bin DV encoding

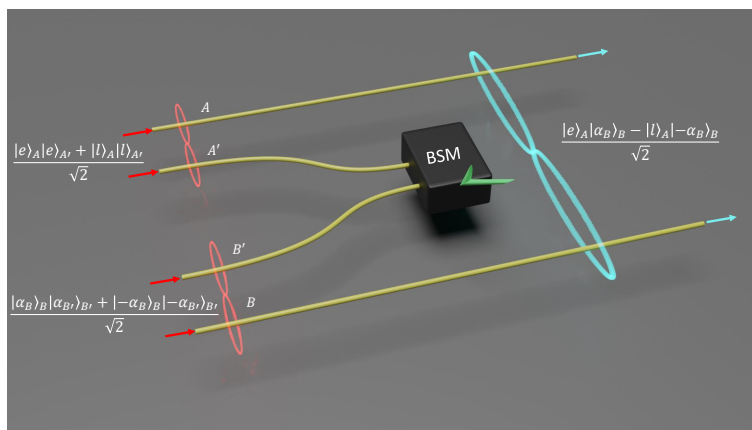


Figure 4.3 – A simplified representation of the time-bin based hybrid entanglement generation protocol proposed in [31].

A simplified representation of the proposed protocol in [31] for hybrid entanglement generation with time-bin encoding in the DV part is illustrated in Figure 4.3. It consists of an entanglement swapping operation [113] using two independent DV (A-A') and CV (B-B') entangled states. The DV state is a pair of time-bin entangled photons given by:

$$|\psi\rangle_{DV} = \frac{|e\rangle_A |e\rangle_{A'} + |l\rangle_A |l\rangle_{A'}}{\sqrt{2}}, \quad (4.4)$$

whereas the CV state is a coherent state-based entangled state:

$$|\psi\rangle_{CV} = \frac{|\alpha_B\rangle_B |\alpha_{B'}\rangle_{B'} + |-\alpha_B\rangle_B |-\alpha_{B'}\rangle_{B'}}{\sqrt{2}}. \quad (4.5)$$

Performing a Bell-state measurement between the two modes A' and B' of the DV and CV entangled states, respectively, allows to herald a remote creation of an entanglement between the DV mode A and the CV mode B. The heralded state is then given by:

$$|\psi\rangle_H = \frac{|e\rangle_A |\alpha_B\rangle_B - |l\rangle_A |-\alpha_B\rangle_B}{\sqrt{2}}. \quad (4.6)$$

4.2.2 The DV and CV resources for time-bin based hybrid entanglement creation

In the previous paragraph, we presented the protocol proposed in [31] for the remote creation of a hybrid entangled state between a DV time-bin encoding and a CV coherent state-based encoding. For this purpose, the DV and CV entangled states given by Equation 4.4 and Equation 4.5 are used as input states for the entanglement swapping operation. These resource states can be produced as illustrated in Figure 4.4.

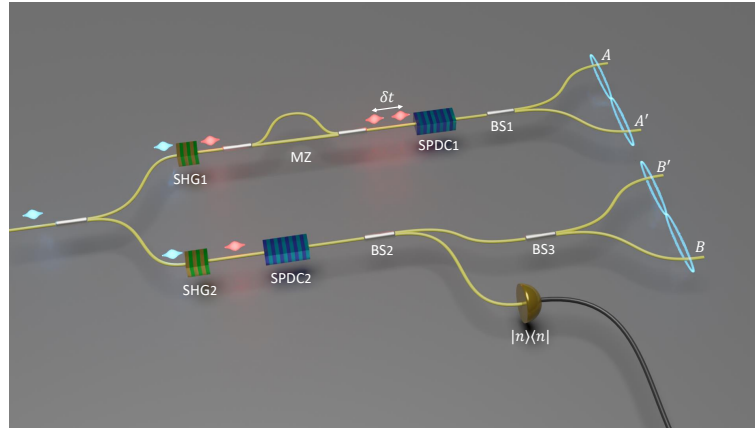


Figure 4.4 – Hybrid entanglement resources generation. SHG: second harmonic generation, SPDC: spontaneous parametric down conversion, MZ: Mach-Zehnder interferometer, BS: beam splitter. See text for description.

4.2.2.1 DV entangled state

The time-bin entangled state can be generated, in pulsed regime, by sending a pump beam to an unbalanced Mach-Zehnder interferometer (MZ), whose output gives two consecutive pulses temporally separated by δt . These two pulses are then used to pump a nonlinear crystal, generating pairs of photons via a non-degenerate SPDC process (SPDC₁). The generated photon pairs, delocalized in the "early" and "late" temporal modes, are then separated in two modes A and A' using BS₁ to produce the state expressed by Equation 4.4 [114].

4.2.2.2 CV entangled state

As shown in Figure 4.4, the CV entangled state can be produced as following, a first stage consists of generating a squeezed vacuum state via SPDC process (SPDC₂) and then subtracting photons using a low reflectivity BS (BS₂) and photoncounters to produce a Schrödinger cat-like state (see subsection 2.3.2 for the model and chapter 3 for experimental realization in CW regime). Once this is done, the Schrödinger cat-like state ($\sim |\alpha\rangle \pm |-\alpha\rangle$) is sent to a BS₃ with transmission and reflection coefficients t and r , respectively. The state at the output modes B and B' of BS₃ is then the one given by Equation 4.5 with $\alpha_B = t\alpha$ and $\alpha_{B'} = r\alpha$. Note that in both cases, the DV and CV entangled states generation is mainly based on SPDC process, whose pump is obtained via SHG stages, and so, the design of both sources is based on engineering this nonlinear interaction. For this purpose, both sources have to be identical and produce single-mode CV and DV states that are able to interfere efficiently at the Bell state measurement stage. In addition, these states will be produced in the picosecond pulsed regime. This particular operation regime is more adapted for guided-wave implementations in optical fiber-based quantum network, offering a robust synchronization of the different nodes in the network while avoiding undesired nonlinear effects induced by ultrashort pulses in optical fibers [115]. The design of these sources is detailed in the next section.

4.3 SPDC BASED SOURCE FOR DV AND CV ENTANGLED STATES

The interaction Hamiltonian introduced in chapter 2 to describe the SPDC process (see Equation 2.16) is actually given in the monomode case, where the signal and idler photons are produced in well defined modes. However, the generated signal and idler photons are actually spectrally broadband, which is the case also for the pump photons in pulsed regime, and the Hamiltonian given by Equation 2.16 is not sufficient anymore to describe the SPDC interaction. A more general formulation of this Hamiltonian is:

$$\hat{H}_{int} = H_0 \iint f(\omega_s, \omega_i) \hat{a}^\dagger(\omega_s) \hat{b}^\dagger(\omega_i) d\omega_s d\omega_i + h.c., \quad (4.7)$$

and the state at the output of the SPDC process is given by:

$$|\psi\rangle_{spdc} = e^{-\frac{i}{\hbar} \hat{H}_{int} t} |0\rangle. \quad (4.8)$$

Here, $\hat{a}^\dagger(\omega_s)$ and $\hat{b}^\dagger(\omega_i)$ are the signal and idler photon creation operators in the spectral mode ω_s and ω_i , respectively, and $f(\omega_s, \omega_i)$ is known as the *joint spectral amplitude* (JSA) [116] of the signal-idler photon pairs. This function, characterizing the spectral properties of the SPDC output, is actually determined by the pump field and the optical properties of the second order nonlinear crystal. It is given by:

$$f(\omega_s, \omega_i) = \tilde{E}_p(\omega_s + \omega_i)\Phi(\omega_s, \omega_i), \quad (4.9)$$

where $\tilde{E}_p(\omega_s + \omega_i)$ is the spectral envelop of the pump field and $\Phi(\omega_s, \omega_i)$ is the phase-matching function, given by:

$$\Phi(\omega_s, \omega_i) = \text{sinc}\left(\frac{\Delta k(\omega_s, \omega_i)L_{spdc}}{2}\right). \quad (4.10)$$

Here, L_{spdc} is the length of the nonlinear crystal and $\Delta k(\omega_s, \omega_i)$ is the wave-vector mismatch, given in the quasi-phasematching case by [117]:

$$\Delta k(\omega_s, \omega_i) = k_p(\omega_p) - k_s(\omega_s) - k_i(\omega_i) \pm \frac{2\pi}{\Lambda}, \quad (4.11)$$

with Λ being the poling period of the nonlinear crystal, which allows to control the central conversion frequencies ω_s^0 and ω_i^0 . For simplicity, we will consider a single spatial mode, which is the case in guided-wave approach. The JSA function $f(\omega_s, \omega_i)$ can be decomposed using two sets of spectral modes $\{\psi_k(\omega_s)\}$ and $\{\phi_k(\omega_i)\}$ as:

$$i\frac{H_0 t}{\hbar}f(\omega_s, \omega_i) = \sum_k \zeta_k \psi_k(\omega_s)\phi_k(\omega_i). \quad (4.12)$$

This is generally called the *Schmidt decomposition*, and the modes $\psi_k(\omega_s)$ and $\phi_k(\omega_i)$ are known as *Schmidt modes*. Doing so, the state at the output of the SPDC process (Equation 4.8) can be written as:

$$|\psi\rangle_{spdc} = e^{-\sum_k [\zeta_k \hat{A}_k^\dagger \hat{B}_k^\dagger - h.c.]} |0\rangle, \quad (4.13)$$

with \hat{A}_k^\dagger and \hat{B}_k^\dagger are the broadband signal and idler creation operators, respectively, given by:

$$\hat{A}_k^\dagger = \int \psi_k(\omega_s)\hat{a}^\dagger(\omega_s)d\omega_s, \quad \hat{B}_k^\dagger = \int \phi_k(\omega_i)\hat{b}^\dagger(\omega_i)d\omega_i. \quad (4.14)$$

The state given by Equation 4.13 can be seen as a multi-two-mode squeezed vacuum states with squeezing parameters ζ_k . This means that in the general case, the output of the SPDC process is a collection of two-mode squeezed states, each of them in a well defined spectral mode $\psi_k(\omega_s)$ for the signal photons and $\phi_k(\omega_i)$ for the idler ones, as represented in Figure 4.5.

The fact that the state is spectrally multimode is actually a source of imperfection in our case since photons from the DV and CV parts have to interfere for performing the entanglement swapping, and thus, must have the same spectro-temporal mode. In addition, the multimode aspect of the SPDC output affects the quality of the produced states used as resources for hybrid entanglement generation. To illustrate this, let us for example take the case of CV resource state, where the SPDC output should be a

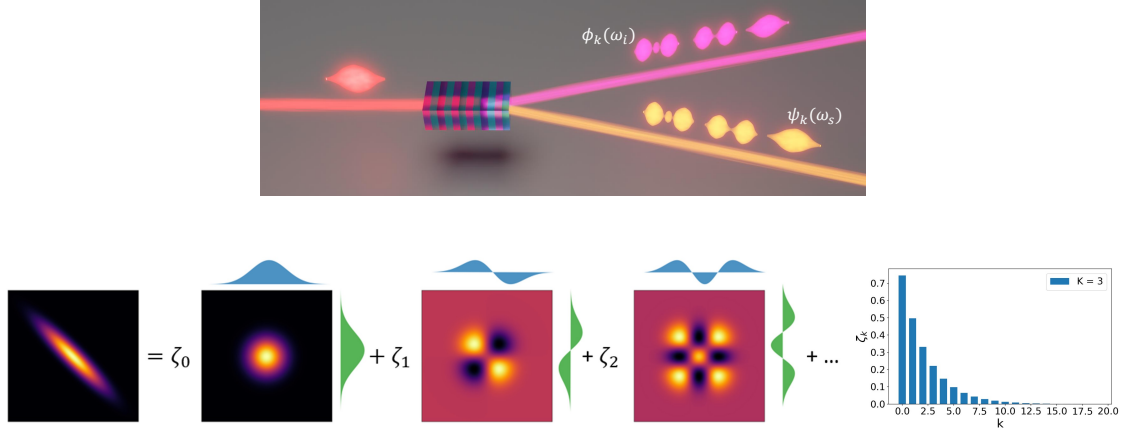


Figure 4.5 – *Top*: spectro-temporal multimode state produced via SPDC process in the pulsed regime. *Bottom*: signal and idler spectral modes and the corresponding squeezing parameters ζ_k obtained via the Schmidt decomposition of the JSA function. For a Gaussian approximation of the JSA, the signal and idler spectral modes are given by the Hermite-Gaussian polynomials.

squeezed vacuum state in order to produce the Schrödinger cat-like state. In this case, making the signal and idler photons indistinguishable ($\hat{A}_k = \hat{B}_k$) leads to the following expression of the SPDC output state:

$$|\psi\rangle_{spdc} = e^{-\sum_k (\zeta_k \hat{A}_k^{\dagger 2} - \zeta_k^* \hat{A}_k^2)} |0\rangle, \quad (4.15)$$

which is a multimode squeezed vacuum state (several spectral modes $\psi_k(\omega)$ squeezed simultaneously with a squeezing parameter $2\zeta_k$). As we will see in [chapter 5](#), the quality of the produced Schrödinger cat-like state decreases with the increase of the number of the squeezed modes, generally quantified using the parameter K defined as:

$$K = \frac{(\sum_k \zeta_k^2)^2}{\sum_k \zeta_k^4}, \quad (4.16)$$

and called *the Schmidt number* [118] ($K = 1$ in the single-mode case and $K > 1$ otherwise). The decreased quality of the produced CV state is related to the fact that the heralding photons can be subtracted from an arbitrary spectral mode $\psi_k(\omega)$, which leads to heralding a statistical mixture of Schrödinger cat-like states in different spectro-temporal modes.

4.3.1 JSA shaping for quasi-single-mode DV and CV state production

In the frequency degenerate case, the wave-vectors $k_p(\omega_p)$, $k_s(\omega_s)$ and $k_i(\omega_i)$, corresponding to the pump, signal and idler beams respectively can be expanded in terms of Taylor series around the central frequencies $\omega_s^0 = \omega_i^0 = \omega_0$ and $\omega_p^0 = 2\omega_0$ as:

$$\begin{aligned}
k_p(\omega_p) &\approx k_p(2\omega_0) + \beta_p(\omega_p - 2\omega_0), \\
k_s(\omega_s) &\approx k_s(\omega_0) + \beta_s(\omega_s - \omega_0), \\
k_i(\omega_i) &\approx k_i(\omega_0) + \beta_i(\omega_i - \omega_0),
\end{aligned} \tag{4.17}$$

where:

$$\beta_x = \left. \frac{\partial k_x(\omega_x)}{\partial \omega_x} \right|_{\omega_x^0}, \tag{4.18}$$

is the inverse of the group velocity of the pump ($x = p$), the signal ($x = s$) and the idler ($x = i$) beams at frequencies $\omega_p^0 = 2\omega_0$, $\omega_s^0 = \omega_0$ and $\omega_i^0 = \omega_0$, respectively. Here, we restricted the Taylor expansion to the first order since, in our case, we operate in the picosecond pulsed regime (few nm of bandwidths) where the second order dispersion is negligible. Knowing that $k_p(2\omega_0) - k_s(\omega_0) - k_i(\omega_0) \pm 2\pi/\Lambda = 0$, and putting $\omega_p = \omega_s + \omega_i$ (energy conservation condition), the wave-vector mismatch given by [Equation 4.11](#) can be written as:

$$\Delta k(\omega_s, \omega_i) = (\beta_p - \beta_s)(\omega_s - \omega_0) + (\beta_p - \beta_i)(\omega_i - \omega_0). \tag{4.19}$$

In order to obtain a quasi-single-mode SPDC output state for both the DV and CV resources, three conditions must be fulfilled:

- a) The JSA function $f(\omega_s, \omega_i)$ must be symmetric with respect to the signal and idler frequencies ($f(\omega_s, \omega_i) = f(\omega_i, \omega_s)$) to obtain spectrally indistinguishable signal and idler photons ($\psi_k(\omega) = \phi_k(\omega)$) necessary for squeezed vacuum state generation [119].
- b) The number of excited spectral modes must be minimized to obtain high quality CV and DV resource states that are able to interfere at the entanglement swapping step.
- c) To be able to spatially separate the signal and idler photons for the DV time-bin entangled photon pairs generation .

The pump spectral envelop contribution $\tilde{E}_p(\omega_s + \omega_i)$ in the JSA expression given by [Equation 4.9](#) fulfills the first condition, and so, the symmetry aspect of the JSA is determined by the phasematching function $\Phi(\omega_s, \omega_i)$. A symmetric JSA function can then be obtained in two cases: a symmetric wave-vector mismatch $\Delta k(\omega_s, \omega_i) = \Delta k(\omega_i, \omega_s)$ and an antisymmetric one $\Delta k(\omega_s, \omega_i) = -\Delta k(\omega_i, \omega_s)$. The symmetric wave-vector mismatch is obtained in the case of frequency degenerate type-0 and type-I SPDC process where the signal and idler photons, polarized in the same direction, have the same group velocity $\beta_s = \beta_i$. However, in this case, both the pump contribution $\tilde{E}_p(\omega_s + \omega_i)$ and the phasematching contribution $\Phi(\omega_s, \omega_i)$ are functions of $\omega_s + \omega_i$, and so, aligned along the $\omega_i = -\omega_s$ direction in the 2-D frequency space as shown in [Figure 4.6-Top](#), which gives a highly multimode SPDC output state, not suitable in our case.

For an antisymmetric wave-vector mismatch, the relation $\Delta k(\omega_s, \omega_i) = -\Delta k(\omega_i, \omega_s)$ applied to the expression given by [Equation 4.19](#) leads to the following condition:

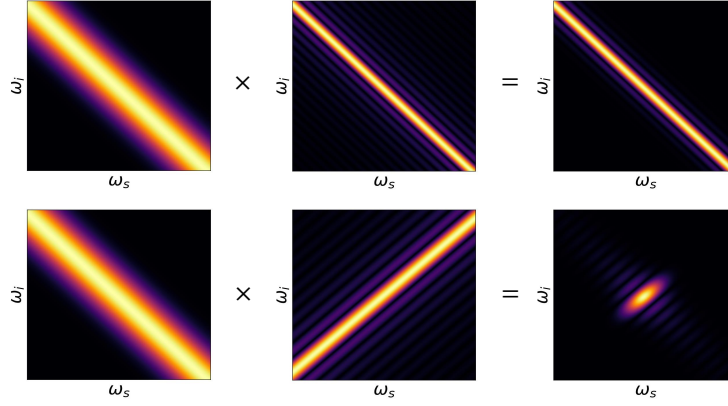


Figure 4.6 – Pump and phasematching contributions for frequency degenerate type-0 and type-I (*top*) and type-II (*bottom*) SPDC process.

$$\beta_p = \frac{\beta_s + \beta_i}{2}. \tag{4.20}$$

In this case, the wave-vector mismatch is given by:

$$\Delta k(\omega_s, \omega_i) = \frac{\beta_i - \beta_s}{2}(\omega_s - \omega_i), \tag{4.21}$$

and the phasematching contribution $\Phi(\omega_s, \omega_i)$ is a function of $\omega_s - \omega_i$, which is aligned along the $\omega_i = \omega_s$ axis in the 2-D frequency space as shown in [Figure 4.6-Bottom](#). This configuration can be obtained for a type-II SPDC process in which, the signal and idler photons are orthogonally polarized leading to different group velocities ($\beta_s \neq \beta_i$). Moreover, type-II interaction allows to spatially separate the signal and idler photons, hence fulfilling the condition c). In this configuration, a proper choice of the nonlinear crystal properties allows to minimize the number of excited modes while maintaining the spectral indistinguishability of the signal and idler photons, as detailed in the next subsection.

4.3.2 SHG and SPDC source design

As mentioned before, the JSA function must be shaped to obtain a quasi-single-mode SPDC output for high quality DV and CV states generation as well as hybrid entanglement creation. To do so, we have principally access to three different parameters:

- The spectral width of the pump pulse, which depends on the fundamental laser pulse and the SHG nonlinear crystal.
- The dispersion properties (β_p , β_s and β_i) of the nonlinear crystal used for SPDC process.
- The phasematching bandwidth of the SPDC process, which depends on the length of the SPDC nonlinear crystal.

Table 4.2 graphically summarizes the effect of each mentioned parameter on the shape of the JSA function characterizing the SPDC process.

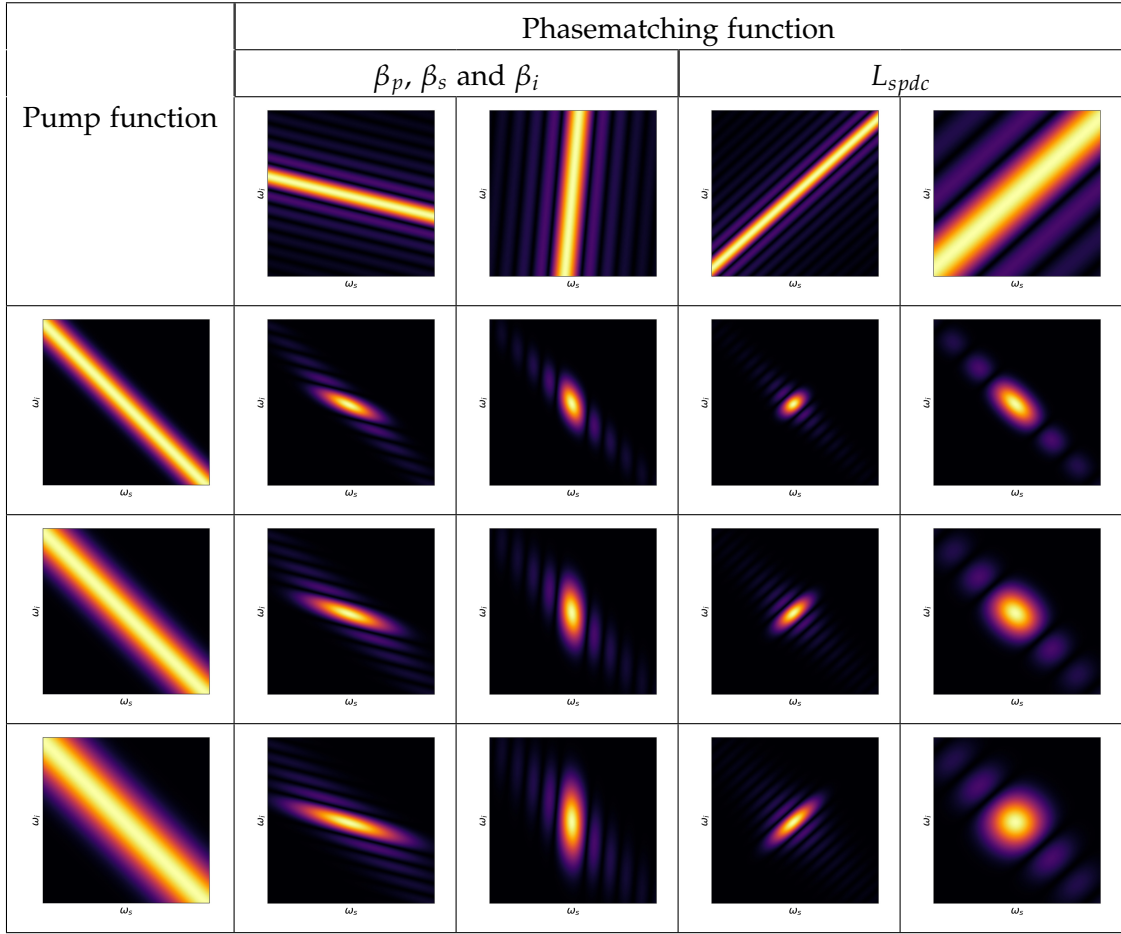


Table 4.2 – The effect of the pump spectral width, the SPDC crystal length and dispersion parameters on the shape of the JSA function. The dispersion parameters determine the direction along which the phasematching function is aligned. The length L_{spdc} of the SPDC crystal fixes the spectral width of the phasematching function. All parameters determine the final shape of the JSA function.

As we can see, the dispersion parameters β_p, β_s and β_i of the SPDC nonlinear crystal determine the direction along which the phasematching function is aligned. On the other hand, the final shape of the JSA function is related to the pump spectral width (determined by the fundamental laser pulses and the SHG crystal characteristics) and the phasematching bandwidth (determined by the SPDC crystal length). At first, the SPDC crystal must be chosen to obtain a phasematching function aligned along the axis $\omega_i = \omega_s$ (45°) in order to have a symmetric JSA function, and so, spectrally indistinguishable signal and idler photons ($\psi_k(\omega) = \phi_k(\omega)$). Then, the length L_{spdc} of the SPDC crystal must be fixed to minimize the exited spectral modes $\psi_k(\omega)$, or equivalently, to minimize the Schmidt number K . This length depends on the spectral properties of the fundamental laser pulses and the SHG stage.

4.3.2.1 Spectral shape of the pump pulses

The pump pulses for the SPDC process are obtained via SHG, and so, their spectral properties are determined by the fundamental telecom laser pulses, supposed to be Gaussian with a FWHM spectral width $\Delta\omega_l = 4 \ln(2)/\tau_l$ where τ_l is the pulse duration, and the SHG crystal, with a length L_{sh} . Let us consider a collinear type-0 SHG in pulsed regime where the pulses are propagating along the x axis of the nonlinear crystal. All the interacting fields in this case are polarized along the same direction, and so, a scalar notation is used here. We note $E_l(x, t)$ and $E_p(x, t)$ the electric fields at a position x and time t of the fundamental laser and the second harmonic (SH) pulses, respectively. In the rest of this chapter, we use both "SH" and "pump" nomination for the pulses obtained via SHG as they serve as pump pulses for the SPDC process. For a Gaussian shape of the fundamental laser pulse, the electric field at the input of the SHG crystal ($x = 0$) can be written as:

$$E_l(0, t) = E_0 f(t) \sin(\omega_0 t), \quad (4.22)$$

where $f(t)$ is the temporal Gaussian envelop, given by:

$$f(t) = e^{-\frac{2 \ln(2)}{\tau_l^2} t^2}. \quad (4.23)$$

In a plane wave basis, both the fundamental and the SH fields $E_l(x, t)$ and $E_p(x, t)$, respectively, can be expanded using the Fourier components $\tilde{E}_l(\omega)$ and $\tilde{E}_p(x, \omega)$ as following:

$$E_l(x, t) = \frac{1}{2} \int_{-\infty}^{\infty} \tilde{E}_l(\omega) e^{i[k(\omega)x - \omega t]} d\omega, \quad \tilde{E}_l(\omega) = \frac{1}{\pi} \int_{-\infty}^{\infty} E_l(0, t) e^{i\omega t} dt, \quad (4.24)$$

$$E_p(x, t) = \frac{1}{2} \int_{-\infty}^{\infty} \tilde{E}_p(x, \omega) e^{i[k(\omega)x - \omega t]} d\omega, \quad \tilde{E}_p(x, \omega) = \frac{1}{\pi} e^{-ik(\omega)x} \int_{-\infty}^{\infty} E_p(x, t) e^{i\omega t} dt, \quad (4.25)$$

Here, we assume that the fundamental laser field is undepleted, and so, the Fourier components $\tilde{E}_l(\omega)$ are considered as independent of x [120]. The spectral shape of the SH field at the output of the SHG crystal can be approximated as [120]:

$$\tilde{E}_p(L_{sh}, \omega) \approx \frac{ik_{shg}^p \chi_{eff} L_{sh}}{2(n_{shg}^p)^2} e^{i(\beta_{shg}^l - \beta_{shg}^p)(\omega - 2\omega_0) \frac{L_{sh}}{2}} \text{sinc} \left(\frac{(\beta_{shg}^l - \beta_{shg}^p)(\omega - 2\omega_0) L_{sh}}{2} \right) G(\omega)|_{\omega > 0}, \quad (4.26)$$

where χ_{eff} is the effective nonlinear susceptibility, $k_{shg}^p = k_{shg}(2\omega_0)$, n_{shg}^p , and $\beta_{shg}^p = \frac{dk_{shg}(\omega)}{d\omega}|_{2\omega_0}$ are the wave-vector, the refractive index and the inverse of the group velocity, respectively, at the SH central frequency $2\omega_0$, $\beta_{shg}^l = \frac{dk_{shg}(\omega)}{d\omega}|_{\omega_0}$ is the inverse of the group velocity at the fundamental pulse central frequency ω_0 , in the SHG nonlinear crystal and $G(\omega)$ depends on the fundamental laser field as:

$$G(\omega) = (\tilde{E}_l * \tilde{E}_l)(\omega) = \int_{-\infty}^{\infty} \tilde{E}_l(\omega - \omega') \tilde{E}_l(\omega') d\omega' = -\frac{E_0^2 \tau_l \sqrt{2\pi}}{8\pi^2 \sqrt{\ln(2)}} e^{-\frac{\ln(2)}{\Delta\omega_l^2} (\omega - 2\omega_0)^2}. \quad (4.27)$$

The *sinc* function in Equation 4.26 can be approximated by a Gaussian one as [121]:

$$\text{sinc}(x) \approx e^{-\gamma x^2}, \quad (4.28)$$

with $\gamma = 0.193$. By doing so, and taking into account the expression given by Equation 4.27, the spectral shape of the SH pulse can be written as:

$$\tilde{E}_p(L_{sh}, \omega) \propto e^{-\left[\gamma \frac{(\beta_{shg}^l - \beta_{shg}^p)^2 L_{sh}^2}{4} + \frac{\ln(2)}{\Delta\omega_l^2}\right] (\omega - 2\omega_0)^2} e^{i(\beta_{shg}^l - \beta_{shg}^p)(\omega - 2\omega_0) \frac{L_{sh}}{2}}, \quad (4.29)$$

giving a FWHM spectral width of:

$$\Delta\omega_p = \frac{2\sqrt{2\ln(2)}\Delta\omega_l}{\sqrt{4\ln(2) + \gamma(\beta_{shg}^l - \beta_{shg}^p)^2 L_{sh}^2 \Delta\omega_l^2}}, \quad (4.30)$$

or equivalently:

$$\Delta\lambda_p = \frac{\lambda_0^2}{8\pi c} \Delta\omega_p = \frac{\sqrt{2\ln(2)}\lambda_0^2 \Delta\lambda_l}{4\sqrt{\lambda_0^4 \ln(2) + \gamma\pi^2 c^2 \Delta\lambda_l^2 (\beta_{shg}^l - \beta_{shg}^p)^2 L_{sh}^2}}. \quad (4.31)$$

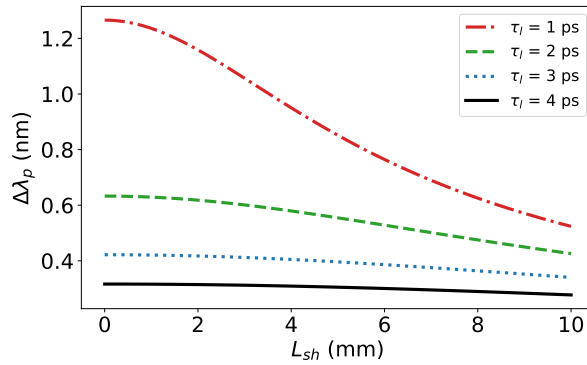


Figure 4.7 – The spectral width of the SH pulse as a function of the SHG nonlinear crystal length L_{sh} for different fundamental laser pulse durations. Here, the SHG crystal is an MgO:PPLN and the fundamental central wavelength is $\lambda_0 = 1560$ nm.

In Figure 4.7, we plot the spectral width of the SH pulse as a function of the SHG crystal length for different laser pulse durations in the case of a Magnesium-doped Periodically Poled Lithium Niobate (MgO:PPLN) crystal pumped at a fundamental central wavelength $\lambda_0 = 1560$ nm. For a short crystal, the SHG phasematching bandwidth is large (6 nm of phasematching bandwidth for a 1 mm long MgO:PPLN crystal) and the spectral width of the SH pulse is determined by the one of the fundamental laser pulses (function $G(\omega)$ in Equation 4.26). For an increased length L_{sh} , the spectral width of the SH pulses decreases due to the fact that in this case, the phasematching bandwidth of the SHG decreases with respect to the one of the fundamental laser pulses, and so, only

the spectral components of the fundamental pulse inside the acceptance window of the SHG phasematching are converted.

4.3.2.2 SPDC crystal choice

In our case, the JSA symmetry condition for Type-II SPDC interaction, given by Equation 4.20, must be satisfied at a telecom wavelength. In Figure 4.8, the constants β_p and $(\beta_s + \beta_i)/2$ are plotted for the Lithium Niobate (LN) and the Potassium Titanyl Phosphate (KTP) crystals as functions of the central wavelength λ_0 of the output of a frequency degenerate SPDC process, using the Sellmeier formulas given in [122] for the LN and in [123] for the KTP crystals.

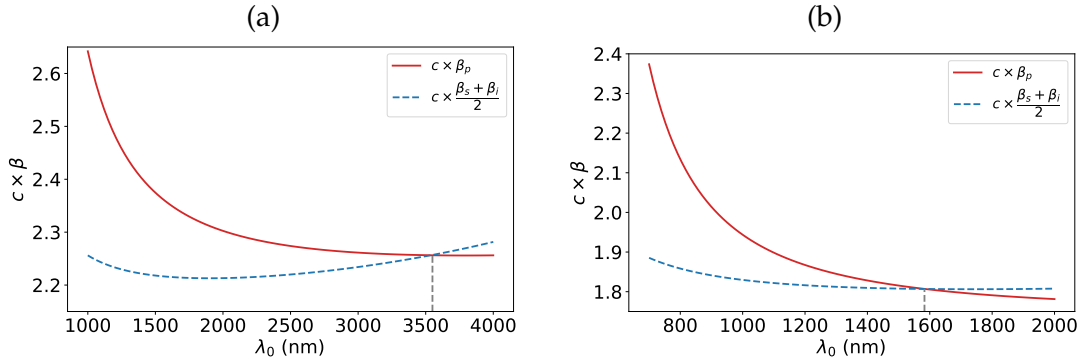


Figure 4.8 – $c \times \beta_p$ (solid red line) and $c \times (\beta_s + \beta_i)/2$ (blue dashed line) as functions of the central wavelength λ_0 of the down converted light via frequency degenerate SPDC process for LN (a) and KTP (b) crystals at a temperature $T = 20^\circ\text{C}$.

As it can be seen, for the LN crystal, this symmetry condition is satisfied around $\lambda = 3550\text{ nm}$, far from the telecom wavelength whereas it can be fulfilled at a telecom wavelength using a KTP crystal. Therefore, this latter is more adapted for the generation of spectrally indistinguishable signal and idler photons at a telecom wavelength.

4.3.2.3 SPDC crystal length

Once SPDC crystal is chosen (KTP), its length L_{spdc} should now be fixed to minimize the number of excited modes at the output of the SPDC process. Ideally, for a perfect single-mode output state, only one spectral mode $\psi_n(\omega)$ is excited ($\zeta_k = 0 \forall k \neq n$ in Equation 4.12) and the JSA function can be factorized, in the symmetric case, as:

$$f(\omega_s, \omega_i) \propto \psi_n(\omega_s) \times \psi_n(\omega_i). \quad (4.32)$$

To choose the length L_{spdc} minimizing the excited spectral modes, we adopt the Gaussian approximation given by Equation 4.28 for the phasematching function $\Phi(\omega_s, \omega_i)$:

$$\Phi(\omega_s, \omega_i) \approx e^{-\gamma \frac{\Delta k^2(\omega_s, \omega_i) L_{spdc}^2}{4}}, \quad (4.33)$$

where $\Delta k(\omega_s, \omega_i)$ is given by Equation 4.19. For a Gaussian approximation of the pump spectral envelop (see Equation 4.29), the JSA function $f(\omega_s, \omega_i)$ can be approximated by:

$$f(\omega_s, \omega_i) \approx e^{-\frac{2\ln(2)}{\Delta\omega_p^2}(\omega_s + \omega_i - 2\omega_0)^2 - \gamma \frac{[(\beta_p - \beta_s)(\omega_s - \omega_0) + (\beta_p - \beta_i)(\omega_i - \omega_0)]^2 L_{spdc}^2}{4}} e^{i(\beta_{shg}^l - \beta_{shg}^p)(\omega_s + \omega_i - 2\omega_0) \frac{L_{sh}}{2}}, \quad (4.34)$$

with $\Delta\omega_p$ given by Equation 4.30. To obtain a factorizable JSA function, the coefficient $c_{s,i}$ that couples the frequencies ω_s and ω_i in the expression given by Equation 4.34 must be null. This coefficient is given by:

$$c_{s,i} = \frac{4\ln(2)}{\Delta\omega_p^2} + \gamma \frac{(\beta_p - \beta_s)(\beta_p - \beta_i)L_{spdc}^2}{2}. \quad (4.35)$$

Imposing $c_{s,i} = 0$ leads to the following condition:

$$L_{spdc} = \frac{\lambda_0^2}{4\pi c \Delta\lambda_p} \sqrt{\frac{2\ln(2)}{\gamma(\beta_p - \beta_s)(\beta_i - \beta_p)}}, \quad (4.36)$$

which gives the optimal SPDC crystal length for which the JSA function $f(\omega_s, \omega_i)$ is factorizable. in Figure 4.9, we plot the optimal length of the KTP crystal, L_{spdc} , as a function of the spectral width of the fundamental laser pulses for different SHG crystal lengths (MgO:PPLN).

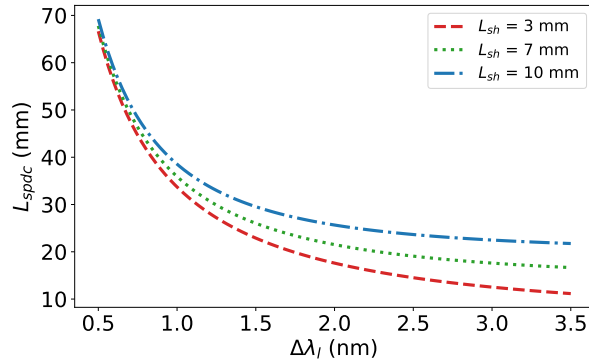


Figure 4.9 – The optimal length L_{spdc} of the SPDC crystal (KTP) to obtain a factorizable JSA function in the Gaussian approximation as a function of the spectral width $\Delta\lambda_l$ of the fundamental laser pulses for different length L_{sh} of the SHG crystal (MgO:PPLN).

Changing the spectral width of the fundamental laser pulses and the length of the SHG crystal leads to a changed spectral width of the pump pulses, and so, to obtain a factorizable JSA function, necessary for single-mode state generation, the length of the SPDC crystal must be adapted. For a symmetric JSA function (pump function aligned along the -45° direction and phasematching function along the 45° direction in the frequency space), this optimal length L_{spdc} is the one for which the spectral width of the phasematching function matches the one of the pump function. It is important to note that both the pump and the phasematching functions were approximated by Gaussian functions, and in this case, the JSA function can be factorized for the optimal chosen parameters. However, by considering the exact *sinc* function for the phasematching, the JSA function cannot be factorized under any configuration (for a periodically poled SPDC crystal), and so, a perfect single-mode state at the output of the SPDC is not

reachable. In this case, the optimal length given by Equation 4.36 and plotted in Figure 4.9 minimize the Schmidt number K of the SPDC output state. In our case, the spectral width of the fundamental laser pulses is around $\Delta\lambda_l = 2\text{ nm}$ (can be slightly changed), and we obtain for a 5 mm SHG crystal (MgO:PPLN) an optimal KTP length of $L_{spdc} \approx 19.3\text{ mm}$. Figure 4.10 shows the JSA function $f(\omega_s, \omega_i)$ for these parameters (a) and the corresponding Schmidt decomposition (b).

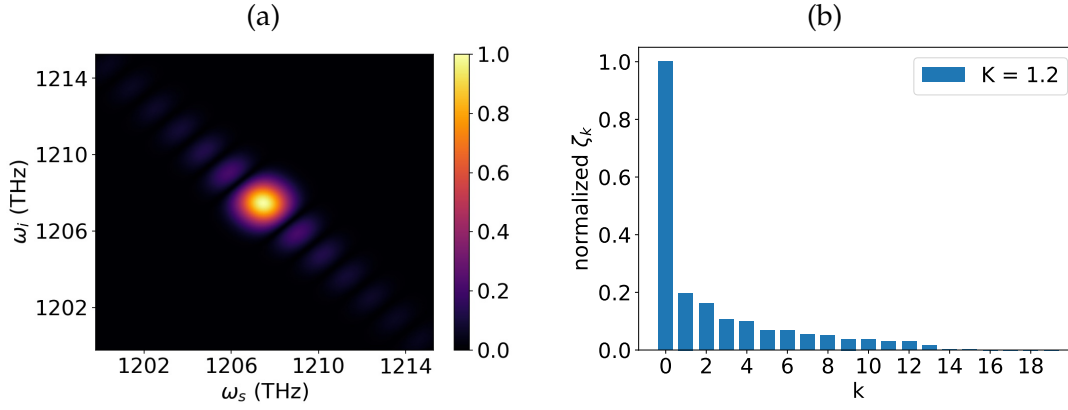


Figure 4.10 – JSA function (a) and the corresponding Schmidt decomposition (b) for a fundamental laser pulse spectral width $\Delta\lambda_l = 2\text{ nm}$, a 5 mm SHG crystal (MgO:PPLN) and a 19.3 mm SPDC crystal (KTP). The output central frequency is $\lambda_0 = 1560\text{ nm}$.

As it can be seen, the JSA function (a) obtained with the optimal parameters is almost circular shaped, and its Gaussian approximation is factorizable. However, due to the side lobes of the *sinc* phasematching function, the real JSA cannot be factorized, but the Schmidt number is minimized $K = 1.2$. It is actually possible to obtain a factorizable JSA with a Gaussian shaped phasematching function by engineering the poling of the SPDC crystal [124–126], which is out of the scope of this thesis.

Spectro-temporal mode matching with the LO

Another important parameter that must be taken into account is the spectro-temporal mode matching between the fundamental laser pulses (used as LO for CV state characterization via homodyne detection) and the main excited mode at the output of the SPDC process (with the highest squeezing parameter ζ_k). The first ingredient to produce the CV entangled state given by Equation 4.5 is a squeezed vacuum state, and in type-II SPDC process, this state can be obtained by applying a BS transformation to the signal and idler photons:

$$\hat{A}_k, \hat{B}_k \longrightarrow \frac{1}{\sqrt{2}} (\hat{A}_k \pm \hat{B}_k), \tag{4.37}$$

which can easily be done using a simple PBS. The mode matching c_0 between the fundamental laser and the main squeezed modes can then be expressed as:

$$c_0 = \frac{|\int \tilde{E}_l(\omega) \varphi_0^*(\omega) d\omega|}{\sqrt{\int |\tilde{E}_l(\omega)|^2 d\omega \int |\varphi_0(\omega)|^2 d\omega}}, \tag{4.38}$$

where $\varphi_0(\omega)$ is the main squeezed mode, given by:

$$\varphi_0(\omega) = \frac{1}{\sqrt{2}} (\psi_0(\omega) + \phi_0(\omega)). \quad (4.39)$$

In [Figure 4.11](#), the optimal length L_{spdc} of the SPDC crystal (KTP) and the mode matching c_0 are plotted as functions of the MgO:PPLN SHG crystal length L_{sh} for a fundamental laser spectral width $\Delta\lambda_l = 1.5$ nm (solid curve) and $\Delta\lambda_l = 2$ nm (dashed curve).

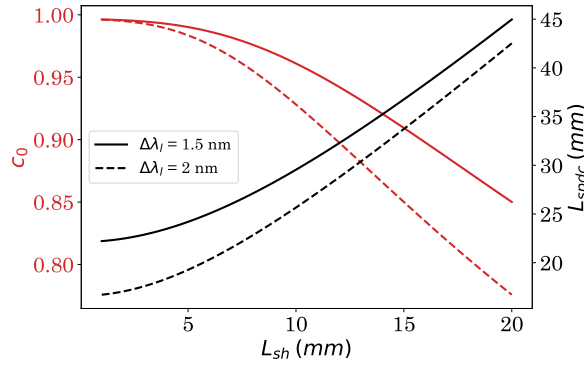


Figure 4.11 – The optimal length L_{spdc} of the KTP crystal (black) and the mode matching between the laser pulses (LO) and the main squeezed vacuum mode (red) as functions of the length L_{sh} of the MgO:PPLN SHG crystal for $\Delta\lambda_l = 1.5$ nm (solid) and $\Delta\lambda_l = 2$ nm (dashed).

At a given SHG crystal length L_{sh} , the lower the spectral width of the fundamental laser pulses, the better the mode matching c_0 . Moreover, this mode matching increases with the decrease of the SHG crystal length. This can be interpreted as following: for a short SHG crystal (and/or a narrowband fundamental laser pulses), the SHG phasematching bandwidth is broader than the one of the fundamental laser, and so, the spectral properties of the pump (SH) pulses are determined essentially by the fundamental laser spectral width. Consequently, it is better to use a short SHG crystal in order to:

- Increase the mode matching between the LO and the main squeezed vacuum mode.
- Reach the length required for quasi-single-mode SPDC output state (long KTP waveguides are not commercially available).
- Reduce the walk-off effect due to the group velocity mismatch inside the SHG crystal and maintain a gaussian temporal envelop of the SH (pump) pulses, as detailed in [Appendix E](#).

As a numerical illustration, [Table 4.3](#) gives four examples of optimal KTP crystal length L_{spdc} and mode matching c_0 for two values of the spectral width $\Delta\lambda_l$ of the fundamental laser pulses and two values of the length L_{sh} of the SHG crystal (MgO:PPLN).

In our case, we work with picosecond fundamental laser pulses with a tunable spectral width, typically in the range between $\Delta\lambda_l = 1$ nm and $\Delta\lambda_l = 2$ nm. The lengths

	$L_{sh} = 3 \text{ mm}$	$L_{sh} = 5 \text{ mm}$
$\Delta\lambda_l = 1.5 \text{ nm}$	$c_0 = 99.46\%$ $L_{spdc} = 22.9 \text{ mm}$	$c_0 = 99\%$ $L_{spdc} = 24.2 \text{ mm}$
$\Delta\lambda_l = 2 \text{ nm}$	$c_0 = 99.28\%$ $L_{spdc} = 17.6 \text{ mm}$	$c_0 = 98.36\%$ $L_{spdc} = 19.3 \text{ mm}$

Table 4.3 – Numerical examples of the optimal KTP crystal length L_{spdc} and the mode matching c_0 for different values of the spectral width of the fundamental laser pulses $\Delta\lambda_l$ and the length of the SHG crystal L_{sh} .

of the SHG crystal (MgO:PPLN) and the SPDC crystal (KTP) are then chosen to be $L_{sh} = 3 \text{ mm}$ and $L_{spdc} = 20 \text{ mm}$, respectively.

4.4 SPDC SOURCE CHARACTERIZATION

In the previous section, we determined the different optimal experimental parameters allowing to produce quasi-single-mode CV and DV states in pulsed regime at a telecom wavelength, needed for the hybrid entanglement generation using time-bin DV encoding via the entanglement swapping operation (see section 4.2). In this section, we present the different experimental characterisation results of the designed SPDC based source. The experimental setup is shown in Figure 4.12.

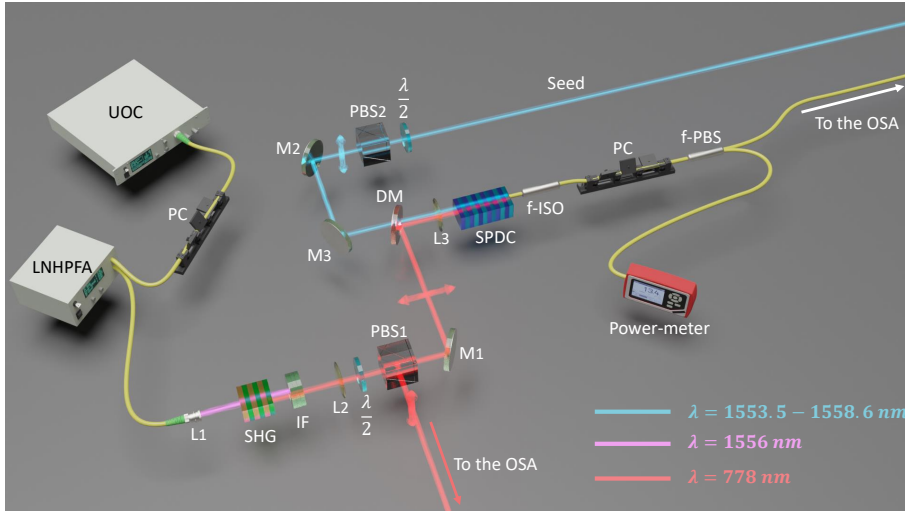


Figure 4.12 – Experimental setup for the SPDC-based source characterization. See text for details. UOC: ultrafast optical clock, LNHPFA: low noise high power fiber amplifier, SHG: second harmonic generation, IF: interferential filter, L₁₋₃: lenses, PBS₁₋₂: polarization beam splitters, M₁₋₃: mirrors, DM: dichroic mirror, SPDC: spontaneous parametric down conversion, f-ISO: fiber isolator, PC: polarization controller, f-PBS: fiber polarization beam splitter, OSA: optical spectrum analyser.

4.4.1 Fundamental pulsed laser source

The fundamental laser source, is an actively-mode-locked erbium-doped fiber laser (UOC from PriTel, Inc.) working at telecom wavelengths (1530 nm – 1565 nm) with a repetition rate $F_{rep} = 1$ GHz. Losses inside the fiber ring cavity are periodically modulated using an LN based Mach-Zehnder modulator driven at an RF frequency corresponding to the working repetition rate of the source. The fundamental free spectral range (FSR) of the fiber cavity is around 16 MHz, and so, any group of cavity modes with a frequency separation corresponding to the working repetition rate can lase, causing an instability of the laser output. In order to avoid this, an angle-tuned etalon filter is used to select the lasing cavity modes at the wanted repetition frequency. In addition, the fiber cavity is housed inside a temperature-controlled chamber and its length is actively controlled in order to stabilise the lasing cavity modes. Figure 4.13 shows the spectrum of the UOC output for a given locking configuration.

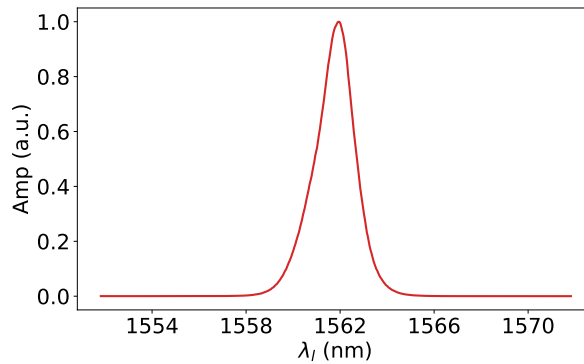


Figure 4.13 – Output spectrum of the laser source.

We note that the spectral width of the laser output can be tuned by changing the etalon filter inside the cavity and/or the pump current (laser diode pump at 976 nm). In Figure 4.14, we plot the FWHM spectral width of the laser output as a function of the pump current for a 2 nm (a) and 8 nm (b) etalon filter bandwidth.

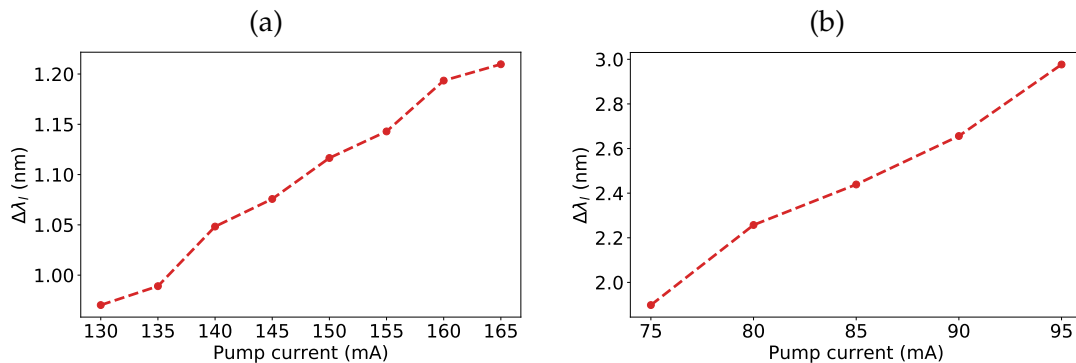


Figure 4.14 – The spectral width of the laser output as a function of the laser diode pump current for a 2 nm (a) and a 8 nm (b) etalon filter bandwidth.

As it can be seen, for a 8 nm etalon filter bandwidth, the spectral width of the laser output can be tuned from $\Delta\lambda_l = 1.9$ nm to $\Delta\lambda_l = 2.9$ nm for a pump current varying between 75 mA and 95 mA, which is useful to choose the appropriate spectral width allowing to minimize the excited modes in the SPDC process.

4.4.2 SHG stage

The fundamental laser pulses are polarization controlled and then amplified using a low-noise high power optical fiber amplifier (LNHPFA from PriTel, Inc.). Inside the LNHPFA, the pulses are first pre-amplified and then amplified with a second amplification stage. A band-pass filter between the pre-amplification and the amplification stages allows to reduce the noise at the output of the amplifier. The amplified pulses are then focused inside the 3 mm long SHG crystal (MgO:PPLN from Covesion Ltd). To optimize the SHG process, the focusing condition $L_{sh}/(2Z_R) \approx 2.8$ must be satisfied [127], where $L_{sh} = 3$ mm is the length of the SHG crystal and Z_R is the Rayleigh length of the focused beam. To do so, a single lens L_1 with a focal length $f_1 = 11$ mm (C220TMD-C from Thorlabs) is sufficient.

At first, the temperature dependence of the SHG phasematching pumped at $\lambda_0 = 1550$ nm is characterized. This phasematching curve is plotted in Figure 4.15.

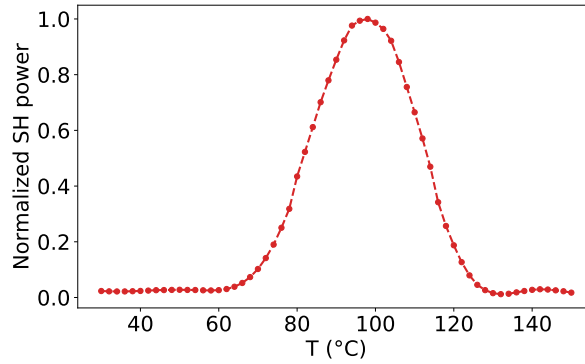


Figure 4.15 – The temperature dependence of SHG phasematching pumped at $\lambda_0 = 1550$ nm.

Then, by setting the temperature at $T = 98^\circ\text{C}$ (maximum of the phasematching curve), The efficiency $\eta_{SH} = P_{SH}/P_l$ of the SHG is characterized, where P_{SH} and P_l are the mean powers of the SH and the fundamental pulses, respectively. To do so, the pump current I_{preamp} of the pre-amplification stage is set to 500 mA and the one of the second amplification stage, I_{amp} , is tuned from 0.6 A to 5 A to change the power of the fundamental laser pulses. In Figure 4.16, the SHG efficiency η_{SH} is plotted as a function of the mean power of the fundamental laser pulses.

As expected, for $P_l < 560$ mW, the SHG efficiency η_{SH} is linear with respect to the power of the fundamental laser pulses P_l . However, for higher power of the fundamental pulses, this efficiency is no more linear and starts to decrease for an increased P_l . This is in fact related to a deformation of the amplified fundamental pulses spectrum inside the optical fibers due to self-phase-modulation effect [128] caused by high peak powers. To optimize both the spectrum and the efficiency, we first monitor the spectrum of the SH pulses, shown in Figure 4.17-(a), while changing the current I_{amp}

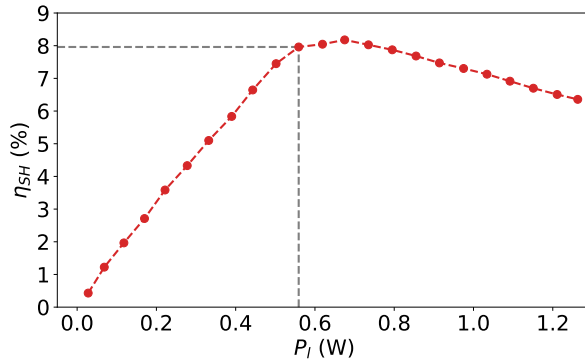


Figure 4.16 – The efficiency η_{SH} of the SHG as a function of the power P_l of fundamental laser pulses.

of the amplification stage for a fixed pre-amplification pump current $I_{preamp} = 100$ mA. As we can see, the maximum pump current allowing to maintain a non-deformed SH spectrum is identified to be $I_{amp} = 0.9$ A (Figure 4.17-(a)-red).

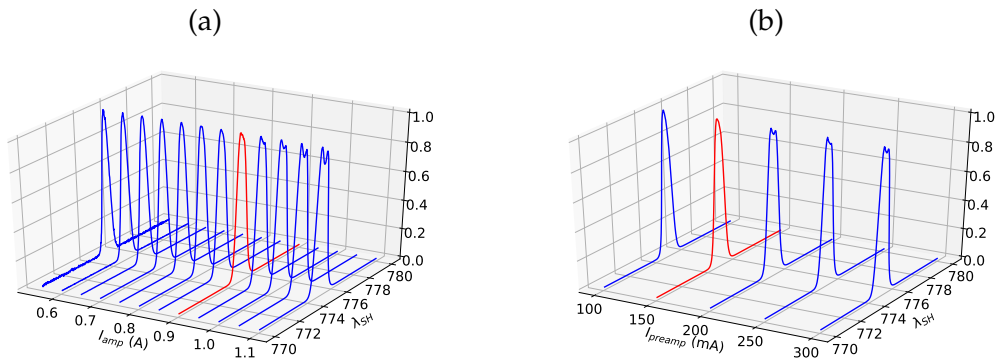


Figure 4.17 – (a): The obtained SH spectra for different amplification pump current I_{amp} and a fixed pre-amplification one $I_{preamp} = 100$ mA. (b): The obtained SH spectra for different pre-amplification pump current I_{preamp} and a fixed amplification one $I_{amp} = 0.9$ A.

After that, the pump current of the amplification stage is fixed at $I_{amp} = 0.9$ A, and the one of the pre-amplification stage is increased. The recorded spectra of the SH pulses are shown in Figure 4.17-(b). Then, the pre-amplification pump current is fixed at $I_{preamp} = 150$ mA allowing to maximize the efficiency of the SHG while maintaining a non-deformed spectrum of the SH pulses.

4.4.3 SPDC stage

The SPDC source is a type-II PPKTP waveguide from AdvR Inc. As detailed in section 4.3, its length is chosen to be $L_{spdc} = 20$ mm in order to minimize the number of excited modes, and so, produce high quality DV and CV states for hybrid entanglement generation. The PPKTP chip contains five groups of six waveguides each, with different waveguide widths. At first, all the waveguides are characterized via SHG

process using a telecom CW tunable laser pump to determine their central conversion wavelengths. The best identified waveguide, in terms of efficiency, is a one having a central conversion frequency of $\lambda_0 = 1556$ nm. Then, we proceed to the measurement of the corresponding joint spectral intensity $|f(\omega_s, \omega_i)|^2$ where $f(\omega_s, \omega_i)$ is given in Equation 4.9. To do so, we opt for a measurement in the stimulated regime for its simplicity and rapidity [129, 130], the corresponding experimental setup is depicted in Figure 4.12.

The laser is locked at $\lambda_0 = 1556$ nm, and the SHG temperature is set to $T = 140^\circ\text{C}$ (maximum phasematching for $\lambda_0 = 1556$ nm). After the SHG stage, the fundamental pulses are blocked using an interferential filter (IF) and the SH beam is collimated using the lens L2. A combination of a half wave-plate and a polarization beam splitter (PBS₁) allows to control the SH beam by sending a part of it (the reflected one by the PBS₁) to an optical spectrum analyser (OSA) to monitor the SH spectrum whereas the transmitted part (horizontally polarized) is sent to the PPKTP waveguide. At the input of the SPDC source, the SH pulses at $\lambda_{SH} = 778$ nm (pump) and a vertically polarized tunable telecom CW beam (seed) are combined using a dichroic mirror (DM) and then coupled to the PPKTP waveguide via a C220TMD-C lens (L₃). In this case, the idler photons are generated at the seed frequency ω_{seed} and the spectrum of the signal photons is given by the section of the JSI function corresponding to $\omega_i = \omega_{seed}$: $|f(\omega_s, \omega_{seed})|^2$. The JSI function can then be reconstructed by concatenating several signal spectra by changing the seed frequency ω_{seed} . To do so, the output of the PPKTP waveguide is collected using a micro-lensed fiber from OZ Optics (AMSTechnologies distributor) and the pump pulses are filtered using a fiber isolator (f-ISO). The remaining seed (with idler photons) and signal photons are separated using a polarization controller (PC) and a fiber PBS (f-PBS) where the signal photons are sent to an OSA whereas the seed is sent to a power-meter. The temperature of the PPKTP waveguide is stabilized at $T = 62.82^\circ\text{C}$ and 52 signal spectra are recorded for a seed going from $\lambda_{seed} = 1553.5$ nm to $\lambda_{seed} = 1558.6$ nm. The obtained JSI is shown in Figure 4.18-(a).

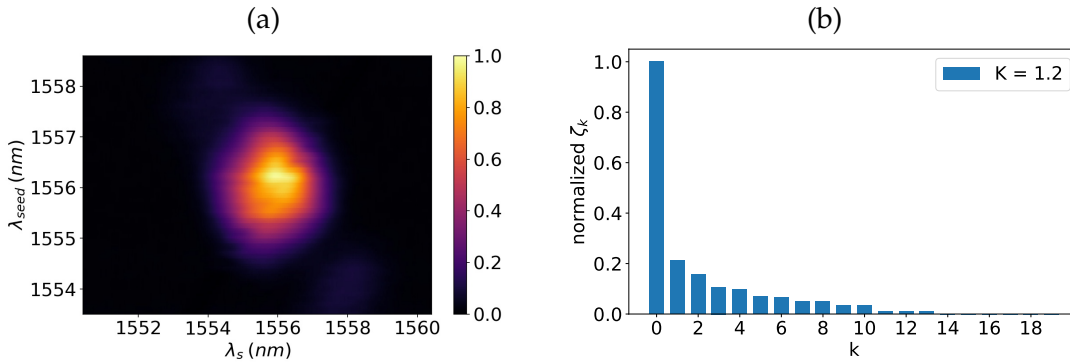


Figure 4.18 – (a) The measured JSI of the SPDC source in the stimulated regime. (b): The corresponding Schmidt decomposition gives a Schmidt number $K = 1.2$.

The obtained JSI is circular shaped (almost factorizable), in agreement with the numerical simulations in the previous section. Furthermore, the Schmidt decomposition, depicted in Figure 4.18-(b), shows a highly excited fundamental mode ($k = 0$) which represent 90% of the SPDC output, showing a Schmidt number of $K = 1.2$. This result

is in total agreement with the simulations presented in [section 4.3](#) and confirms the quasi-single-mode behaviour of our source.

4.5 CONCLUSION

In this chapter, we have presented the design and experimental characterization of an SPDC-based source for the generation of CV and DV entangled states in the picosecond pulsed regime at a telecom wavelength. These states will serve as resources for the creation of hybrid CV-DV entanglement with time-bin encoding in the DV part, which has been proven to be more adapted for guided-wave based implementations in optical fiber telecommunication networks. This source has to produce states in a well defined spectro-temporal mode for an efficient hybrid entanglement generation. We identified the optimal parameters allowing to obtain quasi-single-mode states at a telecom wavelength in the picosecond pulsed regime. The experimental characterization results are in perfect agreement with the target source performances, showing a quasi-single-mode behaviour with a Schmidt number $K = 1.2$.

However, as highlighted in this chapter, a perfect single-mode operation regime ($K = 1$) is not reachable with conventional SPDC sources with periodically poled nonlinear crystals. This limitation leads a reduced purity of the produced CV and DV states, and hence, affects the quality of the hybrid entangled state. We will see in the next chapter that it is possible to produce high purity quantum states even with a multimode resource.

Part III

QUANTUM STATE ENGINEERING WITH MULTIMODE
RESOURCES

NON-MODE-SELECTIVE PHOTON SUBTRACTION: A THEORETICAL STUDY IN THE MULTIMODE CASE

5.1	Photon subtraction operation applied to multimode quantum states . . .	112
5.1.1	Perfect mode-selective single-photon subtraction	112
5.1.2	Non-mode-selective single-photon subtraction	113
5.1.3	Supermode decomposition	115
5.1.4	Heralded single-photon subtracted state	117
5.2	Case study: heralded Schrödinger kitten state production	118
5.2.1	Wigner function of the heralded state in the multimode case . . .	120
5.3	Multimode-induced heralded state impurity	121
5.3.1	Quantification of the heralded state non-classicality	122
5.4	Heralded state with spectrally filtered heralding photons	123
5.4.1	Application to a practical experimental situation	126
5.5	Conclusion	127

As discussed in the previous chapters, single-photon subtraction from squeezed states is a very common way to produce key continuous-variable (CV) non-Gaussian resources, such as Schrödinger kitten- and Fock-states [61, 75], enabling a full exploitation of the CV approach in quantum information science and technologies. At the same time, the performances of this kind of operations are strongly affected by the properties of the protocol input state whose multimode features must be carefully mastered. As highlighted in the previous chapter, most of bulk and guided-wave realisations rely on input squeezed states produced by spontaneous parametric down conversion (SPDC), that, depending on the working conditions, can be multimode in the frequency domain [131, 132]. To comply with this situation, single-mode engineered SPDC sources [133] as well as mode-selective state manipulation [134, 135] have been studied and experimentally demonstrated. Nevertheless, the specific experimental conditions required for such operations remain difficult or inaccessible to many practical situations.

In this context, the work presented in this chapter offers a general and versatile theoretical framework able to describe single-photon subtraction in a highly multimode context and with no hypothesis on the nature, shape or number of involved modes [85]. Previous theoretical models have already treated the case of mode-selective photon-subtraction schemes [134, 136], whose practical implementation demands nonlinear optical stages [135, 137]. This work focuses, instead, on the very common experimental situation in which single-mode or mode-selective operations are not possible or practically unavailable.

In [section 5.1](#), we provide the general framework describing single-photon subtraction operation in the multimode case. In the rest of the chapter, we apply the obtained formalism to the case of Schrödinger kitten state generation. In [section 5.2](#), we give the explicit expression of the heralded state Wigner function, as it is measured by a homodyne detection, obtained via single-photon subtraction from a multimode squeezed vacuum state. In [section 5.3](#) and [section 5.4](#), different experimental configurations for both heralding and detection stages are discussed and compared. All numerical simulations refer to the manipulation of squeezing emitted in the C-band of classical telecommunication, compatible with future practical applications to fiber-based quantum communication networks. The chapter is finally concluded in [section 5.5](#).

5.1 PHOTON SUBTRACTION OPERATION APPLIED TO MULTIMODE QUANTUM STATES

As highlighted in the previous chapter, and following a very common strategy, the output of a multimode quantum optical source can be written as a tensor product of independent single mode states, each being described by a spectral mode $\psi_k(\omega)$ called supermode [[131](#), [138](#), [139](#)]. These supermodes $\{\psi_k(\omega)\}$ form an orthonormal basis ($\int \psi_k(\omega)\psi_l^*(\omega)d\omega = \delta_{k,l}$, $\delta_{k,l}$ being the Kronecker delta) and their associated bosonic operators $\{\hat{A}_k\}$ are:

$$\hat{A}_k = \int \psi_k^*(\omega) \hat{a}(\omega) d\omega, \quad (5.1)$$

where $\hat{a}(\omega)$ are the bosonic operators associated with the individual spectral components of the source output.

The multimode state, generically indicated as $|\psi\rangle$, undergoes the typical subtraction scheme shown in [Figure 5.1](#); it is sent towards a subtraction beam-splitter (BS) with reflection coefficient $r_s \ll 1$. The reflected beam goes towards the heralding path, while the transmitted one carries the heralded state. In experiments, photons in the heralding path are sent to a bucket single-photon detector (SPD), unable to distinguish light from different modes and whose detection signal heralds a successful photon subtraction and the preparation of a desired non-Gaussian state [[75](#)]. At the same time, the subtraction BS, a priori, acts in a similar way on all spectral components of $|\psi\rangle$ or, equivalently, on all supermodes $\{\psi_k(\omega)\}$. This makes it impossible to associate a photon detection event with a subtraction operation on a specific supermode, and can eventually lead to mixed heralded states [[121](#)]. To comply with such a situation, a certain mode selectivity on the heralding path is generally obtained by adding an optical frequency filter before the photon-counting detector [[75](#), [76](#), [121](#), [140](#)]. The filter action can be modelled as a BS: different scenarios can thus be considered based on the shape of the transmission coefficient of the filter BS.

5.1.1 Perfect mode-selective single-photon subtraction

[Figure 5.1](#)-(a) represents a conceptual scheme of mode-selective photon-subtraction. In this case, the filter is modelled as a mode-selective beam splitter, able to transmit

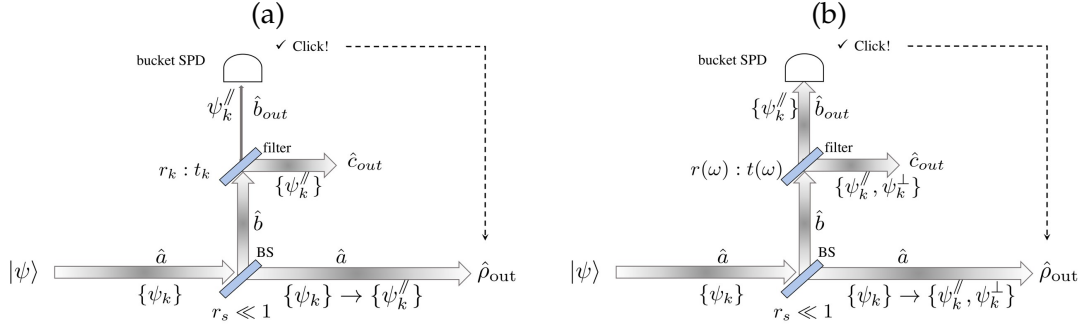


Figure 5.1 – Subtraction scheme applied to a multimode input state $|\psi\rangle$ in case of (a) mode-selective and (b) non mode-selective operations. The working supermode basis for each spatial mode is explicitly indicated in both cases. A hybrid Schrödinger/Heisenberg approach is adopted, as the operators do not evolve on the subtracting beam-splitter, but do evolve on the filter beam-splitter. Mode \hat{b}_{out} represents the spatial mode of the heralding photons downstream of the filter that are directed toward the single-photon detector (SPD). Mode \hat{c}_{out} represents photons that are rejected by the filter and thus disregarded. After the photon-counting operation, mode \hat{a} carries the heralded non-Gaussian state $\hat{\rho}_{out}$.

towards the bucket single-photon detector only one given detection mode $\psi_k''(\omega)$. Depending on the chosen mode, it is possible to manipulate the original multimode state in a controlled manner or even to entangle formerly independent supermodes $\{\psi_k(\omega)\}$ [135]. In particular, in the special case in which the detection mode matches one of the supermode envelopes (i.e. $\psi_k'' = \psi_k$), Schrödinger kitten or Fock states can be heralded. As already discussed, the theory underlying mode-selective operation was already the subject of different works [136, 137] and its treatment is beyond the scope of this chapter. At the same time, it is pertinent to observe that original methods and results reported in the following paragraphs can be adapted to the mode-selective case by considering a filter BS with discrete transmission coefficient t_k equal to zero for all modes excepted for a specific ψ_k'' .

5.1.2 Non-mode-selective single-photon subtraction

Experimentally, mode-selective single-photon subtractions require adapted non linear optical stages [135]. In the large majority of reported experimental works, standard (passive) optical filters are used in the heralding path [75]. In such a non-mode-selective operation, the filter can be modelled as a beam-splitter whose real transmission coefficient $t(\omega)$ depends on the optical frequency. No *a priori* hypothesis on the filter transmission profile is imposed.

In order to perform the mathematical derivation, a hybrid Schrödinger/Heisenberg approach is adopted [141]: the bosonic operators do not evolve on the subtracting beam-splitter, but do evolve on the filter beam-splitter in the heralding path (see Figure 5.1). Such a strategy allows introducing a global evolution operator, \hat{U} , that can be used to describe the state obtained when both the subtraction and filter beam-splitter are explicitly considered:

$$\hat{\mathcal{U}} = e^{\theta \int (\hat{a}^\dagger(\omega)\hat{b}(\omega) - \hat{a}(\omega)\hat{b}^\dagger(\omega)) d\omega} \approx \hat{1} + \theta \int \left(\hat{a}^\dagger(\omega)\hat{b}(\omega) - \hat{a}(\omega)\hat{b}^\dagger(\omega) \right) d\omega, \quad (5.2)$$

where $\sin \theta/2 = r_s \ll 1$ gives the reflection coefficient of the subtraction BS. Spatial modes are named as indicated in [Figure 5.1](#). The operator $\hat{\mathcal{U}}$ correctly encompasses all the spectral components of the field. In the previous expression, each operator $\hat{b}(\omega)$ undergoes the transformation due to the filtering stage and can be rewritten in terms of the bosonic operators $\hat{b}_{out}(\omega)$ and $\hat{c}_{out}(\omega)$ that describe the fields transmitted and reflected by the filter BS, respectively:

$$\hat{b}(\omega) = t(\omega)\hat{b}_{out}(\omega) + r(\omega)\hat{c}_{out}(\omega), \quad (5.3)$$

with $t(\omega)^2 + r(\omega)^2 = 1$. [Equation 5.2](#) can thus be written as:

$$\begin{aligned} \hat{\mathcal{U}} \approx \hat{1} + \theta \int d\omega \left(\hat{a}^\dagger(\omega)t(\omega)\hat{b}_{out}(\omega) + \hat{a}^\dagger(\omega)r(\omega)\hat{c}_{out}(\omega) \right. \\ \left. - \hat{a}(\omega)t^*(\omega)\hat{b}_{out}^\dagger(\omega) - \hat{a}(\omega)r^*(\omega)\hat{c}_{out}^\dagger(\omega) \right). \end{aligned} \quad (5.4)$$

To highlight the multimode features, $\hat{\mathcal{U}}$ can be conveniently expressed in terms of bosonic operators associated with the supermodes $\{\psi_k(\omega)\}$ by inverting [Equation 5.1](#) and by defining, by analogy with \hat{A}_k , operators $\hat{B}_{out,k}$ and $\hat{C}_{out,k}$ associated with the spatial modes downstream of the filter BS:

$$\hat{a}(\omega) = \sum_k \psi_k(\omega)\hat{A}_k, \quad (5.5a)$$

$$\hat{b}_{out}(\omega) = \sum_k \psi_k(\omega)\hat{B}_{out,k}, \quad (5.5b)$$

$$\hat{c}_{out}(\omega) = \sum_k \psi_k(\omega)\hat{C}_{out,k}. \quad (5.5c)$$

Transformation (5.5) leads to the appearance in [Equation 5.4](#) of terms of the kind:

$$\hat{a}^\dagger(\omega)t(\omega)\hat{b}_{out}(\omega) = \sum_{k,k'} \psi_k^*(\omega)\hat{A}_k^\dagger t(\omega)\psi_{k'}(\omega)\hat{B}_{out,k'}, \quad (5.6)$$

and analogous. However, filtered supermode functions $\{t(\omega)\psi_k(\omega)\}$ are no longer appropriate to define optical modes as they are not orthogonal to each other or to the original $\{\psi_k(\omega)\}$ [[121](#)]. This reflects the fact that the contributions of the original input supermodes are mixed together by the mode-insensitive filter. It is thus *a priori* impossible to factorise the action filter BS into that of multiple BS acting each on only a given supermode $\psi_k(\omega)$.

5.1.3 Supermode decomposition

Products involving the filter transmission and the supermodes functions can adequately be decomposed in a suitable orthonormal basis $\{\psi_k''(\omega)\}$ whose support corresponds to spectral regions for which $t(\omega) > 0$ [121]. Thanks to such new modes, it is possible to express the detection of single photons downstream of the filter. However, in principle, the set of $\{\psi_k''(\omega)\}$ is sufficient *only* to describe the state of systems that actually passed through the filter; as-a-matter-of-fact, in a conditional preparation scheme, this restricts the use of such functions to the sole description of the heralding photon detection. To overcome this limitation, in this work, the set $\{\psi_k''(\omega)\}$ is completed with a set of orthonormal functions $\{\psi_k^\perp(\omega)\}$. Functions $\{\psi_k''(\omega), \psi_k^\perp(\omega)\}$ are orthogonal to each other and have disjoint supports. Their properties are detailed in [Appendix F](#). The complete orthonormal basis $\{\psi_k''(\omega), \psi_k^\perp(\omega)\}$ can now be used to decompose all spectral modes involved in the non-Gaussian manipulation scheme, including those of the subsystem carrying the heralded state. In particular, the supermode functions can be written as:

$$\psi_k(\omega) = \sum_n p_{kn} \psi_n''(\omega) + q_{kn} \psi_n^\perp(\omega), \quad (5.7)$$

where:

$$p_{kn} = \int \psi_k(\omega) (\psi_n''(\omega))^* d\omega, \quad q_{kn} = \int \psi_k(\omega) (\psi_n^\perp(\omega))^* d\omega. \quad (5.8)$$

The specific shape of $\{\psi_k''(\omega), \psi_k^\perp(\omega)\}$ depends on that of the input supermodes and on the filter profile $t(\omega)$. In the case of continuous functions $t(\omega)$ with continuous derivatives, such as in the case of Lorentzian-shaped or Gaussian filter profiles, as demonstrated in the [Appendix F](#), the sets of $\{\psi_n''(\omega)\}$ can be in principle sufficient to obtain a complete basis (see [Equation F.3b](#) and [Equation F.9](#)). In all cases in which $t(\omega) = 0$ in one or more spectral regions, both $\{\psi_n''(\omega)\}$ and $\{\psi_n^\perp(\omega)\}$ are non-null and must be taken into account to obtain a complete basis. This concept is illustrated in [Figure 5.2](#) where the first $\{\psi_n''(\omega)\}$ and $\{\psi_n^\perp(\omega)\}$ are represented for the case of a Gaussian and of a rectangular filter.

[Equation 5.7](#) can be used to rewrite the bosonic operators associated with the initial system supermodes in terms of those associated with the filter supermodes $\psi_n''(\omega)$ and $\psi_n^\perp(\omega)$. More explicitly:

$$\hat{A}_k = \sum_n p_{kn}^* \hat{A}_n'' + q_{kn}^* \hat{A}_n^\perp \iff \begin{cases} \hat{A}_n'' = \sum_k p_{kn} \hat{A}_k \\ \hat{A}_n^\perp = \sum_k q_{kn} \hat{A}_k \end{cases} \quad (5.9)$$

Expressions in terms of the coefficients p_{kn} and q_{kn} and identical to [Equation 5.9](#) can be obtained for operators $\hat{B}_{out}(\omega)$ and $\hat{C}_{out}(\omega)$, leading to operators $\hat{B}_{out,n}'', \hat{B}_{out,n}^\perp, \hat{C}_{out,n}''$ and $\hat{C}_{out,n}^\perp$, respectively.

By exploiting the properties given by [Equation F.9](#) and [Equation F.10](#) of functions $\{\psi_n''(\omega), \psi_n^\perp(\omega)\}$, the evolution operator can now be written as:

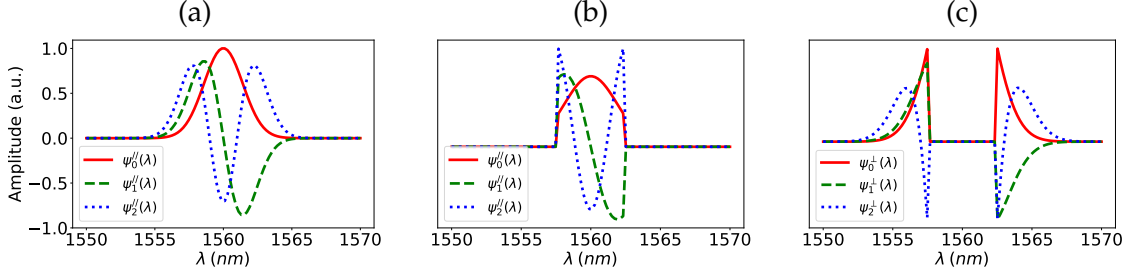


Figure 5.2 – (a): Examples of the first three $\{\psi_n^{\parallel}(\omega)\}$ in the case of a filter with a Gaussian transmission coefficient $t(\omega)$ centred around 1560 nm and with FWHM of 5 nm (≈ 600 GHz). (b) Examples of the first three $\{\psi_n^{\parallel}(\omega)\}$ and (c) $\{\psi_n^{\perp}(\omega)\}$, in the case of a filter with a rectangular profile centred around 1560 nm with a FWHM of 5 nm. For the rectangular filter, the coefficient $t(\omega)$ goes exactly to zero outside the 5 nm transmission bandwidth. The input state supermodes are assumed to be Hermite-Gaussian polynomials. For both filters, $\psi_0^{\parallel}(\omega)$ is given by $\frac{t(\omega)\psi_0(\omega)}{\sqrt{\int |t(\omega)\psi_0(\omega)|^2 d\omega}}$ with a Gaussian $\psi_0(\omega)$ function. $\{\psi_{n>0}^{\parallel}(\omega), \psi_n^{\perp}(\omega)\}$ are constructed by Gram-Schmidt process [4].

$$\begin{aligned}
 \hat{U} \approx & \hat{1} + \theta \sum_{kl} \left[T_{lk} \hat{\mathcal{B}}_{\text{out},l}^{\parallel} \left(\hat{\mathcal{A}}_k^{\parallel} \right)^{\dagger} - T_{lk}^* \left(\hat{\mathcal{B}}_{\text{out},l}^{\parallel} \right)^{\dagger} \hat{\mathcal{A}}_k^{\parallel} \right] \\
 & + \theta \sum_{kl} \left[R_{lk} \hat{\mathcal{C}}_{\text{out},l}^{\parallel} \left(\hat{\mathcal{A}}_k^{\parallel} \right)^{\dagger} - R_{lk}^* \left(\hat{\mathcal{C}}_{\text{out},l}^{\parallel} \right)^{\dagger} \hat{\mathcal{A}}_k^{\parallel} \right] \\
 & + \theta \sum_k \left[\hat{\mathcal{C}}_{\text{out},k}^{\perp} \left(\hat{\mathcal{A}}_k^{\perp} \right)^{\dagger} - \left(\hat{\mathcal{C}}_{\text{out},k}^{\perp} \right)^{\dagger} \hat{\mathcal{A}}_k^{\perp} \right], \quad (5.10)
 \end{aligned}$$

with:

$$T_{lk} = \int \left(\psi_k^{\parallel}(\omega) \right)^* t(\omega) \psi_l^{\parallel}(\omega) d\omega, \quad R_{lk} = \int \left(\psi_k^{\parallel}(\omega) \right)^* r(\omega) \psi_l^{\parallel}(\omega) d\omega. \quad (5.11)$$

The explicit shape of T_{lk} , R_{lk} depends on chosen experimental conditions via $t(\omega)$ and $\psi_l^{\parallel}(\omega)$. In Equation 5.10, operators $\hat{\mathcal{C}}_{\text{out}}$ are associated with the spectral components reflected by the filter and will be eventually traced out; accordingly, the most relevant contribution is given by the term $T_{lk} \hat{\mathcal{B}}_{\text{out},l}^{\parallel} \left(\hat{\mathcal{A}}_k^{\parallel} \right)^{\dagger}$ and its hermitian conjugate.

As shown by the explicit expression of \hat{U} , the introduction of the filter BS defines a new basis of modes and associated bosonic operators that permit to describe the whole subtraction process, although, in general, they do not necessarily match the original $\{\psi_k(\omega)\}$ and corresponding $\{\hat{\mathcal{A}}_k\}$. Due to such a mismatch, any operation performed in a single detection mode $\psi_k^{\parallel}(\omega)$ can have an impact distributed on all original supermodes $\{\psi_k(\omega)\}$ and can even entangle them. This very general result has been experimentally demonstrated in Ref. [135] for the mode-selective case. In the special case of non-mode-selective operation, expressing \hat{U} in terms of the parallel modes (as shown in Equation 5.10) shows that a photon-counting operation on a single $\psi_k^{\parallel}(\omega)$

also affects in a coherent way *all* parallel modes of the heralded state and entangle them too. In the language of single-photon subtraction, measuring a photon-counting event on a single $\psi_k''(\omega)$ would correspond to herald the delocalised subtraction of a single-photon on a set of $\{\psi_k''\}$. It is important to note that since standard photon-counting detectors do not discriminate among signals coming from different $\psi_k''(\omega)$, a photon-counting event downstream of the filter eventually leads to a mixed state as it will be discussed in the next subsection.

5.1.4 Heralded single-photon subtracted state

The above formalism allows explicitly describing the action of the operator \hat{U} on any generic protocol input $|\psi\rangle$ at the port a of the subtraction beam-splitter. The results obtained in this section refer to the case of a pure input state $\hat{\rho}_{\text{in}} = |\psi\rangle\langle\psi|$; however, the entire treatment can be easily extended to a mixed input. The states at the input port b of the subtraction beam-splitter and at the input c of the filter BS are assumed to be the vacuum states $|0\rangle$. The mode entering the subtraction beam-splitter will thus be indicated as $\hat{\rho} = \hat{\rho}_{\text{in}} \otimes |0\rangle\langle 0|$.

The state after the filter BS but right before the heralding detection stage can be written as $\hat{U} \hat{\rho} \hat{U}^\dagger$, with \hat{U} given by Equation 5.10. As discussed, in general, the photon-counting detector on the heralding path is a bucket one unable to distinguish signals that originate from different parallel modes $\{\psi_k''(\omega)\}$. Accordingly, the overall heralded state is given by the mixture:

$$\hat{\rho}_{\text{out}} = \frac{1}{P} \text{Tr}_{\hat{\mathcal{B}}_{\text{out}}, \hat{\mathcal{C}}_{\text{out}}} [\hat{\Pi}_{\hat{\mathcal{B}}_{\text{out}}} \hat{U} \hat{\rho} \hat{U}^\dagger], \quad (5.12)$$

where $P = \text{Tr}[\hat{\Pi}_{\hat{\mathcal{B}}_{\text{out}}} \hat{U} \hat{\rho} \hat{U}^\dagger]$ is the protocol success probability. $\text{Tr}_{\hat{\mathcal{B}}_{\text{out}}, \hat{\mathcal{C}}_{\text{out}}}$ is a partial trace over all detection modes $\{\psi_n''(\omega)\}$ of \hat{b}_{out} and the modes rejected by the spectral filter $\{\psi_n''(\omega), \psi_n^\perp(\omega)\}$ of \hat{c}_{out} . Both $\hat{\rho}_{\text{out}}$ and P depend on the chosen heralding detector and measurement result via the detector POVM $\hat{\Pi}_{\hat{\mathcal{B}}_{\text{out}}}$ that accounts, in principle, for limited detection efficiency, photon counting ability, time resolving ability [50]. Here, the operator $\hat{\Pi}_{\hat{\mathcal{B}}_{\text{out}}}$ reads as:

$$\hat{\Pi}_{\hat{\mathcal{B}}_{\text{out}}} = \sum_n |1\rangle\langle 1|_{\hat{\mathcal{B}}_{\text{out},n}}, \quad (5.13)$$

and is given by the superposition of projectors $|1\rangle\langle 1|_{\hat{\mathcal{B}}_{\text{out},n}}$, each describing the detection of a single photon in a specific mode $\psi_n''(\omega)$. Without any loss of generality, the bucket detector on the heralding path is assumed here to be able to perfectly project its input on a single-photon state. The impact of poor or no photon number resolving ability on heralded state preparation is discussed in subsection 2.2.1 of chapter 2, section 3.1 of chapter 3 and in Ref. [142].

By making use of the explicit expression of \hat{U} reported in Equation 5.10 as well as of Equation 5.9, it is easy to obtain the exact expression of the density matrix $\hat{\rho}_{\text{out}}$ in terms of the bosonic operators associated with the input supermodes:

$$\hat{\rho}_{\text{out}} = \frac{\theta^2}{P} \sum_{n,k} \gamma_{k,n} \hat{A}_k \hat{\rho}_{\text{in}} \hat{A}_n^\dagger, \quad (5.14)$$

where P can be expressed as:

$$P = \theta^2 \sum_n \gamma_{n,n} \text{Tr}[\hat{A}_n \hat{\rho}_{\text{in}} \hat{A}_n^\dagger]. \quad (5.15)$$

The coefficients $\gamma_{k,n}$ can be written in a compact form as functions of the filter BS transmission:

$$\gamma_{k,n} = \int |t(\omega)|^2 \psi_k(\omega) \psi_n^*(\omega) d\omega. \quad (5.16)$$

Equation 5.14 describes in a very simple and general form the mixed state heralded by a single-photon subtraction from the initial input state $\hat{\rho}$ in all cases where no mode-selective operation is possible on the heralding path. This corresponds to the extremely common experimental situation in which passive, linear filters are employed on the heralding path [75, 76, 121, 140]. The special case of mode-selective single-photon subtraction in a given supermode $\psi_{\bar{n}}(\omega)$ corresponds to $\gamma_{k,n} = \delta_{k,\bar{n}} \delta_{n,\bar{n}}$ in Equation 5.14 and correctly leads to a pure output state $\hat{\rho}_{\text{out}} = \frac{\theta^2}{P} \hat{A}_{\bar{n}} \hat{\rho}_{\text{in}} \hat{A}_{\bar{n}}^\dagger$ [136].

5.2 CASE STUDY: HERALDED SCHRÖDINGER KITTEN STATE PRODUCTION

The formalism established in the previous section describes in a general way the heralded state when single-photon subtraction is performed in a non-mode-selective way on an arbitrary input state $\hat{\rho}$. In this section and the rest of the chapter, we focus on the interesting case study of the heralded preparation of Schrödinger kitten states. As mentioned in chapter 2 and experimentally implemented in chapter 3, the typical heralded state generation and detection scheme is represented in Figure 5.3 in the multimode case.

As highlighted in chapter 4, depending on the SPDC working condition, a multipartite squeezed state $\hat{\rho}_{\text{in}}$ is produced. An optical passive filter of FWHM $\Delta\lambda_F$ is set before the SPD on the heralding path of the scheme to implement a non-mode-selective single-photon subtraction. The SPD signal is used to herald the production of the non-Gaussian state $\hat{\rho}_{\text{out}}$ as well as to trigger the homodyne detection (HD). The measured state, represented by its Wigner function $W_H(x, y)$, strongly depends on the spectral profile $\alpha_{\text{LO}}(\omega)$ of the homodyne local oscillator (LO). Ideally, the protocol for generating small size Schrödinger cat states relies on photon subtraction from a single-mode squeezed vacuum state $\hat{\rho}_{\text{in}} = |\zeta\rangle\langle\zeta|$ in a well defined supermode $\psi_k(\omega)$ and exhibiting a low squeezing level [75]. The corresponding state Wigner function is given by:

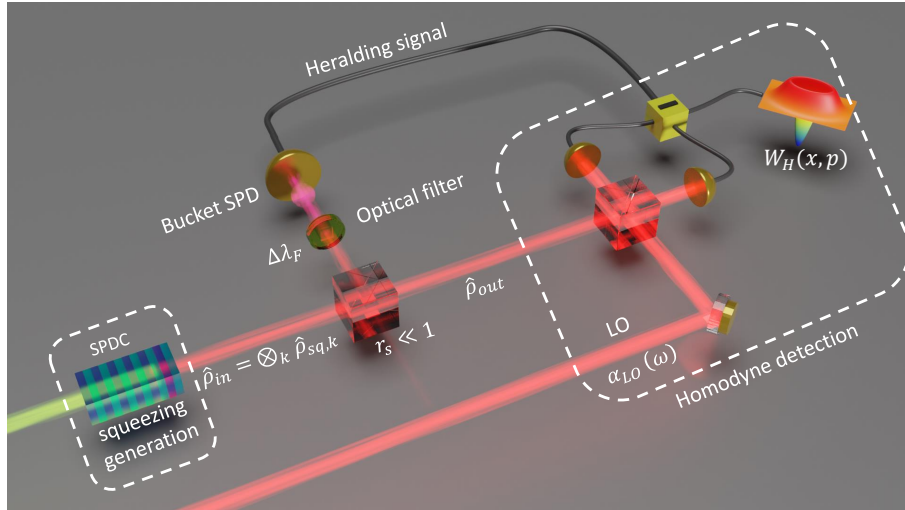


Figure 5.3 – Heralded preparation and detection of Schrödinger kitten states via single-photon subtraction from a multimode squeezed vacuum state.

$$W_T(x, p) = \frac{e^{-\frac{x^2}{2\sigma_0^2/s} - \frac{p^2}{2s\sigma_0^2}}}{2\pi\sigma_0^2} \left[\frac{s}{\sigma_0^2}x^2 + \frac{1}{s\sigma_0^2}p^2 - 1 \right], \quad (5.17)$$

where $s = e^{-2\zeta}$ is the squeezing factor and μ depends on the squeezing parameter ζ as $\mu = \tanh \zeta$. In many experimental situations, squeezed vacuum states are obtained by means of spontaneous parametric down conversion of an optical pump in a non linear optical crystal. However, as mentioned in the previous chapter, SPDC sources demand to be engineered according to specific characteristics to produce single-mode squeezing, that cannot be obtained for all wavelengths and non linear materials [133]. In general, the SPDC process can induce frequency/time correlations among optical components thus leading to a multimode behaviour [121]. In this situation, the squeezed states produced by the SPDC process is rather described by $\hat{\rho}_{in} = \otimes_k \hat{\rho}_{sq,k}$, *i.e.* by the product of independent pure single-mode squeezed vacuum states each in a different supermode $\psi_k(\omega)$. The explicit shape of the supermodes depends on the spectral profile of the SPDC pump beam and phase matching condition; by assuming a pump beam with a Gaussian spectrum, in the weak squeezing regime, $\{\psi_k(\omega)\}$ are given by Hermite-Gaussian functions and have the same global phase factor (leading to real $\gamma_{k,n}$) [131]. The squeezing parameter ζ_k of individual $\hat{\rho}_{sq,k}$ decreases as the supermode index k increases. The effective number of excited modes can be quantified in terms of the Schmidt number given by Equation 4.16, equal to 1 in the single-mode case and increasing with the number of excited supermodes. In experiments, it depends on the SPDC pump spectral width as well as on the nonlinear medium opto-geometrical properties at the chosen working wavelengths (see section 4.3).

5.2.1 Wigner function of the heralded state in the multimode case

As widely discussed in the literature [75, 135], the homodyne detector acts as a logic AND gate, in which the properties of the LO select the mode that will be actually measured. In particular, by expressing the amplitude of the LO beam as $\alpha_{LO}(\omega) = \sum_k c_k \psi_k(\omega)$, it is simple to prove that the homodyne detection measures the observable:

$$\hat{X}_H(\varphi) = \sum_{k=0}^{\infty} c_k \hat{X}_k(\varphi), \quad (5.18)$$

where φ is the LO phase and $\sum_k c_k^2 = 1$. The observable $\hat{X}_k(\varphi) = \sigma_0 (e^{-i\varphi} \hat{A}_k + e^{i\varphi} \hat{A}_k^\dagger)$ is the quadrature associated with the supermode $\psi_k(\omega)$. Amplitude and phase quadratures, \hat{X} and \hat{P} , correspond to $\varphi = 0, \pi/2$, respectively. Depending on the chosen spectral profile of the LO $\alpha_{LO}(\omega)$, it is thus possible to observe the quadratures of a given supermode or a combination of them. This possibility is extremely relevant when it comes to choosing how to measure the multimode features or to optimise the detection of a chosen mode. By exploiting Equation 5.14 and Equation 5.18, the single-mode Wigner function of the state detected by the homodyne detector can be written as:

$$W_H(x, p) = \frac{\theta^2}{4\pi^2 \sigma_0^2 P} \sum_{k,n} \gamma_{k,n} \int e^{i \left[\frac{yp}{\sigma_0^2} - (x-y-c^t \cdot \mathbf{x})z \right]} \langle \mathbf{x} | \hat{A}_k \hat{\rho}_{in} \hat{A}_n^\dagger | \mathbf{x} + 2y\mathbf{c} \rangle d\mathbf{x} dz dy, \quad (5.19)$$

where $\mathbf{c}^t = (c_0, \dots, c_k, \dots)$ and $|\mathbf{x}\rangle = |x_0, \dots, x_k, \dots\rangle$. The previous expression is obtained by tracing out all modes orthogonal to the one defined by the homodyne via the LO profile [132] as expressed by Equation 5.18. Taking into account the expressions of the squeezed vacuum state (Equation 1.82) and the wave-function of Fock states (Equation 1.86), and thanks to the following expression [143]:

$$\sum_{m=0}^{\nu^m} \frac{\nu^m}{m!} H_{2m+k}(x) = (1+4\nu)^{-k/2-1/2} e^{(4\nu x^2)/(1+4\nu)} H_k \left(\frac{x}{\sqrt{1+4\nu}} \right), \quad (5.20)$$

the wave-functions of the squeezed vacuum and single-photon subtracted squeezed vacuum in each supermode $\psi_k(\omega)$ can be written as:

$$\langle x_k | \zeta_k \rangle = \frac{(1-\mu_k^2)^{1/4}}{\sqrt{\sigma_0 \sqrt{2\pi} (1+\mu_k)}} e^{-\frac{1-\mu_k}{4\sigma_0^2(1+\mu_k)} x_k^2}, \quad (5.21)$$

$$\langle x_k | \hat{A}_k | \zeta_k \rangle = \frac{\mu_k (1-\mu_k^2)^{1/4} e^{-x_k^2/4\sigma_0^2}}{\sqrt{2\sigma_0 \sqrt{2\pi}}} \frac{1}{1+\mu_k} e^{\frac{\mu_k}{1+\mu_k} \frac{x_k^2}{2\sigma_0^2}} \frac{2x_k}{\sigma_0 \sqrt{2+2\mu_k}}. \quad (5.22)$$

By inserting these two expressions in Equation 5.19, the Wigner function of the heralded state (obtained after single-photon subtraction from the output of a multimode SPDC process) as measured by the homodyne detector can be expressed in terms of the mean photon number of squeezed states, $n_k = \sinh^2(\zeta_k)$, and of $\mu_k = \tanh \zeta_k$, as:

$$W_H(x, p) = \frac{e^{-\left(\frac{x^2}{2\sigma_x^2} + \frac{p^2}{2\sigma_p^2}\right)}}{2\pi\sigma_x\sigma_p P/\theta^2} \left[\sum_k \gamma_{k,k} n_k + \frac{\sigma_0^2}{\sigma_x^2} \left(\frac{x^2}{\sigma_x^2} - 1\right) \sum_{k,n} \gamma_{k,n} \frac{\mu_k \mu_n c_k c_n}{(1 - \mu_k)(1 - \mu_n)} + \frac{\sigma_0^2}{\sigma_p^2} \left(\frac{p^2}{\sigma_p^2} - 1\right) \sum_{k,n} \gamma_{k,n} \frac{\mu_k \mu_n c_k c_n}{(1 + \mu_k)(1 + \mu_n)} \right], \quad (5.23)$$

with

$$\sigma_x^2 = \sigma_0^2 \sum_n c_n^2 \frac{1 + \mu_n}{1 - \mu_n} \quad \text{and} \quad \sigma_p^2 = \sigma_0^2 \sum_n c_n^2 \frac{1 - \mu_n}{1 + \mu_n}. \quad (5.24)$$

Thanks to [Equation 5.23](#), it is possible to explicitly evaluate the impact on the measured state of both the filter profile, via the $\{\gamma_{k,n}\}$, and of the chosen LO shape via the $\{c_n\}$. The multimode features of the protocol input state are taken into account via n_k and μ_k .

5.3 MULTIMODE-INDUCED HERALDED STATE IMPURITY

The case of heralded states obtained when no filter is used on the heralding path provides a good intuition of the relevance of the filtering stage applied in the protocol. The absence of filter is described by $t(\omega) = 1$ for all ω , *i.e.*, according to [Equation 5.16](#), by $\gamma_{k,n} = \delta_{k,n}$. Trivially, in this case, parallel modes $\{\psi_k''(\omega)\}$ exactly correspond to $\{\psi_k(\omega)\}$ (see [Equation F.1](#)). As indicated by [Equation 5.14](#), the protocol output state is a perfect mixture of photon subtracted states of the kind $\hat{A}_n \hat{\rho}_{\text{in}} \hat{A}_n^\dagger$. Correspondingly, the Wigner function of the detected state can be expressed as:

$$W_{H,\text{NF}}(x, p) = \sum_k p_k \left[c_k^2 W_k^{(1)}(x, p) + (1 - c_k^2) W_{\text{SV}}(x, p) \right], \quad (5.25)$$

with $p_k = \frac{n_k}{\sum_l n_l}$ the probability of subtracting a photon from the mode k . The first term of the previous expression represents the Wigner function of a single-photon subtracted squeezed state in supermode $\psi_k(\omega)$ as seen by the HD:

$$W_k^{(1)}(x, p) = \frac{e^{-\left(\frac{x^2}{2\sigma_x^2} + \frac{p^2}{2\sigma_p^2}\right)}}{2\pi\sigma_x\sigma_p} \left[\frac{\sigma_0^2(1 + \mu_k)}{\sigma_x^2(1 - \mu_k)} \left(\frac{x^2}{\sigma_x^2} - 1\right) + \frac{\sigma_0^2(1 - \mu_k)}{\sigma_p^2(1 + \mu_k)} \left(\frac{p^2}{\sigma_p^2} - 1\right) + 1 \right]. \quad (5.26)$$

This state correctly corresponds to the target state of [Equation 5.17](#) when the homodyne LO is in the supermode $\psi_k(\omega)$. In general cases, the effect of imperfect mode matching with the LO is included in σ_x and σ_p .

The other term corresponds to squeezed vacuum contributions as detected by the homodyne detector.

$$W_{\text{SV}}(x, p) = \frac{e^{-\left(\frac{x^2}{2\sigma_x^2} + \frac{p^2}{2\sigma_p^2}\right)}}{2\pi\sigma_x\sigma_p}. \quad (5.27)$$

Equation 5.25 expresses the fact that, in absence of filter, photon-counting events cannot be associated to a specific supermode (nor to any subset of them); as a consequence, the state measured by the HD only occasionally corresponds to the desired non-Gaussian one. A physical intuition of this idea is provided by the case of a LO in a specific supermode $\alpha_{LO}(\omega) = \psi_n(\omega)$, i.e. $c_k^2 = \delta_{k,n}$. In this condition:

$$W_{H,NF}(x, p)|_{c_n^2=1} = p_n W_n^{(1)}(x, p) + \sum_{k \neq n} p_k W_{SV}(x, p). \quad (5.28)$$

The measured heralded state is equal to $W_n^{(1)}(x, p)$ only with a probability p_n , corresponding to the probability of subtracting a photon in the LO mode $\psi_n(\omega)$. All remaining cases lead to the detection of squeezed vacuum with a probability $\sum_{k \neq n} p_k = 1 - p_n$.

5.3.1 Quantification of the heralded state non-classicality

State non-classicality can be evaluated using several metrics. For a pure state, non-Gaussianity implies a Wigner function that is negative in a given region in phase space [42]. However, mixed states with non-Gaussian features can still exhibit a positive Wigner function. In these conditions, specific criteria can be adopted to quantify the non-Gaussianity of a quantum state [144]. At the same time, to discuss *optimally accessible* features of heralded states, it is pertinent to focus on the Wigner function negativity, as it represents a stricter metric [145]. Note that, in what concerns all results that will be presented in the rest of this chapter, the Wigner function negativity and its non-Gaussianity share the same qualitative behaviour. The negativity is defined as the volume of the negative part of the Wigner function [82] and it can be expressed as:

$$N_g = \frac{1}{2} \left[\int \int |W_H(x, p)| dx dp - 1 \right]. \quad (5.29)$$

The negativity for the ideal case of a single-photon subtraction on a single-mode squeezed vacuum state is computed to be $N_g = 2e^{-1/2} - 1 \approx 0.213$ (for $\sigma_0^2 = 1/2$).

Figure 5.4-(a) shows N_g for the detected heralded state as a function of the local oscillator spectral width and of the Schmidt number K .

To comply with many experimental cases, in which the LO beam is directly provided by the output of a pulsed laser, the LO profile, $\alpha_{LO}(\omega)$, is assumed to be Gaussian with FWHM of $\Delta\lambda_{LO}$. As shown by the figure, optimal N_g values are obtained for low $K \approx 1$ and when the Gaussian LO profile $\alpha_{LO}(\omega)$ is chosen so as to match exactly the first SPDC supermode, i.e. $\alpha_{LO}(\omega) = \psi_0(\omega)$ and $c_0^2 = 1$. This case is represented in the figure by the white dotted line. When the number of supermodes at the SPDC output increases ($K > 1$), N_g rapidly degrades. This behaviour can be understood by observing Figure 5.4-(b), that represents the probability p_n of subtracting a photon in the supermode n ; as it can be seen, the probability p_0 is generally higher than $p_{n>0}$ and the single-photon subtraction mostly takes place on the first supermode ($n = 0$). Accordingly, choosing the LO profile identical to the first supermode ($\alpha_{LO}(\omega) = \psi_0(\omega)$) corresponds to optimising, in Equation 5.28, the detection of the non-Gaussian state $W_n^{(1)}(x, p)$ that shows a negative Wigner function. Note that, to measure high negativities, contributions with $p_{n>0}$, that lead in Equation 5.28 to the detection of

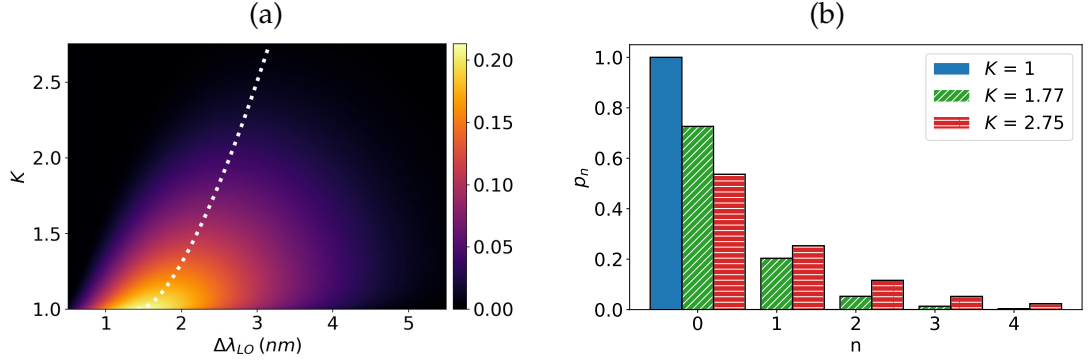


Figure 5.4 – Properties of the measured heralded state $W_{H,NF}(x, p)$ in the absence of filter on the heralding path. (a): Wigner function negativity N_g of $W_{H,NF}(x, p)$ as a function of the local oscillator spectral width and the multimode character of the SPDC source providing the input state $\hat{\rho}_{in}$ via K ; the LO spectrum is assumed to be Gaussian with a FWHM $\Delta\lambda_{LO}$. The white dotted curve indicates the case of a local oscillator perfectly matched with the first SPDC supermode (i.e. $c_0^2 = 1$). (b): Probability p_n of detecting an heralding photon from the supermode $\psi_n(\omega)$ for different SPDC working condition. Probabilities p_n are directly proportional to the excitation of the squeezed supermodes $\{\psi_n(\omega)\}$. In all the simulations, the bandwidth of the SPDC pump beam is set to 0.5 nm. K depends on the SPDC pump spectral width as well as on the the nonlinear medium opto-geometrical parameters at the chosen working wavelength [118].

squeezed vacuum, should be minimised. This condition is easily respected when $K \approx 1$. However, as soon as the Schmidt number increases, the distribution of p_n becomes flatter, thus explaining why, for high K values, N_g progressively decreases along the white dotted line.

5.4 HERALDED STATE WITH SPECTRALLY FILTERED HERALDING PHOTONS

In experiments, the use of narrowband filters on the heralding path represents a widely reported strategy to improve the quality of single-photon subtracted states [75]. At the same time, to our knowledge, no theoretical and quantitative description of the filter impact has been provided so far. The formalism that has been introduced in this chapter can be conveniently used to illustrate the limits and the advantages of different filter strategies. As discussed in section 5.1, the previous sections, the actual spectral profile of the function $t(\omega)$ determines the shape of the filter supermodes $\{\psi_k^//(\omega), \psi_k^\perp(\omega)\}$ and, via Equation 5.16, the explicit shape of the coefficients $\gamma_{k,n}$ to be included in $W_H(x, p)$ of Equation 5.23. Accordingly, different filter profiles and FWHM can have a strong effect on the heralded states as well as on the LO profile that must be chosen to optimise the detection of non-Gaussian features. From the experimental side, different filter spectral profiles can be chosen depending on the specific situation. Plug-and-play filters with a rectangular profile, transmitting light only within a certain bandwidth are widely used in guided-wave experiments, where broadband SPDC

emission is generated in single-pass configuration in nonlinear waveguides [91, 133]. This scenario covers dense wavelength multiplexers (DWM) and Bragg filters and it is quite common when quantum optical states are produced at classical telecommunication wavelengths so as to be compatible with low loss fiber networks. Alternatively, filters with $t(\omega)$ described by continuous and strictly non-null functions, such as Gaussian or Lorentzian, can be used. This is the case, for instance, of bulk configurations in which DWM or Bragg filters with desired characteristics in terms of transmission or spectral width are not available and optical cavities are instead employed on the heralding path [76]. In the following, the cases of a rectangular filter and of a Gaussian-shaped $t(\omega)$ will be considered and compared. The explicit expressions of $\gamma_{k,n}$ for these cases are reported in section F.3. As for the previous section, a Gaussian LO profile $\alpha_{LO}(\omega)$ will be considered.

Figure 5.5 gives the Wigner function negativity for the detected heralded state in the case of a rectangular spectral filter in the heralding path.

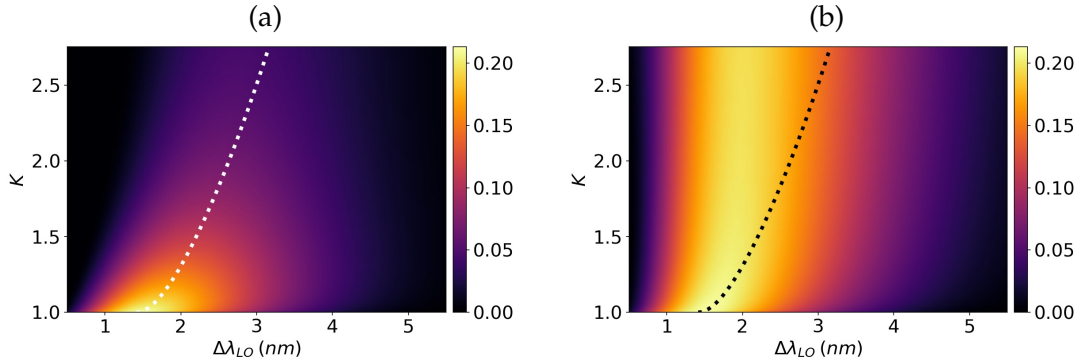


Figure 5.5 – Negativities N_g of the measured heralded Wigner function $W_H(x, p)$ in the case of a rectangular filter on the heralding path expressed as functions of the local oscillator spectral width and Schmidt number K . Two filter bandwidths are considered: (a) 5 nm (≈ 600 GHz) FWHM and (b) 1 nm (≈ 100 GHz) FWHM. In both plots, the dotted curve indicates the case of a local oscillator perfectly matching the first SPDC supermode (i.e. $c_0^2 = 1$).

The first $\{\psi_n^{\parallel}(\omega)\}$ and $\{\psi_n^{\perp}(\omega)\}$ for this kind of $t(\omega)$ are reported in Figure 5.2 for the case of a filter FWHM of 5 nm. Two different filter bandwidths are considered (5 nm and 1 nm). As a general consideration, for both FWHMs, N_g decreases when the number of excited supermodes increases ($K > 1$). In the case of a wide filter (Figure 5.5-(a)), the degradation is quite fast, with a behaviour similar to the one discussed for the case of no filter in the previous section. The optimal LO is still very close to the case of $\alpha_{LO}(\omega) = \psi_0(\omega)$, matching the first SPDC supermode (i.e. $c_0^2 = 1$, see the white dotted curve). The situation dramatically changes when the width of the filter is reduced (Figure 5.5-(b)). In this case, the protocol performances are much robust against the multimode character of the SPDC source and high negativity values can be obtained also for higher $K > 1$, provided the FWHM $\Delta\lambda_{LO}$ for the Gaussian LO is suitably chosen. Remarkably, the optimal $\alpha_{LO}(\omega)$ profile does not match any of the supermodes $\{\psi_k(\omega)\}$, nor any of the filter-defined functions $\{\psi_n^{\parallel}(\omega)\}$ and $\{\psi_n^{\perp}(\omega)\}$ (see Figure 5.2). Its FWHM $\Delta\lambda_{LO}$ can be easily computed numerically. The possibility

of using a Gaussian LO in combination with a narrowband filter confirms qualitative experimental observations [28, 29, 146] and opens the way to simple realisations, free from spectral shaping stages on the local oscillator path and mode-selective single-photon subtraction.

A same qualitative behaviour can also be found in the case of a Gaussian $t(\omega)$ instead of a rectangular one. In this case, only the $\{\psi_n^{//}(\omega)\}$ are non-null. Their profile, similar but not exactly matching the one of the original supermodes, is represented in Figure 5.2-(a). As for the rectangular filter, reducing the FWHM of the Gaussian $t(\omega)$ has the effect of making the protocol robust against higher K and makes it easy to identify an optimal LO bandwidth $\Delta\lambda_{LO}$. A comparison among the different filter shapes is shown in Figure 5.6 in the case of an SPDC pump with spectral width of 0.5 nm.

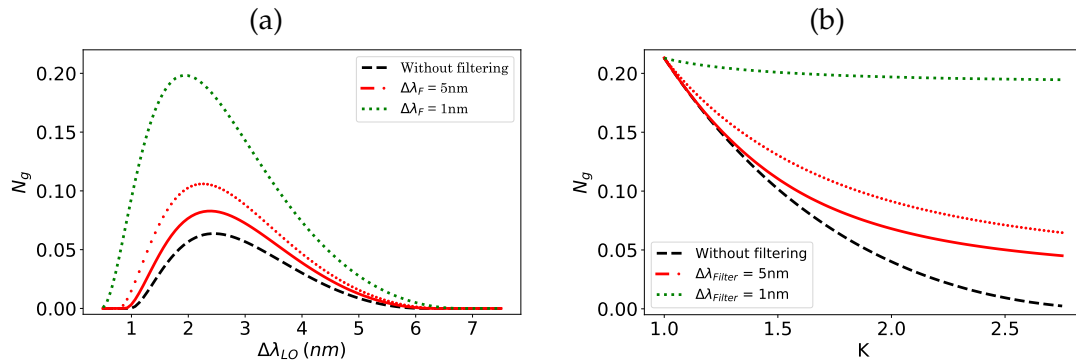


Figure 5.6 – (a): Negativity of the Wigner function as a function of the FWHM of the LO spectral amplitude $\alpha(\omega)$ in the case where $K = 1.77$. (b): Negativity of the Wigner function as a function of the Schmidt number K when imposing an optimal $\Delta\lambda_{LO}$. For both figures, the SPDC pump has a spectral width of 0.5 nm. Curves refer to a single-photon subtraction scheme. Dashed (black): without spectral filter in the heralding path; solid (red): with 5 nm (≈ 600 GHz) rectangular spectral filter in the heralding path; points (red): with 5 nm (≈ 600 GHz) Gaussian spectral filter in the heralding path; dotted (green): with 1 nm (≈ 100 GHz) spectral filter in the heralding path (the Gaussian and rectangular shapes are equivalent in this case).

Figure 5.6-(a) represents the negativity of the Wigner function in the case of no spectral filtering in the heralding path (dashed black), as well as of 5 nm (solid and dotted red) and 1 nm (dotted green) filter bandwidths for $K = 1.77$. The solid red curve represents rectangular spectral filters whereas the dotted red one represents Gaussian spectral filters. As expected, the narrowband spectral filters improve the negativity of the homodyne detected state. Also, the optimal LO bandwidth is slightly shifted to lower values when the filter FWHM decreases. The narrower is the filter, the smaller is the difference between the behaviour obtained with a rectangular or a Gaussian filter profiles (dotted green matches solid green curve). As shown in Figure 5.6-(b), similar results can be found for different values of $K > 1$, where optimal measured negativities (*i.e.* corresponding to the optimal LO profiles) are reported as a function of K and for different filter bandwidths.

5.4.1 Application to a practical experimental situation

Discussed results provide a powerful tool to model single-photon subtraction in a multimode context and to optimise experimental conditions for the generation and detection of high quality non-Gaussian states. As for an example, in what follows, the developed treatment is applied to the practical situation of Schrödinger kitten states obtained from single-photon subtraction from squeezed light emitted by a realistic source. A particularly interesting case is that of a SPDC process occurring in integrated photonic circuits on Lithium Niobate (LN), where on-chip generation and active manipulation of optical quantum states at telecom wavelengths can be provided by the association of the nonlinear material optical and electro-optical properties [91, 92]. At the same time, as highlighted in the previous chapter, LN dispersion properties prevent from working in single-mode conditions in pulsed regime and generated squeezed light can exhibit a high number of modes ($K > 1$). Figure 5.7 considers a typical case of multimode light generated around 1560 nm via type-0 SPDC in a 10 mm long LN crystal pumped by a pulsed beam at 780 nm with a spectral width of 0.5 nm.

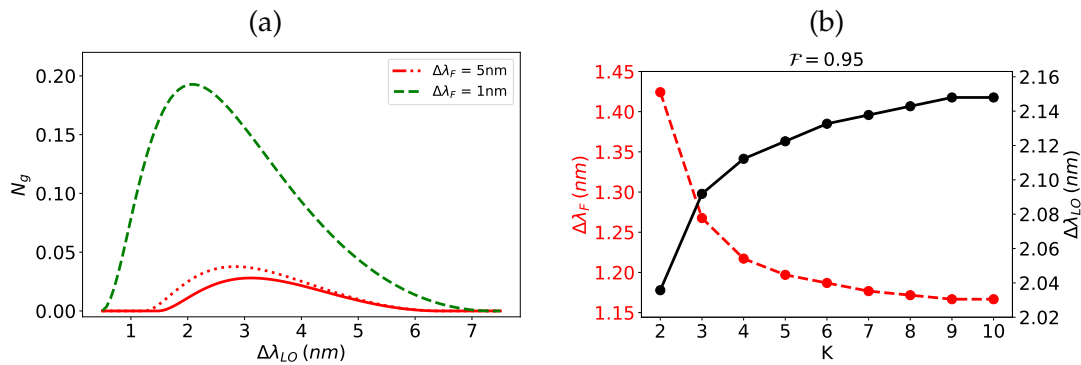


Figure 5.7 – (a): Negativity of the Wigner function as function of the LO spectral width, for $K \approx 9$ as for frequency degenerate SPDC around 1560 nm, pumped with optical pulses at 780 nm with a width of 0.5 nm. The SPDC crystal is taken to be 10 mm long. Curves refer to a single-photon subtraction scheme. Solid (red): with 5 nm rectangular spectral filter in the heralding path; dotted (red): with 5 nm Gaussian spectral filter in the heralding path; dashed (green) with 1 nm spectral filter in the heralding path (the Gaussian and rectangular shapes are equivalent in this case). (b): Optimal $\Delta\lambda_{LO}$ (solid black line) and $\Delta\lambda_F$ (dashed red line) required to ensure, for a given K , a fidelity with the target state of 95%.

In such conditions, the Schmidt number can be calculated to be $K \approx 9$ [131]. Figure 5.7-(a) shows the obtained N_g for different filtering and LO choices. As it can be seen, for a filter of 1 nm, almost optimal N_g values can be reached for experimentally accessible Gaussian LO profiles with $\Delta\lambda_{LO} \approx 2$ nm. This corresponds to optical pulses in picosecond regime, that can be easily employed in guided-wave configurations, with the possibility of limiting parasitic nonlinear optical effects and chromatic dispersion in optical fibres. For a subtraction BS reflectivity $r_s^2 \approx 0.05$, the corresponding protocol success probability, P , is on the order of 0.01, in agreement with typical values reported in the literature [28, 29, 75, 146]. Higher probabilities can in principle be obtained with wider filters at the price of a reduced N_g . The protocol heralding rate is measured

in Hz and it is the product of P with the experiment clock, *i.e.* the pulse repetition rate (PRR) of the laser pumping the SPDC stage used to generate the squeezing. Its value corresponds to the count rate at the output of the DV heralding detector that triggers the homodyne measurement. For a fixed P , the ultimate limit to the protocol heralding rate is given by the bandwidth of the slower between the DV and CV detector. From one side the PRR must be chosen so as to guarantee a DV detection rate below the photon counter saturation level. From the other, even if this condition is satisfied, the heralding rate must also be kept below the homodyne electronic bandwidth, so as to avoid triggering the acquisition at a speed non-compatible with the detector time resolution [147]. Commercial single-photon detectors can safely work with count rate below 10 MHz, corresponding, in the case of $P \approx 0.01$, to a maximum PPR of ≈ 1 GHz. These values are fully compatible with commercial homodyne systems that have typical bandwidths of the order of 100 MHz. Ultrafast heralding rates above 100 MHz (with PRR higher than 10 GHz) could be obtained by multiplexing the DV detectors and employing research-grade homodyne with bandwidth in the GHz regime [147].

Eventually, note that results observed with N_g are confirmed by the fidelity between the measured heralded state and the target one of Equation 5.17 (see section F.2 for the explicit calculation):

$$\mathcal{F} = 4\pi\sigma_0^2 \int \int W_H(x, p) W_T(x, p) dx dp. \quad (5.30)$$

In the simulations, the squeezing parameter of the target state is assumed to be equal to ζ_0 , *i.e.* to the squeezing of the first spectral supermode ($k = 0$) and set to give -3 dB of noise reduction with respect to the standard quantum level; such a value is commonly used in Schrödinger kitten generation [75]. Figure 5.7-(b) shows, for different K , the LO bandwidth and the filter FWHM required to obtain a fidelity with the target state of 95%. As it can be seen for $K = 9$, this leads to a filter FWHM of ≈ 1.15 nm and to a $\Delta\lambda_{LO} \approx 2.15$ nm.

5.5 CONCLUSION

We presented in this chapter a versatile and practical theoretical framework allowing to describe single-photon subtraction in the case where no mode-selective operation is available and a simple spectral filter is considered on the heralding path of the scheme. Such configuration considerably simplifies the experimental setups, making them easier to be implemented. The explicit shape of the heralded state, as measured by a homodyne detector, is provided as a function of the multimode character of the protocol input state, of the spectral profile of the filter and of the local oscillator shape. Based on the desired target features, this allows choosing adequate working conditions for future practical realisations, thus representing a powerful tool for optimally designing future experiments. The strength of the model is illustrated by applying it to the generation of Schrödinger kittens, obtained from single-photon subtraction from a multimode squeezed state. Different working conditions have been investigated and discussed, to determine the features of heralded non-Gaussian states that can be actually obtained and retrieved when single-mode generation or state manipulation are not easy to be implemented.

A MULTIPLEXED SYNTHESIZER FOR NON-GAUSSIAN QUANTUM STATE GENERATION

6.1	Multimode, single-stage quantum state synthesizer	130
6.1.1	Framework: iterative protocols	130
6.1.2	Proposed single-stage generation protocol	131
6.2	Proposed protocol with non-Gaussian input resources	132
6.2.1	The input state state	133
6.2.2	The produced output state	135
6.2.3	Protocol performances	139
6.3	Case study 1: Parallel Schrödinger cat breeding	140
6.3.1	Beam splitter reflectivity	140
6.3.2	Amplitude of the input states	142
6.3.3	Comparison with the iterative cat breeding protocol	142
6.4	Case study 2: GKP state preparation	143
6.4.1	Definition	143
6.4.2	GKP states production with the proposed protocol	146
6.5	Conclusion	146

Non-Gaussian quantum states are crucial for implementing sophisticated protocols such as error-correction [148] and one-way quantum computing [149]. Different strategies for generating such states were reported, relying for instance on high-order non-linearity [150–152], qubit interaction [153] and linear optical interaction with non-Gaussian resources such as Fock states or photon counting [33, 63, 154–156]. A class of protocols of particular interest is that of iterative schemes [33, 63, 65, 154, 155, 157], where photonic resource states are combined together in an iterative fashion, allowing for growing step-by-step the size of the states. However, the experimentally implemented protocols are to date restricted to few operations, due to protocol scalability issues arising from the simultaneous need for multiple heralding signals and from the increase of experimental overhead [34, 89]. This ultimately limits the average photon number in the generated state.

In this chapter, we propose a novel scheme to overcome the current experimental limitations, by relying on a single shot operation with a spectrally multiplexed resources [158]. Our proposal takes advantage of the multimode aspect of state-of-the-art experimentally investigated quantum photonic sources in order to greatly enhance the capabilities of iterative generation protocols. In [section 6.1](#), we recall the principle of iterative protocols and propose a fully parallelized counterpart relying on spectral multimode quantum optics. Then, in [section 6.2](#), analytical formula are given for both

the produced state (density matrix and Wigner function) , and for the protocol performances (output state fidelity and protocol's success probability) in the case where the protocol is fed with Schrödinger cat states (or asymptotically, single-photon Fock states). After that, [section 6.3](#) and [section 6.4](#) are devoted to the investigation of parallelized generation of high amplitude Schrödinger cat states and Gottesman-Kitaev-Preskill (GKP) codes [148]. Finally, The chapter is concluded in [section 6.5](#).

6.1 MULTIMODE, SINGLE-STAGE QUANTUM STATE SYNTHESIZER

6.1.1 Framework: iterative protocols

The protocol proposed in this chapter takes its essence from iterative generation protocols, an elementary brick of which is represented in [Figure 6.1](#).

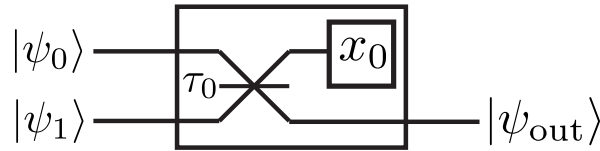


Figure 6.1 – Elementary brick of an iterative protocol.

Such operation consists in mixing two input resource states, $|\psi_0\rangle$ and $|\psi_1\rangle$, on a beam splitter with transmittivity τ_0 , to herald the generation of an output state $|\psi_{\text{out}}\rangle$. The heralding process can be performed in different ways [33, 155], and even if the results derived here can easily be extended to the photon counting case, we focus in the following on homodyne conditioning. In this scenario, one of the two output arms of the beam splitter is measured by a homodyne detector (along a certain quadrature x_θ). When the measurement outcome is close enough to an assigned value ($x_\theta = x_0$ on [Figure 6.1](#)), the target output state is successfully heralded. The strength of such a protocol is that the average photon number of the output state can be higher than the one of the individual input states. Accordingly, it can be used to *breed* complex photonic states by cascading the protocol using $|\psi_{\text{out}}\rangle$ as one of the input of a subsequent operation.

[Figure 6.2](#) shows such a configuration, where states of increasing size are combined with resource states; tree-like configurations are also commonly investigated, thanks to the parallelization capabilities they offer [65].

This idea is at the core of the *cat breeding* scheme discussed in [subsection 2.3.2](#), proposed in [63], where a balanced beam splitter ($\tau = 1/\sqrt{2}$) and $x_i = 0$ homodyne conditioning are used [159, 160]. In this case, mixing two Schrödinger cat states allows to create a single one with an amplitude increased by a factor $\sqrt{2}$. Iterating this protocol N times then allows to create a Schrödinger cat state with an amplitude amplified by a factor $2^{N/2}$. An alternative manner has also been proposed, where the input cat states were replaced by single photons, allowing the production of squeezed Schrödinger cat states, robust to losses [33, 161]. By modifying the quadrature along which the homodyne conditioning is performed ($p = 0$ homodyne conditionings), GKP codes can be

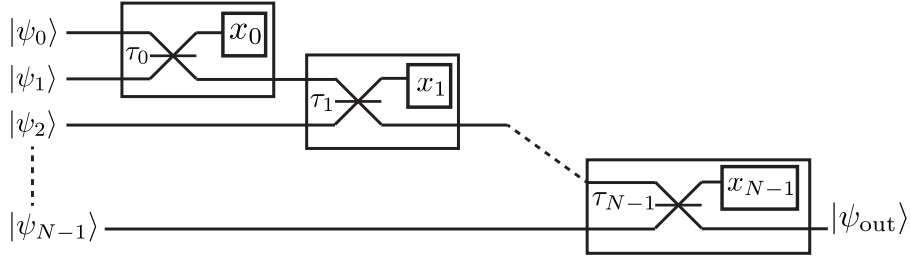


Figure 6.2 – A cascaded architecture for an iterative protocol.

generated all-optically [65, 162]. More generally, all superpositions of up to N photons can be generated by properly adjusting the beam splitter reflectivities and homodyne conditionings [33].

Proof-of-principle experimental validations are currently limited to single stage implementations due to scalability issues [34, 89]: in bulk optics, increasing the number of stages by increasing the number of input state sources indeed leads to intractable complexities. Temporal multiplexing represents a promising alternative that is also investigated [163], but could ultimately lead to a decrease in the overall generation rate of the states. Integrated optics, on the other hand, offers an attractive solution to address spatial scalability issues, but inevitable losses associated with such platforms should be carefully taken into consideration [164].

We propose in this chapter to rely instead on spectral multiplexing, which offers an increased generation efficiency as well as noticeable experimental simplifications. Note also that this protocol can be implemented with spatial multiplexing of transverse spatial modes, or any other degree of freedom.

6.1.2 Proposed single-stage generation protocol

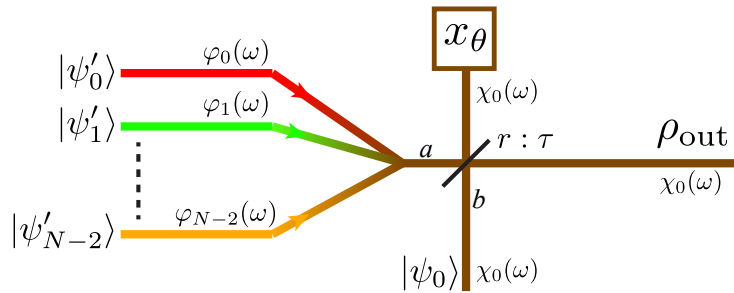


Figure 6.3 – The multiplexed generation protocol (see text for description).

The main idea of the proposal, sketched in Figure 6.3, consists in the following key ingredients. To begin with, a *seed* state $|\psi_0\rangle$ initially populates a spectral mode $\chi_0(\omega)$ in which the quantum engineering process is to be performed. In the output of the protocol, we will focus on the state $\hat{\rho}_{out}$ that populates this same mode $\chi_0(\omega)$. Subsequently, we select a collection of states $|\psi'_0\rangle, |\psi'_1\rangle, \dots, |\psi'_{N-2}\rangle$ respectively in modes $\varphi_0(\omega), \varphi_1(\omega), \dots, \varphi_{N-2}(\omega)$ that are used to *feed* the protocol, so as to grow the overall size of the output state $\hat{\rho}_{out}$. As it will be discussed with a concrete example, the spec-

tral modes $\varphi_i(\omega)$ have to overlap $\chi_0(\omega)$ in a clever way, so that each $|\psi'_i\rangle$ contributes in an efficient manner to the generation protocol. This collection of states is merged in a single spatial mode and sent to the first input port (port a) of a beam splitter of transmittivity τ so as to interfere with the seed state $|\psi_0\rangle$ sent to the other input port of this beam splitter (port b). Importantly, a perfect spatial mode matching of the two states populating modes a and b must be guaranteed. After interaction, one output port of the beam splitter is measured by a homodyne detector along mode $\chi_0(\omega)$, to perform the desired conditioning $x_\theta = x_0$, for successfully heralding the generation of a state $\hat{\rho}_{\text{out}}$ on the other output port.

A major advantage of this method is that it allows mixing N states in a single heralding step, therefore drastically increasing the success probability of the protocol and reducing the experimental complexity as compared with the standard spatial multiplexing strategy, as it will be quantitatively shown later.

The multimode description that we use complies with realistic implementations of Gaussian state sources, such as, for instance, multimode squeezed vacuum sources [131]. As discussed in chapter 4, it is now indeed well established that spontaneous parametric down conversion (SPDC) through three-wave mixing process produces a collection of squeezed vacuum states in separate orthogonal spectral modes $\{\varphi_k(\omega)\}_{k \in \mathbb{N}}$, each with a different squeezing parameter [119, 121].

More generally, we recall that each spectral mode $\varphi_k(\omega)$ can be associated with a bosonic annihilation operator \hat{A}_k :

$$\hat{A}_k = \int \varphi_k^*(\omega) \hat{a}(\omega) d\omega, \quad (6.1)$$

$\{a(\omega)\}$ being the bosonic operators of individual spectral components at the SPDC output. When two different sets of modes $\{\varphi_k(\omega)\}_{k \in \mathbb{N}}$ and $\{\chi_l(\omega)\}_{l \in \mathbb{N}}$ are involved, one can express their *likeness* by using the overlap formula:

$$c_{k,l} = \int \varphi_k^*(\omega) \chi_l(\omega) d\omega. \quad (6.2)$$

This formula allows switching from one mode basis to the other thanks to:

$$\varphi_k(\omega) = \sum_l c_{k,l}^* \chi_l(\omega). \quad (6.3)$$

We show in the rest of the chapter that the proposed protocol can be used to generate highly-fidel Schrödinger cat states and GKP codes with increased success probabilities compared to standard iterative protocols.

6.2 PROPOSED PROTOCOL WITH NON-GAUSSIAN INPUT RESOURCES

In this section, and the rest of the chapter, we will focus on the protocol proposed in subsection 6.1.2 with input Schrödinger cat states as resources. As highlighted in

section 6.1, this kind of input resources can be used for both Schrödinger cat breeding and all optical GKP states generation. Moreover, single-photon Fock state is an odd Schrödinger cat state with amplitude $\alpha = 0$ (see subsection 1.4.2.2), and so, the performances of the proposed protocol with input single-photon Fock states can be studied with the obtained formula in this section, this case is discussed in Appendix G. In the following derivations, we will consider a more general case where:

- The input Schrödinger cat states will be supposed to have arbitrary different amplitudes.
- The parity of the Schrödinger cat states is not fixed.
- The nature of the homodyne conditioning can be arbitrary.

6.2.1 The input state state

The Schrödinger cat states in the spatial mode a are each in a spectral mode $\varphi_k(\omega)$ ($k \in \llbracket 0, N-2 \rrbracket$) and have an amplitude α_k :

$$|\psi'_k\rangle = |\text{Cat}_\pm(\alpha_k)\rangle_{k,a} = \frac{1}{\mathcal{N}_\pm(\alpha_k)} (|\alpha_k\rangle \pm |-\alpha_k\rangle), \quad (6.4)$$

with:

$$\mathcal{N}_\pm(\alpha_k) = \sqrt{2(1 \pm e^{-2|\alpha_k|^2})}. \quad (6.5)$$

Therefore, the state populating the spatial mode a is given by:

$$\begin{aligned} |\Psi_a\rangle &= \frac{1}{\prod_{k=0}^{N-2} \mathcal{N}_\pm(\alpha_k)} \bigotimes_{k=0}^{N-2} (|\alpha_k\rangle_{k,a} \pm |-\alpha_k\rangle_{k,a}) \\ &= \frac{1}{\prod_{k=0}^{N-2} \mathcal{N}_\pm(\alpha_k)} \sum_{m_0=0}^1 \dots \sum_{m_{N-2}=0}^1 (\pm 1)^{\sum_{k=0}^{N-2} m_k} \bigotimes_{k=0}^{N-2} |(-1)^{m_k} \alpha_k\rangle_{k,a}. \end{aligned} \quad (6.6)$$

The spatial mode b , on the other hand, contains a single mode $\chi_0(\omega)$ that is populated by a Schrödinger cat state of amplitude β :

$$|\Psi_b\rangle = |\text{Cat}_\pm(\beta)\rangle_{0,b} = \frac{1}{\mathcal{N}_\pm(\beta)} (|\beta\rangle \pm |-\beta\rangle), \quad (6.7)$$

with:

$$\mathcal{N}_\pm(\beta) = \sqrt{2(1 \pm e^{-2|\beta|^2})}. \quad (6.8)$$

In this notation, the first ket index k (resp. 0) relates to the spectral mode and the second ket index a (resp. b) relates to the spatial mode. As the spectral mode in which

the output state will be detected is $\chi_0(\omega)$, it is relevant to re-express $|\Psi_a\rangle$ in this basis, thanks to the basis change relation:

$$\chi_n(\omega) = \sum_{k=0}^{\infty} c_{n,k} \varphi_k(\omega). \quad (6.9)$$

This relation can be directly transposed to the corresponding annihilation operators: each spectral mode $\varphi_k(\omega)$ is associated to a bosonic annihilation operator \hat{A}_{φ_k} , which can be expressed as a function of the \hat{A}_{χ_n} thanks to:

$$\hat{A}_{\varphi_k} = \int \varphi_k^*(\omega) \hat{a}(\omega) d\omega = \int \sum_n c_{n,k} \chi_n^*(\omega) \hat{a}(\omega) d\omega = \sum_n c_{n,k} \int \chi_n^*(\omega) \hat{a}(\omega) d\omega = \sum_n c_{n,k} \hat{A}_{\chi_n}. \quad (6.10)$$

This simply allows to rewrite the tensor product of coherent states involved in [Equation 6.6](#) as:

$$\begin{aligned} \bigotimes_{k=0}^{N-2} |(-1)^{m_k} \alpha_k\rangle_{k,a} &= \bigotimes_{k=0}^{N-2} \hat{D}_{\varphi_k} [(-1)^{m_k} \alpha_k] |0\rangle \\ &= e^{\sum_{k=0}^{N-2} [(-1)^{m_k} \alpha_k \hat{A}_{\varphi_k}^\dagger - (-1)^{m_k} \alpha_k^* \hat{A}_{\varphi_k}] } |0\rangle \\ &= e^{\sum_{k=0}^{N-2} \sum_{n=0}^{+\infty} [(-1)^{m_k} c_{n,k} \alpha_k \hat{A}_{\chi_n}^\dagger - (-1)^{m_k} c_{n,k} \alpha_k^* \hat{A}_{\chi_n}] } |0\rangle \\ &= \bigotimes_{n=0}^{+\infty} e^{\sum_{k=0}^{N-2} [(-1)^{m_k} c_{n,k} \alpha_k \hat{A}_{\chi_n}^\dagger - (-1)^{m_k} c_{n,k} \alpha_k^* \hat{A}_{\chi_n}] } |0\rangle \\ &= \bigotimes_{n=0}^{+\infty} \left| \sum_{k=0}^{N-2} (-1)^{m_k} c_{n,k} \alpha_k \right\rangle_{n,a}. \end{aligned} \quad (6.11)$$

This expression gives the form of $|\Psi_a\rangle$ expressed in spectral mode basis $\{\chi_n(\omega)\}_n$:

$$|\Psi_a\rangle = \frac{1}{\prod_{k=0}^{N-2} \mathcal{N}_{\pm}(\alpha_k)} \sum_{m_0=0}^1 \dots \sum_{m_{N-2}=0}^1 (\pm 1)^{\sum_{k=0}^{N-2} m_k} \bigotimes_{n=0}^{\infty} \left| \sum_{k=0}^{N-2} (-1)^{m_k} c_{n,k} \alpha_k \right\rangle_{n,a}. \quad (6.12)$$

By gathering expressions [Equation 6.7](#) and [Equation 6.12](#), the global input state, solely expressed in the spectral basis $\{\chi_n(\omega)\}_n$, reads:

$$\begin{aligned} |\Psi_{\text{in}}\rangle &= |\Psi_a\rangle \otimes |\Psi_b\rangle = \frac{1}{\mathcal{N}_{\pm}(\beta) \prod_{k=0}^{N-2} \mathcal{N}_{\pm}(\alpha_k)} \times \\ &\left[\sum_{m_0=0}^1 \dots \sum_{m_{N-2}=0}^1 (\pm 1)^{\sum_{k=0}^{N-2} m_k} \left| \sum_{k=0}^{N-2} (-1)^{m_k} c_{0,k} \alpha_k \right\rangle_{0,a} |\beta\rangle_{0,b} \bigotimes_{n=1}^{\infty} \left| \sum_{k=0}^{N-2} (-1)^{m_k} c_{n,k} \alpha_k \right\rangle_{n,a} |0\rangle_{n,b} \right. \\ &\left. \pm \sum_{m_0=0}^1 \dots \sum_{m_{N-2}=0}^1 (\pm 1)^{\sum_{k=0}^{N-2} m_k} \left| \sum_{k=0}^{N-2} (-1)^{m_k} c_{0,k} \alpha_k \right\rangle_{0,a} |-\beta\rangle_{0,b} \bigotimes_{n=1}^{\infty} \left| \sum_{k=0}^{N-2} (-1)^{m_k} c_{n,k} \alpha_k \right\rangle_{n,a} |0\rangle_{n,b} \right]. \end{aligned} \quad (6.13)$$

As it can be seen, only a part of the input state (for $n = 0$) interferes with the cat state of amplitude β initially in spatial mode b (both terms $|\sum_{k=0}^{N-2} (-1)^{m_k} c_{0,k} \alpha_k\rangle_{0,a} |\beta\rangle_{0,b}$ and $|\sum_{k=0}^{N-2} (-1)^{m_k} c_{0,k} \alpha_k\rangle_{0,a} |-\beta\rangle_{0,b}$). On the other hand, all the higher-order mode contributions ($n > 0$) of the cat states in spatial mode a will interfere with the vacuum in the other port (terms $|\sum_{k=0}^{N-2} (-1)^{m_k} c_{n,k} \alpha_k\rangle_{n,a} |0\rangle_{n,b}$ and $|\sum_{k=0}^{N-2} (-1)^{m_k} c_{n,k} \alpha_k\rangle_{n,a} |0\rangle_{n,b}$), that will not be detected and will therefore lead to a loss of information.

6.2.2 The produced output state

6.2.2.1 State after the beam splitter

By using the simple beam splitter transformation on coherent states, at the output of the (r, τ) beam splitter one has:

$$\begin{aligned}
|\Psi_{\text{BS}}\rangle = & \frac{1}{\mathcal{N}_{\pm}(\beta) \prod_{k=0}^{N-2} \mathcal{N}_{\pm}(\alpha_k)} \sum_{m_0=0}^1 \dots \sum_{m_{N-2}=0}^1 (\pm 1)^{\sum_{k=0}^{N-2} m_k} \times \\
& \bigotimes_{n=1}^{\infty} \left[\tau \sum_{k=0}^{N-2} (-1)^{m_k} c_{n,k} \alpha_k \right]_{n,a} \left[r \sum_{k=0}^{N-2} (-1)^{m_k} c_{n,k} \alpha_k \right]_{n,b} \\
& \times \left[\left| \tau \sum_{k=0}^{N-2} (-1)^{m_k} c_{0,k} \alpha_k - r\beta \right\rangle_{0,a} \left| r \sum_{k=0}^{N-2} (-1)^{m_k} c_{0,k} \alpha_k + \tau\beta \right\rangle_{0,b} \right. \\
& \left. \pm \left| \tau \sum_{k=0}^{N-2} (-1)^{m_k} c_{0,k} \alpha_k + r\beta \right\rangle_{0,a} \left| r \sum_{k=0}^{N-2} (-1)^{m_k} c_{0,k} \alpha_k - \tau\beta \right\rangle_{0,b} \right]. \quad (6.14)
\end{aligned}$$

To alleviate the writing, we use the following notation:

$$\begin{aligned}
x_{\mathbf{m}} &= \tau \sum_{k=0}^{N-2} (-1)^{m_k} c_{0,k} \alpha_k - r\beta & y_{\mathbf{m}} &= r \sum_{k=0}^{N-2} (-1)^{m_k} c_{0,k} \alpha_k + \tau\beta \\
z_{\mathbf{m}} &= \tau \sum_{k=0}^{N-2} (-1)^{m_k} c_{0,k} \alpha_k + r\beta & w_{\mathbf{m}} &= r \sum_{k=0}^{N-2} (-1)^{m_k} c_{0,k} \alpha_k - \tau\beta \\
\mathcal{X}_{\mathbf{m},n} &= \tau \sum_{k=0}^{N-2} (-1)^{m_k} c_{n,k} \alpha_k & \mathcal{Y}_{\mathbf{m},n} &= r \sum_{k=0}^{N-2} (-1)^{m_k} c_{n,k} \alpha_k \\
\mathbf{m}_{\Sigma} &= \sum_{k=0}^{N-2} m_k
\end{aligned}$$

where we introduce the vector:

$$\mathbf{m} = (m_0, m_1, \dots, m_{N-2})^T, \quad (6.15)$$

and the elements m_k take two values: 0 or 1. With these notations, Equation 6.14 can simply be rewritten as:

$$|\Psi_{\text{BS}}\rangle = \frac{1}{\mathcal{N}_{\pm}(\beta) \prod_{k=0}^{N-2} \mathcal{N}_{\pm}(\alpha_k)} \sum_{\mathbf{m}} (\pm 1)^{\mathbf{m}_{\Sigma}} \bigotimes_{n=1}^{\infty} |\mathcal{X}_{\mathbf{m},n}\rangle_{n,a} |\mathcal{Y}_{\mathbf{m},n}\rangle_{n,b} \left[|x_{\mathbf{m}}\rangle_{0,a} |y_{\mathbf{m}}\rangle_{0,b} \pm |z_{\mathbf{m}}\rangle_{0,a} |w_{\mathbf{m}}\rangle_{0,b} \right], \quad (6.16)$$

with the associated density operator:

$$\begin{aligned}
\hat{\rho}_{\text{BS}} = |\Psi_{\text{BS}}\rangle\langle\Psi_{\text{BS}}| &= \frac{1}{\mathcal{N}_{\pm}^2(\beta) \left(\prod_{k=0}^{N-2} \mathcal{N}_{\pm}(\alpha_k)\right)^2} \times \\
&\sum_{\mathbf{m}} \sum_{\mathbf{p}} (\pm 1)^{\mathbf{m}_{\Sigma} + \mathbf{p}_{\Sigma}} \bigotimes_{n=1}^{\infty} |\mathcal{X}_{\mathbf{m},n}\rangle_{n,a} \langle\mathcal{X}_{\mathbf{p},n}| \otimes_{n=1}^{\infty} |\mathcal{Y}_{\mathbf{m},n}\rangle_{n,b} \langle\mathcal{Y}_{\mathbf{p},n}| \\
&\times (|x_{\mathbf{m}}\rangle_{0,a} \langle x_{\mathbf{p}}| \otimes |y_{\mathbf{m}}\rangle_{0,b} \langle y_{\mathbf{p}}| \pm |x_{\mathbf{m}}\rangle_{0,a} \langle z_{\mathbf{p}}| \otimes |y_{\mathbf{m}}\rangle_{0,b} \langle w_{\mathbf{p}}| \\
&\pm |z_{\mathbf{m}}\rangle_{0,a} \langle x_{\mathbf{p}}| \otimes |w_{\mathbf{m}}\rangle_{0,b} \langle y_{\mathbf{p}}| + |z_{\mathbf{m}}\rangle_{0,a} \langle z_{\mathbf{p}}| \otimes |w_{\mathbf{m}}\rangle_{0,b} \langle w_{\mathbf{p}}|). \quad (6.17)
\end{aligned}$$

The output state in the spectral mode $\chi_0(\omega)$ is found by performing the partial trace over $n \geq 1$:

$$\begin{aligned}
\hat{\rho}_{\text{BS}}^{n=0} &= \frac{1}{\mathcal{N}_{\pm}^2(\beta) \left(\prod_{k=0}^{N-2} \mathcal{N}_{\pm}(\alpha_k)\right)^2} \sum_{\mathbf{m}} \sum_{\mathbf{p}} (\pm 1)^{\mathbf{m}_{\Sigma} + \mathbf{p}_{\Sigma}} e^{-\frac{1}{2} \sum_{n=1}^{\infty} [(x_{\mathbf{m},n} - x_{\mathbf{p},n})^2 + (y_{\mathbf{m},n} - y_{\mathbf{p},n})^2]} \\
&(|x_{\mathbf{m}}\rangle_{0,a} \langle x_{\mathbf{p}}| \otimes |y_{\mathbf{m}}\rangle_{0,b} \langle y_{\mathbf{p}}| \pm |x_{\mathbf{m}}\rangle_{0,a} \langle z_{\mathbf{p}}| \otimes |y_{\mathbf{m}}\rangle_{0,b} \langle w_{\mathbf{p}}| \\
&\pm |z_{\mathbf{m}}\rangle_{0,a} \langle x_{\mathbf{p}}| \otimes |w_{\mathbf{m}}\rangle_{0,b} \langle y_{\mathbf{p}}| + |z_{\mathbf{m}}\rangle_{0,a} \langle z_{\mathbf{p}}| \otimes |w_{\mathbf{m}}\rangle_{0,b} \langle w_{\mathbf{p}}|). \quad (6.18)
\end{aligned}$$

By setting:

$$\mathcal{X}_{\Sigma_{\mathbf{m},\mathbf{p}}}^2 = \sum_{n=1}^{\infty} (x_{\mathbf{m},n} - x_{\mathbf{p},n})^2 \quad (6.19)$$

and

$$\mathcal{Y}_{\Sigma_{\mathbf{m},\mathbf{p}}}^2 = \sum_{n=1}^{\infty} (y_{\mathbf{m},n} - y_{\mathbf{p},n})^2, \quad (6.20)$$

we find the expression of the unconditioned state along spectral mode $\chi_0(\omega)$:

$$\begin{aligned}
\hat{\rho}_{\text{BS}}^{n=0} &= \frac{1}{\mathcal{N}_{\pm}^2(\beta) \left(\prod_{k=0}^{N-2} \mathcal{N}_{\pm}(\alpha_k)\right)^2} \sum_{\mathbf{m}} \sum_{\mathbf{p}} (\pm 1)^{\mathbf{m}_{\Sigma} + \mathbf{p}_{\Sigma}} e^{-\frac{1}{2} [\mathcal{X}_{\Sigma_{\mathbf{m},\mathbf{p}}}^2 + \mathcal{Y}_{\Sigma_{\mathbf{m},\mathbf{p}}}^2]} \\
&(|x_{\mathbf{m}}\rangle_{0,a} \langle x_{\mathbf{p}}| \otimes |y_{\mathbf{m}}\rangle_{0,b} \langle y_{\mathbf{p}}| \pm |x_{\mathbf{m}}\rangle_{0,a} \langle z_{\mathbf{p}}| \otimes |y_{\mathbf{m}}\rangle_{0,b} \langle w_{\mathbf{p}}| \\
&\pm |z_{\mathbf{m}}\rangle_{0,a} \langle x_{\mathbf{p}}| \otimes |w_{\mathbf{m}}\rangle_{0,b} \langle y_{\mathbf{p}}| + |z_{\mathbf{m}}\rangle_{0,a} \langle z_{\mathbf{p}}| \otimes |w_{\mathbf{m}}\rangle_{0,b} \langle w_{\mathbf{p}}|). \quad (6.21)
\end{aligned}$$

6.2.2.2 Heralding in port b

The last step of the protocol consists in performing a conditioning in output port b of the beam splitter. This conditioning will be modeled by a POVM $\hat{\Pi}_b$, that we will consider of different nature in the following. In all generality, the output state in spatial mode a will be:

$$\hat{\rho}_{\text{out}} = \frac{\text{Tr}_b [\hat{\Pi}_b \otimes \hat{I}_a \hat{\rho}_{\text{BS}}^{n=0}]}{P_s} = \frac{1}{P_s \mathcal{N}_{\pm}^2(\beta) \left(\prod_{k=0}^{N-2} \mathcal{N}_{\pm}(\alpha_k) \right)^2} \sum_{\mathbf{m}} \sum_{\mathbf{p}} (\pm 1)^{\mathbf{m}_{\Sigma} + \mathbf{p}_{\Sigma}} e^{-\frac{1}{2} [\mathcal{X}_{\Sigma, \mathbf{m}, \mathbf{p}}^2 + \mathcal{Y}_{\Sigma, \mathbf{m}, \mathbf{p}}^2]} \times (\mathcal{A}_{\mathbf{m}, \mathbf{p}} |x_{\mathbf{m}}\rangle_{0,a} \langle x_{\mathbf{p}}| \pm \mathcal{B}_{\mathbf{m}, \mathbf{p}} |x_{\mathbf{m}}\rangle_{0,a} \langle z_{\mathbf{p}}| \pm \mathcal{C}_{\mathbf{m}, \mathbf{p}} |z_{\mathbf{m}}\rangle_{0,a} \langle x_{\mathbf{p}}| + \mathcal{D}_{\mathbf{m}, \mathbf{p}} |z_{\mathbf{m}}\rangle_{0,a} \langle z_{\mathbf{p}}|), \quad (6.22)$$

where $P_s = \text{Tr}_{a,b} [\hat{\Pi}_b \otimes \hat{I}_a \hat{\rho}_{\text{BS}}^{n=0}]$ is the heralding probability and:

$$\begin{aligned} \mathcal{A}_{\mathbf{m}, \mathbf{p}} &= \text{Tr}_b [\hat{\Pi}_b |y_{\mathbf{m}}\rangle_{0,b} \langle y_{\mathbf{p}}|] \\ \mathcal{B}_{\mathbf{m}, \mathbf{p}} &= \text{Tr}_b [\hat{\Pi}_b |y_{\mathbf{m}}\rangle_{0,b} \langle w_{\mathbf{p}}|] \\ \mathcal{C}_{\mathbf{m}, \mathbf{p}} &= \text{Tr}_b [\hat{\Pi}_b |w_{\mathbf{m}}\rangle_{0,b} \langle y_{\mathbf{p}}|] \\ \mathcal{D}_{\mathbf{m}, \mathbf{p}} &= \text{Tr}_b [\hat{\Pi}_b |w_{\mathbf{m}}\rangle_{0,b} \langle w_{\mathbf{p}}|]. \end{aligned} \quad (6.23)$$

In the [Table 6.1](#), we give the expression of these parameters depending on how we perform the heralding measurement. Five scenarios are envisaged:

- $\hat{\Pi}_b = |0\rangle\langle 0|$: vacuum projection. The heralding is performed on the absence of photon detection in port b .
- $\hat{\Pi}_b = \int_{-\frac{\Delta x}{2}}^{\frac{\Delta x}{2}} |x\rangle\langle x| dx$: homodyne conditioning $x \simeq 0$ with a gate acceptance window of full width Δx . In this scenario, the heralding is successfully performed when the homodyne outcome falls within the interval $[-\Delta x/2, \Delta x/2]$, and the state is discarded otherwise.
- $\hat{\Pi}_b = \int_{-\frac{\Delta p}{2}}^{\frac{\Delta p}{2}} |p\rangle\langle p| dp$: homodyne conditioning $p \simeq 0$ with a gate acceptance window of full width Δp . This case is identical as above, with a homodyne measurement along the p quadrature.
- $\hat{\Pi}_b = \int_{-\infty}^{\infty} e^{-\frac{x^2}{2\Delta x^2}} |x\rangle\langle x| dx$: homodyne conditioning $x \simeq 0$ with a gaussian acceptance window of full width Δx . Such gating is relevant in the scenario where homodyne conditioning is very narrow compared to the equivalent effect of losses in the heralding port.
- $\hat{\Pi}_b = \int_{-\infty}^{\infty} e^{-\frac{p^2}{2\Delta p^2}} |p\rangle\langle p| dp$: homodyne conditioning $p \simeq 0$ with a gaussian acceptance window of full width Δp . Same as above with a homodyne measurement along the p quadrature.

The Wigner function of the output state can finally be written as:

$$W_{\text{out}}(x, p) = \frac{1}{N} \sum_{\mathbf{m}} \sum_{\mathbf{p}} (\pm 1)^{\mathbf{m}_{\Sigma} + \mathbf{p}_{\Sigma}} e^{-\frac{1}{2} [\mathcal{X}_{\Sigma, \mathbf{m}, \mathbf{p}}^2 + \mathcal{Y}_{\Sigma, \mathbf{m}, \mathbf{p}}^2]} \left[\mathcal{A}_{\mathbf{m}, \mathbf{p}} W_{|x_{\mathbf{m}}\rangle\langle x_{\mathbf{p}}|}(x, p) \pm \mathcal{B}_{\mathbf{m}, \mathbf{p}} W_{|x_{\mathbf{m}}\rangle\langle z_{\mathbf{p}}|}(x, p) \pm \mathcal{C}_{\mathbf{m}, \mathbf{p}} W_{|z_{\mathbf{m}}\rangle\langle x_{\mathbf{p}}|}(x, p) + \mathcal{D}_{\mathbf{m}, \mathbf{p}} W_{|z_{\mathbf{m}}\rangle\langle z_{\mathbf{p}}|}(x, p) \right], \quad (6.24)$$

with:

Parameters	$\hat{\Pi}_b = 0\rangle\langle 0 $	$\hat{\Pi}_b = \int_{-\frac{\Delta x}{2}}^{\frac{\Delta x}{2}} x\rangle\langle x dx$	$\hat{\Pi}_b = \int_{-\infty}^{\infty} e^{-\frac{x^2}{2\Delta x^2}} x\rangle\langle x dx$
$\mathcal{A}_{m,p}$	$e^{-\frac{1}{2}(y_m^2 + y_p^2)}$	$\frac{e^{-\frac{1}{2}(y_m - y_p)^2}}{2} \left[\operatorname{erf} \left(\frac{y_m + y_p}{\sqrt{2}} + \frac{1}{2\sqrt{2}} \frac{\Delta x_{sq}}{\sigma_0} \right) - \operatorname{erf} \left(\frac{y_m + y_p}{\sqrt{2}} - \frac{1}{2\sqrt{2}} \frac{\Delta x_{sq}}{\sigma_0} \right) \right]$	$\frac{e^{-\frac{1}{2}(y_m^2 + y_p^2)}}{\sqrt{1 + \frac{\sigma_0^2}{\Delta x_s^2}}} e^{\frac{(y_m + y_p)^2}{2 \left(1 + \frac{\sigma_0^2}{\Delta x_s^2}\right)}}$
$\mathcal{B}_{m,p}$	$e^{-\frac{1}{2}(w_m^2 + w_p^2)}$	$\frac{e^{-\frac{1}{2}(y_m - w_p)^2}}{2} \left[\operatorname{erf} \left(\frac{y_m + w_p}{\sqrt{2}} + \frac{1}{2\sqrt{2}} \frac{\Delta x_{sq}}{\sigma_0} \right) - \operatorname{erf} \left(\frac{y_m + w_p}{\sqrt{2}} - \frac{1}{2\sqrt{2}} \frac{\Delta x_{sq}}{\sigma_0} \right) \right]$	$\frac{e^{-\frac{1}{2}(w_m^2 + w_p^2)}}{\sqrt{1 + \frac{\sigma_0^2}{\Delta x_s^2}}} e^{\frac{(y_m + w_p)^2}{2 \left(1 + \frac{\sigma_0^2}{\Delta x_s^2}\right)}}$
$\mathcal{C}_{m,p}$	$e^{-\frac{1}{2}(w_m^2 + y_p^2)}$	$\frac{e^{-\frac{1}{2}(w_m - y_p)^2}}{2} \left[\operatorname{erf} \left(\frac{w_m + y_p}{\sqrt{2}} + \frac{1}{2\sqrt{2}} \frac{\Delta x_{sq}}{\sigma_0} \right) - \operatorname{erf} \left(\frac{w_m + y_p}{\sqrt{2}} - \frac{1}{2\sqrt{2}} \frac{\Delta x_{sq}}{\sigma_0} \right) \right]$	$\frac{e^{-\frac{1}{2}(w_m^2 + y_p^2)}}{\sqrt{1 + \frac{\sigma_0^2}{\Delta x_s^2}}} e^{\frac{(w_m + y_p)^2}{2 \left(1 + \frac{\sigma_0^2}{\Delta x_s^2}\right)}}$
$\mathcal{D}_{m,p}$	$e^{-\frac{1}{2}(w_m^2 + w_p^2)}$	$\frac{e^{-\frac{1}{2}(w_m - w_p)^2}}{2} \left[\operatorname{erf} \left(\frac{w_m + w_p}{\sqrt{2}} + \frac{1}{2\sqrt{2}} \frac{\Delta x_{sq}}{\sigma_0} \right) - \operatorname{erf} \left(\frac{w_m + w_p}{\sqrt{2}} - \frac{1}{2\sqrt{2}} \frac{\Delta x_{sq}}{\sigma_0} \right) \right]$	$\frac{e^{-\frac{1}{2}(w_m^2 + w_p^2)}}{\sqrt{1 + \frac{\sigma_0^2}{\Delta x_s^2}}} e^{\frac{(w_m + w_p)^2}{2 \left(1 + \frac{\sigma_0^2}{\Delta x_s^2}\right)}}$
Parameters	$\hat{\Pi}_b = 0\rangle\langle 0 $	$\hat{\Pi}_b = \int_{-\frac{\Delta p}{2}}^{\frac{\Delta p}{2}} p\rangle\langle p dp$	$\hat{\Pi}_b = \int_{-\infty}^{\infty} e^{-\frac{p^2}{2\Delta p^2}} p\rangle\langle p dp$
$\mathcal{A}_{m,p}$	/	$\frac{e^{-\frac{1}{2}(y_m - y_p)^2}}{2} \left[\operatorname{erf} \left(i \frac{y_m - y_p}{\sqrt{2}} + \frac{1}{2\sqrt{2}} \frac{\Delta p_{sq}}{\sigma_0} \right) - \operatorname{erf} \left(i \frac{y_m - y_p}{\sqrt{2}} - \frac{1}{2\sqrt{2}} \frac{\Delta p_{sq}}{\sigma_0} \right) \right]$	$e^{-\frac{(y_m - y_p)^2}{2 \left(1 + \frac{\sigma_0^2}{\Delta p_s^2}\right)}} \frac{\sigma_0^2}{\sqrt{1 + \frac{\sigma_0^2}{\Delta p_s^2}}}$
$\mathcal{B}_{m,p}$	/	$\frac{e^{-\frac{1}{2}(y_m - w_p)^2}}{2} \left[\operatorname{erf} \left(i \frac{y_m - w_p}{\sqrt{2}} + \frac{1}{2\sqrt{2}} \frac{\Delta p_{sq}}{\sigma_0} \right) - \operatorname{erf} \left(i \frac{y_m - w_p}{\sqrt{2}} - \frac{1}{2\sqrt{2}} \frac{\Delta p_{sq}}{\sigma_0} \right) \right]$	$e^{-\frac{(y_m - w_p)^2}{2 \left(1 + \frac{\sigma_0^2}{\Delta p_s^2}\right)}} \frac{\sigma_0^2}{\sqrt{1 + \frac{\sigma_0^2}{\Delta p_s^2}}}$
$\mathcal{C}_{m,p}$	/	$\frac{e^{-\frac{1}{2}(w_m - y_p)^2}}{2} \left[\operatorname{erf} \left(i \frac{w_m - y_p}{\sqrt{2}} + \frac{1}{2\sqrt{2}} \frac{\Delta p_{sq}}{\sigma_0} \right) - \operatorname{erf} \left(i \frac{w_m - y_p}{\sqrt{2}} - \frac{1}{2\sqrt{2}} \frac{\Delta p_{sq}}{\sigma_0} \right) \right]$	$e^{-\frac{(w_m - y_p)^2}{2 \left(1 + \frac{\sigma_0^2}{\Delta p_s^2}\right)}} \frac{\sigma_0^2}{\sqrt{1 + \frac{\sigma_0^2}{\Delta p_s^2}}}$
$\mathcal{D}_{m,p}$	/	$\frac{e^{-\frac{1}{2}(w_m - w_p)^2}}{2} \left[\operatorname{erf} \left(i \frac{w_m - w_p}{\sqrt{2}} + \frac{1}{2\sqrt{2}} \frac{\Delta p_{sq}}{\sigma_0} \right) - \operatorname{erf} \left(i \frac{w_m - w_p}{\sqrt{2}} - \frac{1}{2\sqrt{2}} \frac{\Delta p_{sq}}{\sigma_0} \right) \right]$	$e^{-\frac{(w_m - w_p)^2}{2 \left(1 + \frac{\sigma_0^2}{\Delta p_s^2}\right)}} \frac{\sigma_0^2}{\sqrt{1 + \frac{\sigma_0^2}{\Delta p_s^2}}}$

Table 6.1 – Values of the parameters for the heralding measurements considered.

$$N = P_s \mathcal{N}_\pm^2(\beta) \left(\prod_{k=0}^{N-2} \mathcal{N}_\pm(\alpha_k) \right)^2, \quad W_{|\alpha\rangle\langle\beta|}(x, p) = \frac{e^{-\frac{1}{2}\left(\alpha+\beta-\frac{x}{\sigma_0}\right)^2} e^{-\frac{p^2}{2\sigma_0^2}} e^{-ip\frac{\alpha-\beta}{\sigma_0}}}{\left(\sigma_0\sqrt{2\pi}\right)^2}. \quad (6.25)$$

6.2.3 Protocol performances

6.2.3.1 Success probability

The explicit value of the success probability is given by:

$$P_s = \text{Tr}_{a,b} [\hat{\Pi}_b \otimes \hat{I}_a \hat{\rho}_{\text{BS}}^{n=0}] = \frac{1}{\mathcal{N}_\pm^2(\beta) \left(\prod_{k=0}^{N-2} \mathcal{N}_\pm(\alpha_k) \right)^2} \sum_{\mathbf{m}} \sum_{\mathbf{p}} (\pm 1)^{\mathbf{m}_\Sigma + \mathbf{p}_\Sigma} e^{-\frac{1}{2} [\mathcal{X}_{\Sigma, \mathbf{m}, \mathbf{p}}^2 + \mathcal{Y}_{\Sigma, \mathbf{m}, \mathbf{p}}^2]} \left(\mathcal{A}_{\mathbf{m}, \mathbf{p}} e^{-\frac{1}{2}(x_{\mathbf{m}} - x_{\mathbf{p}})^2} \pm \mathcal{B}_{\mathbf{m}, \mathbf{p}} e^{-\frac{1}{2}(x_{\mathbf{m}} - z_{\mathbf{p}})^2} \pm \mathcal{C}_{\mathbf{m}, \mathbf{p}} e^{-\frac{1}{2}(z_{\mathbf{m}} - x_{\mathbf{p}})^2} + \mathcal{D}_{\mathbf{m}, \mathbf{p}} e^{-\frac{1}{2}(z_{\mathbf{m}} - z_{\mathbf{p}})^2} \right). \quad (6.26)$$

6.2.3.2 Fidelity of the output state with a cat state

Our study shows that the protocol can be used to generate, among others, Schrödinger cat states of high amplitudes. By using the explicit expression of the output state we have derived in Equation 6.22, we can express its *likeness* with an even (resp. odd) Schrödinger cat state of amplitude γ with density matrix $\hat{\rho}_+(\gamma)$ (resp. $\hat{\rho}_-(\gamma)$) by using the fidelity as a comparison criterion. The expression for this fidelity reads:

$$\mathcal{F} = \text{Tr}_{0,a} [\hat{\rho}_{\text{out}} \hat{\rho}_\pm(\gamma)] = \frac{1}{P_s \mathcal{N}_\pm^2(\beta) \mathcal{N}_\pm^2(\gamma) \left(\prod_{k=0}^{N-2} \mathcal{N}_\pm(\alpha_k) \right)^2} \sum_{\mathbf{m}} \sum_{\mathbf{p}} (\pm 1)^{\mathbf{m}_\Sigma + \mathbf{p}_\Sigma} e^{-\frac{1}{2} [\mathcal{X}_{\Sigma, \mathbf{m}, \mathbf{p}}^2 + \mathcal{Y}_{\Sigma, \mathbf{m}, \mathbf{p}}^2]} \left[\mathcal{A}_{\mathbf{m}, \mathbf{p}} \left(e^{-\frac{1}{2} [(x_{\mathbf{m}} - \gamma)^2 + (x_{\mathbf{p}} - \gamma)^2]} \pm e^{-\frac{1}{2} [(x_{\mathbf{m}} - \gamma)^2 + (x_{\mathbf{p}} + \gamma)^2]} \right. \right. \\ \left. \pm e^{-\frac{1}{2} [(x_{\mathbf{m}} + \gamma)^2 + (x_{\mathbf{p}} - \gamma)^2]} + e^{-\frac{1}{2} [(x_{\mathbf{m}} + \gamma)^2 + (x_{\mathbf{p}} + \gamma)^2]} \right) \\ \pm \mathcal{B}_{\mathbf{m}, \mathbf{p}} \left(e^{-\frac{1}{2} [(x_{\mathbf{m}} - \gamma)^2 + (z_{\mathbf{p}} - \gamma)^2]} \pm e^{-\frac{1}{2} [(x_{\mathbf{m}} - \gamma)^2 + (z_{\mathbf{p}} + \gamma)^2]} \right. \\ \left. \pm e^{-\frac{1}{2} [(x_{\mathbf{m}} + \gamma)^2 + (z_{\mathbf{p}} - \gamma)^2]} + e^{-\frac{1}{2} [(x_{\mathbf{m}} + \gamma)^2 + (z_{\mathbf{p}} + \gamma)^2]} \right) \\ \pm \mathcal{C}_{\mathbf{m}, \mathbf{p}} \left(e^{-\frac{1}{2} [(z_{\mathbf{m}} - \gamma)^2 + (x_{\mathbf{p}} - \gamma)^2]} \pm e^{-\frac{1}{2} [(z_{\mathbf{m}} - \gamma)^2 + (x_{\mathbf{p}} + \gamma)^2]} \right. \\ \left. \pm e^{-\frac{1}{2} [(z_{\mathbf{m}} + \gamma)^2 + (x_{\mathbf{p}} - \gamma)^2]} + e^{-\frac{1}{2} [(z_{\mathbf{m}} + \gamma)^2 + (x_{\mathbf{p}} + \gamma)^2]} \right) \\ \left. + \mathcal{D}_{\mathbf{m}, \mathbf{p}} \left(e^{-\frac{1}{2} [(z_{\mathbf{m}} - \gamma)^2 + (z_{\mathbf{p}} - \gamma)^2]} \pm e^{-\frac{1}{2} [(z_{\mathbf{m}} - \gamma)^2 + (z_{\mathbf{p}} + \gamma)^2]} \right. \right. \\ \left. \left. \pm e^{-\frac{1}{2} [(z_{\mathbf{m}} + \gamma)^2 + (z_{\mathbf{p}} - \gamma)^2]} + e^{-\frac{1}{2} [(z_{\mathbf{m}} + \gamma)^2 + (z_{\mathbf{p}} + \gamma)^2]} \right) \right]. \quad (6.27)$$

6.3 CASE STUDY 1: PARALLEL SCHRÖDINGER CAT BREEDING

The proposed multiplexed single-stage protocol can be applied to the generation of large amplitude Schrödinger cat states, inspired by *cat breeding* iterative protocols. To perform such a generation, we simply consider here $N \geq 2$ identical Schrödinger cat input states of amplitude α in the $N - 1$ input modes $\varphi_k(\omega)$:

$$\forall k, \in \llbracket 0, N - 2 \rrbracket, |\psi'_k\rangle = |\psi_0\rangle = \frac{1}{\mathcal{N}_+} (|\alpha\rangle + |-\alpha\rangle), \quad (6.28)$$

where $\mathcal{N}_+ = \sqrt{2(1 + e^{-2|\alpha|^2})}$ is a normalization factor. Note that we restrict the discussion to even cat states, but similar reasoning is also valid with odd cat states. Then we set that each mode $\varphi_k(\omega)$ is of equal contribution in the generation process, namely $\forall k \in \llbracket 0, N - 2 \rrbracket$:

$$c_{k,0} = \int \varphi_k^*(\omega) \chi_0(\omega) d\omega = \frac{1}{\sqrt{N-1}}. \quad (6.29)$$

In this way, each input *feeding* cat $|\psi'_k\rangle$ will *breed* the input seed cat $|\psi_0\rangle$ by the same amount. Subsequently, homodyne conditioning is performed along the x quadrature (in-phase with the input states) around $x = 0$, within a given acceptance window $[-\Delta x/2, \Delta x/2]$. The analytical formula for the output Wigner function, given by [Equation 6.24](#), allows to predict the performances of the protocol as a function of key parameters such as r , N , α and the heralding width Δx . Many different metrics can be used to quantify the distance between an output state and a target state. Here, the fidelity of $\hat{\rho}_{\text{out}}$ with the nearest ideal Schrödinger cat state of amplitude λ is used.

6.3.1 Beam splitter reflectivity

The aforementioned fidelity of the output state is plotted in [Figure 6.4](#)-(a) to (d) for $N = 2, 3, 6$ and 8 input Schrödinger cat states of amplitude $\alpha = 3$, as a function of the beam splitter reflectivity r and of the output state amplitude γ .

These plots clearly reveal that the output amplitude of the cat state in mode $\chi_0(\omega)$ that corresponds to optimal fidelities with $\hat{\rho}_{\text{out}}$ grows with the number of input states. This successfully proves the *breeding* of the input Schrödinger cat states. [Figure 6.4](#) also shows that the reflectivity should be optimized in a non-trivial way, according to the number of input breeding states, in order to maximize the output state fidelity with high amplitude Schrödinger cat state.

To gain a qualitative intuition on the quality of the multimode breeding operation, the Wigner functions of the corresponding output states are plotted in [Figure 6.4](#)-(e) to (h), showing their strong non-classical signature, as the Wigner functions contain oscillations with negative values. To be more quantitative on this result, the numerical values of fidelity, optimal reflectivity and output Schrödinger cat state amplitudes are also written on [Figure 6.4](#)-(a) to (d), revealing the very high fidelities of the output states with high amplitude Schrödinger cat states. In addition, it confirms that the

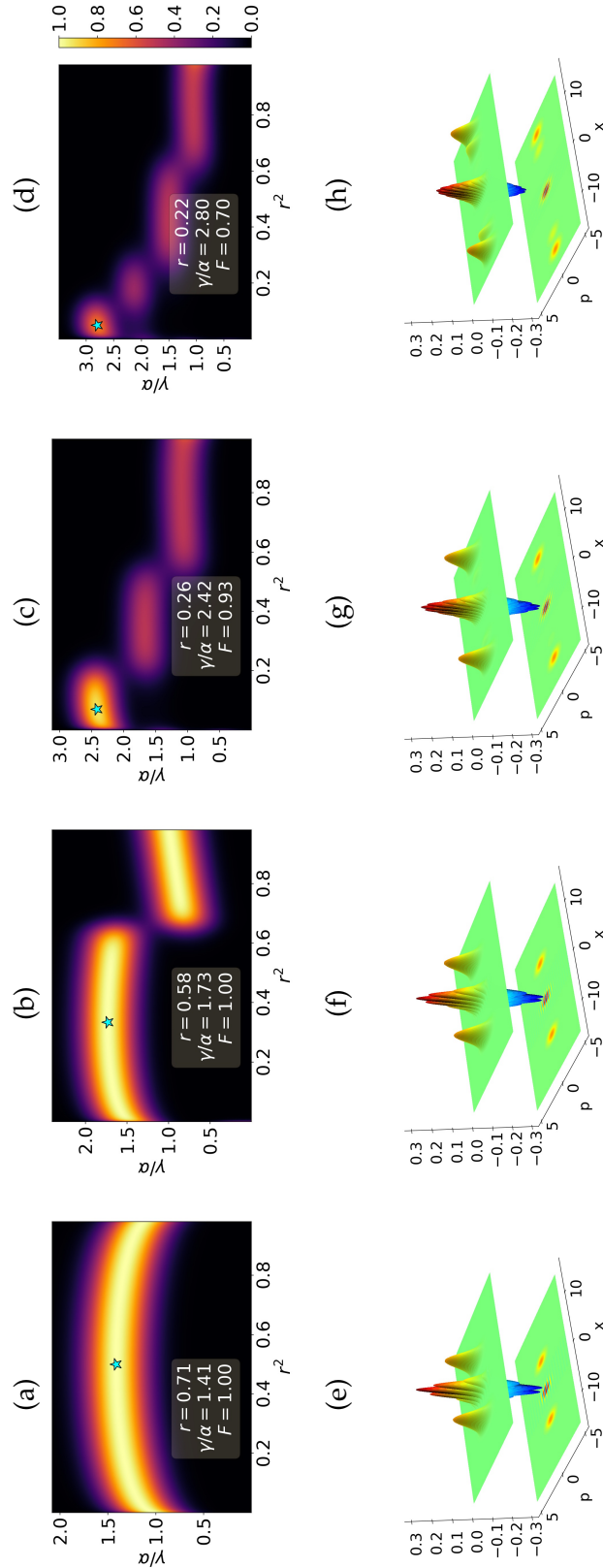


Figure 6.4 – Fidelity of the output state with a cat state of amplitude γ as a function of the beam splitter reflectivity r , for (a) $N = 2$, (b) $N = 3$, (c) $N = 6$ and (d) $N = 8$ input cat states of amplitude $\alpha = 3$. In each plot, a star spots the highest fidelity point, and the corresponding parameters are given in the insets. The Wigner functions corresponding to this maximal fidelity point are represented in (e), (f), (g), (h), respectively.

amplitude of the output Schrödinger cat state increases with N , with a scaling of the order of $\gamma \sim \sqrt{N}\alpha$.

6.3.2 Amplitude of the input states

The protocol is also sensitive to the amplitude of the input cat states. This is illustrated in Figure 6.5, where the output state fidelity with the nearest cat state is represented as a function of the input Schrödinger cat states amplitude α , for different numbers of input states N . Two important trends shall be noticed: (i) for a given α , increasing N decreases the overall output state fidelity. However, (ii) increasing α for a given N leads to an increased global fidelity. For instance, to create states with 99% fidelity with $N = 2$, an input amplitude $\alpha = 1.13$ is sufficient, whereas $\alpha = 2.49$ is required to reach the same fidelity with $N = 4$ input states. In the case of even cat states that are considered here, there is also an increase of the fidelity for vanishing α simply because vacuum is a perfect even cat state with zero amplitude, a case of no interest for us.

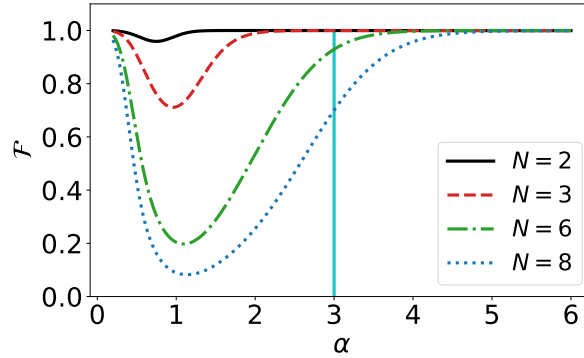


Figure 6.5 – Fidelity of the output state with the nearest Schrödinger cat state as a function of α , for different N . The cases represented in Figure 6.4 correspond to the vertical blue line ($\alpha = 3$).

6.3.3 Comparison with the iterative cat breeding protocol

Interestingly, we can draw a direct parallel with the iterative cat breeding protocol, where $N - 1$ heralding steps are performed on N input resources. The main difference, however, is that the multimode protocol that we propose here is inevitably accompanied with information loss due to partial overlap of the spectral modes $\varphi_k(\omega)$ with the output mode of interest $\chi_0(\omega)$. Equation 6.29 directly shows that each mode $\varphi_i(\omega)$ overlaps only partially with $\chi_0(\omega)$, therefore, all of the components of the input states $|\psi'_i\rangle$ along $\chi_{l>0}(\omega)$ are purely lost during the process, where $\{\chi_l(\omega)\}_{l \in \mathbb{N}}$ constitutes a complete spectral basis. Therefore, the output state $\hat{\rho}_{\text{out}}$ cannot be a pure state as long as more than two modes are populated in total.

To give an intuitive model, we propose a simple parallel between spatial and spectral modes: in Figure 6.3, the spectral component $\chi_0(\omega)$ of the input state in the spatial mode a and interfering with the one at the input port b of the beam splitter can actually

be simply modeled as the output state of an $N - 1$ input / $N - 1$ output beam splitter transformation, where $N - 2$ outputs are lost in the environment. This transformation is exactly the one depicted in Figure 6.2 for input states $|\psi_0\rangle$ to $|\psi_{N-2}\rangle$, with $\tau_i = 1/\sqrt{i+2}$ so as to obtain $c_{0,k} = 1/\sqrt{N-1}$. In other words, our protocol is equivalent to the iterative breeding scheme of Figure 6.2, where only the last heralding step $x = x_{N-1}$ is performed and all the other ones are simply ignored. The direct consequence for this is that the overall success probability of the protocol is increased by several orders of magnitude as compared to the iterative scheme. This is illustrated in Figure 6.6, where the success probability of our scheme, for input Schrödinger cat states of amplitude $\alpha = 3$ and $N = 4$, is plotted, in comparison with the iterative scheme of Figure 6.2 in the case where all the heralding widths are identical. The cost obviously is the overall fidelity, which is degraded in the multimode case, but nevertheless remains very high, as we have seen in Figure 6.4. The multimode protocol therefore takes advantage of the robustness of the breeding protocol for imperfect heralding at sufficiently high Schrödinger cat state amplitudes.

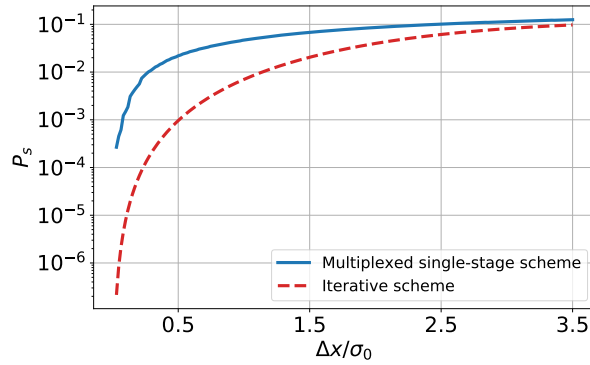


Figure 6.6 – Comparison between the success probability of the multimode (multiplexed single-stage) scheme and the iterative scheme for $N = 4$, as a function of the heralding window Δx normalized to the shot noise standard deviation σ_0 .

6.4 CASE STUDY 2: GKP STATE PREPARATION

6.4.1 Definition

First introduced in [148], GKP states are extremely important quantum states as they allow to encode quantum information in a continuous-variable way with the ability to implement error correcting codes. Contrary to Schrödinger cat states (where digits of information are encoded in coherent states: $|0\rangle = |\alpha\rangle$ and $|1\rangle = |-\alpha\rangle$), in the two dimensional case, digits $|\bar{0}\rangle = \sum_{k=-\infty}^{\infty} |x = 2ka\rangle$ and $|\bar{1}\rangle = \sum_{k=-\infty}^{\infty} |x = (2k+1)a\rangle$ as well as their superposition $|\bar{0}\rangle + |\bar{1}\rangle$ and $|\bar{0}\rangle - |\bar{1}\rangle$ can be discriminated more efficiently by means of a simple homodyne measurement along the \hat{x} and \hat{p} quadratures, respectively. These two digits ($|\bar{0}\rangle$ and $|\bar{1}\rangle$) being non-physical, an approximation of them can be given, in terms of wave-function, as:

$$\langle x|\tilde{0}\rangle = \frac{1}{\mathcal{N}_0} \sum_{k \in \mathbb{Z}} e^{-\frac{1}{2\sigma^2}(ka)^2} e^{-\frac{1}{2\sigma_x^2}(x-ka)^2}, \quad (6.30)$$

and:

$$\langle x|\tilde{1}\rangle = \frac{1}{\mathcal{N}_1} \sum_{k \in \mathbb{Z}} e^{-\frac{1}{2\sigma^2}(k+\frac{1}{2})^2 a^2} e^{-\frac{1}{2\sigma_x^2}[x-(k+\frac{1}{2})a]^2}, \quad (6.31)$$

with:

$$\mathcal{N}_0^2 = \sigma_x \sqrt{\pi} \sum_{k \in \mathbb{Z}} \sum_{m \in \mathbb{Z}} e^{-\frac{a^2}{2} \left[\frac{k^2+m^2}{\sigma^2} + \frac{(k-m)^2}{2\sigma_x^2} \right]}, \quad (6.32)$$

and:

$$\mathcal{N}_1^2 = \sigma_x \sqrt{\pi} \sum_{k \in \mathbb{Z}} \sum_{m \in \mathbb{Z}} e^{-\frac{a^2}{2} \left[\frac{(k+\frac{1}{2})^2 + (m+\frac{1}{2})^2}{\sigma^2} + \frac{(k-m)^2}{2\sigma_x^2} \right]}. \quad (6.33)$$

Using the relation between the quadrature eigenstates $|x\rangle$ and $|p\rangle$:

$$|p\rangle = \frac{1}{2\sigma_0 \sqrt{\pi}} \int_{-\infty}^{\infty} e^{\frac{ixp}{2\sigma_0^2}} |x\rangle dx, \quad (6.34)$$

one can show that:

$$\langle p|\tilde{0}\rangle = \frac{\sigma_x}{\mathcal{N}_0 \sigma_0 \sqrt{2}} \sum_{k \in \mathbb{N}} e^{-\frac{1}{2\sigma^2}(ka)^2} e^{-\frac{\sigma_x^2 p^2}{8\sigma_0^4}} (2 - \delta_{k,0}) \cos\left(\frac{kap}{2\sigma_0^2}\right), \quad (6.35)$$

and:

$$\langle p|\tilde{1}\rangle = \frac{\sigma_x}{\mathcal{N}_1 \sigma_0 \sqrt{2}} \sum_{k \in \mathbb{N}} e^{-\frac{1}{2\sigma^2}(k+\frac{1}{2})^2 a^2} e^{-\frac{\sigma_x^2 p^2}{8\sigma_0^4}} (2 - \delta_{k,0}) \cos\left(\frac{(k+\frac{1}{2})ap}{2\sigma_0^2}\right), \quad (6.36)$$

with $\delta_{k,0}$ being the Kronecker delta. In [Figure 6.7](#), the probability distributions of the quadrature \hat{x} (a) and \hat{p} (b) are plotted for the states $|\tilde{0}\rangle$ and $|\tilde{1}\rangle$ (a) and for $|\tilde{0}\rangle + |\tilde{1}\rangle$ and $|\tilde{0}\rangle - |\tilde{1}\rangle$ (b), respectively.

As it can be seen, for the states $|\tilde{0}\rangle$ and $|\tilde{1}\rangle$, the probability distribution $P(x)$ of the quadrature \hat{x} is a comb with Gaussian "teeth" of a variance $\sigma_x^2/\sqrt{2}$, modulated by a larger Gaussian function with variance $\sigma^2/\sqrt{2}$ ([Figure 6.7\(a\)](#)). Smaller is σ_x , better is the discrimination between the states $|\tilde{0}\rangle$ and $|\tilde{1}\rangle$ with homodyne measurement. On the other hand, the same behaviour is obtained with the probability distribution $P(p)$ for the states $|\tilde{0}\rangle + |\tilde{1}\rangle$ and $|\tilde{0}\rangle - |\tilde{1}\rangle$ ([Figure 6.7\(b\)](#)), allowing to discriminate these two states with a homodyne measurement on the quadrature \hat{p} . The Wigner functions $W_{\tilde{0}}(x, p)$ and $W_{\tilde{1}}(x, p)$ of the states $|\tilde{0}\rangle$ and $|\tilde{1}\rangle$, respectively, are given by:

$$W_{\tilde{0}}(x, p) = \frac{\sigma_x}{2\mathcal{N}_0^2 \sigma_0^2 \sqrt{\pi}} e^{-\frac{x^2}{\sigma_x^2}} e^{-\frac{\sigma_x^2}{4\sigma_0^4} p^2} \sum_{k \in \mathbb{Z}} \sum_{m \leq k} e^{-\frac{1}{2} \left(\frac{1}{\sigma^2} + \frac{1}{\sigma_x^2} \right) (k^2+m^2) a^2} e^{-\frac{1}{4\sigma_x^2} (k-m)^2 a^2} e^{\frac{1}{\sigma_x^2} (k+m) ax} \times (2 - \delta_{k,m}) \cos\left(\frac{k-m}{2\sigma_0^2} ap\right), \quad (6.37)$$

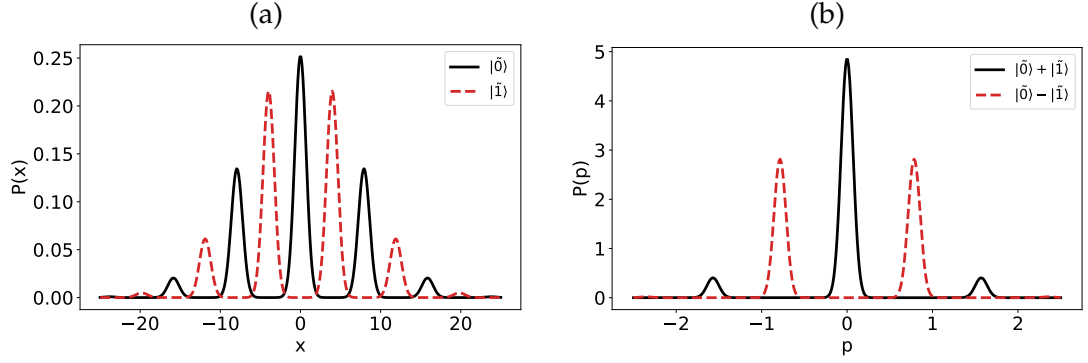


Figure 6.7 – (a): The probability distribution $P(x)$ of the quadrature \hat{x} for the states $|\tilde{0}\rangle$ (solid black curve) and $|\tilde{1}\rangle$ (dashed red curve). (b): The probability distribution $P(p)$ of the quadrature \hat{p} for the states $|\tilde{0}\rangle + |\tilde{1}\rangle$ (solid black curve) and $|\tilde{0}\rangle - |\tilde{1}\rangle$ (dashed red curve).

and:

$$W_{\tilde{1}}(x, p) = \frac{\sigma_x}{2\mathcal{N}_1^2 \sigma_0^2 \sqrt{\pi}} e^{-\frac{x^2}{\sigma_x^2}} e^{-\frac{\sigma_x^2}{4\sigma_0^4} p^2} \sum_{k \in \mathbb{Z}} \sum_{m \leq k} e^{-\frac{1}{2} \left(\frac{1}{\sigma^2} + \frac{1}{\sigma_x^2} \right) \left[\left(k + \frac{1}{2} \right)^2 + \left(m + \frac{1}{2} \right)^2 \right] a^2} e^{-\frac{1}{4\sigma_x^2} (k-m)^2 a^2} \times e^{\frac{1}{\sigma_x^2} (k+m+1)ax} (2 - \delta_{k,m}) \cos \left(\frac{k-m}{2\sigma_0^2} ap \right). \quad (6.38)$$

Figure 6.9 illustrate these Wigner functions in the case of $\sigma = 10$, $\sigma_x = 1$ and $a = 2\sqrt{5\pi}$.

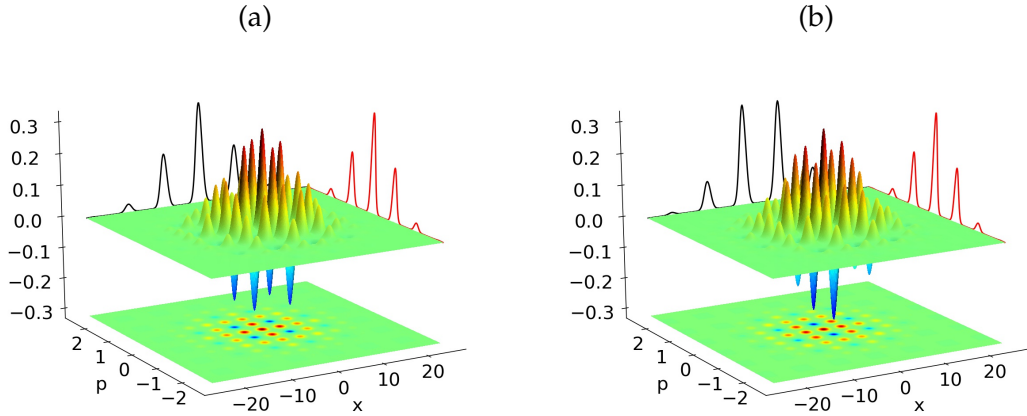


Figure 6.8 – Wigner function of the approximated GKP states $|\tilde{0}\rangle$ (a) and $|\tilde{1}\rangle$ (b) and the corresponding quadrature distributions $P(x)$ (black) and $P(p)$ (red) in the case of $\sigma = 10$, $\sigma_x = 1$ and $a = 2\sqrt{5\pi}$.

6.4.2 GKP states production with the proposed protocol

In addition to the generation of Schrödinger cat states, our protocol can also advantageously be applied to for the generation of more complex states such as the GKP states [148]. They were recently generated and used in trapped ions [165] and superconducting circuits [166], but still remain out of reach of all-optical protocols. Here, we can use the same protocol as the one depicted in section 6.3 ($N - 1$ input cat states in modes φ_k and one cat state in mode χ_0 , all of amplitude α), with the only difference that homodyne conditioning is performed along $p = 0$. Such conditioning has already been investigated in the context of all-optical generation of GKP with iterative protocol [65, 162]. We show here that it can be transposed to our multiplexed approach.

Figure 6.9 shows the shape of the Wigner function of the output state for $N = 3$ (a) and $N = 4$ (b), revealing the grid structure specific to GKP states.

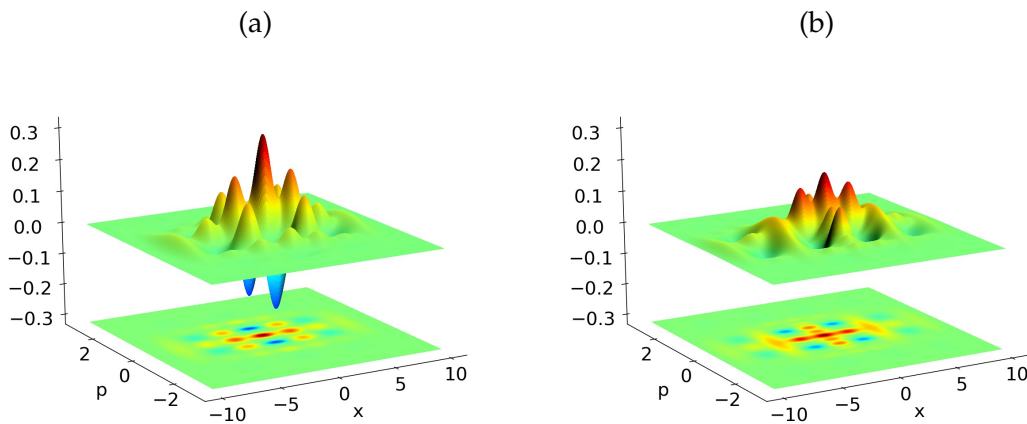


Figure 6.9 – Wigner function of the output state with $N = 3$ (a) and $N = 4$ (b) input Schrödinger cat states of amplitude $\alpha = 3$.

In Figure 6.10, the amplitude of the output state along the quadrature \hat{p} (separation between the teeth of the quadrature comb) is plotted as a function of the number of input Schrödinger cat states N . For each case (a given N), the fidelity between the output state and the nearest GKP state as well as the optimal reflectivity r of the beam splitter are given.

This plot shows that augmenting the amount of input resources indeed increases the amplitude of the output state along the quadrature \hat{p} ($1/a$), while requiring an optimization of the beam splitter reflectivity r . Similarly to the case of Schrödinger cat state generation, the fidelity of the output state decreases with respect to the number N of input resources.

6.5 CONCLUSION

In this chapter, we have proposed and discussed an innovative protocol for the generation of non-Gaussian states of light. Our scheme is inspired by iterative protocols but takes advantage of multiplexing capabilities of photonics resources. It relies on the

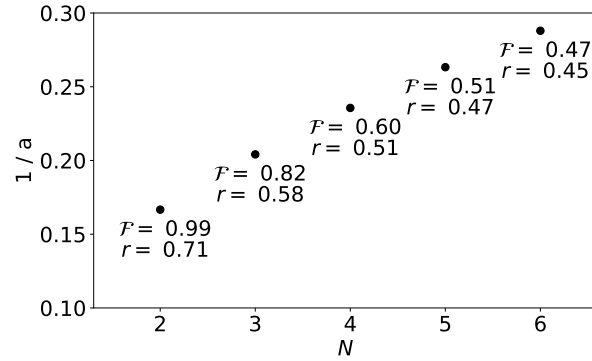


Figure 6.10 – The amplitude of the approximated GKP output state along the quadrature \hat{p} ($1/a$) as a function of the number of input Schrödinger cat states N . For each case, the fidelity between the output state and the nearest GKP state as well as the optimal value r of the beam splitter reflectivity are given in the plot.

use of multiple states in a single spatial mode but multiplexed in an other degree of freedom, mixed with a resource state whose mode partially overlaps all input states. By performing a homodyne conditioning after mixing the states at a beam splitter, complex output states can be produced. The major strength of our proposal is that no cascade manipulation steps are required for the state breeding, therefore strongly simplifying the experimental implementation in a one-shot scheme, and allowing to access high-success rates. We have shown that frequency multiplexing can be used for the generation of high quality and high amplitude Schrödinger cat and GKP states, by using as input states small-amplitude Schrödinger cat states, or alternatively, readily accessible experimental resources such as multiplexed single photon Fock states (discussed in [Appendix G](#)). Note that current state-of-the-art nonlinear sources offer the capability for generating such states by providing the native generation of frequency multiplexed single- and two-mode squeezing. Due to its high efficiency and simplified implementation as well as to the possibility of implementing it with already available experimental resources, we believe that our approach to non-Gaussian state preparation represents a major breakthrough in the domain of non-classical photonic state generation, and will open a wide range of applications.

Part IV

TOWARDS HIGH DIMENSION INTEGRATED QUANTUM
OPTICS

SILICON NITRIDE CHIP CHARACTERIZATION FOR MULTIMODE QUANTUM STATE GENERATION

7.1	Silicon nitride photonic chip	152
7.1.1	Micro-ring resonator	152
7.1.2	Chip structure	152
7.2	Micro-ring resonators characterization	153
7.2.1	Propagation losses	154
7.2.2	Quality factor	155
7.3	Kerr frequency comb generation	157
7.4	Conclusion and perspectives	159

Continuous-variable (CV) multimode entangled states are at the heart of many quantum information applications such as quantum computation [167–169] and communication [170]. Among the various possible platforms enabling quantum technologies, silicon (Si) and silicon nitride (Si_3N_4) combine optical linear and nonlinear properties with the possibility of high integration density. In particular, low-loss and high confinement Si and Si_3N_4 waveguides [171, 172] enable the creation and manipulation of high quality quantum states with high fidelities [173]. Integrated micro-ring resonators are of particular interest, as they allow to produce highly multimode quantum frequency combs via four-wave-mixing (FWM) process and optical parametric oscillation [174]. They have been theoretically investigated in both continuous-wave (CW) [175–177] and pulsed [178] regimes. Experimental production and characterization of two-mode intensity and quadrature CV entangled quantum state has been reported in more recent works [93, 179, 180].

In this chapter, we present the first characterization results of low-loss micro-ring resonators. This work is in collaboration with the CEA-Leti laboratory in Grenoble, C2N of Paris-Saclay and the FEMTO-ST institute. It aims at experimentally investigate high-dimension entanglement in a Kerr frequency comb produced by Si_3N_4 micro-ring resonators. In [section 7.1](#), we present the structure of the Si_3N_4 photonic chip. Then, in [section 7.2](#), we give the first experimental results of propagation losses and quality factors characterization. After that, generated Kerr frequency comb is shown in [section 7.3](#). The chapter is concluded and perspectives are given in [section 7.4](#).

7.1 SILICON NITRIDE PHOTONIC CHIP

7.1.1 Micro-ring resonator

An optical micro-ring resonator (μ -RR) is a closed-loop waveguide in which the intensity of a resonant light is built up thanks to constructive interferences. Light is coupled to/from the μ -RR using one or multiple waveguides via evanescent wave coupling. In addition to optical and thermo-optical properties, a unidirectional coupled μ -RR (coupling with only one waveguide) is mainly characterized by three geometric parameters, namely the radius R of the μ -RR, the width W of the ring and the coupling waveguides, and the gap G , defined as the distance between the coupling waveguide and the μ -RR. These geometric parameters are depicted in Figure 7.1-(a).

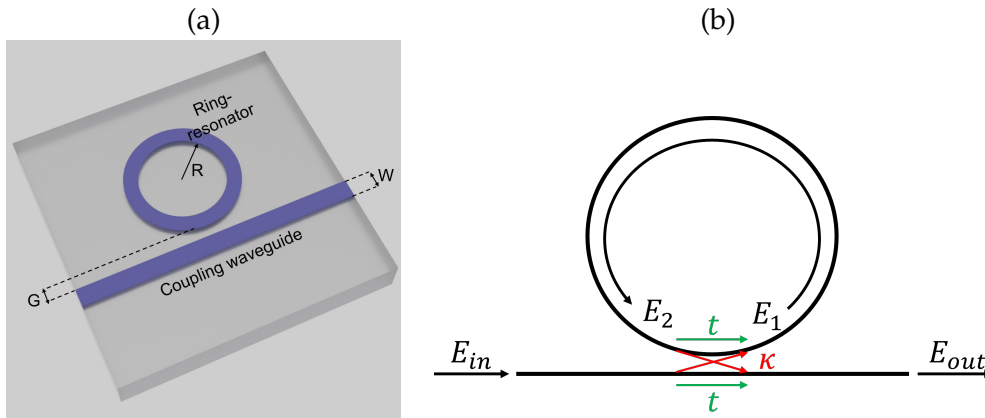


Figure 7.1 – (a): Geometric parameters of a μ -RR (R : ring radius, W : waveguide width, G : gap). (b): Interacting fields within a μ -RR.

The radius R defines the free spectral range (FSR) of the resonator, and thus, the resonant wavelengths whereas the width W and the gap G determine the coupling parameters κ and t , connecting the interacting fields shown in Figure 7.1-(b) through the following matrix relation [181]:

$$\begin{pmatrix} E_{out} \\ E_1 \end{pmatrix} = \begin{pmatrix} t & \kappa \\ -\kappa^* & t^* \end{pmatrix} \begin{pmatrix} E_{in} \\ E_2 \end{pmatrix}, \quad (7.1)$$

with $|\kappa|^2 + |t|^2 = 1$. Note that the radius R affects also the coupling parameters as the interaction distance between the coupling waveguide and the μ -RR changes with respect to R .

7.1.2 Chip structure

The characterization work presented in this chapter was performed on a low-loss silicon nitride (Si_3N_4) photonic chip, designed and fabricated by CEA-Leti [182]. The structure of this photonic chip is shown in Figure 7.2.

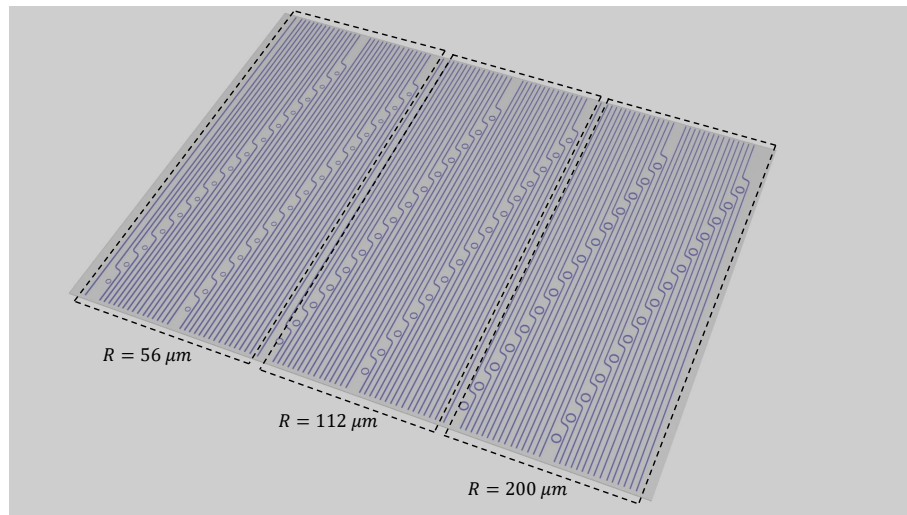


Figure 7.2 – The structure of the Si_3N_4 photonic chip. In each group of 30 μ -RRs with a given radius, the width W and the gap G vary. See text for details.

It contains mainly three groups of 30 μ -RRs each with different geometric parameters. In each group, the radius R of the μ -RRs is fixed ($R = 56 \mu\text{m}$, $R = 112 \mu\text{m}$ and $R = 200 \mu\text{m}$) whereas the waveguides width W and the gap G vary ($W = 1.4 \rightarrow 1.7 \mu\text{m}$ and $G = 300 \rightarrow 600 \text{ nm}$).

7.2 MICRO-RING RESONATORS CHARACTERIZATION

In this section, we present the characterization of the group of μ -RRs with a radius $R = 112 \mu\text{m}$, which corresponds to a free spectral range of around 200 GHz. The characterization setup is shown in [Figure 7.3](#).

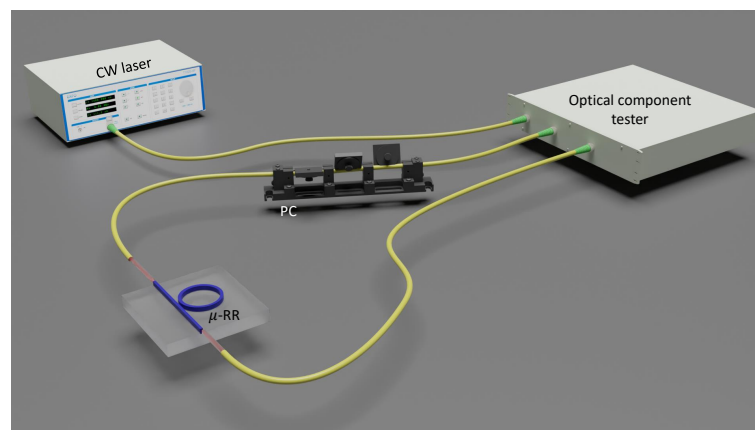


Figure 7.3 – Experimental setup for μ -RR characterization. PC: polarization controller.

An optical component tester (CT440 from EXFO) controls the wavelength of a high power continuously tunable CW telecom laser (T100S-HP from EXFO), whose output passes through the CT440 and then is sent to the μ -RR under characterization. At the input of the Si_3N_4 chip, the CW telecom beam is controlled in polarization and then

injected into the coupling waveguide using a micro-lensed fiber with a spot diameter of $2\mu\text{m}$ from OZ Optics. At the output of the chip, light is collected using another micro-lensed fiber and then sent to the CT440 photodetector. The transmission signal is then stored on a computer for post-processing.

7.2.1 Propagation losses

Optical losses are critical for CV quantum state generation and manipulation, and thus, choosing a configuration that minimizes these losses is an important task. For this purpose, we start by characterizing losses for both transverse electric (TE) and transverse magnetic (TM) polarization modes. Figure 7.4 shows the transmission spectrum, in the wavelength range from 1535 nm to 1565 nm, of a 200 GHz μ -RR with $W = 1.4\mu\text{m}$ and $G = 550\text{ nm}$.

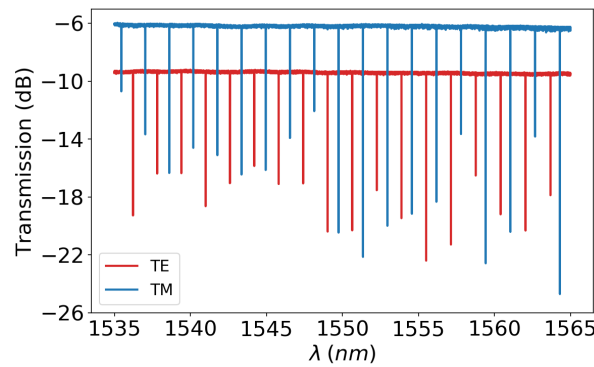


Figure 7.4 – Transmission spectrum of a μ -RR with a radius $R = 112\mu\text{m}$ (a free spectral range of 200 GHz), a width $W = 1.4\mu\text{m}$ and a gap $G = 550\text{ nm}$ for both the TE (red) and TM (blue) polarization modes.

As it can be seen, we observe a transmission of -6 dB for the TM polarization mode and -9 dB for the TE one out of the resonant wavelengths. As these values are not compatible with propagation losses in a 20 mm long Si_3N_4 coupling waveguide, these losses are mainly due to coupling efficiency at the input/output of the photonic chip. The difference between the two coupling efficiencies is related to the fact that the coupling waveguide section is rectangular ($H < W$ where H is the waveguide height), which leads to different fundamental TE and TM transverse modes. In both cases, the coupling losses being at least 3 dB per input/output, light at the output of the chip must be collected in a free space configuration to increase the collection efficiency and to be able to exploit the produced quantum light. In this case, the chosen polarization mode will be the one having less propagation losses inside the μ -RR. To estimate these losses, we adopt a simple model making the analogy between a ring and a Fabry-Pérot resonators [183]. In this case, and by defining the two parameters δ and δ_p as:

$$|t|^2 = e^{-\delta} \quad (7.2a)$$

$$|t_p|^2 = e^{-\delta_p}, \quad (7.2b)$$

where $|t_p|^2$ is the power transmission due to propagation losses inside the μ -RR after a round trip, the resonator finesse can be approximated, for low-loss cavities, as [183]:

$$F \approx \frac{2\pi}{\delta + \delta_p}. \quad (7.3)$$

Figure 7.5 shows a Lorentzian fit of the resonance around $\lambda = 1550$ nm for the TE (a) and TM (b) polarization modes.

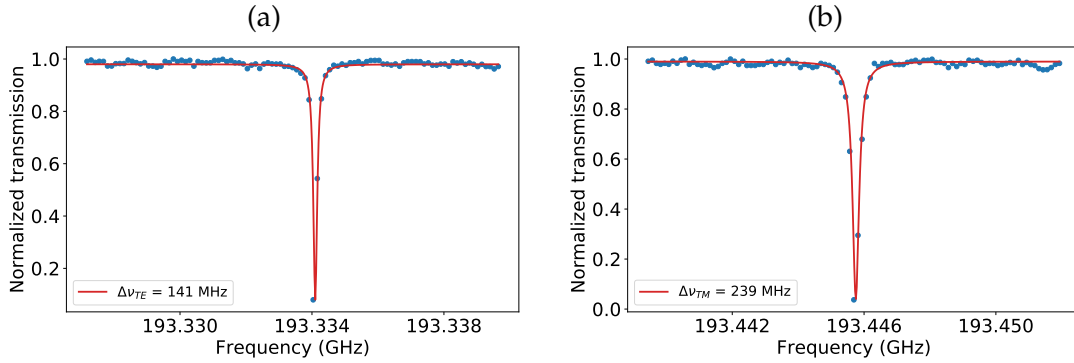


Figure 7.5 – Lorentzian fit of the resonance around $\lambda = 1550$ nm for the TE (a) and TM (b) polarization modes in the case of a μ -RR with $R = 112 \mu\text{m}$, $W = 1.4 \mu\text{m}$ and $G = 550$ nm.

The fit gives a linewidth of 141 MHz for the TE polarization mode and 239 MHz for the TM one, which corresponds to a finesse $F_{TE} = 1426$ ($\delta + \delta_p \approx 0.44\%$) and $F_{TM} = 837$ ($\delta + \delta_p \approx 0.75\%$) for the TE and TM polarization modes, respectively. On the other hand, the depth of the resonance, defined as the minimum value T_{min} of the normalized power transmission, can be approximated as [183]:

$$T_{min} \approx \left(1 - 2\frac{\delta}{\delta + \delta_p}\right)^2, \quad (7.4)$$

which allows to retrieve both the coupling parameter $|t|^2$ and the propagation transmission $|t_p|^2$ via Equation 7.2. The fitting curve in Figure 7.5 gives $\delta_p^{TE} = 0.28\%$ and $\delta_p^{TM} = 0.45\%$, which corresponds to propagation losses of 0.17 dB/cm for the TE polarization mode and 0.29 dB/cm for the TM one. This gives a coupling parameter $|t|^2 = 99.8\%$ and a propagation transmission $|t_p|^2 = 99.7\%$ for the TE mode and $|t|^2 = 99.7\%$ and $|t_p|^2 = 99.6\%$ for the TM mode.

7.2.2 Quality factor

Using the same setup depicted in Figure 7.3, we now perform a quality factor (Q) measurement of all μ -RRs with a radius $R = 112 \mu\text{m}$ for TE and TM polarization modes. To do so, the transmission spectra for different widths W and gaps G are recorded. Figure 7.6 shows this spectra for the TE (a) and TM (b) polarization modes.

For each particular geometric configuration (a given W and G), resonance dips between $\lambda = 1535$ nm and $\lambda = 1565$ nm are fitted with Lorentzian function. The quality factor Q , given by:

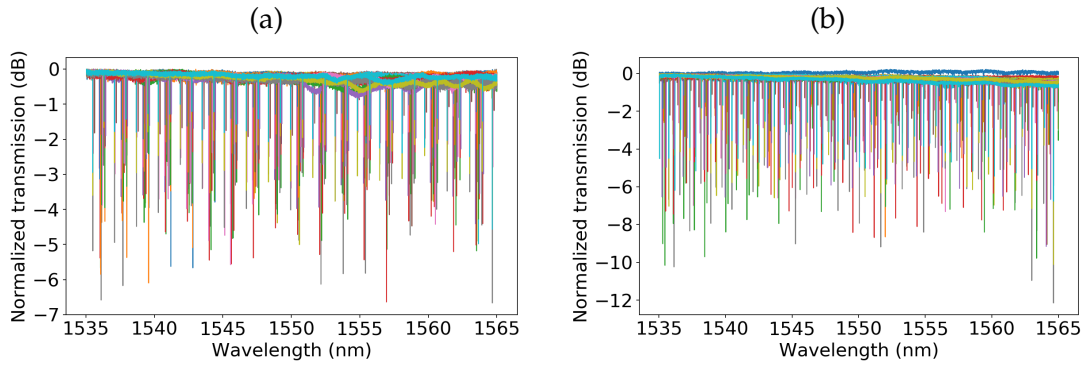


Figure 7.6 – Normalized transmission spectra of μ -RRs with $R = 112 \mu\text{m}$ and different W and G for the TE (a) and TM (b) polarization modes.

$$Q = \frac{\nu_0}{\Delta\nu}, \tag{7.5}$$

can then be extracted. Here, ν_0 is the resonant frequency and $\Delta\nu$ is the resonance linewidth. In Figure 7.7, the measured Q is plotted as a function of the resonance wavelengths for both TE and TM polarization modes in the case of a μ -RR with $R = 112 \mu\text{m}$, $W = 1.4 \mu\text{m}$ and $G = 550 \text{ nm}$.

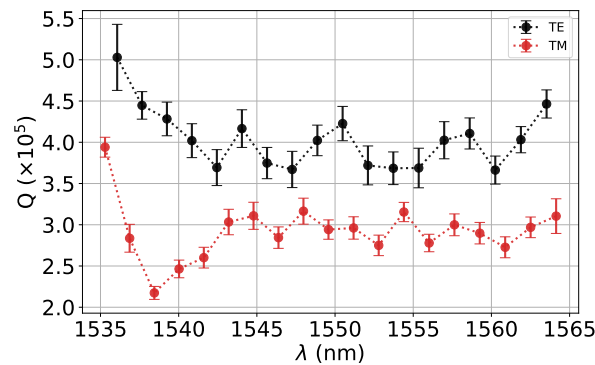


Figure 7.7 – The quality factor Q as a function of the resonance wavelengths for the TE (black) and TM (red) polarization modes in the case of a μ -RR with $R = 112 \mu\text{m}$, $W = 1.4 \mu\text{m}$ and $G = 550 \text{ nm}$.

This result shows a better Q for the TE polarization mode compared to the TM one for the considered μ -RR ($R = 112 \mu\text{m}$, $W = 1.4 \mu\text{m}$ and $G = 550 \text{ nm}$). This is an expected result since propagation losses, quantified in the previous paragraph, are found to be lower for the TE mode, which should be the case based on the chip design. Such a measurement is repeated for all μ -RRs with $R = 112 \mu\text{m}$ (different W and G). The obtained results are shown in Figure 7.8 for TE (a) and TM (b) polarization modes. Each point in Figure 7.8 is obtained by computing the mean value of the measured quality factors between $\lambda = 1535 \text{ nm}$ and $\lambda = 1565 \text{ nm}$.

It is important to note that these measured Q , called loaded quality factor, account for both the propagation losses (intrinsic losses) and the coupling losses between the

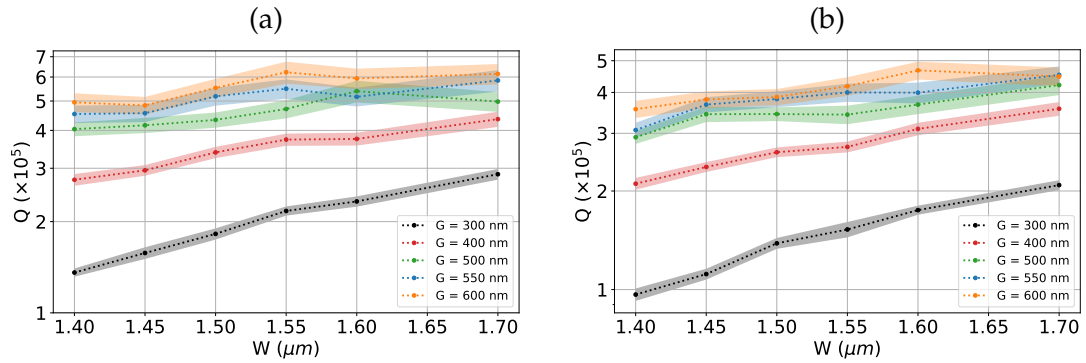


Figure 7.8 – The measured quality factor Q as a function of the width W of the coupling and ring waveguides for different values of the gap G . (a): TE polarization mode, (b): TM polarization mode.

waveguide and the μ -RR. It can be expressed as a function of the intrinsic quality factor Q_i and the coupling quality factor Q_c as [184]:

$$\frac{1}{Q} = \frac{1}{Q_i} + \frac{1}{Q_c}. \quad (7.6)$$

As shown in Figure 7.8, for a given gap G , the quality factor increases with respect to the width W . This can be explained as following; increasing the width of the waveguides reduces the amount of evanescent fields, and thus, reduces the coupling losses κ between the coupling waveguide and the μ -RR. In this case, the coupling quality factor Q_c increases and the loaded quality factor Q approaches the intrinsic one (Q_i). The same reasoning can be applied to explain the effect of increasing the gap G for a given width W . The bigger the gap G , the lower the coupling losses κ , which leads to an increased coupling and loaded quality factors.

7.3 KERR FREQUENCY COMB GENERATION

Measurement results presented in the previous section show a measured loaded quality factor up to 600000 for the TE polarization mode. The association of this high Q and the third order nonlinearity within the Si_3N_4 μ -RR allows to produce the so called Kerr frequency comb via four wave mixing (FWM) process with relatively low pump power. Figure 7.9 shows the experimental setup for frequency comb generation.

A tunable CW laser (T100S-HP from EXFO) is amplified via an Erbium Doped Fiber Amplifier (EDFA) and then injected into the coupling waveguide (TE polarization mode) using a micro-lensed fiber. The output of the μ -RR ($R = 112 \mu\text{m}$, $W = 1.4 \mu\text{m}$ and $G = 550 \text{ nm}$) is collected using another micro-lensed fiber and then sent to an optical spectrum analyzer (OSA). Figure 7.10 shows the μ -RR output spectrum for different pump powers.

A well known Kerr frequency comb creation dynamics can be observed here [185]. When the pump power just goes above threshold, a primary comb is created via degenerate and non-degenerate four-wave-mixing process (see Figure 7.11). This primary frequency lines are separated by several cavity FSR. Once the power circulating inside

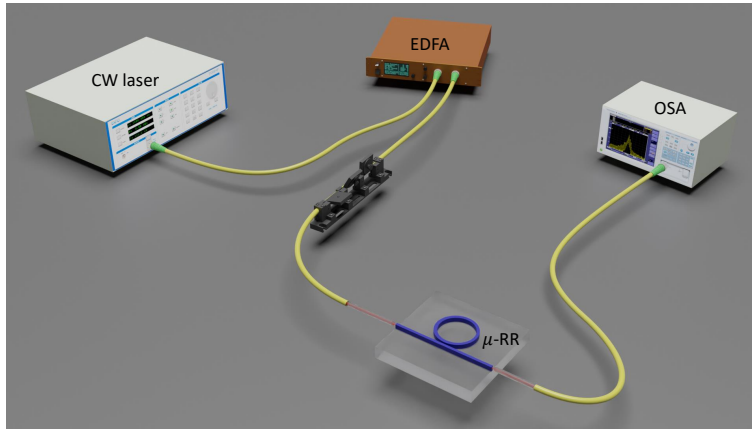


Figure 7.9 – Experimental setup for Kerr frequency comb generation using an Si_3N_4 $\mu\text{-RR}$. EDFA: Erbium Doped Fiber Amplifier, OSA: Optical Spectrum Analyzer.

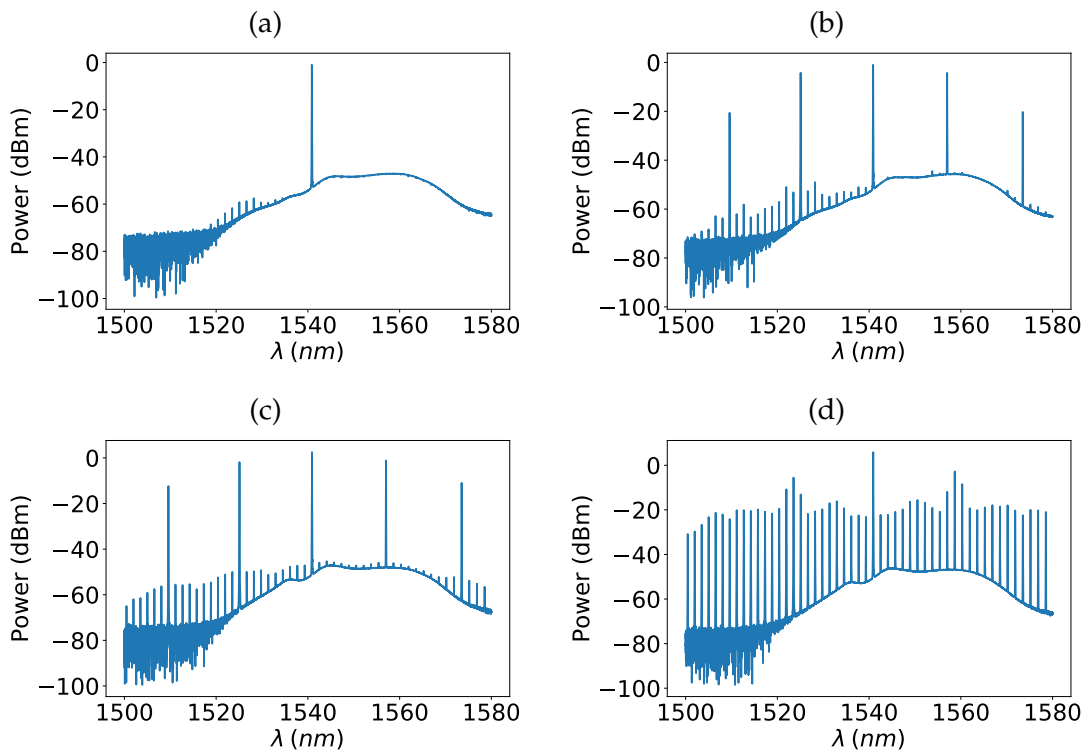


Figure 7.10 – The spectrum of a $\mu\text{-RR}$ output ($R = 112 \mu\text{m}$, $W = 1.4 \mu\text{m}$ and $G = 550 \text{nm}$) for different pump powers. (a): $P_{in} = 16 \text{mW}$, (b): $P_{in} = 26 \text{mW}$, (c): $P_{in} = 48 \text{mW}$, (d): $P_{in} = 64 \text{mW}$. The $\mu\text{-RR}$ is pumped at $\lambda = 1540.9 \text{nm}$ with TE polarization mode. P_{in} is the power injected in the coupling waveguide.

the μ -RR increases, a secondary comb appears with a spacing corresponding to the cavity FSR. A further increasing of pump power leads to an increased non-degenerate FWM process, filling the gap between the primary comb to form a final one.

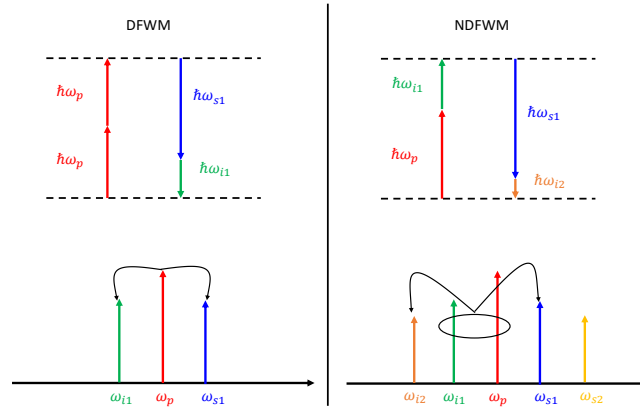


Figure 7.11 – Primary frequency comb generation. DFWM: degenerate four-wave-mixing, NDFWM: non-degenerate four-wave-mixing. *Top*: Energy diagram, *Bottom*: frequency comb creation.

7.4 CONCLUSION AND PERSPECTIVES

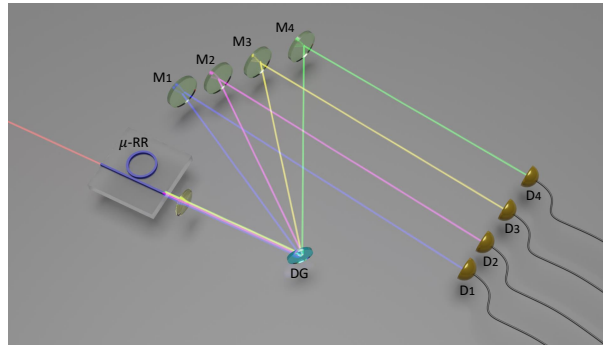


Figure 7.12 – Free space collection of the produced multimode CV entangled state at the output of the Si_3N_4 μ -RRs. M1-M4: mirrors, DG: diffraction grating, D1-D4: photodetectors. The number of the output modes is restricted to 4 for illustration.

In this chapter, we have presented the first characterization results of low-loss, high Q Si_3N_4 μ -RRs. The obtained results show a very low propagation losses (0.17 dB/cm) and high loaded quality factor ($Q = 600000$) for the TE polarization mode. This allowed to generate a primary and secondary Kerr frequency combs, with frequency lines spacing of multiple resonator FSR for the primary comb and a single FSR for the secondary one, with relatively low pump powers. These properties are very promising for experimental generation and measurement of multimode CV entanglement, which is an important resource for advanced quantum communication and computation applications.

As highlighted in [section 7.2](#), although the propagation losses are very low, the coupling efficiency at the input/output of the Si_3N_4 photonic chip is relatively high. To be able to reach and exploit the quantum properties of the produced multimode CV entangled state, light must be collected in a free space configuration at the output of the chip (see [Figure 7.12](#)). The large majority of the experimental setup is already built. At the output of the Si_3N_4 μ -RR, produced Kerr frequency comb is collimated using a high numerical aperture lens (C330TMD-C from Thorlabs). Then, frequency lines are spatially separated using a diffraction grating, and each frequency component is sent to a photodetector. Theoretical investigations of quantum correlations in a Kerr frequency comb, as well as experimental characterizations of the photodetectors are in progress.

CONCLUSION

CONCLUSION

In this thesis, we pushed the study of the generation and manipulation of quantum states of light with highly non-classical properties in the view of out-of-the-laboratory implementations of quantum communication protocols. In addition to theoretical investigations, experimental implementations in this work are based on off-the-shelf fiber components from guided-wave optics as well as integrated photonics technologies.

In [chapter 3](#), we have produced a Schrödinger cat-like state with a negative Wigner function at a telecom wavelength by subtracting single-photons from a squeezed vacuum. So far, this is the first experimental generation of non-Gaussian states in a guided-wave configuration based on plug-&-play fiber components from the classical communication technologies. The obtained result enables reconfigurable and easy-to-mount systems, which represents a big step towards robust CV optical realizations compatible with existing fiber-based communication networks and with considerably reduced resource overhead, spatial alignment, and mode matching issues.

In [chapter 4](#), we presented the design and experimental characterization of an SPDC-based guided-wave source in the picosecond pulsed regime at a telecom wavelength. This source is designed to be used for the generation of DV (time-bin entangled photon pairs) and CV (Schrödinger cat-like state) resources in the view of experimental production of time-bin based hybrid DV-CV entangled state in a guided-wave configuration. The experimental characterization results show a quasi-single-mode behaviour in the spectro-temporal domain of the SPDC source. This aspect is extremely important for the generation of both high fidelity DV and CV state as well as high quality hybrid entangled state. The combination of time-bin DV encoding and guided-wave implementation makes this kind of entanglement well adapted for out-of-the-laboratory, long distance quantum communication protocols in fiber-based communication networks [31].

In [chapter 5](#) and [chapter 6](#), we studied non-Gaussian quantum state engineering with multimode resources. The first study in [chapter 5](#) is motivated by the fact that depending on the working conditions, SPDC-based sources are naturally spectrally multimode, which represents a limitation for heralded non-Gaussian state production [85]. In this context, we developed a general theoretical framework describing heralded non-Gaussian state generation by subtracting single-photons from a multimode input resource in a non-mode-selective way. By considering the particular case of single-photon subtraction from multimode squeezed vacuum states, we show that high quality Schrödinger cat-like states can be produced using a non-mode-selective, simple passive spectral filtering stage in the heralding path. The developed framework allows choosing adequate working conditions for future practical realizations, thus representing a powerful tool for optimally designing future experiments.

On the other hand, we can benefit from the multimode aspect of the SPDC output state. The generation of non-Gaussian states of large amplitude (i.e. with a large mean photon number) is experimentally challenging. Indeed, the protocol presented in [chapter 5](#) can be iterated by subtracting a large number of photons in order to increase step-

by-step the size of the produced state. However, increasing the amount of subtracting operations comes at the cost of a highly reduced success probability, ultimately limiting the generation rate of the states. A different class of protocol, called iterative protocols, propose to bypass this limitation. In such protocols, resource states are mixed and "breeding" operations can be performed iteratively [33, 34]. In chapter 6, we proposed an alternative protocol based on spectrally multiplexing input state to perform a single-shot mixing of a large amount of resources. If the spectral overlap is properly chosen between the different modes of the input states, a single homodyne conditioning heralds the generation of a large amplitude state. We show that the proposed setup can generate large-amplitude Schrödinger cat-like states as well as GKP states, which can be used as error-correcting codes for quantum information protocols [148]. In this case, the protocol requires small-amplitude Schrödinger cat states as resource states and $x = 0$ or $p = 0$ homodyne heralding [158]. Moreover, single photons as input of the protocol can also allow for the generation of squeezed Schrödinger cat states. Note that multiplexing is not restricted to spectral modes, it can also be extended to transverse spatial modes. Due to its high efficiency and simplified implementation as well as to the possibility of implementing it with already available experimental resources, we believe that our approach to non-Gaussian state preparation represents a major breakthrough in the domain of non-classical photonic state generation, and will open a wide range of applications.

Finally, we perform in chapter 7 an experimental characterization of micro-ring resonators integrated in a silicon nitride (Si_3N_4) photonic chip. The results reveal very low propagation losses and high quality factors, making this kind of integrated platforms suitable for highly compact CV applications out-of-the-laboratory. This photonic chip will serve as a source for experimental investigation of high dimension quantum correlations in Kerr frequency comb.

PERSPECTIVES

"Perfection is not physical"
Jean Etesse

As no physical implementation is perfect, obtained experimental results can always be improved. Indeed, as highlighted in chapter 3, the main limitation in the presented experimental implementation of fully guided-wave generation of non-Gaussian quantum states is related to the homodyne detection (HD) system. In particular, the lack of efficient photodiodes, that represent the most critical loss factor in the HD, affects in the same way both guided-wave and bulk realizations. A further improvement of the experimental setup would be the development of a homodyne detection with better overall efficiency, allowing to affect less the quantum features of the produced non-Gaussian states. Moreover, propagation and coupling losses at the SPDC stage degrade the purity of the squeezed state on which the subtraction protocol is applied. This deleterious effect can be circumvented by adopting a fully integrated setup including on-chip squeezing generation, photon subtraction and homodyne detection. This strategy would further improve the Wigner function negativity of the produced non-Gaussian states.

The continuity of the experimental work presented in [chapter 4](#) consists in the following steps:

- The validation of developed source by experimental generation of the time-bin entangled photon pairs (DV) and Schrödinger cat-like state (CV). The theoretical framework presented in [chapter 5](#) can be useful to enhance the quality of the produced states.
- The implementation of the interferometric stage for the experimental protocol of hybrid DV-CV entanglement generation via entanglement swapping operation.
- Real field implementation of quantum communication protocols based on time-bin based hybrid DV-CV information encoding.

The last experimental characterization results presented in [chapter 7](#) are the first obtained on an ongoing project. A PhD student is working, both theoretically and experimentally, on this project. The theoretical work consists in the investigation of possible hidden correlations in a multimode Kerr frequency comb produced by micro-ring resonators. This theoretical investigation would allow to identify the optimal quantum observables that would reveal these correlations. At the same time, efforts are invested to develop detection systems allowing to measure the optimal identified observables for the experimental validation of multimode quantum correlation.

Finally, further improvement of the proposed protocol in [chapter 6](#) is being considered. Typically, investigation of the influence of the properties of the input resources as well as the heralding strategy would allow to identify optimal scenarios for better protocol performances.

APPENDIX

NUMBER STATE BASIS

A.1 EIGENSTATES AND EIGENVALUES OF THE NUMBER OPERATOR

As mentioned in [subsection 1.1.3](#), the eigenstates of the Hamiltonian \hat{H}_l of the radiation mode l are given by the eigenstates of the number operator $\hat{N}_l = \hat{a}_l^\dagger \hat{a}_l$. The eigenstate $|v_l\rangle_l$, associated with the eigenvalue v_l , satisfies the relation:

$$\hat{N}_l |v_l\rangle_l = v_l |v_l\rangle_l. \quad (\text{A.1})$$

The squared norm of the state $\hat{a}_l |v_l\rangle_l$, noted $\|\hat{a}_l |v_l\rangle_l\|^2$, is given by:

$$\|\hat{a}_l |v_l\rangle_l\|^2 = \langle v_l | \hat{a}_l^\dagger \hat{a}_l |v_l\rangle_l = \langle v_l | \hat{N}_l |v_l\rangle_l = v_l \langle v_l | v_l \rangle = v_l \geq 0, \quad (\text{A.2})$$

this means that the eigenvalue v_l is non-negative. Moreover, using the commutation relations given by [Equation 1.20](#), we can show that $[\hat{N}_l, \hat{a}_l] = -\hat{a}_l$, and so, applying the number operator to the state $\hat{a}_l |v_l\rangle_l$ gives the following result:

$$\hat{N}_l \hat{a}_l |v_l\rangle_l = (\hat{a}_l \hat{N}_l - \hat{a}_l) |v_l\rangle_l = (v_l - 1) \hat{a}_l |v_l\rangle_l, \quad (\text{A.3})$$

which means that either $\hat{a}_l |v_l\rangle_l$ is a null vector, or it is an eigenstate of the number operator \hat{N}_l with associated eigenvalue $v_l - 1$, we note it $|v_l - 1\rangle_l$. More generally, the states $\{|v_l - p\rangle_l = \hat{a}_l^p |v_l\rangle_l\}$ with $p \leq p_{max}$ are all eigenstates of the number operator \hat{N}_l with associated eigenvalues $\{v_l - p\}$. We note the minimum eigenvalue by $v_l - p_{max}$, and hence, the associated eigenvector is $|v_l - p_{max}\rangle_l = \hat{a}_l^{p_{max}} |v_l\rangle_l$. Since $v_l - p_{max} - 1$ is not an eigenvalue of \hat{N}_l , the state $\hat{a}_l |v_l - p_{max}\rangle_l$ is null. And according to [Equation A.2](#), we find that:

$$v_l - p_{max} = 0. \quad (\text{A.4})$$

In the same way, we can show that the states $\{|v_l + p\rangle_l = (\hat{a}_l^\dagger)^p |v_l\rangle_l\}$ are also eigenstates of the operator \hat{N}_l with associated eigenvalues $\{v_l + p\}$. So, the eigenvalues are the set of non-negative integer $\{n_l\}_{n_l \geq 0}$ and the eigenstates $\{|n_l\rangle_l\}$ are called number states.

A.2 ANNIHILATION AND CREATION OPERATORS

As seen in [section A.1](#), the states $\hat{a}_l |n_l\rangle_l$ and $\hat{a}_l^\dagger |n_l\rangle_l$ are eigenstates of \hat{N}_l with associated eigenvalues $n_l - 1$ and $n_l + 1$, respectively. So we can write them as:

$$\hat{a}_l |n_l\rangle_l = c_1 |n_l - 1\rangle_l, \quad n_l > 0, \quad (\text{A.5})$$

$$\hat{a}_l |0\rangle_l = 0, \quad (\text{A.6})$$

$$\hat{a}_l^\dagger |n_l\rangle_l = c_2 |n_l + 1\rangle_l, \quad (\text{A.7})$$

with c_1 and c_2 are two constants chosen to be real. Taking the squared norm of [Equation A.5](#) and [Equation A.7](#), we find that:

$$\|\hat{a}_l |n_l\rangle_l\|^2 = \langle n_l | \hat{a}_l^\dagger \hat{a}_l |n_l\rangle_l = \langle n_l | \hat{N}_l |n_l\rangle_l = n_l \langle n_l | n_l \rangle = n_l = c_1^2, \quad (\text{A.8})$$

$$\|\hat{a}_l^\dagger |n_l\rangle_l\|^2 = \langle n_l | \hat{a}_l \hat{a}_l^\dagger |n_l\rangle_l = \langle n_l | \hat{a}_l^\dagger \hat{a}_l + 1 |n_l\rangle_l = (n_l + 1) \langle n_l | n_l \rangle = n_l + 1 = c_2^2, \quad (\text{A.9})$$

and so, we find that $c_1 = \sqrt{n_l}$ and $c_2 = \sqrt{n_l + 1}$.

USEFUL FORMULA

B.1 GAUSSIAN INTEGRAL

$$\int_{-\infty}^{\infty} e^{-a(x-x_0)^2} dx = \sqrt{\frac{\pi}{a}}. \quad (\text{B.1})$$

B.2 INTEGRATION FORMULAS INVOLVING COHERENT STATE WAVE-FUNCTIONS

The following integrals are given for real amplitudes α and β . Using the wavefunction of coherent states ([Equation 1.77](#)), we find:

$$\int_{-\frac{\Delta x}{2}}^{\frac{\Delta x}{2}} \langle x|\alpha\rangle_a \langle \beta|x\rangle dx = \frac{e^{-\frac{1}{2}(\alpha-\beta)^2}}{2} \left[\operatorname{erf} \left(\frac{\alpha+\beta}{\sqrt{2}} + \frac{1}{2\sqrt{2}} \frac{\Delta x}{\sigma_0} \right) - \operatorname{erf} \left(\frac{\alpha+\beta}{\sqrt{2}} - \frac{1}{2\sqrt{2}} \frac{\Delta x}{\sigma_0} \right) \right], \quad (\text{B.2})$$

$$\int_{-\frac{\Delta p}{2}}^{\frac{\Delta p}{2}} \langle p|\alpha\rangle_a \langle \beta|p\rangle dp = \frac{e^{-\frac{1}{2}(\alpha-\beta)^2}}{2} \left[\operatorname{erf} \left(i \frac{\alpha-\beta}{\sqrt{2}} + \frac{1}{2\sqrt{2}} \frac{\Delta p}{\sigma_0} \right) - \operatorname{erf} \left(i \frac{\alpha-\beta}{\sqrt{2}} - \frac{1}{2\sqrt{2}} \frac{\Delta p}{\sigma_0} \right) \right], \quad (\text{B.3})$$

$$\int_{-\infty}^{\infty} e^{-\frac{x^2}{2\Delta x^2}} \langle x|\alpha\rangle_a \langle \beta|x\rangle dx = \frac{e^{-(\alpha^2+\beta^2)}}{\sqrt{1+\frac{\sigma_0^2}{\Delta x^2}}} e^{-\frac{(\alpha+\beta)^2}{2\left(1+\frac{\sigma_0^2}{\Delta x^2}\right)}}, \quad (\text{B.4})$$

$$\int_{-\infty}^{\infty} e^{-\frac{p^2}{2\Delta p^2}} \langle p|\alpha\rangle_a \langle \beta|p\rangle dp = \frac{e^{-\frac{(\alpha-\beta)^2}{2\left(1+\frac{\sigma_0^2}{\Delta p^2}\right)}}}{\sqrt{1+\frac{\sigma_0^2}{\Delta p^2}}}. \quad (\text{B.5})$$

GAUSSIAN BEAM PROPAGATION

In this appendix, we give the main formulas and equations used to align the Fabry-Pérot cavity for the fundamental TEM₀₀ Gaussian beam.

C.1 GAUSSIAN BEAM

A Gaussian beam propagating along the z axis is characterized by a transverse Gaussian intensity profile (in the (x, y) plane) given by:

$$I(x, y, z) = I_0(z) e^{-2\frac{x^2+y^2}{w^2(z)}}, \quad (\text{C.1})$$

where $w(z)$ is the beam size at the position z given by:

$$w(z) = w_0 \sqrt{1 + \left(\frac{\lambda(z - z_0)}{\pi w_0^2} \right)^2}. \quad (\text{C.2})$$

The minimum beam size w_0 , located at the position z_0 , is called the beam waist. The curvature radius of the wave-front of the beam at the position z , noted $R(z)$, is given by:

$$R(z) = (z - z_0) \left[1 + \left(\frac{\pi w_0^2}{\lambda(z - z_0)} \right)^2 \right]. \quad (\text{C.3})$$

C.2 GAUSSIAN BEAM TRANSFORMATION USING TWO LENSES

For a Gaussian beam propagating in an optical system characterized by its ABCD matrix [186, 187], the beam size w and its wave-front curvature radius R are transformed as:

$$q' = \frac{Aq + B}{Cq + D}, \quad (\text{C.4})$$

where:

$$\frac{1}{q} = -i \frac{\lambda}{\pi w^2} + \frac{1}{R}. \quad (\text{C.5})$$

Let us consider the case of Gaussian beam propagation in a system of two lenses as depicted in [Figure C.1](#). The ABCD matrices for a free propagation over a distance d ($M_{prob}(d)$) and a transmission via a lens with focal length f ($M_{lens}(f)$) are given by:

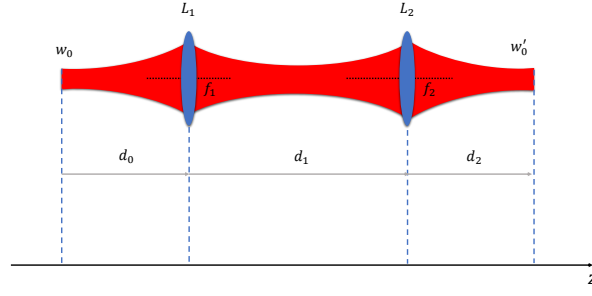


Figure C.1 – Gaussian beam propagation in a system of two lenses.

$$M_{\text{prob}}(d) = \begin{pmatrix} 1 & d \\ 0 & 1 \end{pmatrix}, \quad M_{\text{lens}}(f) = \begin{pmatrix} 1 & 0 \\ -\frac{1}{f} & 1 \end{pmatrix}, \quad (\text{C.6})$$

and so, the ABCD matrix of the whole system in [Figure C.1](#) is given:

$$M = M_{\text{prob}}(d_2)M_{\text{lens}}(f_2)M_{\text{prob}}(d_1)M_{\text{lens}}(f_1)M_{\text{prob}}(d_0) = \begin{pmatrix} A & B \\ C & D \end{pmatrix}, \quad (\text{C.7})$$

with:

$$A = 1 - \frac{d_1}{f_1} - \frac{d_2}{f_1} - \frac{d_2}{f_2} + \frac{d_1d_2}{f_1f_2}, \quad (\text{C.8})$$

$$B = d_0 + d_1 + d_2 - \frac{d_0d_1}{f_1} - \frac{d_0d_2}{f_1} - \frac{d_0d_2}{f_2} - \frac{d_1d_2}{f_2} + \frac{d_0d_1d_2}{f_1f_2}, \quad (\text{C.9})$$

$$C = \frac{-1}{f_1} - \frac{-1}{f_2} + \frac{d_1}{f_1f_2}, \quad (\text{C.10})$$

$$D = 1 - \frac{d_0}{f_1} - \frac{d_0}{f_2} - \frac{d_1}{f_2} + \frac{d_0d_1}{f_1f_2}. \quad (\text{C.11})$$

Applying now [Equation C.4](#) with $R = R' = 0$, we find that:

$$Aq_0 + B = Cq_0q'_0 + Dq'_0, \quad (\text{C.12})$$

and since q_0 and q'_0 are imaginary ($q_0q'_0$ is real), we can identify two equations:

$$Dq'_0 = Aq_0, \quad (\text{C.13})$$

$$Cq_0q'_0 = B. \quad (\text{C.14})$$

By considering the simple case where $d_0 = f_1$ (the waist w_0 is located at the focal plane of the lens L_1), [Equation C.14](#) leads to the following formula:

$$d_2 = f_2 - \pi^2 \frac{w_0^2 w_0'^2}{\lambda^2 f_1} \left(1 + \frac{f_2 - d_1}{f_1} \right), \quad (\text{C.15})$$

and by replacing it in [Equation C.13](#), we find:

$$c_1 d_1^2 + c_2 d_1 + c_3 = 0, \quad (\text{C.16})$$

with:

$$c_1 = \frac{\pi^2 w_0^4 w_0'^2}{\lambda^2 f_1^3 f_2}, \quad (\text{C.17})$$

$$c_2 = -2 \frac{\pi^2 w_0^4 w_0'^2}{\lambda^2 f_1^2} \left(\frac{1}{f_1} + \frac{1}{f_2} \right), \quad (\text{C.18})$$

$$c_3 = \frac{\pi^2 w_0^4 w_0'^2}{\lambda^2 f_1} \left(\frac{1}{f_1} + \frac{1}{f_2} \right) \left(1 + \frac{f_2}{f_1} \right) + \frac{f_1}{f_2} w_0'^2 - \frac{f_2}{f_1} w_0^2. \quad (\text{C.19})$$

So, for a given initial waist w_0 and a target final one w_0' , resolving [Equation C.16](#) allows to retrieve the distance d_1 that must be imposed between the two lenses of focal lengths f_1 and f_2 .

CAVITY LOCKING USING PDH TECHNIQUE

D

In [chapter 3](#), the Fabry-Pérot cavity filtering the heralding photons is locked using the Pound Drever Hall (PDH) technique. The locking scheme is illustrated in [Figure D.1](#).

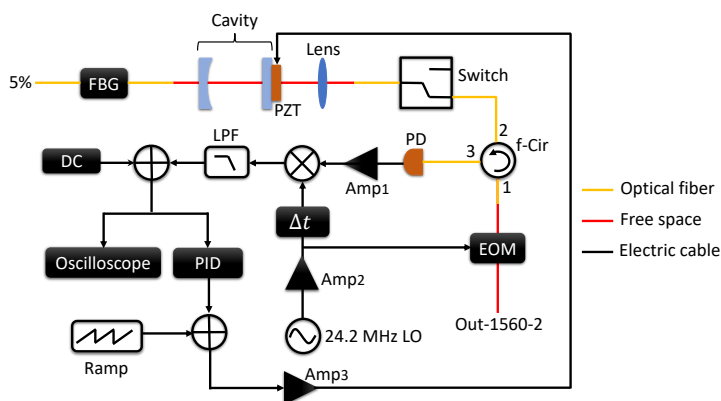


Figure D.1 – Cavity Locking using the PHD technique. Amp: amplifier, f-Cir: fiber optic circulator, LPF: low pass filter, PD: photodiode, EOM: electro optic modulator, PZT: piezo stack actuator, FBG: fiber Bragg grating filter. See details in the text.

The output Out-1560-2 of the master laser source is modulated using an EOM (PM7-SWIR from QUBIG GmbH) at a frequency of 24.2 MHz and sent to the Fabry-Pérot cavity through the fiber optic circulator (f-Cir) and the Switch. The reflected light from the cavity is detected at port 3 of the circulator using an AC coupled photodiode with a bandwidth of 100 MHz (PD100 from Koheron) whose output is amplified using the 20 dB Amp1 amplifier. The output of this amplifier is then mixed with the amplified, time delayed 24.2 MHz LO using the ZX05-1MHW-S+ mixer from Mini-Circuits and filtered with a low pass filter (BLP-2.5+ from Mini-Circuits). To obtain a positive error signal that can be read by the PID controller (Teensy 3.2), the filtered output of the ZX05-1MHW-S+ mixer is shifted with a DC component. The control signal delivered by the PID controller is amplified using a TD250 amplifier from PiezoDrive and sent to the PZT actuator attached to on of the Fabry-Pérot cavity mirrors (the plane mirror). The addition of a ramp (generated by a servo controller from Toptica) to the control signal allows to scan the length of the cavity during its alignment. The LO signal at 24.2 MHz is generated using Adafruit Si5351 clock generator breakout board combined with Arduino Uno R3 chip, and then amplified with Amp2 (15 dB ZX60-100VH+ from Mini-Circuits) to be sent to the EOM and the ZX05-1MHW-S+ mixer.

PULSED SHG IN TIME DOMAIN

For an SHG process with picosecond fundamental pulses given by:

$$E_l(x = 0, t) = E_0 f(t) \sin(\omega_0 t), \quad (\text{E.1})$$

the electric field of the SH pulses at the output of the SHG crystal ($x = L_{sh}$) can be written as [120]:

$$E_p(L_{sh}, t) = \frac{k_{shg}^p \chi_{eff}}{4(n_{shg}^p)^2 (\beta_{shg}^p - \beta_{shg}^l)} \sin(k_{shg}^p L_{sh} - 2\omega_0 t) \int_{\beta_{shg}^l L_{sh}}^{\beta_{shg}^p L_{sh}} f^2(t - t') dt', \quad (\text{E.2})$$

with $k_{shg}^p = k_{shg}(2\omega_0)$, n_{shg}^p , and $\beta_{shg}^p = \frac{dk_{shg}(\omega)}{d\omega}|_{2\omega_0}$ are the wave-vector, the refractive index and the inverse of the group velocity, respectively, at the SH central frequency $2\omega_0$ and $\beta_{shg}^l = \frac{dk_{shg}(\omega)}{d\omega}|_{\omega_0}$ is the inverse of the group velocity at the fundamental pulse central frequency ω_0 , in the SHG nonlinear crystal. For Gaussian fundamental pulses: $f(t) = e^{-\frac{2\ln(2)}{\tau_l^2} t^2}$, we find:

$$E_p(L_{sh}, t) = \frac{k_{shg}^p \chi_{eff} \tau_l}{16(n_{shg}^p)^2 (\beta_{shg}^p - \beta_{shg}^l)} \sin(k_{shg}^p L_{sh} - 2\omega_0 t) \sqrt{\frac{\pi}{\ln(2)}} \left[\text{erf} \left(\frac{2\sqrt{\ln(2)}}{\tau_l} (t - \beta_{shg}^l L_{sh}) \right) - \text{erf} \left(\frac{2\sqrt{\ln(2)}}{\tau_l} (t - \beta_{shg}^p L_{sh}) \right) \right]. \quad (\text{E.3})$$

In our case, we use an MgO:PPLN crystal for the second harmonic generation. [Figure E.1](#) shows the normalized temporal envelop of the SH pulse as a function of the length L_{sh} of the SHG crystal (MgO:PPLN).

We can see that the second harmonic pulse duration increases with the length L_{sh} . For a fundamental laser pulse duration of $\tau_l = 1$ ps (a), the SH pulse envelop is no more Gaussian after a propagation distance around 5 mm whereas for a duration $\tau_l = 6$ ps, the SH pulse still have a Gaussian envelop even after a propagation distance of 20 mm inside the SHG crystal. This is essentially due to the walk-off effect related to the group velocity mismatch between the laser pulse and the second harmonic pulse inside the nonlinear crystal. During the propagation, the fundamental and the SH pulses are separated by a time delay $\Delta\tau = \Delta\beta_{shg} L_{sh}$ where $\Delta\beta_{shg} = |\beta_{shg}^p - \beta_{shg}^l|$. A characteristic length, called the walk-off length L_{wo} , is a limit length for which the fundamental and the SH pulses can still be considered as overlapping, this characteristic length is given by [188]:

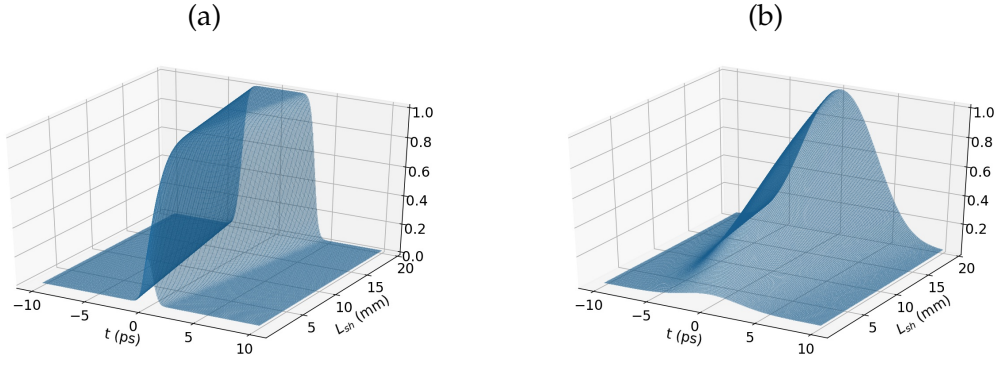


Figure E.1 – The normalized temporal shape of the SH pulse as a function of the length L_{sh} of the SHG crystal (MgO:PPLN) for fundamental pulses of duration $\tau_l = 1$ ps (a) and $\tau_l = 6$ ps (b). The SHG crystal is an MgO:PPLN.

$$L_{wo} = \frac{\tau_l}{\Delta\beta_{shg}}. \quad (\text{E.4})$$

For a PPLN crystal pumped at $\lambda_0 = 1560$ nm, this characteristic length can be approximated as $L_{wo} [\text{mm}] \approx 3.39 \tau_l [\text{ps}]$, which is equal to 3.39 mm for $\tau_l = 1$ ps and 20.34 mm for $\tau_l = 6$ ps. For $L_{sh} < L_{wo}$, the SH pulse can be approximated by [120]:

$$E_p(L_{sh}, t) = \frac{k_{shg}^p \chi_{eff} L_{sh}}{4(n_{shg}^p)^2} \sin(k_{shg}^p L_{sh} - 2\omega_0 t) f^2 \left(t - \frac{\beta_{shg}^l + \beta_{shg}^p}{2} L_{sh} \right), \quad (\text{E.5})$$

conserving then it Gaussian envelop.

SINGLE-PHOTON SUBTRACTION FROM MULTIMODE QUANTUM STATES

F.1 PROPERTIES OF FUNCTIONS $\{\psi_n''(\omega), \psi_n^\perp(\omega)\}$

In this appendix, we provide some important properties of the functions $\{\psi_n''(\omega)\}$ and $\{\psi_n^\perp(\omega)\}$ that are used in the main text. The starting point consists in decomposing the functions $t(\omega)\psi_k(\omega)$ in an orthonormal basis $\{\psi_n''(\omega)\}$:

$$t(\omega)\psi_k(\omega) = \sum_n a_{kn} \psi_n''(\omega), \quad (\text{F.1})$$

with

$$a_{kn} = \int t(\omega)\psi_k(\omega) \left(\psi_n''(\omega)\right)^* d\omega, \quad (\text{F.2})$$

and to complete this basis with the set $\{\psi_n^\perp(\omega)\}$. The functions $\{\psi_n^\perp(\omega)\}$ are orthogonal to each other and to the $\{\psi_n''(\omega)\}$, such that the ensemble of $\{\psi_n''(\omega), \psi_n^\perp(\omega)\}$ forms a complete orthonormal basis. By inverting [Equation 5.8](#), one obtains:

$$\psi_n''(\omega) = \sum_k p_{kn}^* \psi_k(\omega) \quad (\text{F.3a})$$

$$\psi_n^\perp(\omega) = \sum_k q_{kn}^* \psi_k(\omega). \quad (\text{F.3b})$$

Also, by noting that

$$\sum_k p_{kn_1} p_{kn_2}^* = \sum_k q_{kn_1} q_{kn_2}^* = \delta_{n_1, n_2}, \quad (\text{F.4a})$$

$$\sum_k p_{kn_1} q_{kn_2}^* = \sum_k q_{kn_1} p_{kn_2}^* = 0, \quad (\text{F.4b})$$

it can be proved, thanks to [Equation 5.7](#), that

$$\sum_k \psi_k(\omega) \psi_k^*(\omega') = \delta(\omega - \omega') \quad (\text{F.5})$$

and

$$\sum_l \psi_l''(\omega) \left(\psi_l''(\omega') \right)^* + \psi_l^\perp(\omega) \left(\psi_l^\perp(\omega') \right)^* = \delta(\omega - \omega'), \quad (\text{F.6})$$

thus providing a completeness relations for the ensemble of functions $\{\psi_n''(\omega), \psi_n^\perp(\omega)\}$.

By multiplying Equation F.3a and Equation F.3b by $t(\omega)$ and remembering definition given by Equation F.1, one obtains:

$$t(\omega)\psi_n''(\omega) = \sum_l \left(\sum_k p_{kn}^* a_{kl} \right) \psi_l''(\omega) = \sum_l T_{nl} \psi_l'', \quad (\text{F.7a})$$

$$t(\omega)\psi_n^\perp(\omega) = \sum_l \left(\sum_k q_{kn}^* a_{kl} \right) \psi_l''(\omega). \quad (\text{F.7b})$$

Then:

$$\int |t(\omega)|^2 |\psi_n^\perp(\omega)|^2 d\omega = \int \left[|t(\omega)|^2 \psi_n^\perp(\omega) \right] \left(\psi_n^\perp(\omega) \right)^* d\omega. \quad (\text{F.8})$$

However, according to the two relations given by Equation F.7, $|t(\omega)|^2 \psi_n^\perp(\omega)$ only has components along ψ_n'' , which implies that $\int |t(\omega)|^2 |\psi_n^\perp(\omega)|^2 d\omega = 0$, and, as a consequence, that:

$$\forall \omega, \quad t(\omega)\psi_n^\perp(\omega) = 0. \quad (\text{F.9})$$

This result is quite strong, and implies that $\psi_n^\perp(\omega)$ is **only nonzero where** $r(\omega) = 1$, *i.e.* in all region for which the filter transmission coefficient $t(\omega)$ goes exactly to 0. This also means that

$$\forall \omega, \quad r(\omega) \psi_n^\perp(\omega) = \psi_n^\perp(\omega). \quad (\text{F.10})$$

Note also that Equation F.1 implies that if $t(\omega) = 0$ then $\psi_n''(\omega) = 0$, for regular enough continuous functions, with continuous derivatives, such as for a Gaussian or Lorentzian filter transmission profile. This implies that $\psi_n^\perp(\omega)$ and $\psi_n''(\omega)$ have disjoint supports.

F.2 FIDELITY OF THE MEASURED STATE WITH A TARGET NON-GAUSSIAN STATE

The quality of the detected state can be evaluated by its fidelity with a single-mode photon-subtracted squeezed vacuum state as target state thanks to the overlap formula:

$$\mathcal{F} = 4\pi\sigma_0^2 \int \int W_H(x, p) W_t(x, p) dx dp. \quad (\text{F.11})$$

By replacing Equation 5.23 and Equation 5.17 in Equation F.11, we find that:

$$\mathcal{F} = \frac{2}{\sigma_x \sigma_p P / \theta^2 \sqrt{(\frac{1}{\sigma_x^2} + \frac{s}{\sigma_0^2})(\frac{1}{\sigma_p^2} + \frac{1}{s\sigma_0^2})}} \left[-A + \left(\frac{sA}{\sigma_0^2} - B \right) \frac{1}{\frac{1}{\sigma_x^2} + \frac{s}{\sigma_0^2}} + \left(\frac{A}{s\sigma_0^2} - C \right) \frac{1}{\frac{1}{\sigma_p^2} + \frac{1}{s\sigma_0^2}} \right. \\ \left. + \frac{sB}{\sigma_0^2} \frac{3}{(\frac{1}{\sigma_x^2} + \frac{s}{\sigma_0^2})^2} + \frac{C}{s\sigma_0^2} \frac{3}{(\frac{1}{\sigma_p^2} + \frac{1}{s\sigma_0^2})^2} \left(\frac{Cs}{\sigma_0^2} + \frac{B}{s\sigma_0^2} \right) \frac{1}{(\frac{1}{\sigma_x^2} + \frac{s}{\sigma_0^2})(\frac{1}{\sigma_p^2} + \frac{1}{s\sigma_0^2})} \right], \quad (\text{F.12})$$

with

$$A = \frac{P}{\theta^2} - \frac{\sigma_0^2}{\sigma_x^2} \sum_{k,n} \gamma_{k,n} \frac{\mu_k \mu_n c_k c_n}{(1 - \mu_k)(1 - \mu_n)} - \frac{\sigma_0^2}{\sigma_p^2} \sum_{k,n} \gamma_{k,n} \frac{\mu_k \mu_n c_k c_n}{(1 + \mu_k)(1 + \mu_n)} \quad (\text{F.13a})$$

$$B = \frac{\sigma_0^2}{\sigma_x^4} \sum_{k,n} \gamma_{k,n} \frac{\mu_k \mu_n c_k c_n}{(1 - \mu_k)(1 - \mu_n)} \quad (\text{F.13b})$$

$$C = \frac{\sigma_0^2}{\sigma_p^4} \sum_{k,n} \gamma_{k,n} \frac{\mu_k \mu_n c_k c_n}{(1 + \mu_k)(1 + \mu_n)}. \quad (\text{F.13c})$$

F.3 GAUSSIAN AND RECTANGULAR FILTERS ON THE HERALDING PATH

In the case of a Gaussian shaped JSA, the explicit shape of the supermode is given as in [131]:

$$\psi_k(\omega) \propto \sqrt{\frac{\tau_s}{\sqrt{\pi} 2^k k!}} H_k [\tau_s(\omega - \omega_p/2)] e^{-\tau_s^2(\omega - \omega_p/2)^2/2}, \quad (\text{F.14})$$

where ω_p is the SPDC pump central frequency and τ_s is given by the pump and by the process K [131]. In general,

$$\gamma_{k,n} = \int |t(\omega)|^2 \psi_k(\omega) \psi_n^*(\omega) d\omega, \quad (\text{F.15})$$

where $\psi_k(\omega)$ is the signal mode k given by Equation F.14 with a phase factor which does not depend on the mode order k [131].

A Gaussian filter with transmittance $t(\omega)$ can be described by:

$$t(\omega) = e^{-\frac{4 \ln(2)}{\Delta\omega_F^2} (\omega - \frac{\omega_p}{2})^2}, \quad (\text{F.16})$$

where $\Delta\omega_F$ is the FWHM bandwidth. Accordingly, by defining $\bar{\tau}^2 = \frac{8 \ln(2)}{\Delta\omega_F^2} + \tau_s^2$, the coefficients $\gamma_{k,n}$ are:

$$\gamma_{k,n} = \frac{\tau_s}{\sqrt{2^{k+n}k!n!\pi}} \int e^{-\bar{\tau}^2(\omega - \frac{\omega_p}{2})^2} H_k \left[\tau_s \left(\omega - \frac{\omega_p}{2} \right) \right] H_n \left[\tau_s \left(\omega - \frac{\omega_p}{2} \right) \right] d\omega. \quad (\text{F.17})$$

By using the integration formula given in [189]:

$$\int e^{-y^2} H_k(ay) H_n(ay) dy = \sqrt{\pi} \sum_{m=0}^{\min[k,n]} 2^m m! \binom{k}{m} \binom{n}{m} (1-a^2)^{\frac{k+n}{2}-m} H_{k+n-2m}(0), \quad (\text{F.18})$$

it is possible to write:

$$\gamma_{k,n} = \frac{\tau_s}{\sqrt{\bar{\tau}^2 2^{k+n}k!n!}} \sum_{m=0}^{\min[k,n]} 2^m m! \binom{k}{m} \binom{n}{m} \left(1 - \frac{\tau_s^2}{\bar{\tau}^2}\right)^{\frac{k+n}{2}-m} H_{k+n-2m}(0). \quad (\text{F.19})$$

As the Hermite-Gauss polynomials verify:

$$H_k(0) = \begin{cases} 0 & \text{if } k \text{ is odd} \\ (-1)^{\frac{k}{2}} \frac{k!}{(\frac{k}{2})!} & \text{if } k \text{ is even,} \end{cases} \quad (\text{F.20})$$

then, for a Gaussian filter, $\gamma_{k,n} = 0$ if $k+n$ is odd, and

$$\gamma_{k,n} = \frac{\tau_s}{\sqrt{\nu 2^{k+n}k!n!}} \sum_{m=0}^{\min[k,n]} 2^m m! \binom{k}{m} \binom{n}{m} \left(\frac{\tau_s^2}{\nu} - 1\right)^{\frac{k+n}{2}-m} \frac{(k+n-2m)!}{(\frac{k+n}{2}-m)!}, \quad (\text{F.21})$$

if $k+n$ is even.

Following a similar reasoning, the case of a rectangular filter can also be described. We have:

$$t(\omega) = \begin{cases} T_0 & \text{if } \omega \in \left[-\frac{\Delta\omega_F}{2}, +\frac{\Delta\omega_F}{2}\right] \\ 0 & \text{elsewhere.} \end{cases} \quad (\text{F.22})$$

In this case, $\gamma_{k,n} = 0$ if $k+n$ is odd, and:

$$\gamma_{k,n} = \frac{1}{\sqrt{2^{k+n}k!n!}} \int_{-\tau_s \frac{\Delta\omega_F}{2}}^{+\tau_s \frac{\Delta\omega_F}{2}} e^{-x^2} H_k(x) H_n(x) dx, \quad (\text{F.23})$$

if $k+n$ is even.

MULTIPLEXED NON-GAUSSIAN STATE SYNTHESIZER WITH SINGLE-PHOTON RESOURCES

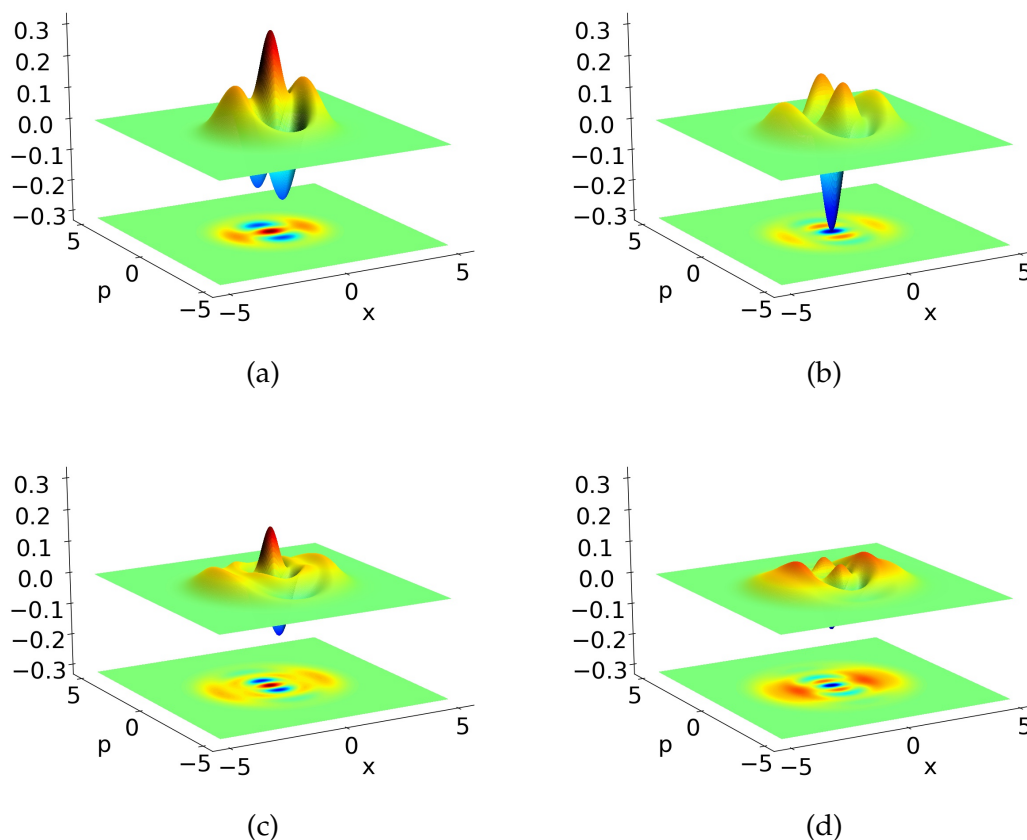


Figure G.1 – Wigner functions of the output state of the protocol fed by single-photon Fock states, with (a): $N = 2$, (b): $N = 3$, (c): $N = 4$ and (d): $N = 5$.

An important aspect of our strategy is that it can directly be implemented with already accessible experimental resources. Even if high amplitude Schrödinger cat states are not trivial to generate experimentally, good approximation of them at low amplitudes, also called Schrödinger kitten states, are commonly produced states. Moreover, the breeding principle has been experimentally demonstrated with kittens [89], showing the validity of the approach. In addition, single-photon Fock states also constitute a valid alternative to them, as theoretically and experimentally demonstrated [34, 65], to generate squeezed Schrödinger cat-like output states with high fidelity. It is worth

noting that squeezing the output states constitutes a high advantage, as it can increase their robustness to losses [28, 161]. Accordingly, the results presented here will focus on input single-photon Fock states. Very similar results are expected with kitten states.

We recall that our protocol requires the use of a multiplexed input state source. This can simply be achieved by taking advantage of the spectral tailoring possibility that processes like spontaneous parametric down conversion offer [121]. Indeed, depending on the pumping and phase-matching conditions, two-mode squeezing can be generated along a large number of spectral modes, offering the ideal platform for multiplexed generation [119]. Then, single-photon Fock states are simply heralded by performing a projective measurement over one of the two mode squeezing subsystems. This method, although very commonly used for the generation of high quality single-photon Fock states for a couple of decades now, has recently been extended experimentally to high-dimension mode-selective quantum state tailoring [135]. This allows to tweak the supermode in which the single-photon detection occurs, therefore heralding a single-photon Fock state in a given supermode. Here we can take advantage of such capabilities, by using multiplexed photon sources to feed the protocol and generate complex photonic states in a single shot.

The output Wigner functions of the protocol fed by an increasing number N of single-photon Fock states are shown in Figure G.1. They clearly reveal that the output state contains more and more oscillations at its center with increasing N . To be more quantitative, Table G.1 gathers the parameters of the closest Schrödinger cat state, where α is the amplitude, s its squeezing factor and \mathcal{F} the fidelity between the two states.

	$N = 2$	$N = 3$	$N = 4$	$N = 5$
α	1.63	2.03	2.30	2.12
s	-1.80 dB	-1.87 dB	-1.80 dB	-1.31 dB
\mathcal{F}	99%	90%	66%	49%

Table G.1 – Fidelity of the output state with a squeezed Schrödinger cat state of amplitude α and squeezing factor s .

This table reveals that the amplitude of the state increases with N for low values, but degrades after $N = 4$. Further simulations show that this is true for larger N as well. Such an evolution can qualitatively be explained by the phase invariance of the two states impinging the beam splitter: as the only rotation symmetry breaking operation is the homodyne measurement, the fidelity of the created state with a highly non-phase invariant state decreases with its size.

This analysis reveals that few-mode single photon states are relevant resources for our protocol in order to produce high quality Schrödinger cat states, essential brick in continuous-variable quantum information processing.

BIBLIOGRAPHY

- [1] MTCAJ Thomas and A Thomas Joy. *Elements of information theory*. Wiley-Interscience, 2006. URL: <https://www.wiley.com/en-fr/Elements+of+Information+Theory%2C+2nd+Edition-p-9781118585771> (cit. on p. 3).
- [2] John Bardeen and Walter Hauser Brattain. « The transistor, a semi-conductor triode ». In: *Physical Review* 74.2 (1948), p. 230. URL: <https://journals.aps.org/pr/abstract/10.1103/PhysRev.74.230> (cit. on p. 3).
- [3] Theodore H Maiman et al. « Stimulated optical radiation in ruby ». In: (1960) (cit. on p. 3).
- [4] Michael A Nielsen and Isaac L Chuang. « Quantum Computation and Quantum Information ». In: (2010). URL: <https://www.cambridge.org/highereducation/books/quantum-computation-and-quantum-information/01E10196D0A682A6AEFFEA52D53BE9A/overview> (cit. on pp. 3, 9, 17, 84, 116).
- [5] Pieter Kok and Brendon W Lovett. *Introduction to optical quantum information processing*. Cambridge university press, 2010. URL: <https://www.cambridge.org/fr/academic/subjects/physics/quantum-physics-quantum-information-and-quantum-computation/introduction-optical-quantum-information-processing?format=HB&isbn=9780521519144> (cit. on p. 3).
- [6] Frank Arute, Kunal Arya, Ryan Babbush, Dave Bacon, Joseph C Bardin, Rami Barends, Rupak Biswas, Sergio Boixo, Fernando GSL Brandao, David A Buell, et al. « Quantum supremacy using a programmable superconducting processor ». In: *Nature* 574.7779 (2019), pp. 505–510. URL: <https://www.nature.com/articles/s41586-019-1666-5?categoryid=2849273&discountcode=DSI19S?categoryid=2849273> (cit. on p. 3).
- [7] Han-Sen Zhong, Hui Wang, Yu-Hao Deng, Ming-Cheng Chen, Li-Chao Peng, Yi-Han Luo, Jian Qin, Dian Wu, Xing Ding, Yi Hu, et al. « Quantum computational advantage using photons ». In: *Science* 370.6523 (2020), pp. 1460–1463. URL: <https://www.science.org/doi/abs/10.1126/science.abe8770> (cit. on p. 3).
- [8] Lars S Madsen, Fabian Laudenbach, Mohsen Falamarzi Askarani, Fabien Rortais, Trevor Vincent, Jacob FF Bulmer, Filippo M Miatto, Leonhard Neuhaus, Lukas G Helt, Matthew J Collins, et al. « Quantum computational advantage with a programmable photonic processor ». In: *Nature* 606.7912 (2022), pp. 75–81. URL: <https://www.nature.com/articles/s41586-022-04725-x> (cit. on p. 3).
- [9] Stefano Pirandola, Ulrik L Andersen, Leonardo Banchi, Mario Berta, Darius Bunandar, Roger Colbeck, Dirk Englund, Tobias Gehring, Cosmo Lupo, Carlo Ottaviani, et al. « Advances in quantum cryptography ». In: *Advances in optics and photonics* 12.4 (2020), pp. 1012–1236. URL: <https://opg.optica.org/aop/fulltext.cfm?uri=aop-12-4-1012&id=444736> (cit. on p. 3).

- [10] Feihu Xu, Xiongfeng Ma, Qiang Zhang, Hoi-Kwong Lo, and Jian-Wei Pan. « Secure quantum key distribution with realistic devices ». In: *Reviews of Modern Physics* 92.2 (2020), p. 025002. URL: <https://journals.aps.org/rmp/abstract/10.1103/RevModPhys.92.025002> (cit. on p. 3).
- [11] Stefano Pirandola, Jens Eisert, Christian Weedbrook, Akira Furusawa, and Samuel L Braunstein. « Advances in quantum teleportation ». In: *Nature photonics* 9.10 (2015), pp. 641–652. URL: <https://www.nature.com/articles/nphoton.2015.154> (cit. on p. 3).
- [12] Meiru Huo, Jiliang Qin, Jialin Cheng, Zhihui Yan, Zhongzhong Qin, Xiaolong Su, Xiaojun Jia, Changde Xie, and Kunchi Peng. « Deterministic quantum teleportation through fiber channels ». In: *Science advances* 4.10 (2018), eaas9401. URL: <https://www.science.org/doi/full/10.1126/sciadv.aas9401> (cit. on p. 3).
- [13] Vittorio Giovannetti, Seth Lloyd, and Lorenzo Maccone. « Quantum metrology ». In: *Physical review letters* 96.1 (2006), p. 010401. URL: <https://journals.aps.org/prl/abstract/10.1103/PhysRevLett.96.010401> (cit. on p. 3).
- [14] Vittorio Giovannetti, Seth Lloyd, and Lorenzo Maccone. « Advances in quantum metrology ». In: *Nature photonics* 5.4 (2011), pp. 222–229. URL: <https://www.nature.com/articles/nphoton.2011.35> (cit. on p. 3).
- [15] Erwan Bimbard, Nitin Jain, Andrew MacRae, and AI Lvovsky. « Quantum-optical state engineering up to the two-photon level ». In: *Nature Photonics* 4.4 (2010), pp. 243–247. URL: <https://www.nature.com/articles/nphoton.2010.6> (cit. on p. 4).
- [16] Jerome Esteve, Christian Gross, Andreas Weller, Stefano Giovanazzi, and Markus K Oberthaler. « Squeezing and entanglement in a Bose–Einstein condensate ». In: *Nature* 455.7217 (2008), pp. 1216–1219. URL: <https://www.nature.com/articles/nature07332> (cit. on p. 4).
- [17] TA Palomaki, JD Teufel, RW Simmonds, and Konrad W Lehnert. « Entangling mechanical motion with microwave fields ». In: *Science* 342.6159 (2013), pp. 710–713. URL: <https://www.science.org/doi/abs/10.1126/science.1244563> (cit. on p. 4).
- [18] MA Castellanos-Beltran, KD Irwin, GC Hilton, LR Vale, and KW Lehnert. « Amplification and squeezing of quantum noise with a tunable Josephson metamaterial ». In: *Nature Physics* 4.12 (2008), pp. 929–931. URL: <https://www.nature.com/articles/nphys1090> (cit. on p. 4).
- [19] Christopher Eichler, Deniz Bozyigit, C Lang, M Baur, L Steffen, JM Fink, Stefan Filipp, and Andreas Wallraff. « Observation of two-mode squeezing in the microwave frequency domain ». In: *Physical Review Letters* 107.11 (2011), p. 113601. URL: <https://journals.aps.org/prl/abstract/10.1103/PhysRevLett.107.113601> (cit. on p. 4).
- [20] Emanuel Knill, Raymond Laflamme, and Gerald J Milburn. « A scheme for efficient quantum computation with linear optics ». In: *nature* 409.6816 (2001), pp. 46–52. URL: <https://www.nature.com/articles/35051009> (cit. on pp. 4, 84).

- [21] Samuel L Braunstein and Peter Van Loock. « Quantum information with continuous variables ». In: *Reviews of modern physics* 77.2 (2005), p. 513. URL: <https://journals.aps.org/rmp/abstract/10.1103/RevModPhys.77.513> (cit. on pp. 4, 32, 84).
- [22] Akira Furusawa and Peter Van Loock. *Quantum teleportation and entanglement: a hybrid approach to optical quantum information processing*. John Wiley & Sons, 2011. URL: <https://www.wiley.com/en-us/Quantum+Teleportation+and+Entanglement%3A+A+Hybrid+Approach+to+Optical+Quantum+Information+Processing-p-9783527635290> (cit. on p. 4).
- [23] Tom Darras. « Quantum teleportation-based protocols with hybrid entanglement of light ». PhD thesis. Sorbonne université, 2021. URL: <https://tel.archives-ouvertes.fr/tel-03712015> (cit. on p. 4).
- [24] Julien Niset, Jaromír Fiurášek, and Nicolas J Cerf. « No-go theorem for Gaussian quantum error correction ». In: *Physical review letters* 102.12 (2009), p. 120501. URL: <https://journals.aps.org/prl/abstract/10.1103/PhysRevLett.102.120501> (cit. on pp. 4, 25, 59, 86).
- [25] Hiroki Takahashi, Jonas S Neergaard-Nielsen, Makoto Takeuchi, Masahiro Takeoka, Kazuhiro Hayasaka, Akira Furusawa, and Masahide Sasaki. « Entanglement distillation from Gaussian input states ». In: *Nature photonics* 4.3 (2010), pp. 178–181. URL: <https://www.nature.com/articles/nphoton.2010.1> (cit. on pp. 4, 25, 59).
- [26] Anders Tipsmark, Jonas S Neergaard-Nielsen, and Ulrik L Andersen. « Displacement-enhanced entanglement distillation of single-mode-squeezed entangled states ». In: *Optics Express* 21.6 (2013), pp. 6670–6680. URL: <https://opg.optica.org/oe/fulltext.cfm?uri=oe-21-6-6670&id=250720> (cit. on pp. 4, 25, 59).
- [27] Alexander I Lvovsky, Hauke Hansen, T Aichele, O Benson, J Mlynek, and S Schiller. « Quantum state reconstruction of the single-photon Fock state ». In: *Physical Review Letters* 87.5 (2001), p. 050402. URL: <https://journals.aps.org/prl/abstract/10.1103/PhysRevLett.87.050402> (cit. on p. 4).
- [28] Alexei Ourjoumteev, Rosa Tualle-Brouri, Julien Laurat, and Philippe Grangier. « Generating optical Schrodinger kittens for quantum information processing ». In: *Science* 312.5770 (2006), pp. 83–86. URL: <https://www.science.org/doi/abs/10.1126/science.1122858> (cit. on pp. 4, 125, 126, 186).
- [29] Jonas S Neergaard-Nielsen, B Melholt Nielsen, C Hettich, Klaus Mølmer, and Eugene S Polzik. « Generation of a superposition of odd photon number states for quantum information networks ». In: *Physical review letters* 97.8 (2006), p. 083604. URL: <https://journals.aps.org/prl/abstract/10.1103/PhysRevLett.97.083604> (cit. on pp. 4, 125, 126).
- [30] Valentina Parigi, Alessandro Zavatta, Myungshik Kim, and Marco Bellini. « Probing quantum commutation rules by addition and subtraction of single photons to/from a light field ». In: *Science* 317.5846 (2007), pp. 1890–1893. URL: <https://www.science.org/doi/abs/10.1126/science.1146204> (cit. on p. 4).

- [31] Elie Gouzien, Floriane Brunel, Sébastien Tanzilli, and Virginia d'Auria. « Scheme for the generation of hybrid entanglement between time-bin and wavelike encodings ». In: *Physical Review A* 102.1 (2020), p. 012603. URL: <https://journals.aps.org/pr/abstract/10.1103/PhysRevA.102.012603> (cit. on pp. 5, 83, 86, 88, 89, 163).
- [32] MF Melalkia, J Huynh, L Brunel, S Tanzilli, V D'Auria, and J Etesse. « Optical quantum state engineering with multimode resources: between a drawback to be circumvented and an advantage to be exploited ». In: *Quantum Technologies 2022*. Vol. 12133. SPIE. 2022, pp. 47–54. URL: <https://www.spiedigitallibrary.org/conference-proceedings-of-spie/12133/1213309/Optical-quantum-state-engineering-with-multimode-resources--between-a/10.1117/12.2621373.short> (cit. on p. 5).
- [33] Jean Etesse, Bhaskar Kanseri, and Rosa Tualle-Brouri. « Iterative tailoring of optical quantum states with homodyne measurements ». In: *Optics Express* 22.24 (2014), pp. 30357–30367. URL: <https://opg.optica.org/oe/fulltext.cfm?uri=oe-22-24-30357&id=305360> (cit. on pp. 6, 129–131, 164).
- [34] Jean Etesse, Martin Bouillard, Bhaskar Kanseri, and Rosa Tualle-Brouri. « Experimental generation of squeezed cat states with an operation allowing iterative growth ». In: *Physical review letters* 114.19 (2015), p. 193602. URL: <https://journals.aps.org/prl/abstract/10.1103/PhysRevLett.114.193602> (cit. on pp. 6, 129, 131, 164, 185).
- [35] Gilbert Grynberg, Alain Aspect, and Claude Fabre. *Introduction to quantum optics: from the semi-classical approach to quantized light*. Cambridge university press, 2010. URL: <https://www.cambridge.org/fr/academic/subjects/physics/optics-optoelectronics-and-photonics/introduction-quantum-optics-semi-classical-approach-quantized-light?format=HB&isbn=9780521551120> (cit. on p. 9).
- [36] Claude Cohen-Tannoudji, Bernard Diu, and Franck Laloë. *Quantum Mechanics*. John Wiley & Sons, 2019. URL: <https://www.wiley.com/en-fr/Quantum+Mechanics%2C+Volume+3%3A+Fermions%2C+Bosons%2C+Photons%2C+Correlations%2C+and+Entanglement-p-9783527345557> (cit. on p. 9).
- [37] Jean-Louis Basdevant and Jean Dalibard. *Quantum mechanics*. Springer Science & Business Media, 2005. URL: https://link.springer.com/book/10.1007/3-540-28805-8?utm_medium=referral&utm_source=google_books&utm_campaign=3_pier05_buy_print&utm_content=en_08082017 (cit. on pp. 9, 13).
- [38] Richard Jozsa. « Fidelity for mixed quantum states ». In: *Journal of modern optics* 41.12 (1994), pp. 2315–2323. URL: <https://doi.org/10.1080/09500349414552171> (cit. on p. 16).
- [39] E Wigner. « On the Quantum Correction For Thermodynamic Equilibrium ». In: *Physical Review* 40.5 (1932), p. 749. URL: <https://journals.aps.org/pr/abstract/10.1103/PhysRev.40.749> (cit. on p. 19).
- [40] Roy J Glauber. « Coherent and incoherent states of the radiation field ». In: *Physical Review* 131.6 (1963), p. 2766. URL: <https://journals.aps.org/pr/abstract/10.1103/PhysRev.131.2766> (cit. on p. 21).

- [41] Stephen Barnett and Paul M Radmore. *Methods in theoretical quantum optics*. Vol. 15. Oxford University Press, 2002. URL: <https://global.oup.com/academic/product/methods-in-theoretical-quantum-optics-9780198563617?cc=fr&lang=en> (cit. on p. 22).
- [42] Robin L Hudson. « When is the Wigner quasi-probability density non-negative? » In: *Reports on Mathematical Physics* 6.2 (1974), pp. 249–252. URL: <https://www.sciencedirect.com/science/article/pii/003448777490007X> (cit. on pp. 25, 122).
- [43] Erwin Schrödinger. « Naturwissenschaften 23 ». In: *English trans* (1935) (cit. on p. 25).
- [44] Michael Reck, Anton Zeilinger, Herbert J Bernstein, and Philip Bertani. « Experimental realization of any discrete unitary operator ». In: *Physical review letters* 73.1 (1994), p. 58. URL: <https://journals.aps.org/prl/abstract/10.1103/PhysRevLett.73.58> (cit. on p. 32).
- [45] R_E Slusher, LW Hollberg, Bernard Yurke, JC Mertz, and JF Valley. « Observation of squeezed states generated by four-wave mixing in an optical cavity ». In: *Physical review letters* 55.22 (1985), p. 2409. URL: <https://journals.aps.org/prl/abstract/10.1103/PhysRevLett.55.2409> (cit. on pp. 34, 42).
- [46] Henning Vahlbruch, Moritz Mehmet, Simon Chelkowski, Boris Hage, Alexander Franzen, Nico Lastzka, Stefan Gossler, Karsten Danzmann, and Roman Schnabel. « Observation of squeezed light with 10-dB quantum-noise reduction ». In: *Physical review letters* 100.3 (2008), p. 033602. URL: <https://journals.aps.org/prl/abstract/10.1103/PhysRevLett.100.033602> (cit. on p. 34).
- [47] Robert W Boyd. *Nonlinear optics*. Academic press, 2020. URL: <https://www.elsevier.com/books/nonlinear-optics/boyd/978-0-12-811002-7> (cit. on p. 34).
- [48] Marlan O Scully, M Suhail Zubairy, et al. *Quantum Optics*. Cambridge University Press, 1997. URL: <https://www.cambridge.org/fr/academic/subjects/physics/optics-optoelectronics-and-photonics/quantum-optics?format=PB&isbn=9780521435956> (cit. on p. 35).
- [49] Junjie Wu, Lixing You, Sijing Chen, Hao Li, Yuhao He, Chaolin Lv, Zhen Wang, and Xiaoming Xie. « Improving the timing jitter of a superconducting nanowire single-photon detection system ». In: *Applied optics* 56.8 (2017), pp. 2195–2200. URL: <https://opg.optica.org/ao/fulltext.cfm?uri=ao-56-8-2195&id=360607> (cit. on p. 37).
- [50] Élie Gouzien, Bruno Fedrici, Alessandro Zavatta, Sébastien Tanzilli, and Virginia D’Auria. « Quantum description of timing jitter for single-photon on-off detectors ». In: *Physical Review A* 98.1 (2018), p. 013833. URL: <https://journals.aps.org/pra/abstract/10.1103/PhysRevA.98.013833> (cit. on pp. 37, 117).

- [51] Tatsuki Sonoyama, Warit Asavanant, Kosuke Fukui, Mamoru Endo, Jun-ichi Yoshikawa, and Akira Furusawa. « Analysis of optical quantum state preparation using photon detectors in the finite-temporal-resolution regime ». In: *Physical Review A* 105.4 (2022), p. 043714. URL: <https://journals.aps.org/prabstract/10.1103/PhysRevA.105.043714> (cit. on p. 37).
- [52] Alessandro Ferraro, Stefano Olivares, and Matteo GA Paris. « Gaussian states in continuous variable quantum information ». In: *arXiv preprint quant-ph/0503237* (2005). URL: <https://arxiv.org/abs/quant-ph/0503237> (cit. on p. 38).
- [53] Horace P Yuen and Vincent WS Chan. « Noise in homodyne and heterodyne detection ». In: *Optics letters* 8.3 (1983), pp. 177–179. URL: <https://opg.optica.org/ol/fulltext.cfm?uri=ol-8-3-177&id=60009> (cit. on p. 39).
- [54] DT Smithey, M Beck, Michael G Raymer, and A Faridani. « Measurement of the Wigner distribution and the density matrix of a light mode using optical homodyne tomography: Application to squeezed states and the vacuum ». In: *Physical review letters* 70.9 (1993), p. 1244. URL: <https://journals.aps.org/prl/abstract/10.1103/PhysRevLett.70.1244> (cit. on p. 39).
- [55] ZY Ou, Silvana F Pereira, HJ Kimble, and KC Peng. « Realization of the Einstein-Podolsky-Rosen paradox for continuous variables ». In: *Physical Review Letters* 68.25 (1992), p. 3663. URL: <https://journals.aps.org/prl/abstract/10.1103/PhysRevLett.68.3663> (cit. on p. 39).
- [56] Xiongfeng Ma, Xiao Yuan, Zhu Cao, Bing Qi, and Zhen Zhang. « Quantum random number generation ». In: *npj Quantum Information* 2.1 (2016), pp. 1–9. URL: <https://www.nature.com/articles/npjqi201621> (cit. on p. 39).
- [57] Akira Furusawa, Jens Lykke Sørensen, Samuel L Braunstein, Christopher A Fuchs, H Jeff Kimble, and Eugene S Polzik. « Unconditional quantum teleportation ». In: *science* 282.5389 (1998), pp. 706–709. URL: <https://www.science.org/doi/abs/10.1126/science.282.5389.706> (cit. on p. 39).
- [58] Frédéric Grosshans and Philippe Grangier. « Continuous variable quantum cryptography using coherent states ». In: *Physical review letters* 88.5 (2002), p. 057902. URL: <https://journals.aps.org/prl/abstract/10.1103/PhysRevLett.88.057902> (cit. on p. 39).
- [59] Ling-An Wu, HJ Kimble, JL Hall, and Huifan Wu. « Generation of squeezed states by parametric down conversion ». In: *Physical review letters* 57.20 (1986), p. 2520. URL: <https://journals.aps.org/prl/abstract/10.1103/PhysRevLett.57.2520> (cit. on p. 42).
- [60] Robert M Shelby, Marc D Levenson, Stephen H Perlmutter, Ralph G DeVoe, and Daniel F Walls. « Broad-band parametric deamplification of quantum noise in an optical fiber ». In: *Physical review letters* 57.6 (1986), p. 691. URL: <https://journals.aps.org/prl/abstract/10.1103/PhysRevLett.57.691> (cit. on p. 42).

- [61] Mohammed Dakna, Tiemo Anhut, Tomáš Opatrný, Ludwig Knöll, and D-G Welsch. « Generating Schrödinger-cat-like states by means of conditional measurements on a beam splitter ». In: *Physical Review A* 55.4 (1997), p. 3184. URL: <https://journals.aps.org/prabstract/10.1103/PhysRevA.55.3184> (cit. on pp. 45, 111).
- [62] Alexei Ourjoumtsev, Hyunseok Jeong, Rosa Tualle-Brouri, and Philippe Grangier. « Generation of optical ‘Schrödinger cats’ from photon number states ». In: *Nature* 448.7155 (2007), pp. 784–786. URL: <https://www.nature.com/articles/nature06054> (cit. on pp. 46, 59).
- [63] AP Lund, H Jeong, TC Ralph, and MS Kim. « Conditional production of superpositions of coherent states with inefficient photon detection ». In: *Physical Review A* 70.2 (2004), p. 020101. URL: <https://journals.aps.org/prabstract/10.1103/PhysRevA.70.020101> (cit. on pp. 46, 129, 130).
- [64] Amine Laghaout, Jonas S Neergaard-Nielsen, Ioannes Rigas, Christian Kragh, Anders Tipsmark, and Ulrik L Andersen. « Amplification of realistic Schrödinger-cat-state-like states by homodyne heralding ». In: *Physical Review A* 87.4 (2013), p. 043826. URL: <https://journals.aps.org/prabstract/10.1103/PhysRevA.87.043826> (cit. on p. 49).
- [65] Jean Etesse, Rémi Blandino, Bhaskar Kanseri, and Rosa Tualle-Brouri. « Proposal for a loophole-free violation of Bell’s inequalities with a set of single photons and homodyne measurements ». In: *New Journal of Physics* 16.5 (2014), p. 053001. URL: <https://iopscience.iop.org/article/10.1088/1367-2630/16/5/053001/meta> (cit. on pp. 49, 129–131, 146, 185).
- [66] Alexander I Lvovsky and Michael G Raymer. « Continuous-variable optical quantum-state tomography ». In: *Reviews of modern physics* 81.1 (2009), p. 299. URL: <https://journals.aps.org/rmp/abstract/10.1103/RevModPhys.81.299> (cit. on pp. 53, 79).
- [67] Ulf Leonhardt. *Measuring the quantum state of light*. Vol. 22. Cambridge university press, 1997. URL: <https://www.cambridge.org/fr/academic/subjects/physics/optics-optoelectronics-and-photonics/measuring-quantum-state-light?format=HB&isbn=9780521497305> (cit. on pp. 53, 80).
- [68] GM D’ariano. « Measuring quantum states ». In: *Quantum Optics and the Spectroscopy of Solids*. Springer, 1997, pp. 175–202. URL: https://link.springer.com/chapter/10.1007/978-94-015-8796-9_9 (cit. on p. 53).
- [69] Matteo Paris and Jaroslav Rehacek. *Quantum state estimation*. Vol. 649. Springer Science & Business Media, 2004. URL: https://link.springer.com/book/10.1007/b98673?wt_mc=GoogleBooks.GoogleBooks.3.EN&token=gbgen (cit. on p. 53).
- [70] GM d’Ariano, C Macchiavello, and MGA Paris. « Detection of the density matrix through optical homodyne tomography without filtered back projection ». In: *Physical Review A* 50.5 (1994), p. 4298. URL: <https://journals.aps.org/prabstract/10.1103/PhysRevA.50.4298> (cit. on p. 55).

- [71] U Leonhardt, M Munroe, Th Kiss, Th Richter, and MG Raymer. « Sampling of photon statistics and density matrix using homodyne detection ». In: *Optics Communications* 127.1-3 (1996), pp. 144–160. URL: <https://www.sciencedirect.com/science/article/pii/0030401896000612> (cit. on p. 55).
- [72] Alexander I Lvovsky. « Iterative maximum-likelihood reconstruction in quantum homodyne tomography ». In: *Journal of Optics B: Quantum and Semiclassical Optics* 6.6 (2004), S556. URL: <https://iopscience.iop.org/article/10.1088/1464-4266/6/6/014/meta> (cit. on p. 55).
- [73] Zdenek Hradil. « Quantum-state estimation ». In: *Physical Review A* 55.3 (1997), R1561. URL: <https://journals.aps.org/pr/abstract/10.1103/PhysRevA.55.R1561> (cit. on p. 55).
- [74] Olivier Morin, Virginia d’Auria, Claude Fabre, and Julien Laurat. « High-fidelity single-photon source based on a Type II optical parametric oscillator ». In: *Optics letters* 37.17 (2012), pp. 3738–3740. URL: <https://opg.optica.org/ol/fulltext.cfm?uri=ol-37-17-3738&id=241093> (cit. on p. 59).
- [75] AI Lvovsky, Philippe Grangier, Alexei Ourjoumtsev, Valentina Parigi, Masahide Sasaki, and Rosa Tualle-Brouri. « Production and applications of non-Gaussian quantum states of light ». In: *arXiv preprint arXiv:2006.16985* (2020). URL: <https://arxiv.org/abs/2006.16985> (cit. on pp. 59, 66, 80, 111–113, 118, 120, 123, 126, 127).
- [76] Warit Asavanant, Kota Nakashima, Yu Shiozawa, Jun-Ichi Yoshikawa, and Akira Furusawa. « Generation of highly pure Schrödinger’s cat states and real-time quadrature measurements via optical filtering ». In: *Optics Express* 25.26 (2017), pp. 32227–32242. URL: <https://opg.optica.org/oe/fulltext.cfm?uri=oe-25-26-32227&id=379434> (cit. on pp. 59, 112, 118, 124).
- [77] Kan Takase, Akito Kawasaki, Byung Kyu Jeong, Mamoru Endo, Takahiro Kashiwazaki, Takushi Kazama, Koji Enbutsu, Kei Watanabe, Takeshi Umeki, Shigehito Miki, et al. « Generation of Schrödinger cat states with Wigner negativity using a continuous-wave low-loss waveguide optical parametric amplifier ». In: *Optics Express* 30.9 (2022), pp. 14161–14171. URL: <https://opg.optica.org/oe/fulltext.cfm?uri=oe-30-9-14161&id=471332> (cit. on p. 59).
- [78] Mohamed F. Melalkia, Tecla Gabbrielli, Antoine Petitjean, Léandre Brunel, Alessandro Zavatta, Sébastien Tanzilli, Jean Etesse, and Virginia D’Auria. « Plug-and-play generation of non-Gaussian states of light at a telecom wavelength ». In: *Opt. Express* 30.25 (2022), pp. 45195–45201. URL: <https://opg.optica.org/oe/abstract.cfm?URI=oe-30-25-45195> (cit. on p. 59).
- [79] Olivier Morin. « Non-Gaussian states and measurements for quantum information ». PhD thesis. Université Pierre et Marie Curie-Paris VI, 2013. URL: <https://tel.archives-ouvertes.fr/tel-01066655/> (cit. on p. 60).
- [80] Alexei Ourjoumtsev. « Étude théorique et expérimentale de superpositions quantiques cohérentes et d’états intriqués non-gaussiens de la lumière ». PhD thesis. Université Paris Sud-Paris XI, 2007. URL: <https://tel.archives-ouvertes.fr/tel-00200715/> (cit. on p. 60).

- [81] Virginia d’Auria, Noriyuki Lee, Taoufik Amri, Claude Fabre, and Julien Laurat. « Quantum decoherence of single-photon counters ». In: *Physical review letters* 107.5 (2011), p. 050504. URL: <https://journals.aps.org/prl/abstract/10.1103/PhysRevLett.107.050504> (cit. on p. 62).
- [82] Anatole Kenfack and Karol Życzkowski. « Negativity of the Wigner function as an indicator of non-classicality ». In: *Journal of Optics B: Quantum and Semiclassical Optics* 6.10 (2004), p. 396. URL: <https://iopscience.iop.org/article/10.1088/1464-4266/6/10/003/meta> (cit. on pp. 63, 122).
- [83] Jürgen Appel, Dallas Hoffman, Eden Figueroa, and AI Lvovsky. « Electronic noise in optical homodyne tomography ». In: *Physical Review A* 75.3 (2007), p. 035802. URL: <https://journals.aps.org/pra/pdf/10.1103/PhysRevA.75.035802> (cit. on p. 69).
- [84] Jun-ichi Yoshikawa, Warit Asavanant, and Akira Furusawa. « Purification of photon subtraction from continuous squeezed light by filtering ». In: *Physical Review A* 96.5 (2017), p. 052304. URL: <https://journals.aps.org/pra/abstract/10.1103/PhysRevA.96.052304> (cit. on p. 69).
- [85] MF Melalkia, L Brunel, S Tanzilli, J Etesse, and V D’Auria. « Theoretical framework for photon subtraction with non-mode-selective resources ». In: *Physical Review A* 105.1 (2022), p. 013720. URL: <https://journals.aps.org/pra/abstract/10.1103/PhysRevA.105.013720> (cit. on pp. 69, 111, 163).
- [86] RWP Drever, John L Hall, FV Kowalski, J_ Hough, GM Ford, AJ Munley, and H Ward. « Laser phase and frequency stabilization using an optical resonator ». In: *Applied Physics B* 31.2 (1983), pp. 97–105. URL: <https://link.springer.com/article/10.1007/BF00702605> (cit. on p. 73).
- [87] Alexander I Lvovsky. « Squeezed light ». In: *Photonics: Scientific Foundations, Technology and Applications* 1 (2015), pp. 121–163. URL: <https://onlinelibrary.wiley.com/doi/abs/10.1002/9781119009719.ch5> (cit. on p. 75).
- [88] Olivier Morin, Claude Fabre, and Julien Laurat. « Experimentally accessing the optimal temporal mode of traveling quantum light states ». In: *Physical review letters* 111.21 (2013), p. 213602. URL: <https://journals.aps.org/prl/abstract/10.1103/PhysRevLett.111.213602> (cit. on p. 76).
- [89] Demid V Sychev, Alexander E Ulanov, Anastasia A Pushkina, Matthew W Richards, Ilya A Fedorov, and Alexander I Lvovsky. « Enlargement of optical Schrödinger’s cat states ». In: *Nature Photonics* 11.6 (2017), pp. 379–382. URL: <https://www.nature.com/articles/nphoton.2017.57> (cit. on pp. 80, 129, 131, 185).
- [90] Alexei Ourjoumtsev, Rosa Tualle-Brouri, and Philippe Grangier. « Quantum homodyne tomography of a two-photon Fock state ». In: *Physical review letters* 96.21 (2006), p. 213601. URL: <https://journals.aps.org/prl/abstract/10.1103/PhysRevLett.96.213601> (cit. on p. 80).

- [91] François Mondain, Tommaso Lunghi, Alessandro Zavatta, Elie Gouzien, Florent Doutre, Marc De Micheli, Sébastien Tanzilli, and Virginia D'Auria. « Chip-based squeezing at a telecom wavelength ». In: *Photonics Research* 7.7 (2019), A36–A39. URL: <https://opg.optica.org/prj/abstract.cfm?uri=prj-7-7-a36> (cit. on pp. 81, 124, 126).
- [92] Francesco Lenzini, Jiri Janousek, Oliver Thearle, Matteo Villa, Ben Haylock, Sachin Kasture, Liang Cui, Hoang-Phuong Phan, Dzung Viet Dao, Hidehiro Yonezawa, et al. « Integrated photonic platform for quantum information with continuous variables ». In: *Science advances* 4.12 (2018), eaat9331. URL: <https://www.science.org/doi/full/10.1126/sciadv.aat9331> (cit. on pp. 81, 126).
- [93] Yun Zhao, Yoshitomo Okawachi, Jae K Jang, Xingchen Ji, Michal Lipson, and Alexander L Gaeta. « Near-degenerate quadrature-squeezed vacuum generation on a silicon-nitride chip ». In: *Physical Review Letters* 124.19 (2020), p. 193601. URL: <https://journals.aps.org/prl/abstract/10.1103/PhysRevLett.124.193601> (cit. on pp. 81, 151).
- [94] Marcel Bergmann and Peter van Loock. « Hybrid quantum repeater for qudits ». In: *Physical Review A* 99.3 (2019), p. 032349. URL: <https://journals.aps.org/pra/abstract/10.1103/PhysRevA.99.032349> (cit. on p. 83).
- [95] Shuntaro Takeda, Maria Fuwa, Peter van Loock, and Akira Furusawa. « Entanglement swapping between discrete and continuous variables ». In: *Physical review letters* 114.10 (2015), p. 100501. URL: <https://journals.aps.org/prl/abstract/10.1103/PhysRevLett.114.100501> (cit. on p. 83).
- [96] H Le Jeannic, A Cavaillès, J Raskop, K Huang, and J Laurat. « Remote preparation of continuous-variable qubits using loss-tolerant hybrid entanglement of light ». In: *Optica* 5.8 (2018), pp. 1012–1015. URL: <https://opg.optica.org/optica/fulltext.cfm?uri=optica-5-8-1012&id=396288> (cit. on p. 83).
- [97] Adrien Cavaillès, Hanna Le Jeannic, Jeremy Raskop, Giovanni Guccione, Damian Markham, Eleni Diamanti, Matthew D Shaw, Varun B Verma, Sae Woo Nam, and Julien Laurat. « Demonstration of Einstein-Podolsky-Rosen steering using hybrid continuous-and discrete-variable entanglement of light ». In: *Physical Review Letters* 121.17 (2018), p. 170403. URL: <https://journals.aps.org/prl/abstract/10.1103/PhysRevLett.121.170403> (cit. on p. 83).
- [98] Ulrik L Andersen, Jonas S Neergaard-Nielsen, Peter Van Loock, and Akira Furusawa. « Hybrid discrete-and continuous-variable quantum information ». In: *Nature Physics* 11.9 (2015), pp. 713–719. URL: <https://www.nature.com/articles/nphys3410> (cit. on pp. 83, 86).
- [99] Christian Weedbrook, Stefano Pirandola, Raúl García-Patrón, Nicolas J Cerf, Timothy C Ralph, Jeffrey H Shapiro, and Seth Lloyd. « Gaussian quantum information ». In: *Reviews of Modern Physics* 84.2 (2012), p. 621. URL: <https://journals.aps.org/rmp/abstract/10.1103/RevModPhys.84.621> (cit. on p. 84).
- [100] Ulrik L Andersen, Gerd Leuchs, and Christine Silberhorn. « Continuous-variable quantum information processing ». In: *Laser & Photonics Reviews* 4.3 (2010), pp. 337–354. URL: <https://onlinelibrary.wiley.com/doi/abs/10.1002/lpor.200910010> (cit. on p. 84).

- [101] SA Babichev, B Brezger, and AI Lvovsky. « Remote preparation of a single-mode photonic qubit by measuring field quadrature noise ». In: *Physical review letters* 92.4 (2004), p. 047903. URL: <https://journals.aps.org/prl/abstract/10.1103/PhysRevLett.92.047903> (cit. on p. 85).
- [102] Alexei Ourjoumtsev, Aurelien Dantan, Rosa Tualle-Brouiri, and Philippe Grangier. « Increasing entanglement between Gaussian states by coherent photon subtraction ». In: *Physical review letters* 98.3 (2007), p. 030502. URL: <https://journals.aps.org/prl/abstract/10.1103/PhysRevLett.98.030502> (cit. on p. 86).
- [103] H Jeong and Myung Shik Kim. « Efficient quantum computation using coherent states ». In: *Physical Review A* 65.4 (2002), p. 042305. URL: <https://journals.aps.org/prl/abstract/10.1103/PhysRevA.65.042305> (cit. on p. 86).
- [104] Timothy C Ralph, Alexei Gilchrist, Gerard J Milburn, William J Munro, and Scott Glancy. « Quantum computation with optical coherent states ». In: *Physical Review A* 68.4 (2003), p. 042319. URL: <https://journals.aps.org/prl/abstract/10.1103/PhysRevA.68.042319> (cit. on p. 86).
- [105] Austin P Lund, Timothy C Ralph, and Henry L Haselgrove. « Fault-tolerant linear optical quantum computing with small-amplitude coherent states ». In: *Physical review letters* 100.3 (2008), p. 030503. URL: <https://journals.aps.org/prl/abstract/10.1103/PhysRevLett.100.030503> (cit. on p. 86).
- [106] Kimin Park and Hyunseok Jeong. « Entangled coherent states versus entangled photon pairs for practical quantum-information processing ». In: *Physical Review A* 82.6 (2010), p. 062325. URL: <https://journals.aps.org/prl/abstract/10.1103/PhysRevA.82.062325> (cit. on p. 86).
- [107] Peter Van Loock. « Optical hybrid approaches to quantum information ». In: *Laser & Photonics Reviews* 5.2 (2011), pp. 167–200. URL: <https://onlinelibrary.wiley.com/doi/abs/10.1002/lpor.201000005> (cit. on p. 86).
- [108] Seung-Woo Lee and Hyunseok Jeong. « Near-deterministic quantum teleportation and resource-efficient quantum computation using linear optics and hybrid qubits ». In: *Physical Review A* 87.2 (2013), p. 022326. URL: <https://journals.aps.org/prl/abstract/10.1103/PhysRevA.87.022326> (cit. on p. 86).
- [109] Hyunseok Jeong, Alessandro Zavatta, Minsu Kang, Seung-Woo Lee, Luca S Costanzo, Samuele Grandi, Timothy C Ralph, and Marco Bellini. « Generation of hybrid entanglement of light ». In: *Nature Photonics* 8.7 (2014), pp. 564–569. URL: <https://www.nature.com/articles/nphoton.2014.136> (cit. on p. 86).
- [110] Olivier Morin, Kun Huang, Jianli Liu, Hanna Le Jeannic, Claude Fabre, and Julien Laurat. « Remote creation of hybrid entanglement between particle-like and wave-like optical qubits ». In: *Nature Photonics* 8.7 (2014), pp. 570–574. URL: <https://www.nature.com/articles/nphoton.2014.137> (cit. on p. 86).
- [111] Demid V Sychev, Alexander E Ulanov, Egor S Tiunov, Anastasia A Pushkina, A Kuzhamuratov, Valery Novikov, and AI Lvovsky. « Entanglement and teleportation between polarization and wave-like encodings of an optical qubit ». In: *Nature communications* 9.1 (2018), pp. 1–7. URL: <https://www.nature.com/articles/s41467-018-06055-x> (cit. on p. 86).

- [112] Giovanni Guccione, Tom Darras, Hanna Le Jeannic, Varun B Verma, Sae Woo Nam, Adrien Cavallès, and Julien Laurat. « Connecting heterogeneous quantum networks by hybrid entanglement swapping ». In: *Science advances* 6.22 (2020), eaba4508. URL: <https://www.science.org/doi/full/10.1126/sciadv.aba4508> (cit. on p. 86).
- [113] Marek Żukowski, Anton Zeilinger, Michael A Horne, and Artur K Ekert. « “Event-ready-detectors” Bell experiment via entanglement swapping ». In: *Physical Review Letters* 71.26 (1993), p. 4287. URL: <https://journals.aps.org/prl/abstract/10.1103/PhysRevLett.71.4287> (cit. on p. 89).
- [114] Ivan Marcikic, Hugues de Riedmatten, Wolfgang Tittel, Valerio Scarani, Hugo Zbinden, and Nicolas Gisin. « Time-bin entangled qubits for quantum communication created by femtosecond pulses ». In: *Physical Review A* 66.6 (2002), p. 062308. URL: <https://journals.aps.org/pra/abstract/10.1103/PhysRevA.66.062308> (cit. on p. 90).
- [115] Virginia D’Auria, Bruno Fedrici, Lutfi Arif Ngah, Florian Kaiser, Laurent Labonté, Olivier Alibert, and Sébastien Tanzilli. « A universal, plug-and-play synchronisation scheme for practical quantum networks ». In: *npj Quantum Information* 6.1 (2020), pp. 1–6. URL: <https://www.nature.com/articles/s41534-020-0245-9> (cit. on p. 90).
- [116] Warren P Grice and Ian A Walmsley. « Spectral information and distinguishability in type-II down-conversion with a broadband pump ». In: *Physical Review A* 56.2 (1997), p. 1627. URL: <https://journals.aps.org/pra/abstract/10.1103/PhysRevA.56.1627> (cit. on p. 91).
- [117] Lawrence E Myers, RC Eckardt, Martin M Fejer, Robert L Byer, and Walter R Bosenberg. « Multigrating quasi-phase-matched optical parametric oscillator in periodically poled LiNbO₃ ». In: *Optics letters* 21.8 (1996), pp. 591–593. URL: <https://opg.optica.org/ol/fulltext.cfm?uri=ol-21-8-591&id=44803> (cit. on p. 91).
- [118] Andreas Christ, Kaisa Laiho, Andreas Eckstein, Katiúscia N Cassemiro, and Christine Silberhorn. « Probing multimode squeezing with correlation functions ». In: *New Journal of Physics* 13.3 (2011), p. 033027. URL: <https://iopscience.iop.org/article/10.1088/1367-2630/13/3/033027/meta> (cit. on pp. 92, 123).
- [119] V Roman-Rodriguez, B Brecht, K Srinivasan, C Silberhorn, N Treps, Eleni Diamanti, and V Parigi. « Continuous variable multimode quantum states via symmetric group velocity matching ». In: *New Journal of Physics* 23.4 (2021), p. 043012. URL: <https://iopscience.iop.org/article/10.1088/1367-2630/abef96/meta> (cit. on pp. 93, 132, 186).
- [120] W Glenn. « Second-harmonic generation by picosecond optical pulses ». In: *IEEE Journal of Quantum Electronics* 5.6 (1969), pp. 284–290. URL: https://ieeexplore.ieee.org/abstract/document/1081948?casa_token=cb1vMse2suEAAAAA:EQjp4Wnr3BBE2dUE5L9dydSb7f-zIS0r0MAKzeaHvV5fhuXCxhiKFB6YORMtUAhu_8yjvTP6NCQ (cit. on pp. 96, 179, 180).

- [121] Agata M Brańczyk, TC Ralph, Wolfram Helwig, and Christine Silberhorn. « Optimized generation of heralded Fock states using parametric down-conversion ». In: *New Journal of Physics* 12.6 (2010), p. 063001. URL: <https://iopscience.iop.org/article/10.1088/1367-2630/12/6/063001/meta> (cit. on pp. 97, 112, 114, 115, 118, 119, 132, 186).
- [122] David E Zelmon, David L Small, and Dieter Jundt. « Infrared corrected Sellmeier coefficients for congruently grown lithium niobate and 5 mol.% magnesium oxide-doped lithium niobate ». In: *JOSA B* 14.12 (1997), pp. 3319–3322. URL: <https://opg.optica.org/josab/fulltext.cfm?uri=josab-14-12-3319&id=35250> (cit. on p. 98).
- [123] Kiyoshi Kato and Eiko Takaoka. « Sellmeier and thermo-optic dispersion formulas for KTP ». In: *Applied optics* 41.24 (2002), pp. 5040–5044. URL: <https://opg.optica.org/ao/fulltext.cfm?uri=ao-41-24-5040&id=69785> (cit. on p. 98).
- [124] Annamaria Dosseva, Łukasz Cincio, and Agata M Brańczyk. « Shaping the joint spectrum of down-converted photons through optimized custom poling ». In: *Physical Review A* 93.1 (2016), p. 013801. URL: <https://journals.aps.org/prabstract/10.1103/PhysRevA.93.013801> (cit. on p. 100).
- [125] Jean-Luc Tambasco, Andreas Boes, LG Helt, MJ Steel, and Arnan Mitchell. « Domain engineering algorithm for practical and effective photon sources ». In: *Optics express* 24.17 (2016), pp. 19616–19626. URL: <https://opg.optica.org/oe/fulltext.cfm?uri=oe-24-17-19616&id=348856> (cit. on p. 100).
- [126] Francesco Graffitti, Dmytro Kundys, Derryck T Reid, Agata M Brańczyk, and Alessandro Fedrizzi. « Pure down-conversion photons through sub-coherence-length domain engineering ». In: *Quantum Science and Technology* 2.3 (2017), p. 035001. URL: <https://iopscience.iop.org/article/10.1088/2058-9565/aa78d4/meta> (cit. on p. 100).
- [127] GD Boyd and DA Kleinman. « Parametric interaction of focused Gaussian light beams ». In: *Journal of Applied Physics* 39.8 (1968), pp. 3597–3639. URL: <https://aip.scitation.org/doi/abs/10.1063/1.1656831> (cit. on p. 104).
- [128] Rogers H Stolen and Chinlon Lin. « Self-phase-modulation in silica optical fibers ». In: *Physical Review A* 17.4 (1978), p. 1448. URL: <https://journals.aps.org/prabstract/10.1103/PhysRevA.17.1448> (cit. on p. 104).
- [129] Marco Liscidini and JE Sipe. « Stimulated emission tomography ». In: *Physical review letters* 111.19 (2013), p. 193602. URL: <https://journals.aps.org/prl/abstract/10.1103/PhysRevLett.111.193602> (cit. on p. 106).
- [130] Bin Fang, Offir Cohen, Marco Liscidini, John E Sipe, and Virginia O Lorenz. « Fast and highly resolved capture of the joint spectral density of photon pairs ». In: *Optica* 1.5 (2014), pp. 281–284. URL: <https://opg.optica.org/optica/fulltext.cfm?uri=optica-1-5-281&id=303477> (cit. on p. 106).
- [131] Wojciech Wasilewski, Alexander I Lvovsky, Konrad Banaszek, and Czesław Radzewicz. « Pulsed squeezed light: Simultaneous squeezing of multiple modes ». In: *Physical Review A* 73.6 (2006), p. 063819. URL: <https://journals.aps.org/prabstract/10.1103/PhysRevA.73.063819> (cit. on pp. 111, 112, 119, 126, 132, 183).

- [132] Masahide Sasaki and Shigenari Suzuki. « Multimode theory of measurement-induced non-Gaussian operation on wideband squeezed light: Analytical formula ». In: *Physical Review A* 73.4 (2006), p. 043807. URL: <https://journals.aps.org/pr/abstract/10.1103/PhysRevA.73.043807> (cit. on pp. 111, 120).
- [133] Andreas Eckstein, Andreas Christ, Peter J Mosley, and Christine Silberhorn. « Highly efficient single-pass source of pulsed single-mode twin beams of light ». In: *Physical Review Letters* 106.1 (2011), p. 013603. URL: <https://journals.aps.org/prl/abstract/10.1103/PhysRevLett.106.013603> (cit. on pp. 111, 119, 124).
- [134] Mattia Walschaers, Supratik Sarkar, Valentina Parigi, and Nicolas Treps. « Tailoring non-Gaussian continuous-variable graph states ». In: *Physical review letters* 121.22 (2018), p. 220501. URL: <https://journals.aps.org/prl/abstract/10.1103/PhysRevLett.121.220501> (cit. on p. 111).
- [135] Young-Sik Ra, Adrien Dufour, Mattia Walschaers, Clément Jacquard, Thibault Michel, Claude Fabre, and Nicolas Treps. « Non-Gaussian quantum states of a multimode light field ». In: *Nature Physics* 16.2 (2020), pp. 144–147. URL: <https://www.nature.com/articles/s41567-019-0726-y> (cit. on pp. 111, 113, 116, 120, 186).
- [136] V Averchenko, C Jacquard, V Thiel, C Fabre, and N Treps. « Multimode theory of single-photon subtraction ». In: *New Journal of Physics* 18.8 (2016), p. 083042. URL: <https://iopscience.iop.org/article/10.1088/1367-2630/18/8/083042/meta> (cit. on pp. 111, 113, 118).
- [137] Andreas Eckstein, Benjamin Brecht, and Christine Silberhorn. « A quantum pulse gate based on spectrally engineered sum frequency generation ». In: *Optics express* 19.15 (2011), pp. 13770–13778. URL: <https://opg.optica.org/oe/fulltext.cfm?uri=oe-19-15-13770&id=219560> (cit. on pp. 111, 113).
- [138] Giuseppe Patera, Nicolas Treps, Claude Fabre, and German J De Valcarcel. « Quantum theory of synchronously pumped type I optical parametric oscillators: characterization of the squeezed supermodes ». In: *The European Physical Journal D* 56.1 (2010), pp. 123–140. URL: <https://link.springer.com/article/10.1140/epjd/e2009-00299-9> (cit. on p. 112).
- [139] Elie Gouzien, Sébastien Tanzilli, Virginia d’Auria, and Giuseppe Patera. « Morphing supermodes: a full characterization for enabling multimode quantum optics ». In: *Physical Review Letters* 125.10 (2020), p. 103601. URL: <https://journals.aps.org/prl/abstract/10.1103/PhysRevLett.125.103601> (cit. on p. 112).
- [140] Andreas Christ, Cosmo Lupo, Matthias Reichelt, Torsten Meier, and Christine Silberhorn. « Theory of filtered type-II parametric down-conversion in the continuous-variable domain: Quantifying the impacts of filtering ». In: *Physical Review A* 90.2 (2014), p. 023823. URL: <https://journals.aps.org/pr/abstract/10.1103/PhysRevA.90.023823> (cit. on pp. 112, 118).
- [141] A. Ourjoumtsev. « Theoretical and experimental study of quantum coherent superpositions and of non-Gaussian entangled states of the light ». In: *PhD Thesis* (2008) (cit. on p. 113).

- [142] Virginia d’Auria, Olivier Morin, Claude Fabre, and Julien Laurat. « Effect of the heralding detector properties on the conditional generation of single-photon states ». In: *The European Physical Journal D* 66.10 (2012), pp. 1–7. URL: <https://link.springer.com/article/10.1140/epjd/e2012-30351-6> (cit. on p. 117).
- [143] Michael Martin Nieto. « Displaced and squeezed number states ». In: *Physics Letters A* 229.3 (1997), pp. 135–143. URL: <https://www.sciencedirect.com/science/article/pii/S0375960197001837> (cit. on p. 120).
- [144] Marco G Genoni, Mattia L Palma, Tommaso Tufarelli, Stefano Olivares, MS Kim, and Matteo GA Paris. « Detecting quantum non-Gaussianity via the Wigner function ». In: *Physical Review A* 87.6 (2013), p. 062104. URL: <https://journals.aps.org/pr/abstract/10.1103/PhysRevA.87.062104> (cit. on p. 122).
- [145] Radim Filip and Ladislav Mišta Jr. « Detecting quantum states with a positive Wigner function beyond mixtures of Gaussian states ». In: *Physical Review Letters* 106.20 (2011), p. 200401. URL: <https://journals.aps.org/prl/abstract/10.1103/PhysRevLett.106.200401> (cit. on p. 122).
- [146] Kentaro Wakui, Hiroki Takahashi, Akira Furusawa, and Masahide Sasaki. « Photon subtracted squeezed states generated with periodically poled KTiOPO₄ ». In: *Optics Express* 15.6 (2007), pp. 3568–3574. URL: <https://opg.optica.org/oe/abstract.cfm?uri=OE-15-6-3568> (cit. on pp. 125, 126).
- [147] Joel F Tasker, Jonathan Frazer, Giacomo Ferranti, Euan J Allen, Léandre F Brunel, Sébastien Tanzilli, Virginia D’Auria, and Jonathan CF Matthews. « Silicon photonics interfaced with integrated electronics for 9 GHz measurement of squeezed light ». In: *Nature Photonics* 15.1 (2021), pp. 11–15. URL: <https://www.nature.com/articles/s41566-020-00715-5> (cit. on p. 127).
- [148] Daniel Gottesman, Alexei Kitaev, and John Preskill. « Encoding a qubit in an oscillator ». In: *Physical Review A* 64.1 (2001), p. 012310. URL: <https://journals.aps.org/pr/abstract/10.1103/PhysRevA.64.012310> (cit. on pp. 129, 130, 143, 146, 164).
- [149] Yu Zheng, Oliver Hahn, Pascal Stadler, Patric Holmvall, Fernando Quijandría, Alessandro Ferraro, and Giulia Ferrini. « Gaussian conversion protocols for cubic phase state generation ». In: *PRX Quantum* 2.1 (2021), p. 010327. URL: <https://journals.aps.org/prxquantum/abstract/10.1103/PRXQuantum.2.010327> (cit. on p. 129).
- [150] Bastian Hacker, Stephan Welte, Severin Daiss, Armin Shaukat, Stephan Ritter, Lin Li, and Gerhard Rempe. « Deterministic creation of entangled atom–light Schrödinger-cat states ». In: *Nature Photonics* 13.2 (2019), pp. 110–115. URL: <https://www.nature.com/articles/s41566-018-0339-5> (cit. on p. 129).
- [151] Kosuke Fukui, Mamoru Endo, Warit Asavanant, Atsushi Sakaguchi, Jun-ichi Yoshikawa, and Akira Furusawa. « Generating the Gottesman-Kitaev-Preskill qubit using a cross-Kerr interaction between squeezed light and Fock states in optics ». In: *Physical Review A* 105.2 (2022), p. 022436. URL: <https://journals.aps.org/pr/abstract/10.1103/PhysRevA.105.022436> (cit. on p. 129).

- [152] Zhiling Wang, Zenghui Bao, Yukai Wu, Yan Li, Weizhou Cai, Weiting Wang, Yuwei Ma, Tianqi Cai, Xiyue Han, Jiahui Wang, et al. « A flying Schrödinger's cat in multipartite entangled states ». In: *Science advances* 8.10 (2022), eabn1778. URL: <https://www.science.org/doi/full/10.1126/sciadv.abn1778> (cit. on p. 129).
- [153] Jacob Hastrup, Kimin Park, Jonatan Bohr Brask, Radim Filip, and Ulrik Lund Andersen. « Measurement-free preparation of grid states ». In: *npj Quantum Information* 7.1 (2021), pp. 1–8. URL: <https://www.nature.com/articles/s41534-020-00353-3> (cit. on p. 129).
- [154] Daniel J Weigand and Barbara M Terhal. « Generating grid states from Schrödinger-cat states without postselection ». In: *Physical Review A* 97.2 (2018), p. 022341. URL: <https://journals.aps.org/prabstract/10.1103/PhysRevA.97.022341> (cit. on p. 129).
- [155] Miller Eaton, Rajveer Nehra, and Olivier Pfister. « Non-Gaussian and Gottesman–Kitaev–Preskill state preparation by photon catalysis ». In: *New Journal of Physics* 21.11 (2019), p. 113034. URL: <https://iopscience.iop.org/article/10.1088/1367-2630/ab5330/meta> (cit. on pp. 129, 130).
- [156] Miller Eaton, Carlos González-Arciniegas, Rafael N Alexander, Nicolas C Menicucci, and Olivier Pfister. « Measurement-based generation and preservation of cat and grid states within a continuous-variable cluster state ». In: *Quantum* 6 (2022), p. 769. URL: <https://quantum-journal.org/papers/q-2022-07-20-769/> (cit. on p. 129).
- [157] Jaromír Fiurášek, Raúl García-Patrón, and Nicolas J Cerf. « Conditional generation of arbitrary single-mode quantum states of light by repeated photon subtractions ». In: *Physical Review A* 72.3 (2005), p. 033822. URL: <https://journals.aps.org/prabstract/10.1103/PhysRevA.72.033822> (cit. on p. 129).
- [158] MF Melalkia, J Huynh, S Tanzilli, V d'Auria, and J Etesse. « A multiplexed synthesizer for non-Gaussian photonic quantum state generation ». In: *arXiv preprint arXiv:2206.14915* (2022). URL: <https://arxiv.org/abs/2206.14915> (cit. on pp. 129, 164).
- [159] Masahiro Takeoka and Masahide Sasaki. « Conditional generation of an arbitrary superposition of coherent states ». In: *Physical Review A* 75.6 (2007), p. 064302. URL: <https://journals.aps.org/prabstract/10.1103/PhysRevA.75.064302> (cit. on p. 130).
- [160] Jonatan B Brask, Ioannes Rigas, Eugene S Polzik, Ulrik L Andersen, and Anders S Sørensen. « Hybrid long-distance entanglement distribution protocol ». In: *Physical review letters* 105.16 (2010), p. 160501. URL: <https://journals.aps.org/prl/abstract/10.1103/PhysRevLett.105.160501> (cit. on p. 130).
- [161] Hanna Le Jeannic, Adrien Cavaillès, Kun Huang, Radim Filip, and Julien Laurat. « Slowing quantum decoherence by squeezing in phase space ». In: *Physical Review Letters* 120.7 (2018), p. 073603. URL: <https://journals.aps.org/prl/abstract/10.1103/PhysRevLett.120.073603> (cit. on pp. 130, 186).

- [162] Hilma M Vasconcelos, Liliana Sanz, and Scott Glancy. « All-optical generation of states for “Encoding a qubit in an oscillator” ». In: *Optics letters* 35.19 (2010), pp. 3261–3263. URL: <https://opg.optica.org/ol/fulltext.cfm?uri=ol-35-19-3261&id=205925> (cit. on pp. 131, 146).
- [163] Martin Bouillard, Guillaume Boucher, J Ferrer Ortas, Benjamin Pointard, and Rosa Tualle-Brouri. « Quantum storage of single-photon and two-photon fock states with an all-optical quantum memory ». In: *Physical review letters* 122.21 (2019), p. 210501. URL: <https://journals.aps.org/prl/abstract/10.1103/PhysRevLett.122.210501> (cit. on p. 131).
- [164] Olivier Alibart, Virginia D’Auria, Marc De Micheli, Florent Doutre, Florian Kaiser, Laurent Labonté, Tommaso Lunghi, Éric Picholle, and Sébastien Tanzilli. « Quantum photonics at telecom wavelengths based on lithium niobate waveguides ». In: *Journal of Optics* 18.10 (2016), p. 104001. URL: <https://iopscience.iop.org/article/10.1088/2040-8978/18/10/104001/meta> (cit. on p. 131).
- [165] Christa Flühmann, Thanh Long Nguyen, Matteo Marinelli, Vlad Negnevitsky, Karan Mehta, and JP Home. « Encoding a qubit in a trapped-ion mechanical oscillator ». In: *Nature* 566.7745 (2019), pp. 513–517. URL: <https://www.nature.com/articles/s41586-019-0960-6> (cit. on p. 146).
- [166] Philippe Campagne-Ibarcq, Alec Eickbusch, Steven Touzard, Evan Zalys-Geller, Nicholas E Frattini, Volodymyr V Sivak, Philip Reinhold, Shruti Puri, Shyam Shankar, Robert J Schoelkopf, et al. « Quantum error correction of a qubit encoded in grid states of an oscillator ». In: *Nature* 584.7821 (2020), pp. 368–372. URL: <https://www.nature.com/articles/s41586-020-2603-3> (cit. on p. 146).
- [167] Nicolas C Menicucci, Peter Van Loock, Mile Gu, Christian Weedbrook, Timothy C Ralph, and Michael A Nielsen. « Universal quantum computation with continuous-variable cluster states ». In: *Physical review letters* 97.11 (2006), p. 110501. URL: <https://journals.aps.org/prl/abstract/10.1103/PhysRevLett.97.110501> (cit. on p. 151).
- [168] Giulia Ferrini, Jonathan Roslund, Francesco Arzani, Yin Cai, Claude Fabre, and Nicolas Treps. « Optimization of networks for measurement-based quantum computation ». In: *Physical Review A* 91.3 (2015), p. 032314. URL: <https://journals.aps.org/prl/abstract/10.1103/PhysRevA.91.032314> (cit. on p. 151).
- [169] Mikkel V Larsen, Christopher Chamberland, Kyungjoo Noh, Jonas S Neergaard-Nielsen, and Ulrik L Andersen. « Fault-tolerant continuous-variable measurement-based quantum computation architecture ». In: *Prx Quantum* 2.3 (2021), p. 030325. URL: <https://journals.aps.org/prxquantum/abstract/10.1103/PRXQuantum.2.030325> (cit. on p. 151).
- [170] Johannes Nokkala, Francesco Arzani, Fernando Galve, Roberta Zambrini, Sabrina Maniscalco, Jyrki Piilo, Nicolas Treps, and Valentina Parigi. « Reconfigurable optical implementation of quantum complex networks ». In: *New Journal of Physics* 20.5 (2018), p. 053024. URL: <https://iopscience.iop.org/article/10.1088/1367-2630/aabc77/meta> (cit. on p. 151).

- [171] Sven Ramelow, Alessandro Farsi, Zachary Vernon, Stephane Clemmen, Xingchen Ji, JE Sipe, Marco Liscidini, Michal Lipson, and Alexander L Gaeta. « Strong nonlinear coupling in a 3×4 ring resonator ». In: *Physical review letters* 122.15 (2019), p. 153906. URL: <https://journals.aps.org/prl/abstract/10.1103/PhysRevLett.122.153906> (cit. on p. 151).
- [172] Houssein El Dirani, Laurene Youssef, Camille Petit-Etienne, Sebastien Kerdiles, Philippe Grosse, Christelle Monat, Erwine Pargon, and Corrado Sciancalepore. « Ultralow-loss tightly confining 3×4 waveguides and high-Q microresonators ». In: *Optics express* 27.21 (2019), pp. 30726–30740. URL: <https://opg.optica.org/oe/fulltext.cfm?uri=oe-27-21-30726&id=422176> (cit. on p. 151).
- [173] Alberto Politi, Martin J Cryan, John G Rarity, Siyuan Yu, and Jeremy L O'brien. « Silica-on-silicon waveguide quantum circuits ». In: *Science* 320.5876 (2008), pp. 646–649. URL: <https://www.science.org/doi/abs/10.1126/science.1155441> (cit. on p. 151).
- [174] Alessia Pasquazi, Marco Peccianti, Luca Razzari, David J Moss, Stéphane Coen, Miro Erkintalo, Yanne K Chembo, Tobias Hansson, Stefan Wabnitz, Pascal Del'Haye, et al. « Micro-combs: A novel generation of optical sources ». In: *Physics Reports* 729 (2018), pp. 1–81. URL: <https://www.sciencedirect.com/science/article/pii/S0370157317303253> (cit. on p. 151).
- [175] Yanne K Chembo and Nan Yu. « Modal expansion approach to optical-frequency-comb generation with monolithic whispering-gallery-mode resonators ». In: *Physical Review A* 82.3 (2010), p. 033801. URL: <https://journals.aps.org/prabstract/10.1103/PhysRevA.82.033801> (cit. on p. 151).
- [176] Yanne K Chembo. « Quantum dynamics of Kerr optical frequency combs below and above threshold: Spontaneous four-wave mixing, entanglement, and squeezed states of light ». In: *Physical Review A* 93.3 (2016), p. 033820. URL: <https://journals.aps.org/prabstract/10.1103/PhysRevA.93.033820> (cit. on p. 151).
- [177] Melissa A Guidry, Daniil M Lukin, Ki Youl Yang, Rahul Trivedi, and Jelena Vučković. « Quantum optics of soliton microcombs ». In: *Nature Photonics* 16.1 (2022), pp. 52–58. URL: <https://www.nature.com/articles/s41566-021-00901-z> (cit. on p. 151).
- [178] Élie Gouzien, Laurent Labonté, Alessandro Zavatta, Jean Etesse, Sébastien Tanzilli, Virginia d'Auria, and Giuseppe Patera. « Hidden and detectable squeezing from micro-resonators ». In: *arXiv preprint arXiv:2207.00360* (2022). URL: <https://arxiv.org/abs/2207.00360> (cit. on p. 151).
- [179] Avik Dutt, Kevin Luke, Sasikanth Manipatruni, Alexander L Gaeta, Paulo Nussenzveig, and Michal Lipson. « On-chip optical squeezing ». In: *Physical Review Applied* 3.4 (2015), p. 044005. URL: <https://journals.aps.org/prapplied/abstract/10.1103/PhysRevApplied.3.044005> (cit. on p. 151).
- [180] Zijiao Yang, Mandana Jahanbozorgi, Dongjin Jeong, Shuman Sun, Olivier Pfister, Hansuek Lee, and Xu Yi. « A squeezed quantum microcomb on a chip ». In: *Nature Communications* 12.1 (2021), pp. 1–8. URL: <https://www.nature.com/articles/s41467-021-25054-z> (cit. on p. 151).

- [181] Dominik G Rabus. *Integrated ring resonators*. Springer, 2007. URL: <https://link.springer.com/book/10.1007/978-3-030-60131-7> (cit. on p. 152).
- [182] Houssein El Dirani. « Development of high quality silicon nitride chips for integrated nonlinear photonics ». PhD thesis. Université de Lyon, 2019. URL: <https://tel.archives-ouvertes.fr/tel-02460563/> (cit. on p. 152).
- [183] Joaquin Matres and Wayne V Sorin. « Simple model for ring resonators backscatter ». In: *Optics Express* 25.4 (2017), pp. 3242–3251. URL: <https://opg.optica.org/oe/fulltext.cfm?uri=oe-25-4-3242&id=359862> (cit. on pp. 154, 155).
- [184] Ioannis Chremmos, Otto Schwelb, and Nikolaos Uzunoglu. *Photonic microresonator research and applications*. Vol. 156. Springer, 2010. URL: https://link.springer.com/book/10.1007/978-1-4419-1744-7?utm_medium=referral&utm_source=google_books&utm_campaign=3_pier05_buy_print&utm_content=en-08082017 (cit. on p. 157).
- [185] T Herr, K Hartinger, J Riemensberger, CY Wang, E Gavartin, R Holzwarth, ML Gorodetsky, and TJ Kippenberg. « Universal formation dynamics and noise of Kerr-frequency combs in microresonators ». In: *Nature photonics* 6.7 (2012), pp. 480–487. URL: <https://www.nature.com/articles/nphoton.2012.127?message-global=remove&page=3> (cit. on p. 157).
- [186] Herwig Kogelnik and Tingye Li. « Laser beams and resonators ». In: *Applied optics* 5.10 (1966), pp. 1550–1567. URL: <https://opg.optica.org/ao/fulltext.cfm?uri=ao-5-10-1550&id=14408> (cit. on p. 173).
- [187] PA Bélanger. « Beam propagation and the ABCD ray matrices ». In: *Optics letters* 16.4 (1991), pp. 196–198. URL: <https://opg.optica.org/ol/fulltext.cfm?uri=ol-16-4-196&id=59803> (cit. on p. 173).
- [188] Bahaa EA Saleh and Malvin Carl Teich. *Fundamentals of photonics*. John Wiley & Sons, 2019. URL: <https://www.wiley.com/en-fr/Fundamentals+of+Photonics%2C+2+Volume+Set%2C+3rd+Edition-p-9781119506874> (cit. on p. 179).
- [189] Izrail Solomonovich Gradshteyn and Iosif Moiseevich Ryzhik. *Table of integrals, series, and products*. Academic press, 2014. URL: <https://www.elsevier.com/books/table-of-integrals-series-and-products/gradshteyn/978-0-12-294760-5> (cit. on p. 184).